



## Doctoral Thesis

# **From Fresh Concrete Microstructure to Digitally Fabricated HPFRC: A Challenging Journey up From the Nanoscale in Search of Precious Digital Macro-Applications**

**Author(s):**

Ruffray, Nicolas

**Publication Date:**

2020-07

**Permanent Link:**

<https://doi.org/10.3929/ethz-b-000447710> →

**Rights / License:**

[In Copyright - Non-Commercial Use Permitted](#) →

This page was generated automatically upon download from the [ETH Zurich Research Collection](#). For more information please consult the [Terms of use](#).

DISS. ETH NO. 26937

***FROM FRESH CONCRETE MICROSTRUCTURE TO DIGITALLY  
FABRICATED HPFRC: A CHALLENGING JOURNEY UP FROM THE  
NANOSCALE IN SEARCH OF PRECIOUS DIGITAL MACRO-APPLICATIONS***

A thesis submitted to attain the degree of  
DOCTOR OF SCIENCES of ETH ZURICH

(Dr. Sc. ETH Zurich)

presented by

NICOLAS RUFFRAY

M. Sc. in Materials Science and Engineering  
École Polytechnique Fédérale de Lausanne (EPFL), Switzerland

born on 23.05.1986

citizen of

Pregny-Chambésy

accepted on the recommendation of

Prof. Dr. Robert J. Flatt, examiner  
Prof. Dr. Benjamin Dillenburger, co-examiner  
Prof. Dr. Dirk Lowke, co-examiner

2020

*Je dédie cette thèse à Fabrice qui, tel le petit prince, nous a quitté trop tôt pour rejoindre les étoiles, ta passion de toujours. Merci de m'avoir donné ton gout à la science et à sa rigueur enivrante que tu chérissais tant et qui a fait de moi le docteur que je suis devenu aujourd'hui.*

# Acknowledgements

*The epic journey that my PhD was, would never have been possible without the moral, physical and especially technical help and support of many people that I would like to heartily thank here.*

*First of all, I would like to thank Prof. Dr. Robert J. Flatt, my PhD supervisor and the head of the Physical Chemistry of Building Materials Laboratory at ETH Zürich. You are by far the best boss and colleague I ever had to work with in both my professional and academic lives. I think the best example of that is that I was never nervous or anxious before or after any of our numerous meetings. On the contrary I was always eager to talk to you, listen to your knowledge and take your always good, humane and diplomatic advices. And I honestly think it is the best indicator of what a great boss and person you are. Thank you very much for giving me the opportunity to do my PhD in your lab and I really hope our paths will cross again at some point for another even more epic journey. By the same occasion I would also like to thank Dr. Paul Bowen, who directed me towards Robert and his team. Also, I would like to thank here my PhD jury for having the courage of reading this manuscript and for giving me the opportunity to defend my thesis. Thanks also to the ETH Zürich Grant Projects program for sponsoring my PhD.*

*I would like to warmly thank all my colleagues at PCBM for being such amazing mates and source of knowledge, laughter and inspiration for all these years. Especially I would like to thank: Andrea Louys, for being like my second mom in the lab and for all your precious everyday help with the lab's administration, but also for always cheering me up in moments of doubts. Heinz Richner, for being like my second dad who I always went to bother with all my technical problems. Thank you very much for all your immeasurable help in the lab with my experiments and for always coming up with simple working solutions avoiding me to go astray in way too complicated approaches. Dr. Marta Palacios, for your precious help and supervision at the beginning of my PhD coupled with your Iberic and always positive mood. Asel Maria, for your knowledge of electron microscopy, but also for our long chats and your unbeatable cheerful Cuban mood. Dr. Timothy Wangler, for all your advices on academic life and for our always interesting chats about geopolitics.*



*Outside of ETH Zürich I would like to thank everyone who gave me their support in any kind of way during these five years.*

*Among those I would like to especially thank: Ekaterina Nadibaidze, my lovely wife, for following me to Zürich into this journey. I cannot thank you enough for the sacrifice you made by coming to Zürich but also for supporting me (and my 3D printer) in every sense of the word during this period and for always being my lifeline in moments of stress, doubts and difficulties. For all this among many other things; I love you. And also, thanks for proofreading this entire manuscript three times over... For someone not scientific I sincerely appreciate the love-hatred pain you went through and I am sure that you could have without doubts defended my PhD in my place after that.*

*My parents, Patrick and Valentina Ruffray, who, let's be honest, were not very fond of my decision of quitting my previous job to do a PhD, but who ended up (as usual) my most solid fans and supporters. Mom, dad, if I am the person I am today, it will always be thanks to you and to the love and energy you put into me and my education. And for this I will always be grateful to you. The success of this PhD is as certainly my merit as it is yours. Thank you from the bottom of my heart for everything you have done for me to make me the person I am today.*

*Anastasia Chrissanthakopoulos, for being an amazing friend of the family and for supporting me and especially Katia during these years as I am not sure we would have survived without you coming to cheer us up regularly on the week-ends. Also, thanks for running my 3D printer together with Katia at the end of my PhD while I was working in the lab when every minute was counting in order to get the final results in time for my defense. Michel Bolliger, for being my best friend during these years, for always making jokes calling me a doctor while I was not one (yet), and for all the good mood and the crazy but always working ideas you brought in our home. Thanks man! Gilles Nahon, Imran Quaine, Thomas Corthay and Anton Lebedev, my friends since my years at EPFL and my childhood, for supporting me in my decision of doing a PhD and for always cheering me up.*

*I would also like to thank the following persons on specific related projects:*

#### *Cryo-FIB-SEM Nano-Tomography*

*All member of ETH Zürich's ScopeM microscopy center and especially: Philippe Gasser, for your unmeasurable knowledge, help and hours on the Helios microscope when we were trying to make the cryo-FIB-SEM nano-tomography work. Even if in the end we didn't succeed, I will keep a very pleasant memory of our collaboration and your professionalism. Dr. Anne Greet Bittermann, for your help on the Leo microscope and the SEM-FIB-tomography part, as well as your always good and positive mood. Dr. Roger Wepf for your help and deep knowledge of the cryo-samples preparation. Dr. Falk Lucas, for your everyday help when I was performing cryo-samples preparation on my own and was (usually) encountering technical problems.*

*I would also like to thank all members of the ZMB microscopy center at the University of Zürich for their help in this complex and challenging topic, especially Dr. Andreas Kaech and Dr. Moritz Kirschmann.*

*Special thanks go to Stéphane Le Nédic for helping me out with drawing the diagrams explaining the supposedly origin of the scaling artefact.*

#### *Digital Fabrication*

*I would first like to thank the bachelor students with who I worked on the two subjects regarding concrete digital fabrication for their formidable work and for paying careful attention to the specificities of these projects: Neil Montague de Taisne and Felix Stutz for the topology optimised ceiling element and Kathrin Ziegler, Oliver Wach and Moritz Studer for the concrete canoe “skelETHon”.*

*I would like to warmly thank all the members of the DBT research group at ETH Zürich for their precious help in these collaborations and in particular: Mihail-Andrei Jipa for his always original but nevertheless excellent ideas and unquestionable expertise on FDM 3D printing. Dr. Mathias Berhard for his help on the powder bed printing. And Prof. Dr. Benjamin Dillenburger for his inexhaustible enthusiasm about digital fabrication technologies and for making these collaborations possible.*

*Also, I would like to thank Dr. Emmanuel Dénarié from the Structural Maintenance and Safety research group at EPFL for his precious help on the formulation of the high-performance fiber-reinforced concrete used in these projects. Special thanks also go to Christophe Gromas from LafargeHolcim for helping me finding the specific cement used for the formulation of this particular concrete easily found in France but much more exotic in Switzerland. Thanks to Dr. Lex Reiter for his welcoming help regarding the modified three-points bending tests of FDM 3D printed samples. Last but not least, I would like to heartily thank Prof. Dr. Alexander Puzrin, professor of Geotechnical Engineering at ETH Zürich for his help on the soil mechanic aspects of counter-pressure casting technology, with who I had the pleasure of talking science in my second mother tongue: Russian.*

*Finally, I would like to thank anyone who I have not explicitly mentioned in these acknowledgments and who brought me any kind of help and/or support during this PhD.*

*Thank you all from the bottom of my heart for this amazing journey in the world of science that I love and for which I have the deepest respect and unmeasurable passion.*

# Abstract

Since the invention of Portland cement during the first industrial revolution, concrete has become an inseparable aspect of modern societies by being the predilection material used for the construction of the vast majority of housing and infrastructure. The recent development of concrete digital fabrication holds promises of a much more efficient way to build by granting access to free form geometrical complexity with appealing cost efficiency, reduced environmental footprint and increased worker safety. However, this transition to the digital era of concrete requires a greater mastery of this complex material which calls for a deeper and better understanding of its chemistry and microstructural behaviour. In this regard, the rheology of low water to cement ratio concretes and in particular the behaviour of superplasticisers in such systems remains difficult to predict and control, not only for digital fabrication, but much more broadly for concrete technology at large.

In this thesis, the impact of PCE superplasticisers on the nucleation and formation of hydrates in fresh model cement pastes was investigated by using cryo-FIB-SEM nano-tomography. Qualitative results showed that direct addition of PCE increases the dispersion as well as the amount of formed hydrates while reducing their size. However, this work faced insurmountable holdbacks with regard to the acquisition of unbiased tomographic quantitative data due to a recurring imaging issue budded “scaling artefact” and supposedly originating from the inhomogeneous nature of frozen cement pastes.

The second part of this PhD was dedicated to investigating the possible usage of thin digitally fabricated formworks in combination with low water to cement ratio fibre-reinforced concretes in order to produce topologically optimised elements. The approach chosen by this work was to avoid any advanced setting and hardening controls of the concrete in opposition to other techniques of digital casting. Two structurally viable elements were produced over two collaborative projects with the *dbt* research group (D-ARCH, ETH Zürich). The production of these elements led to the development and usage of several HPFRC formulations that were meeting the specific rheology and mechanical requirements of the projects.

The first produced element was a ceiling/flooring panel cast in a sand binder-jetting 3D printed lost formwork. The second element was a fully functional concrete canoe, the load bearing skeletal structure of which was 3D

printed as a sub-millimetric formwork by FDM. Cast using a specially developed technique called “counter-pressure casting” to counteract the mechanical fragility of the formwork, the “*skelETHon*” canoe successfully participated in the 2017 Concrete Canoe Regatta winning the first prize of Design Innovation Awards.

These two demonstrators showed the great potential of 3D printing thin formworks for complex concrete elements highlighting the “complexity for free” promise made by concrete Digital Fabrication in general. Importantly it has served to define a new digital fabrication process with concrete, defined as counter-pressure casting that presents many advantages for a possible adoption by industry.

In summary, this thesis relates the importance of a better understanding of concrete chemical and microstructural aspects that are unconditionally needed for any advanced macro-application, including but not limited to concrete digital fabrication.

# Résumé

Depuis l'invention du ciment Portland lors de la première révolution industrielle, le béton est devenu un élément indissociable de la société moderne et s'est imposé comme le matériau de prédilection pour la construction de logements et d'infrastructures. Le développement récent des technologies de fabrication digitale promet une manière de bâtir plus efficace en comparaison des coffrages conventionnels, donnant accès à une liberté géométrique et un rapport coût-efficacité jamais atteints jusqu'à présent. De plus, l'empreinte carbone d'un tel procédé de construction est moindre et la sécurité des ouvriers sur le chantier se trouve également augmentée. Néanmoins, cette transition vers l'ère digitale nécessite une maîtrise parfaite de ce matériau complexe requérant une compréhension poussée de sa chimie et de sa microstructure. A cet égard, la rhéologie des bétons à faible rapport eau sur ciment et, en particulier, le comportement des superplastifiants dans de tels systèmes restent difficiles à prédire et à contrôler non seulement pour des applications de fabrication digitale, mais également dans le domaine de la technologie du béton en général.

Dans cette thèse, l'impact des superplastifiants de type PCE sur la nucléation et la formation d'hydrates dans des pâtes de ciment modèle est étudié par cryo-nano-tomographie FIB-MEB. Les résultats qualitatifs de cette étude montrent que l'ajout direct de PCE augmente la dispersion ainsi que la quantité d'hydrates formés tout en réduisant leur taille. Cependant, ce travail a fait face à des difficultés insurmontables quant à l'acquisition de données tomographiques quantitatives non-biaisées en raison d'un artefact d'imagerie récurrent baptisé « artefact d'écaillement » supposé provenir de l'inhomogénéité des échantillons de pâtes de ciment vitrifiées.

La seconde partie de cette thèse est dédiée au développement et à l'utilisation de coffrages fins fabriqués de manière digitale en combinaison avec des bétons fibrés haute performance (BFHP) afin de produire des éléments structuraux optimisés topologiquement. L'approche choisie dans ce travail a permis d'éviter l'utilisation de moyens de contrôles avancés de prise et de durcissement du béton contrairement à d'autres techniques de coulage digital. Deux éléments structuraux ont été produits au travers de deux projets collaboratifs avec le groupe de recherche dbt (D-ARCH, ETH Zürich). La production de ces éléments a également conduit au développement et à l'usage

de plusieurs formulations de BFHP répondant à des cahiers des charges spécifiques aux projets en matière de rhéologie et de propriétés mécaniques.

Le premier élément produit est un panneau de plafond coulé dans un coffrage perdu imprimé en 3D par jet de liant sur lit de sable. Le second élément est un canoë en béton fonctionnel dont la structure squelettique porteuse en BFHP a été coulée dans un coffrage d'épaisseur submillimétrique imprimé en 3D par dépôt de fil fondu. Fabriqué grâce au développement d'une nouvelle technique appelée « coulage par contre-pression » pour compenser la fragilité relative du coffrage, le « *skelETHon* » a participé avec succès à l'édition 2017 de la Régate de Canoës en Béton tenue à Cologne en Allemagne en y remportant le premier prix pour l'Innovation Design.

Ces deux démonstrateurs prouvent l'importance du potentiel des coffrages fins imprimés en 3D pour produire des éléments structurels complexes soulignant ainsi le principe de « complexité gratuite » promise par la fabrication digitale. Par ailleurs, ces travaux ont permis le développement d'une nouvelle technique dans ce domaine, appelée coulage par contre-pression, qui présente de nombreux avantages pour un transfert potentiel de cette technologie vers l'industrie.

En résumé, cette thèse souligne l'importance d'une meilleure compréhension des aspects chimiques et microstructuraux des matériaux cimentaires frais qui est incontestablement nécessaire au développement de macro-applications avancées dans le domaine de la fabrication digitale en particulier et des technologies du béton en général.

# Table of Contents

<b>Acknowledgements.....</b>	<b>i</b>
<b>Abstract.....</b>	<b>iv</b>
<b>Résumé.....</b>	<b>vi</b>
<b>Table of Contents.....</b>	<b>viii</b>
<b>Chapter 1 – Introduction .....</b>	<b>1</b>
1.1. General Introduction.....	1
1.1.1. Cryo-FIB-SEM nano-Tomography .....	3
1.1.2. Digital Fabrication .....	3
1.2. Objectives of the Thesis.....	5
1.3. Structure of the Thesis.....	7
<b>Chapter 2 – State of the Art.....</b>	<b>9</b>
2.1. Cryo-FIB-SEM tomography of fresh model cement pastes .....	9
2.1.1. Cement-Admixture Chemistry .....	9
2.1.2. Electron cryo-microscopy .....	14
2.1.3. Cryo-FIB-SEM tomography of fresh cement pastes .....	17
2.2. Digital Fabrication .....	21
2.2.1. Extrusion printing.....	21
2.2.2. Powder-bed 3D printing.....	23
2.2.3. Digital Casting.....	24
2.2.3.1. Digitally articulated slip form formwork.....	24
2.2.3.2. Admixture Controlled Digital Casting.....	26
2.2.3.3. Digitally fabricated formworks .....	27
2.2.4. Implications from the State of the Art .....	30
<b>Chapter 3 – Cryo-FIB-SEM nano-tomography of fresh model cement pastes</b>	<b>31</b>
3.1. Introduction.....	31
3.2. Scanning Electron and Focused Ion Beam Microscopy .....	33
3.3. Materials and Methods .....	35
3.3.1. Model cement paste.....	35
3.3.2. High pressure freezing.....	36

3.3.3. Cryo-transfer and conductive coating .....	39
3.3.4. Cryo-FIB-SEM tomography.....	41
3.3.4.1. Microscope setup .....	41
3.3.4.2. Tomography preparations .....	43
3.3.4.3. FIB-SEM nano-tomography .....	46
3.4. Results & Discussion .....	50
3.4.1. Qualitative analysis of model cement pastes microstructures.....	50
3.4.2. Challenges faced during cryo-FIB-SEM nano-tomography .....	54
3.4.2.1. Artefact description.....	54
3.4.2.2. Investigations on the origin of the artefact .....	56
3.4.2.3. Attempts to attenuate the artefact.....	62
3.4.2.4. Miscellaneous observations .....	66
3.4.2.5. Previously unreported occurrence of scaling.....	68
3.5. Conclusions and Outlook.....	71
<b>Chapter 4 – HPFRC casted in 3D powder printed moulds.....</b>	<b>73</b>
4.1. Introduction.....	73
4.1.1. Binder jetting .....	74
4.1.2. Binder Jetting as Stay-in-Place Formwork .....	76
4.2. Materials and Methods .....	77
4.2.1. Binder-Jetting 3D Printing Technology .....	77
4.2.2. HPFRC Mix.....	78
4.2.2.1. Formulation .....	79
4.2.2.2. Mixing Procedure .....	79
4.2.2.3. Measured properties .....	79
4.3. Results & Discussion .....	80
4.3.1. Digital design of the slab .....	80
4.3.2. Mix requirements and optimisation.....	82
4.3.2.2. Filling tests.....	83
4.3.2.3. Resulting mechanical properties .....	87
4.3.3. Slab element preparation and infill.....	88
4.4. Conclusions and Outlook.....	90
<b>Chapter 5 – HPFRC casted in FDM printed moulds.....</b>	<b>92</b>
5.1. Introduction.....	92
5.2. Methodology .....	94
5.2.2. Why a Concrete Canoe?.....	94
5.2.3. Design through Topology Optimisation .....	96
5.2.4. FDM 3D Printing.....	99
5.2.5. Submillimetre Formwork for Concrete .....	100
5.2.6. Formwork Fabrication.....	101
5.2.7. Discretisation.....	103



5.2.8. Concrete Casting .....	105
5.2.9. Additional counter-pressure casting trials.....	111
5.3. Results and Discussion .....	112
5.3.1. Concrete canoe .....	112
5.3.2. Characterisation of counter-pressure effectiveness .....	115
5.3.2.1. Brief description of counter pressure-casting experiments.....	115
5.3.2.2. Nature of observed damage with counter-pressure casting.....	117
5.3.2.3. Nature of failure for direct casting.....	121
5.3.3. Suggested follow-up experiments.....	125
5.3.3.1. Stress induced corrosion.....	125
5.3.3.2. Density of counter-pressure material .....	126
5.3.3.3. Lightweight concrete.....	126
5.4. Outlook.....	127
5.4.1. Casting Technology needs.....	127
5.4.2. Mould printing needs.....	128
5.4.3. Industrial process needs .....	129
5.5. Conclusion .....	130
<b>Chapter 6 – Conclusions and Outlook.....</b>	<b>131</b>
6.1. Cryo-FIB-SEM nano-tomography of fresh model cement pastes.....	131
6.1.1. Main Outcomes .....	131
6.1.2. Outlooks.....	134
6.2. Digital Casting.....	135
6.2.1. Main Outcomes .....	135
6.2.2. Outlook.....	139
<b>References .....</b>	<b>141</b>
<b>Appendix A : HPFRC formulation design data .....</b>	<b>152</b>
<b>Appendix B : Resolving stress induced corrosion of FMD 3D printed formwork to enable digital counter-pressure casting .....</b>	<b>154</b>
Abstract .....	155
B.1. Introduction .....	155
B.2. Materials and Methods.....	157
B.2.1. FDM 3D printed formworks.....	157
B.2.2. Inverted three points bending tests .....	158
B.2.3. Concrete Casting .....	159
B.2.3.1. Concrete formulation and mixing procedure .....	159
B.2.3.2. Counter-pressure casting .....	159
B.3. Results and Discussion.....	160
B.3.1. Preliminary PLA testing.....	160
B.3.2. Stress induced corrosion attenuation investigations .....	162

B.3.3. Enabling failure-free counter-pressure casting.....	164
B.3.3.1. Tubular formworks.....	164
B.3.3.2. Prismatic formworks .....	166
B.3.3.2. Outlooks .....	170
B.4. Conclusions .....	171
Acknowledgements.....	171

# Chapter 1 – Introduction

## 1.1. General Introduction

With serious concerns regarding the vulnerable state of the environment, material efficiency is becoming a critical design driver in civil engineering. This is especially relevant for materials that are difficult to recycle, such as concrete. Concrete is of particular relevance in relation to material efficiency because it is by far the most used construction material in the world, being used twice as much as all the other construction materials combined [1]. Moreover, the amount of concrete used annually is predicted to double in the next thirty years.

Concrete is used in such vast amounts for good reasons. Its excellent structural properties, combined with its versatility, make concrete indispensable in a wide variety of environments and applications, both for buildings and infrastructure works. Furthermore, concrete is celebrated by architects because it can be cast into any shape and thus it is in theory capable of materialising almost any imaginable design.

Since the invention of modern Portland cement during the first industrial revolution, the construction industry has gone through a never-ending evolution driven by the always increasing demand for housing and infrastructure. Nevertheless, for the last couple of decades the construction sector suffers from a rather low productivity and creativity compared to other economic sectors; pressured by more and more demanding ecological and cost efficiency aspects combined with a modern architecture, which is still strongly limited to prismatic shapes due to traditional use of wooden formwork.

This increasing pressure on the construction sector translates in an important driving force for research and development of new, better and smarter ways to build. A perfect example of this evolution is the robotically assisted manufacturing recently introduced in the construction sector<sup>1</sup>. Generally called

---

<sup>1</sup> <https://www.apis-cor.com/>  
<https://cobod.com/>  
<https://3dprint.com/94558/3d-printed-hotel-lewis-grand/>

digital fabrication, this technology remains for the moment mainly at an academic research level, but its already initiated transfer towards the construction industry promises to revolutionise the way we build.

However, concrete and generally speaking cementitious materials, regardless of their important usage, remain complex materials and present a wide variety of new challenges to overcome for flawless industrial applications of digital fabrication. In particular, their dynamic placement required for the majority of such applications brings research to push the understanding of chemistry and microstructural behaviour of cementitious materials even further.

In this regard chemical admixtures in general and superplasticisers in particular play an important role. These organic polymers are used as dispersants in cementitious materials and are produced yearly in amounts of 2-5 Mio tons [2]. Such compounds play an important role in allowing concrete with low environmental impact to be produced [3,4]. Moreover, these admixtures also have an important role to play in digital fabrication, along with other admixtures, including viscosity modifiers and accelerators [5]. An important aspect of superplasticisers, is that they interact during the early formation of hydrates, in particular ettringite, and that this modifies their overall performance, regardless of the application [6–8]. Despite its central importance, this process remains poorly understood and deserves further investigation.

The global objective of this PhD was to investigate different aspects of superplasticisers in cementitious systems, starting from basic investigations on how these polymers affect ettringite nucleation and growth in terms of initial microstructure formation. For this, work began exploring possibilities of an advanced electronic microscopy technique called cryo-FIB-SEM nanotomography in order to investigate in both qualitative and quantitative ways the impact of Poly-Carboxylate Ether (PCE), a widely used type of superplasticiser, on the precipitation of the first hydrates in a controlled system of fresh model cement pastes. Such results on initial impact of PCEs on microstructure can be of particular interest for a better understanding and control of low water containing systems where the rheology could be impacted by close packing interactions of unhydrated cement and hydrates particles.

In a complimentary aspect of the above, another objective of this PhD thesis was to use such systems and in particular high-performance fibre reinforced concrete (HPFRC) in combination with thin digitally fabricated formworks in order to investigate and develop new processes for digital fabrication in general and digital casting in particular.

### 1.1.1. Cryo-FIB-SEM nano-Tomography

Concrete material science has always faced non-negligible challenges to study the microstructure of cementitious materials. While the study of unhydrated cement and hardened concrete is rather accessible through a wide range of established observation techniques such as Brunauer-Emmett-Teller specific surface measurements, Blaine or Malvern granulometry, X-ray diffraction analysis, optical and electron microscopy or various porosimetry measurement techniques; unbiased microstructural observations of fresh cementitious pastes always were and up to this day remain challenging. This is mainly due to the dynamic transient nature of this stage of concrete and to the presence of water of which the removal or substitution for observation almost always results in an alteration of the material microstructure.

The usage of cryo-FIB-SEM nano-tomography was originally developed for observation of biological samples that face similar issues. It allows, at the expense of considerable time and resource consumption, to volumetrically observe and characterise water containing microstructures with the resolution of modern scanning electron microscopy with only minimal to no alterations. This makes Cryo-FIB-SEM nano-tomography a very interesting and promising technique in order to analyse in both qualitative and quantitative ways the microstructure of fresh cement pastes.

### 1.1.2. Digital Fabrication

Robotically assisted manufacturing has been successfully used for decades in numerous sectors such as the automotive industry. However, the recent advent and generalisation of digital fabrication is considered by many to be the third industrial revolution and its introduction into the construction industry promises to revolutionise the way we build with the potential of freeform architecture, reduced costs for complex construction, and increased worker safety [9]. Digital fabrication also promises to bring a major increase in productivity without being at the expense of sustainability. Indeed, efficient material placement without the need of custom-made and usually one-time use formwork, allows both a reduction of construction waste and a greater material efficiency in design, fabrication and exploitation stages.

By far the most popular approach to digital fabrication with concrete is 3D extrusion printing, a process pioneered by Prof. Khoshnevis [10,11]. In this process concrete is extruded layer by layer. Important demonstrators have been completed as described in Chapter 2, Chapter 4 and Chapter 5.

Digital fabrication with concrete is not restricted to extrusion printing. While it is not the objective to cover all processes, a brief overview is given here of those developed with the Swiss National Centre for Competence in Research on Digital Fabrication in Architecture ([www.dfab.ch](http://www.dfab.ch)) and to which the author of this thesis has most been exposed.

Many of these processes were demonstrated in the large-scale demonstration project that has been realised by building the dfab-house (Figure 1.1). This experimental but nevertheless fully habitable house was the first one built with multiple robotically driven processes. It combines several radically different approaches to digital fabrication such as unique shaped mullions produced by robotic slipping of an actuated formwork (Smart Dynamic Casting) [12], formwork-free multi-curvature wall using Mesh Mould technology [13] and a 3D printed topologically optimised Smart Slab, which apart from having pleasing aesthetics, reduces the amount of material compared to a traditional slab by 50%, and also integrates several building facilities such as electrical and water conduits [14].



*Figure 1.1: Interior of the dfab-house, EMPA, Zürich. Left: Mullions produced by Smart Dynamic Casting. Top: Smart Slab. Right: Multi-curvature Mesh Mould wall (Photo: Roman Keller)*

## 1.2. Objectives of the Thesis

This thesis was divided into two main objectives as presented above.

The first part of this work consists of using cryo-FIB-SEM nano-tomography to study the impact of PCE superplasticisers on the formation of first hydrates in a fresh model cement paste. In particular, the known different impacts of PCE direct and delayed additions on the nucleation, precipitation and flocculation of first hydrates were targeted through the observation of fresh model cement pastes microstructures. For this we planned to rely on cryo-SEM-FIB nano-tomography in order to make quantifiable observations on the first hydrates particles size, amount, aspect ratio and agglomeration. The results provided by this part should have brought a better understanding of the microstructural behaviour of fresh cementitious materials in general and be of particular use for low water containing systems such as HPFRC, used in the second part of this thesis, in which particles close packing mechanics can impact the rheology. However, this work faced major technique-related holdbacks and challenges regarding the exploitation of cryo-FIB-SEM nano-tomography that only lead to qualitative-grade analysis without allowing unbiased quantitative one. These issues and the conclusions of the related systematic work are described in details in Chapter 3.

The purpose of the second part of this thesis was to explore and develop new digital casting processes for structural elements through two separate approaches of using thin digitally fabricated formworks casted with high-performance steel-fibre reinforced concrete. In opposition to other digital fabrication processes presented in Chapter 2, the goal here was to avoid using finely tuned setting controls of the concrete medium.

The first approach investigated the possibility of using powder bed sand 3D printing in order to produce topologically optimised slabs as flooring/ceiling elements. A high-performance fibre-reinforced concrete (HPFRC) was formulated and adapted to the specific mechanical and workability needs of this project. The 3D printed lost formwork of the ceiling element was successfully casted (Figure 1.2).



Figure 1.2: Topologically optimised ceiling element. (Photo: dbt, ETH Zürich)

The second work consisted of developing and fabricating a concrete canoe to participate in the 2017 *Beton Kanu Regatta* (Concrete Canoe Regatta) competition in Köln (Germany). A skeletal structure of the canoe was obtained by topological optimisation and 3D printed as formwork by Fused Deposition Modelling (FDM) 3D printers. This formwork was then casted with one of the HPFRC formulations developed in the previous work in order to obtain a structurally viable skeleton of the canoe. Because of the sub-millimetre thickness and therefore high fragility of the 3D printed formwork, a special method of casting was investigated and implemented to counteract hydrostatic pressure of the concrete using loose sand as counter-pressure medium dubbed Counter Pressure Casting. The skeletal structure (Figure 1.3) of the canoe was finally water-proofed through the usage of textile painted with liquid mortar. The concrete canoe was successfully fabricated and participated in the the 2017 *Beton Kanu Regatta* winning the first prize for Construction Innovation Awards.

Additionally to the canoe, the process of counter pressure casting was further investigated through a series of more controlled systems in order to better understand the limits of this fabrication process and investigate ways to improve it with the objective of a potential transfer to industrial applications.





*Figure 1.3: Skeletal structure of the concrete canoe. (Photo: dbt, ETH Zürich)*

## 1.3. Structure of the Thesis

The present manuscript is structured as follows:

Chapter 2 presents the state of the art and is divided in two main parts. The first one, dedicated to cryo-FIB-SEM nano-tomography, presents a brief theoretical base of scanning electron microscopy concepts needed for a better understanding of Chapter 3. It is followed by the state of the art regarding this technique in general and its past usage to study fresh cement pastes in particular. The second part of the chapter is dedicated to the state of the art regarding concrete digital fabrication in general and techniques involving digital casting in particular.

Chapter 3 presents the work performed on the subject of cryo-FIB-SEM nano-tomography of fresh model cement pastes. This chapter contains a substantially detailed Material and Methods section of which the goal is to accentuate the heavy technique-oriented aspect of this work and provide detailed guidance for any future research that would use this technique. The chapter then presents and discusses the obtained qualitative results. After this it describes in detail the challenges and issues that were faced in obtaining quantitative tomography data. Importantly, it proposes an explanation of the probable origins and possible solutions to overcome these problems in future. Finally, this chapter puts in perspective the results obtained by a previous work using this technique in regards to the problems faced during this PhD. In short it appears that previous work on the subject faced similar artefact-issues much beyond the scope of what can be reasonably understood through the available publications. While

the image treatments that seem to have been applied to deal with these issues do not compromise most of the published work, they profoundly affect the observations that this thesis had set itself as objective.

Chapter 4 presents the work realised for the fabrication of a topologically optimised ceiling/flooring element by using sand binder-jetting 3D printed lost formwork and HPFRC. The chapter presents and discusses the details of the design phases as well as the consequent work dedicated to optimise the HPFRC formulation to meet the rheological requirements needed to cast a tubular shaped formwork.

Chapter 5 presents the work realised for the fabrication of a topologically optimised concrete canoe dubbed “*skeleTHon*” that participated in the 2017 Concrete Canoe Regatta in Germany, as well as the more detailed investigation on counter pressure casting. The chapter presents the details of the design phase with a particular focus on the possibilities and limitations of FDM 3D printing. It also presents and discusses the new casting process of counter-pressure casting, the development of which was motivated by the rather fragile mechanical aspects of FDM prints and the intricate tubular shape of the concrete canoe formwork that was casted with HPFRC developed for the work described in Chapter 4. The chapter also presents and describes additional counter-pressure trials realised to better understand the mechanics and limitations of this technique. It leads to several promising outlooks aimed at improving this process for a potential future industrial application.

Chapter 6 presents a summary of the results and challenges faced in this work, and details the conclusions drawn by this thesis. It also presents an outlook of the possible future usage of cryo-FIB-SEM nano-tomography for studying fresh cementitious materials as well as of the possible evolution of the two digital casting techniques presented in this thesis. It is argued that while not the most elegant, counter pressure casting may offer industry several important advantages in terms of efficiency, robustness and quality of surface finish.

# Chapter 2 – State of the Art

Due to the overall structure of this PhD thesis, this chapter is divided in two parts allowing to separately present the scientific state of the art of the cryo-FIB-SEM nano-tomography and digital casting related topics.

## 2.1. Cryo-FIB-SEM tomography of fresh model cement pastes

### 2.1.1. Cement-Admixture Chemistry

Concrete, even if being the most widely used material in the world after water, remains nevertheless a rather complex one both in terms of chemical and physical aspects.

Cement is the most important ingredient of concrete, because as a hydraulic binder its reaction with water is responsible for the hardening behaviour of concrete. In this hydration process, cement goes through several stages commonly described as dissolution, induction and hardening phases. It is during the first two of those that concrete can be handled and ultimately placed in the desired mould or shaped into the final desired element by other means as digital fabrication.

An important aspect in any concrete material is the ratio between the mass of water and the mass of cement that is used to formulate it, commonly referred to as the w/c ratio. In theory a w/c ratio of 0.25 (1 mass of water for 4 masses of cement) is enough, chemically speaking, to ensure the total hydration of cement. In common practice, a w/c ratio of 0.25 is virtually impossible to use without additional chemical help, as the resulting concrete will never reach a workable semi-liquid state and rather remain in a semi-dry and lumpy one making it impossible to place. An increased amount of water leading to higher w/c ratios is therefore commonly used in practice. However, and as mentioned above, any excess of water above a w/c ratio of 0.25 is not consumed by the hydration

reaction of cement ultimately leading to increased porosity in the final concrete element as the excess water will end up evaporating over time leaving behind empty spaces.

Porosity, even if useful in some specific cases when well controlled such as in light weight concrete or freeze and thaw protection, is an aspect in concrete that usually leads to major durability issues and weaker mechanical properties. On the durability side, porosity grants access to exterior elements to penetrate in concrete leading to problems such as carbonation, reinforcement corrosion or sulphate attack. Mechanically speaking, increased porosity directly decreases mechanical properties such as compressive and tensile strengths. This is illustrated in Figure 2.1, where a series of micrographs of cement pastes prepared with different w/c values include text boxes giving their approximate compressive strengths. An important aspect to note in this figure is that porosity (black areas) increases with w/c.

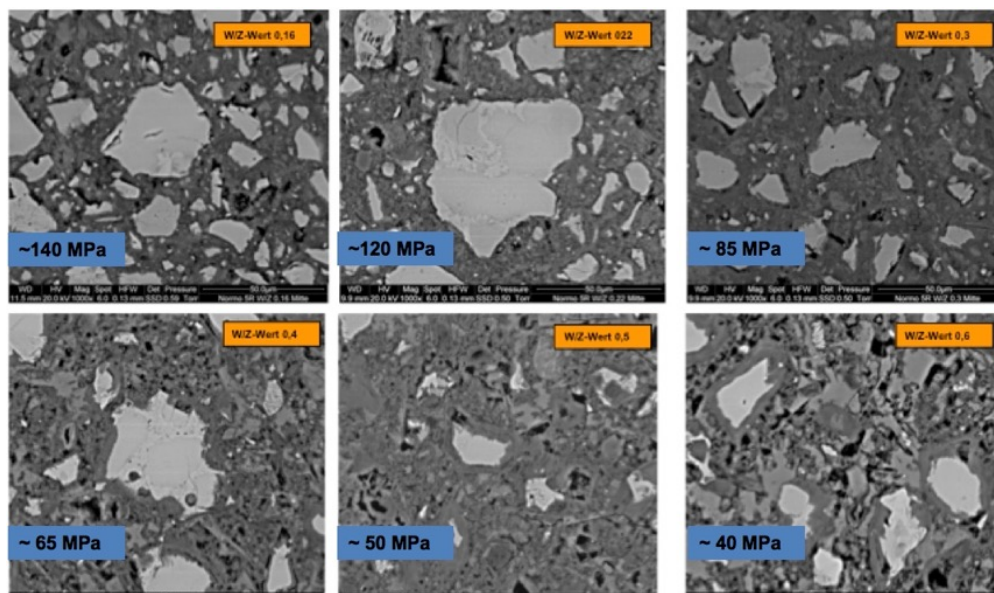


Figure 2.1: w/c ratio impact on cement paste microstructure and compressive strength.

In order to avoid problems linked to the usage of high w/c ratios both durability and mechanically wise, the usage of specific chemical admixtures became common in the construction industry over the last decades with the progress and development of modern chemistry [15]. Commonly called superplasticisers (SP), these chemical admixtures have known for the last century a constant and rapid evolution through several generations of products [16]. From polymelamine sulfonates, naphthalene sulfonates and lignosulfonates in the nineteen-thirties and nineteen-sixties to polycarboxylates and polycarboxylate-ethers comb copolymers recently, superplasticisers allow to keep the w/c ratio relatively low while ensuring a good workability of concrete.

Polycarboxylate-ethers (PCE) comb copolymers are the most modern and currently among the most commonly used superplasticisers. Comb shaped, they possess a negatively charged back-bone allowing them to adsorb on cement particles exposing their side chains outwards the cement grains as can be seen in Figure 2.2 [2,7,17]. This adsorption configuration results in a strong dispersion of otherwise agglomerated cement grains throughout a combination of electrochemical and steric repulsions. This dispersion effect is the main mechanism allowing a better workability of concrete while keeping w/c ratios at relatively low values [18].

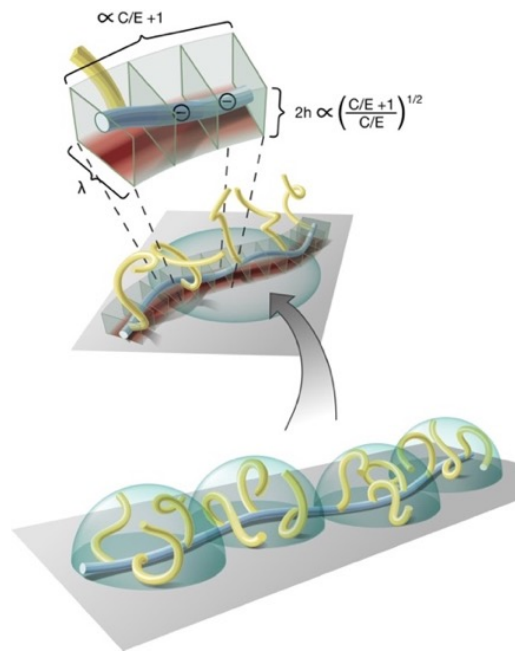


Figure 2.2: Schematic representation of molecular and submolecular scale characteristics of an adsorbed comb-copolymer. Source: [7] (Illustration by Fabian Rüdy, [www.andraia.ch](http://www.andraia.ch))

Adsorption mechanics of PCEs and their effects on cement hydration especially at very early age are complex and numerous [17,19]. PCEs are also known for their variable delaying effects on setting of concrete and their variable efficiency over time depending on their molecular structure, their amount and the way they are added to the concrete mix.

Comb copolymers such as PCEs have a well-known setting delaying effect on concrete [20,21]. The amplitude of this effect is linked to the PCEs molecular structure and dosage, as visually summarised in Figure 2.3. Importantly this impact is linked to the ability of these polymers to inhibit the dissolution of tricalcium silicate [7,22], but also to how much polymer gets consumed during the initial stage of ettringite formation, as illustrated in Figure 2.4 for the case when the polymer is included in the mixing water (direct addition).



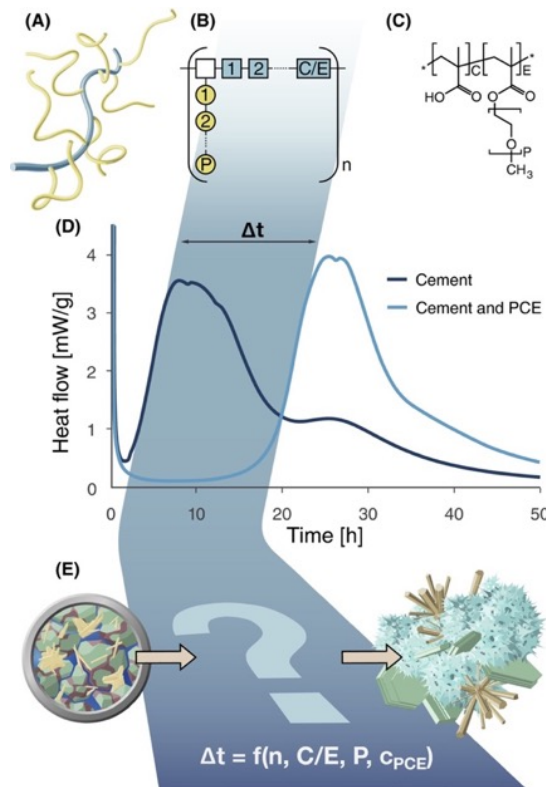


Figure 2.3: Schematic representation of the retarding effect of comb-copolymers on cement hydration kinetics. Source: [7] (Illustration by Fabian Rüdy, [www.andraia.ch](http://www.andraia.ch))

Indeed, the way of adding PCEs to the mix plays a major role in the formation of very first hydrates and in the efficiency of the superplasticiser over time until setting. The most commonly used method is the above-mentioned “direct addition” and consists of adding the superplasticiser to water prior to the cement. It contrasts with “delayed addition” where cement is added to water before the superplasticiser. The direct addition is known to promote the formation of smaller, more numerous and more dispersed crystals of ettringite and other early hydrates in the very first seconds of mixing, which in combination with a preferred adsorption of PCEs on ettringite, reduces the amount of polymer adsorbed on cement grains and in particular on  $C_3S$ . As can be observed in Figure 2.4 a minimal dosage of superplasticiser  $c^*$  is needed to saturate the ettringite crystals surfaces, before a fraction of the added polymer can adsorb on other cement phases such as silicates. Below this concentration  $c^*$ , very little to no effect is observable on both retardation and workability of concrete.

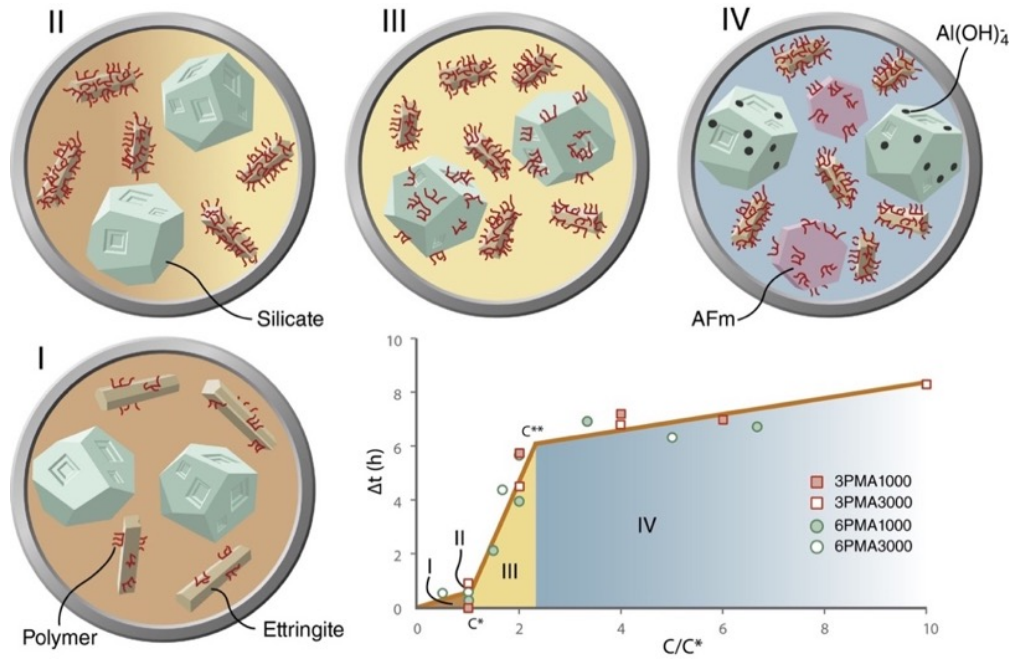


Figure 2.4: Hydration delay in case of direct addition. Source: [7] (Illustration by Fabian Rüdy, [www.andraia.ch](http://www.andraia.ch))

An important observation here is that PCEs enhance the nucleation of ettringite. This is apparent by an experimentally demonstrated increase of the specific surface of the model cement used in the study by Marchon et al [7]. This specific surface increase continues with increasing dosage including for ones in excess of  $c^*$ . This makes the process particularly difficult to quantify, in particular with regard to the role of molecular structure. Such behaviour also affects the impact of PCEs on rheology, but while this effect is known, it also remains to be understood in terms of dosage and molecular structure.

Getting back to Figure 2.4, a second critical dosage noted  $c^{**}$  can be identified. It corresponds to the point where so much ettringite is formed that the sulfate carrier is fully consumed or not able to dissolve fast enough. This leads to a silicate-aluminate-sulfate imbalance, something often referred to as undersulfation. If the dosage used is above  $c^{**}$  not only ettringite but also AFm forms. This has two consequences. First there is a rise in specific surface due to the AFm sheet structure. Second, there should be an increase in the concentration of aluminate ions in solution that is a well-known result of the higher solubility of AFm as compared to ettringite. Through this higher concentration of aluminates and the full consumption of PCEs by the aluminate hydrate surfaces, the retardation of C3S is not more governed by PCE adsorption but by the adsorption of aluminate ions. To confirm this hypothesis, Marchon et al showed that a (model) cement paste without PCEs, but containing too low amounts of the sulfate carrier, leads to the same retardation as the one in the plateau above  $c^{**}$  in Figure 2.4. Consequences on rheology are again difficult to establish.

However, it is generally accepted that the polymers “consumed” in the formation of aluminate hydrates do not contribute to dispersing cement grains [6].

In comparison, a cement paste that would be subjected to a delayed addition of PCE would require smaller dosages of superplasticiser in order to reach the same level of workability as the ettringite is believed to would have formed in less dispersed and bigger crystals usually agglomerated on the surface of cement grains resulting in a lower overall specific surface and therefore a lower “consumption” of the superplasticiser.

It is the details of this particular difference between PCE direct and delayed addition that this PhD initially set off to investigate through the observation of fresh cement paste microstructure. For this we planned to rely on cryo-SEM-FIB nano-tomography in order to make quantifiable observations on the first hydrates particles size, amount, aspect ratio and agglomeration.

### 2.1.2. Electron cryo-microscopy

The advent of electron microscopy was an important step for science and industrial quality control allowing detailed observation, analysis and quantification of microstructures below the micrometric scale with resolutions now reaching a few nanometres for Scanning Electron Microscopy (SEM) and of few tenths of nanometres for the Transmission Electron Microscopy (TEM).

In concrete research, the use of SEM became common in the last several decades in order to observe and study the complex microstructure of both anhydrous and hydrated cementitious materials (e.g. Figure 2.1). Samples for SEM undergo a meticulous cutting, polishing and conductive coating procedure. Traditional electronic microscopy requires the samples to be placed in a chamber under low vacuum for observation (e.q. 1 Torr = 1.33 mbar), making the presence of liquid water and therefore observation of fresh cement pastes impossible. However, Environmental Scanning Electronic Microscopes (ESEM) allow the observation of samples containing small amounts of water thanks to increased pressures in the vacuum chamber (e.q. 20 Torr). While this is helpful in limiting decomposition of hydrate phases and consequent morphology changes, such microscopes remain limited to exterior observations, mainly of fractured samples. Thus, in the case of fresh cement pastes ESEM does not provide any insights on the inner microstructure of the hydrating paste.

The invention and development of modern cryo-electron microscopy took place in the nineteen-eighties and was mainly conducted by Alasdair McDowall and Jacques Dubochet, who in 2017 received the Nobel prize in chemistry<sup>1</sup> for his work in this field [23]. The development of this technique was driven by the

---

<sup>1</sup> <https://www.nobelprize.org/prizes/chemistry/2017/dubochet/facts/>



needs in the fields of biology and microbiology to be able to observe and characterise the microstructure of biological samples without altering them by the necessity of removing or replacing water [23,24]. In order to be observable with cryo-electronic microscopy, samples containing water are frozen. To avoid damage to the samples due to both the volume change of water upon freezing and the formation of ice crystals, the technique of high-pressure freezing was developed by Hans Moor et al. around the same period [25].

This process takes advantage of the specificity of the water phase diagram (Figure 2.5). Of particular importance in that figure is the Ih phase, which corresponds to the ice phase that would normally form upon freezing at ambient pressure. It is characterised by hexagonal crystalline structure and a lower density than liquid water, causing volume expansion and possible micro and macrostructural damage upon freezing.

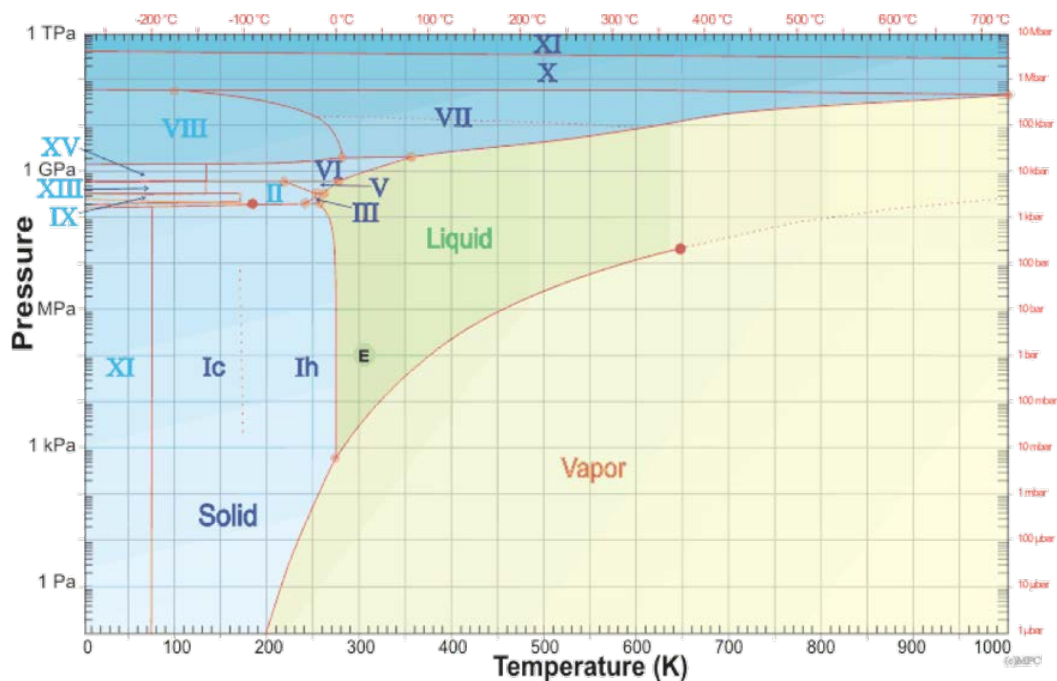


Figure 2.5: Phase diagram of water. “E” represents ambient conditions. Ih is the crystalline hexagonal structure phase of ice that forms when water is freezing at ambient pressure involving volumetric expansion. The combination of the crystalline structure and the volumetric expansion usually alters the microstructure of any material containing water. The Ic ice phase, if formed rapidly at high pressure, forms in a vitreous state without volume change therefore preserving the microstructure.

As illustrated in Figure 2.6, high-pressure freezing brings the sample containing liquid water from ambient conditions (“E” in Figure 2.5) to the condition of formation of the vitreous ice phase Ic (-195.7 to -120 °C) without passing through the Ih phase or other crystalline phases that could harm the microstructure of a material containing water due to both volumetric change and

crystals formation upon freezing. This is achieved by the following steps illustrated in Figure 2.6:

1. From ambient conditions the pressure is increased to 2200 bars.
2. While keeping the pressure at 2200 bars, the temperature is lowered to  $-195.7^{\circ}\text{C}$  using liquid nitrogen.
3. The pressure is returned to ambient while the sample stays in liquid nitrogen.

The whole process is technologically very challenging because these extreme changes must go very fast in order to only form amorphous Ic phase. This is however possible with dedicated instruments, but it should be noted that samples have to be very small for fast enough heat transfer. This is why special metallic sample carriers of volumes from 2 to 12 mm<sup>3</sup> are used.

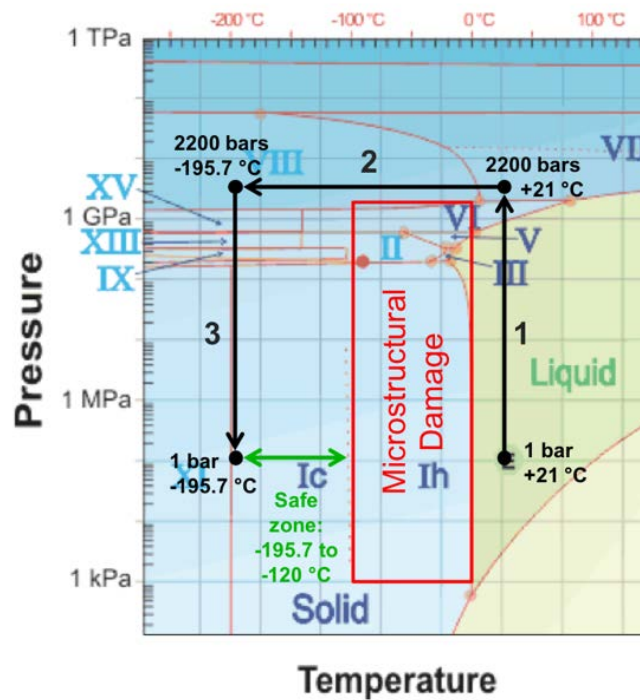


Figure 2.6: High-pressure freezing principle. The path represented on this diagram allows the transformation of liquid water into vitreous ice phase Ic without formation of any crystalline ice Ih and volume change. The sample is brought from ambient temperature to the temperature of liquid nitrogen ( $-195.7^{\circ}\text{C}$ ) by undergoing the freezing process at a pressure of 2200 bars. As the kinetics of phases transitions play an important role in the vitrification of the ice and therefore the preservation of the sample's microstructure, this process should be realised in a time lapse under 25 msec. Once the process is completed the sample should remain in the safe temperature range between  $-195.7$  and  $-120^{\circ}\text{C}$  at ambient pressure in order to avoid any crystallisation in the ice.

High-pressure frozen samples can be kept for indefinite periods of time in liquid nitrogen before their observation in an electron cryo-microscope. The preparation of the samples prior to observation in a cryo-fitted electronic microscope differs however from traditional electron microscopy. Indeed, specific and additional steps such as freeze fracture and etching as well as sample conductive coating under cryo-conditions are necessary. The handling of such samples also requires a particular attention as their temperature must never rise above -120°C and once exposed by freeze fracture they should always remain in relatively low vacuum in order to avoid ice contamination from ambient humidity by direct vapor to solid deposition. These specific steps and aspects as well as the modifications to a scanning electron microscope required for cryogenic observations will be presented and discussed in Chapter 3 of this thesis.

### 2.1.3. Cryo-FIB-SEM tomography of fresh cement pastes

Three dimensional tomographies of materials containing water with resolutions of modern scanning electron microscopes are possible by using the combination of a Focused Ion Beam and Scanning Electron Microscopy under cryogenic conditions (cryo-FIB-SEM tomography). This technique is a special application of cryo-microscopy described in the previous section with additional complexity that allows volumetric analysis of a material's microstructure.

The principle of this technique, described in details in the Material & Methods section of Chapter 3, consists of taking Backscattered Electrons (BSE) images of successive thin slices of the material sequentially alternating with FIB milling of a cryo-vitrified sample (Figure 2.7). Images of slices obtained this way can be then combined in a stack that can be used for 3D reconstruction of the sample's microstructure using specific software. These 3D reconstructions allow qualitative and quantitative analysis of the material's three-dimensional microstructure with the SEM resolution in the two dimensions of the BSE imaging and the FIB resolution in the third dimension. Mostly used for biological samples, cryo-FIB-SEM tomography remains a rather complicated, challenging, time consuming and costly technique to put in place, in addition to requiring advanced microscopy skills and expertise. This technique is also very sensible to the imaging quality and consistency, and often requires additional image processing that must be performed with care and reported in order to avoid any mis-interpretation of the results.

To the knowledge of the author, investigations on fresh cement paste's microstructure using cryo-FIB-SEM tomography were performed only once before by Dr. Anatol Zingg during his PhD thesis: *"Cement-Superplasticizer Interaction: Link between Macroscopic Phenomena and Microstructural Data of the Early Cement Hydration"* [26]. This technique was used to study the effect of pure

PCE superplasticisers supplied by an industrial sponsor on the precipitation and dispersion of early hydrates in a fresh commercial CEM I 42.5 N cement paste. The main conclusions of this study can be summarised as follows:

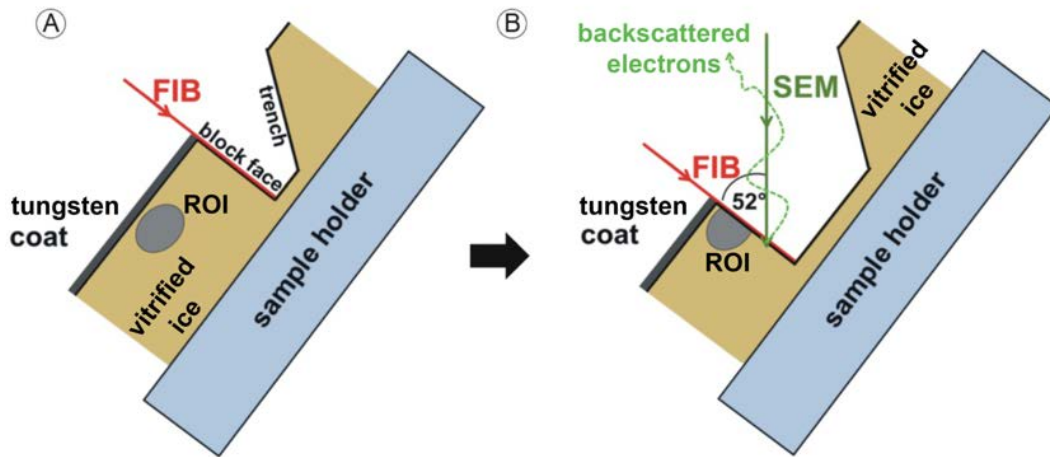


Figure 2.7: Cryo-FIB-SEM tomography process using focused ion beam (FIB) and backscattered electron imaging in a cryo-fitted dual-beam scanning electron microscope (SEM). (A): The previously vitrified and tungsten coated sample is transferred inside the cryo-fitted chamber of a dual-beam scanning electron microscope and tilted to an angle of 52° allowing it to perpendicularly face the FIB. A trench is opened in front of the region of interest (ROI) using the FIB generating an imaging surface (block face) facing the SEM beam. (B): A thin layer of the block face is removed by FIB milling (“slice”) generating a new block face advancing in the ROI. After every “slice” step the newly generated block face is imaged by detecting backscattered electrons generated by the interaction of the SEM beam and the block face (“view”). The “slice and view” cycle is repeated to gain a three-dimensional image stack of the ROI. Adapted from [27].

Cryo-FIB-SEM tomography seems to be a viable and promising technique to study the microstructure of fresh cement pastes minimising the risk of damaging it in comparison to other observation techniques.

Direct addition of PCE superplasticisers shows an important impact on the way the first hydrates (ettringite) precipitate. Cement pastes without PCE showed important thick rims of hydrates (Figure 2.8) around the clinker particles compared to the cement paste containing PCE.

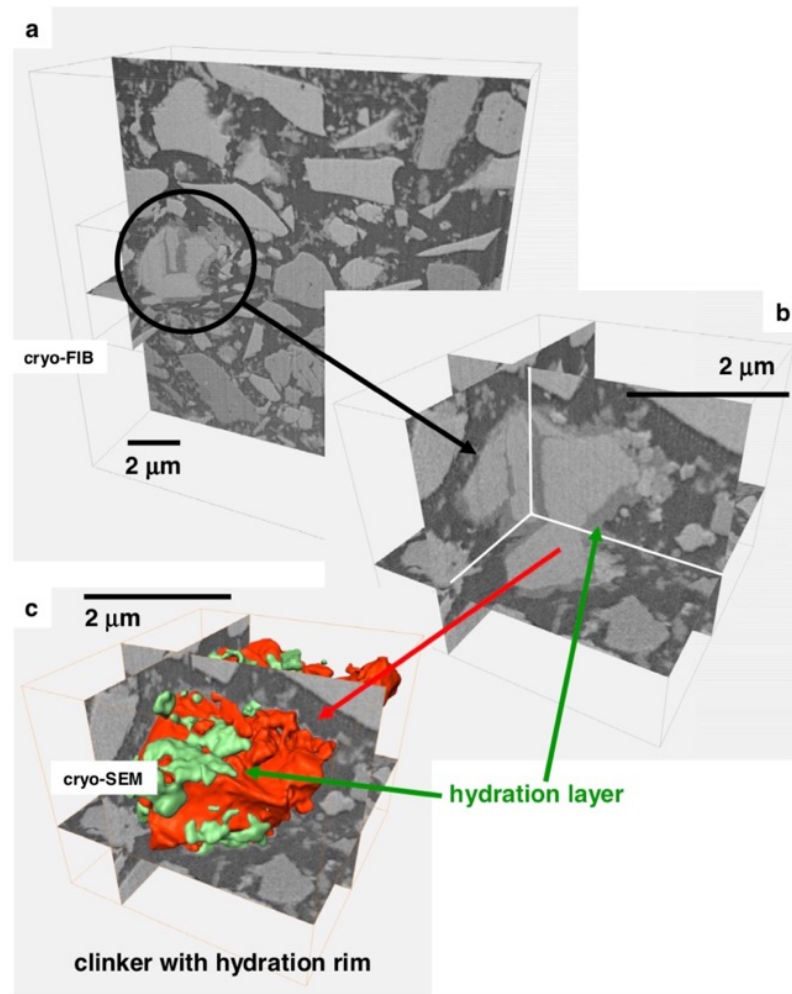
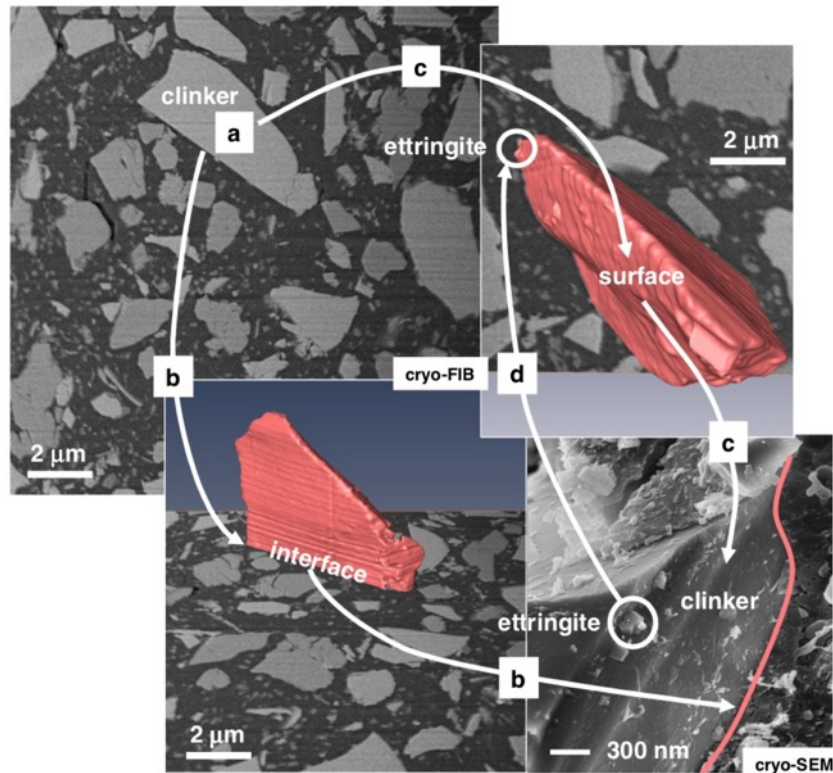


Figure 2.8: Orthoslice (b) is a close-up from a cryo-FIB-SEM nanotomography stack (a) of a fresh cement paste without PCE. The clinker particle (light grey) is surrounded by a hydration layer (medium grey). The reconstructed (c) 3D particle (red) is discontinuously covered by the hydration layer (green). Source: [26].

In presence of PCE in direct addition, these hydration rims seem to be almost inexistent around cement particles while a large amount of much smaller hydrates' particles were observed in suspension around the cement grains (Figure 2.9).





*Figure 2.9: FIB-SEM tomography of fresh cement paste containing PCE in direct addition: Cryo-FIB cross section shows clean clinker particle surfaces (a). The interfaces (b) between the sliced particle and the interstitial pore space are very sharp, almost no attached hydrate particles can be seen at clinker surfaces (c). A large number of fine hydrates' particles can be observed dispersed in the vitrified ice around the clinker particles. Source: [26].*

Direct addition of PCE also influences the volume of hydration phases and their spatial distribution. This effect leads to changes of the particle size distribution, specific surface area and numbers of particles and thus, changes the rheological behaviour of fresh cement pastes.

The exploratory work done by Dr. Anatol Zingg during his PhD thesis on commercial cements and superplasticisers showed the potential of using cryo-FIB-SEM tomography to study the complex microstructure of fresh cement pastes without altering it. The initial aim of the present thesis was to take advantage of this potential as well as the technological advancements in electron microscopy since Dr. Zingg's thesis to further study the impact of PCE superplasticisers on early cement paste hydration by using model cements and custom tailored PCEs developed and investigated by Dr. Delphine Marchon during her PhD [28]. The challenges that were faced in this endeavour are presented and discussed in Chapter 3 of this manuscript.

## 2.2. Digital Fabrication

The premises of digital fabrication for construction purposes go back to the nineteen-eighties with two unrelated men who are now considered to be the pioneers in this domain: Berok Koshnevis and Enrico Dini, respectively for extrusion printing and powder bed printing.

### 2.2.1. Extrusion printing

Extrusion printing with concrete was pioneered in the works of Behrokh Khoshnevis on layer-by-layer extrusion of concrete. It aims at achieving 3D printed structures and was among the first processes to reach a certain level of industrial viability resulting in what today is known as Contour Crafting [10,11]. This technique relies on a robotically controlled gantry, which by using an extrusion nozzle, deposits concrete in a layered manner in order to produce elements requiring an advanced control of the concrete hydration and hardening processes in order to avoid failure during the printing [29–32]. Upscaled, this technique makes nowadays possible to print entire housing like the recently printed Dubai administrative building by the company Apis Core<sup>1</sup> (Figure 2.10) or the visionary Marsha Project<sup>2</sup> that received an award from NASA in 2018<sup>3</sup> for working on a housing 3D printing system for the first Mars colonists.

Other important large-scale demonstrators include a bicycle bridge in Eindhoven [33] and various houses like the BOD house in Denmark<sup>4</sup>, a residential house built in 24 hours in Russia<sup>5</sup> or a suite at the Lewis Grand Hotel in the Philippines<sup>6</sup>. Also worth noting is the Concrete Choreography demonstrator [34] (Figure 2.11) because of its remarkably fast vertical build up. Thus, material chemistry challenges were particularly high in this case. This project produced freeform columns with a height of 2.7 meters within a single printing process of 2.5 hours demonstrating.

---

<sup>1</sup> <https://www.apis-cor.com/dubai-project>

<sup>2</sup> <https://www.aispacefactory.com/marsha>

<sup>3</sup> <https://all3dp.com/4/nasa-awarded-marsha-project-brings-space-age-architecture-to-mars/>

<sup>4</sup> <https://cobod.com/the-bod/>

<sup>5</sup> <https://www.youtube.com/watch?v=xktwDfasPGQ>

<sup>6</sup> <https://3dprint.com/94558/3d-printed-hotel-lewis-grand/>



*Figure 2.10: Dubai administrative building produced by concrete extrusion 3D printing. (Photo: Apis Cor, 2019)*

As summarised in various recent reviews and publications [9,29,35–38], key open questions for extrusion printing are the inclusion of reinforcement and control of the rate of strength gain. Indeed, the latter must be fast enough to allow the accumulation of layers on top of each other, but it must not be too fast as this would enhance the risk of forming cold joints between the layers.



*Figure 2.11: Concrete Choreography. (Photo: dbt, ETH Zürich)*



### 2.2.2. Powder-bed 3D printing

Another pioneer approach on digital fabrication in construction industry that must be mentioned is the works of Enrico Dini on large scale powder-bed 3D printing [39–43]. This technique of targeted powder binding allowed the realisation of several full-scale constructions such as the pedestrian bridge in Castilla-La Mancha urban Park in Alcobendas, Madrid<sup>1</sup> (Figure 2.12).

There is comparatively little information published about this process. It is understood that Dini, initially was working with Sorell cements, but that he has since successfully turned to Portland cement, which seems to have been used in the above-mentioned bridge.

Recent papers on the subject expand the concept of powder bed printing to the injection of a paste in a bed of aggregates. This approach loses in resolution but can ambition substantial gains in production speed.



*Figure 2.12: Powder-bed 3D printed pedestrian bridge in Castilla-La Mancha urban Park in Alcobendas, Madrid. (Photo: IAAC)*

Other large-scale applications have included a 3x3x3 metres digital grotesque. In this case, the printed material is sand and the binder is an organic resin that is not suitable for outdoor exposure because soluble in water. However, the importance of this demonstrator presented in more details in Chapter 4 (Figure 4.1, page 75), was to show the level of resolution that the method can achieve even on a large scale.

---

<sup>1</sup> <https://iaac.net/project/3d-printed-bridge/>

Remaining with sand instead of cement, this approach can be used to produce moulds into which concrete is cast. This essentially mimics a process that has become very successful in the metallurgy industry. Doing this with concrete however includes a number of challenges, to which this thesis brings some answers in Chapter 4, where additional information on powder bed printing is also given.

To overcome the challenges of casting concrete in a sand printed formwork, it is possible to spray the concrete onto a single surface. Doing so, however requires a careful treatment of the surface with epoxy, to toughen it and make it possible to detach from the concrete once it has hardened. Demonstrations of this approach have been given with the Incidental Space at the 2016 biennale of Architecture in Venice presented in Chapter 4 (section 4.1.2, Figure 4.2, page 76), as well as by the Smart Slab of the DFAB house in Chapter 1 (section 1.1.2, Figure 1.1, page 4).

### 2.2.3. Digital Casting

In opposition to the concept of directly shaping the printing material into the desired element without formwork as in the works presented above, a new field is developing that can be defined as Digital Casting [44]. Here, the idea is to use concrete in a more traditional casting, setting and hardening configuration while digitalising either the delivery and activation of the concrete, or the formwork itself or both. This approach offers a high degree of geometrical freedom as well as the easier integration of reinforcement than in the above-mentioned processes.

#### 2.2.3.1. *Digitally articulated slip form formwork*

Slipforming is used in construction in cases when the reassembling of the formwork at every concrete layer casting needs to be avoided in order to considerably increase the productivity during the construction of structures of greater height in relation to their width such as bridge or oil rig pylons [45]. However traditional slipforming requires the produced elements to keep a relatively constant cross-section throughout their height as the slipforming formwork rarely allows any degree of articulation.

Active digital articulation of the formwork brings the possibility of additional geometrical freedom as it allows a variable cross-section throughout the element without the burden of costly custom-made formworks. One of these methods called Smart Dynamic Casting (SDC) was developed at ETH Zürich and implemented to produce columns and mullions with variable shapes [12,46].

SDC development required an important interdisciplinary collaboration as a lot of challenges had to be overcome on several aspects such as robotics, concrete chemistry and architecture. From the first prototype of SDC using an assembly robot usually used in industries such as automotive construction, to the latest one consisting of a custom-made articulated slip forming bench that produced reinforced mullions for the DFAB house (Figure 2.13), the various evolutions of the SDC can be observed in Figure 2.14.

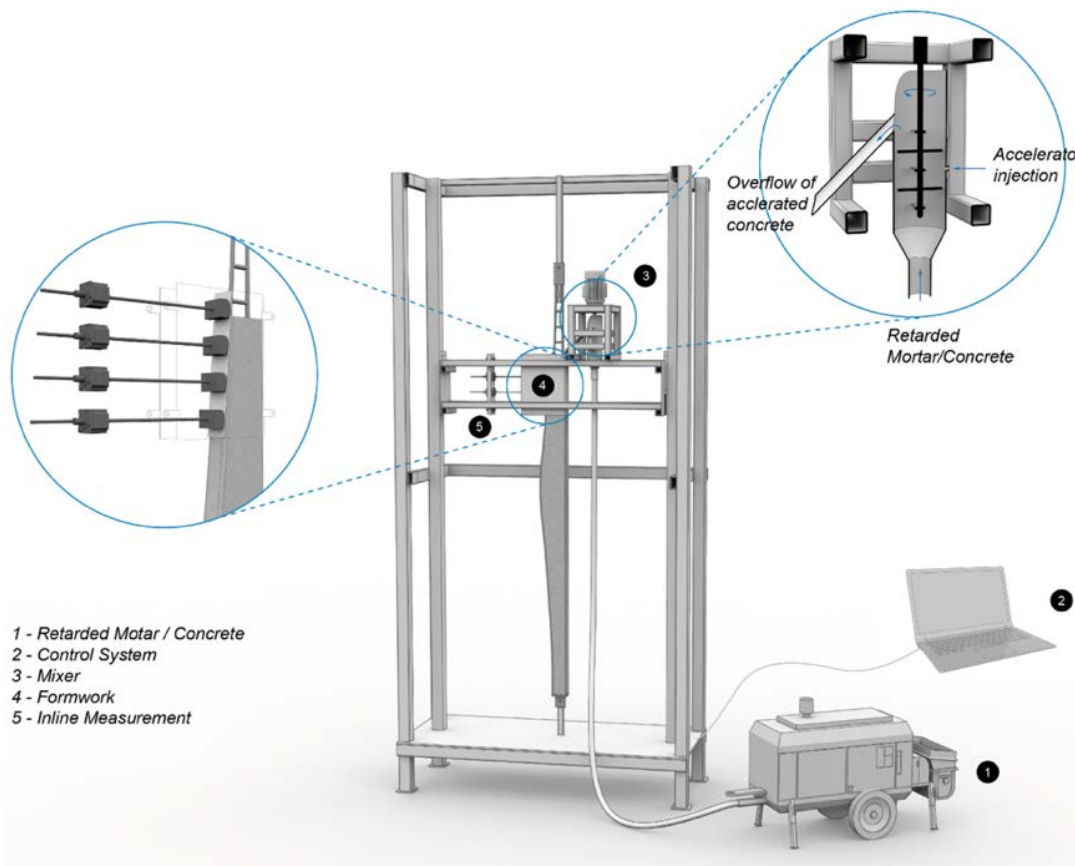


Figure 2.13: Smart Dynamic Casting diagram of fabrication set up with a linear axis system used for the mullions installed in the DFAB HOUSE at EMPA in 2018 (Dübendorf, Switzerland): 1. Pump with retarded mix, 2. Customised control system for simultaneous control of pumping, slipping and filling, 3. Mixer for accelerating the retarded mortar/concrete, 4. Actuated formwork for mullion production, 5. Inline measurement sensor placed in formwork. Source: [12]

As one of the main objectives of SDC is to produce elements in a relatively short period of time (less than a working day per column) an important array of challenges arose regarding the concrete behaviour inside the formwork leading to the development of “setting on demand” formulations [47] as well as the overall control of the process presented in Figure 2.13.

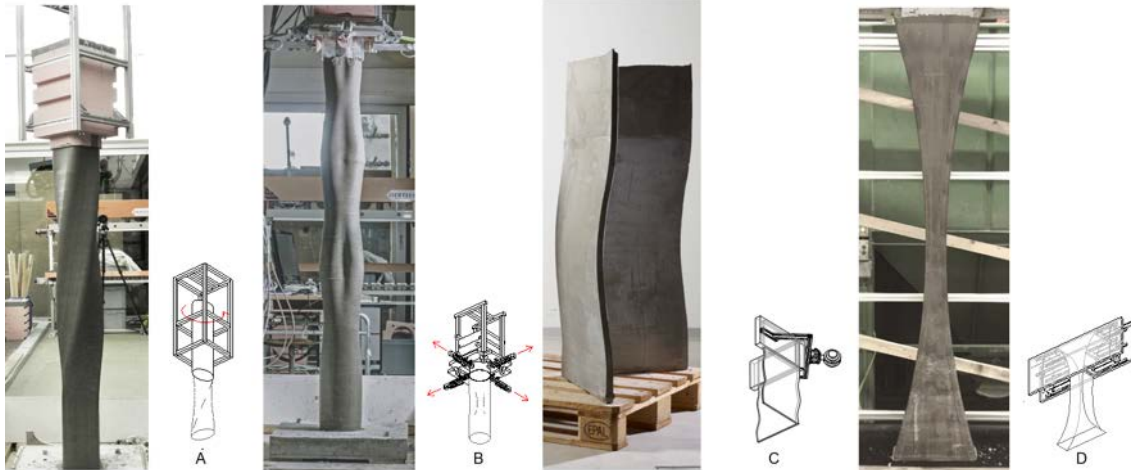


Figure 2.14: Different formwork typologies used in Smart Dynamic Casting early stage: A) Local deformation rigid formwork that can be configured with different shapes, such as ellipse, circle, square or star shape; B) Local deformation flexible formwork where shaping actuators are only at the exit of the formwork; C) Local deformation formwork for thin folded structures, and D) global deformation formwork for significant cross section change. Source: [44]

### 2.2.3.2. Admixture Controlled Digital Casting

The development of setting on demand solutions started with SDC and was further challenged by trying to apply this process to thin folded structures [48]. While it has since been shown that robustly producing such shapes is difficult because of the more substantial friction forces at stake [49], it leads to the development of improved material chemistry that has since found further and more promising applications [48,50].

In particular, with materials maintaining a high fluidity directly after activation, but the rapidly setting and hardening, it becomes possible to cast concrete in very weak formworks without suffering from hydrostatic pressure. An extreme example of this has been to use tensioned plastic foils [51]. The usage of such tensioned foils lends cachet to the concept of “cheap formwork” as these are tensioned in a digitally modelled configuration and gradually filled with constantly accelerated concrete allowing minimal to no deformation of the formwork as presented in Figure 2.15. Still under development at ETH Zürich, this new technology has a great potential of implementing the “complexity for free” promise of concrete Digital Fabrication.

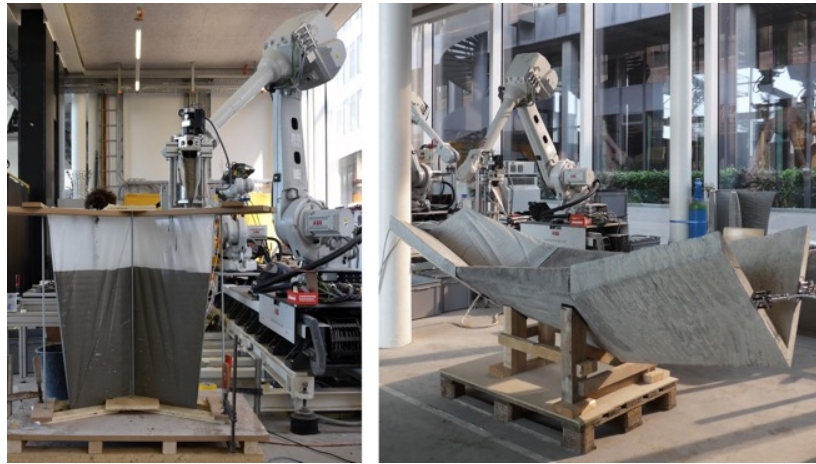


Figure 2.15: Digital casting of a thin folded concrete element into a foil formwork: (left) Filling process of thin PVC formwork; (right) Post-tensioned folded structures Source: [51,52]

### 2.2.3.3. Digitally fabricated formworks<sup>1</sup>

In addition to admixture controlled digital casting and digitally articulated slip formworks previously mentioned in this chapter, digital casting is best complimented by simple, cost and time effective production of thin formworks. The digitalisation of the formwork fabrication presents considerable advantages regarding both cost-effectiveness and complexity in opposition to traditional formwork that is on average the source of roughly 50% of the overall construction costs (Figure 2.16) and is usually limited to prismatic geometry [53].

Taking advantage of the recent development and popularisation of Fused Deposition Modelling (FDM) technology, the Egg Shell approach was developed as an additional approach to digital fabrication with concrete [54].

In this process, a thin plastic formwork (1.5 mm thickness in examples given herein) is 3D printed using an FDM robotic arm. This can be done either before the concrete is placed, as shown in Figure 2.17, or simultaneously, as shown in Figure 2.18. In both cases, the formwork is filled with a set-on-demand concrete. Also, following a casting procedure inherited from Smart Dynamic Casting technology (section 2.2.3.1), this is done at a speed that is regulated to limit the build-up of hydrostatic pressure to values that the formwork can support. Due to the controlled hydration of the concrete, no external scaffolding or counter-pressure measures are necessary. Moreover, this is one of the few additive manufacturing processes with concrete in which reinforcement can be easily integrated.

<sup>1</sup> Section largely based on [29] of which the author of the present thesis is a co-author.



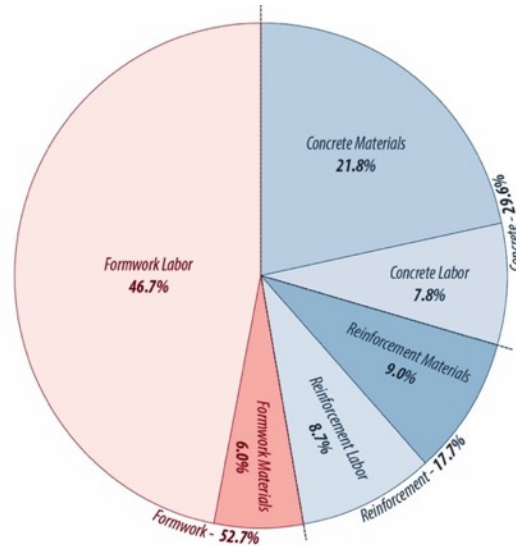


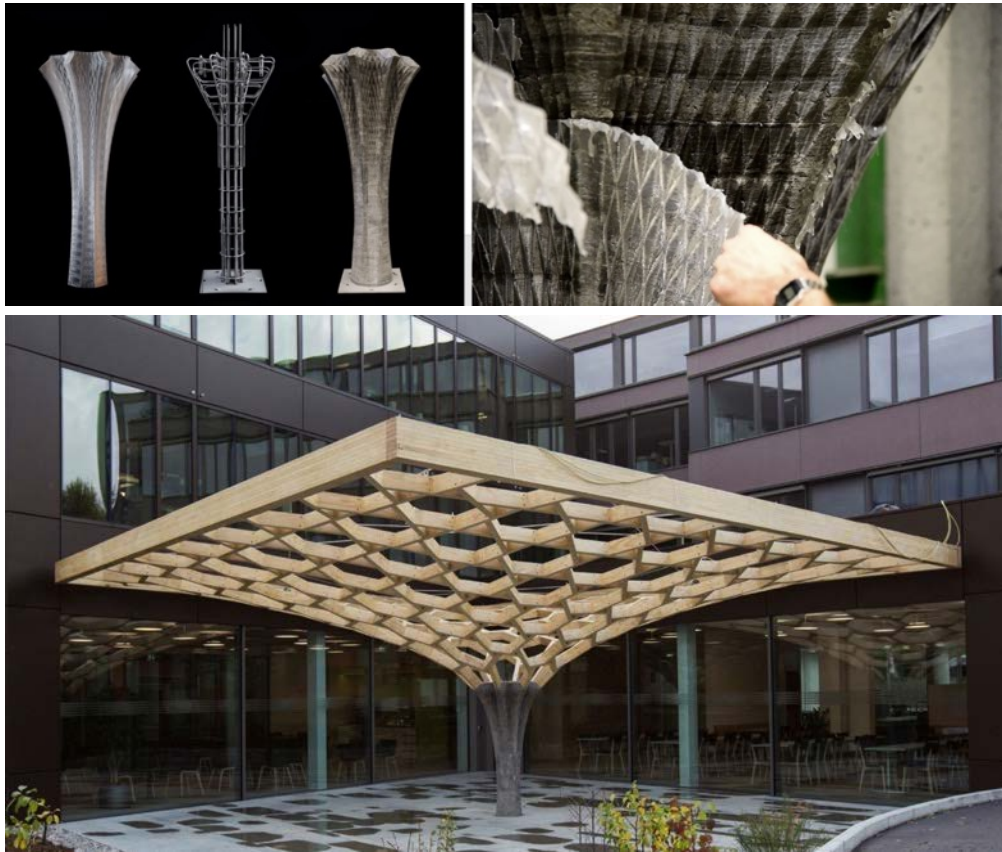
Figure 2.16: The average distribution of costs for concrete constructions. Formwork raw materials and labour are responsible for roughly half the overall costs. This figure highlights the importance of optimising formwork fabrication processes. Source: dbt, ETH Zürich, 2017

One example of a thin formwork, which was filled with set-on-demand concrete, is the 2.1-meter-tall reinforced column presented in Figure 2.17 that was fabricated as part of the Future Tree project and recently installed in Esslingen (Switzerland)<sup>1</sup>. In that case a full-height plastic formwork was 3D printed by FDM, after which it was combined with conventional reinforcement and filled with concrete. After the concrete had cured enough, the thin formwork could be removed and theoretically recycled as it was made of a polymer suitable for this purpose. As a first built example using this fabrication method, this demonstrator showed that non-standard concrete structures can be fabricated efficiently, economically and sustainably<sup>2,3</sup> (while stated as such in [44], the present author considers this demonstrator to rather define the potential of such benefits, than to factually establish them).

<sup>1</sup> <https://www.erne.net/de/news/news-details/der-future-tree-von-basler-hofmann-parametrisch-geplant-digital-gebaut/>

<sup>2</sup> <https://www.baslerhofmann.ch/de/aktuelles/individuelle-newseintraege/reportage-gha-future-tree.html>

<sup>3</sup> <http://gramazio-kohler.arch.ethz.ch/web/e/projekte/330.html>



*Figure 2.17: Future Tree project developed using thin printed formwork based on Eggshell technology: (upper left) 3D printed formwork, reinforcement and final structure of the Future Tree; (upper right) the demoulding process of the 1.5 mm thick formwork after curing, and (bottom) final structure of the Future Tree installed at the premises of the engineering firm Basler Hofmann AG in Esslingen (Switzerland) in 2019 (Photo: Gramazio Kohler Research).*

A shortcoming of this approach and in general of setting on demand are the rather stringent requirements put on the control of concrete chemistry due to the limited mechanical properties of thin plastic formworks produced by FDM. A solution to this has been described as “counter pressure casting”, whereby a sand bed is used to oppose the hydrostatic pressure. This approach is described in Chapter 5 of this thesis.



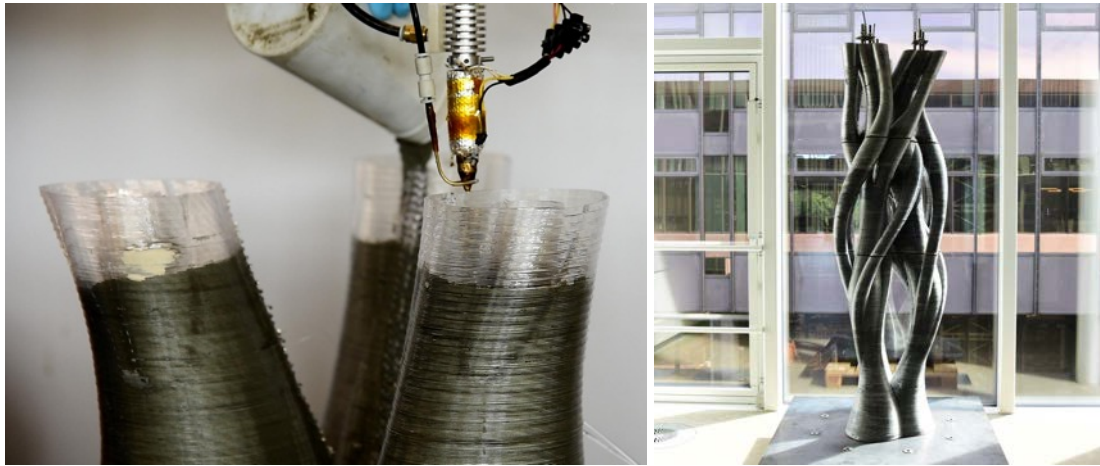


Figure 2.18: Simultaneous concrete filling and formwork printing processes: (left) a thermoplastic polymer is extruded and moved according to a defined geometry to build the formwork, whilst set-on-demand concrete is filled in it; (right) a 1.8 m tall branching column, fabricated with the simultaneous printing and filling approach. (Design and fabrication by: W. Yang & A. Barney, MAS ETH DFAB).

## 2.2.4. Implications from the State of the Art

Digital fabrication with concrete holds many promises. However, in most cases these still remain to be held beyond one-of demonstrator objects, which even if representing very important steps, still falls short of demonstrating economic viability and competitiveness.

Digital fabrication with concrete includes a family of different processes with their respective strengths and weaknesses. As a result, each one will have specific applications where it can be expected to be most competitive. However, in all cases they do share a similar reality. They will have to compete with other solutions and have to be easy to implement and robust enough to be considered for large scale use.

This PhD has identified two specific technological challenges in relation to concrete casting, which if overcome would substantially enhance the competitiveness of two digital casting processes. The first of these processes consisting of using sand 3D printed lost formwork, has been described above in section 2.2.2 and is dealt with in Chapter 4. The second of these processes is mentioned at the end of section 2.2.3.3 of this chapter. It concerns the usage of sand counter pressure casting with sub-millimetre FDM printed plastic formwork, filled with high performance fibre reinforced concrete without setting on demand control. Work related to this subject is described in Chapter 5 of this thesis.

# Chapter 3 – Cryo-FIB-SEM nano-tomography of fresh model cement pastes

## 3.1.Introduction

Understanding the hydration mechanisms of cementitious materials at early stages is vital for the scientific community in order to answer the demand for better, smarter and more durable concrete needed by the construction sector. Nevertheless, the study of the chemistry and mechanics involved in the hydration and hardening of concrete remains a great challenge. The impact of the first minutes, hours and days of hydration on properties such as workability, mechanical strength and durability are known to be crucial [55–57].

Scanning Electron Microscopy (SEM) offers nowadays very powerful observation techniques for studying surface features of cementitious materials [58,59]. However, taken alone it is rather limited for studying internal microstructure. Nevertheless, in combination with Focused Ion Beam (FIB) techniques, it provides access to the third dimension of samples by sequentially etching away slices of matter using the FIB. Repeating this slicing hundreds of times and acquiring images by SEM in back-scattered electron (BSE) mode (“slice & view”) provides a tomogram of the sample’s microstructures, allowing both qualitative and quantitative analysis through segmentation and software 3D reconstruction. This can provide us information about the microstructural development of cementitious materials from very early ages, in particular on the way in which hydrates bind particles.

The development of Cryo-FIB-SEM nano-tomography has opened new possibilities for the microstructural characterisation of fresh cement pastes. This technique allows both the preservation of the sample’s microstructure as well as

a high-resolution imaging. Cryo-FIB-SEM nano-tomography makes it possible to study microstructures containing water with minimal alterations, providing qualitative and quantitative information almost unreachable by other techniques. To the best knowledge of the author, in the literature there is only one study about the use of cryo-FIB-SEM nano-tomography on cementitious systems. In particular, it dealt with the impact of pure PCE superplasticisers supplied by an industrial sponsor on the precipitation of the first hydrates in cement pastes within the PhD thesis of Dr. Anatol Zingg [26].

The initial objective of the present PhD was to use cryo-FIB-SEM nano-tomography in order to study the impact of polycarboxylate ethers (PCE) superplasticisers on the nucleation and formation of the first ettringite hydrates using a well-defined and controlled system of model cement paste and custom tailored PCE. This can provide very promising information about the microstructural development of cementitious materials from very early ages, in particular on the way in which hydrate particles precipitate and impact both fresh and hardened concrete properties. The obtained data can be of particular relevance for better understanding and improving the formulations of low water containing systems such as high-performance fibre-reinforced concrete (HPFRC) where the amount and shape of the first hydrates can play an important role on their rheology owing to dense packing of such formulations.

Nevertheless, this endeavour presented an important number of challenges to overcome, as various artefacts can be introduced during the whole process including sample preparation, high pressure freezing, sample handling and imaging.

The qualitative results obtained during this work will be presented in this chapter as well as the holdbacks and challenges faced during this project. Importantly, substantial details will be given, about why, after much effort, we came to the conclusion that it was not possible to obtain unbiased and exploitable quantitative data for our topic due to an unexpected imaging artefact named “scaling artefact”.

This chapter will first present a short basic theoretical part on the main electron-microscopy aspects needed for a better understanding of the rest of this work. It will then present the materials and specific methods used for this project before presenting and discussing the results obtained by qualitative analysis. Finally, and as eluded to above, this chapter will expose the problems faced in obtaining exploitable tomographic data including the scaling artefact description. This is done by presenting the investigations that were made in order to understand its hypothetical origin, what was done to try to overcome it and a few suggestions for future works that could be performed to obtain reliable tomography images in order to provide new insights into cement hydration at very early stages.

## 3.2. Scanning Electron and Focused Ion Beam Microscopy

The purpose of this section is to provide a short basic theoretical overview of scanning electron and focused ion beam microscopy required for further understanding of this chapter.

Light microscopy uses a source of visible light to illuminate the sample. The light reflected by the sample's surface is then channelled and focused with the help of optical lenses into a detector that can be directed to the operator's eye, a photographic film or a digital camera allowing to display the image on a screen and digitally capture it.

In the case of electronic microscopy, a beam of electrons is used instead of light to irradiate the sample. The electrons are produced and accelerated by an electron gun into a beam which is channelled and focused on the sample by several powerful electromagnets that act as lenses. The properties of this beam are usually described by the electron gun acceleration voltage and current translating into the amount of energy delivered by the beam to the sample, and its spot size (diameter) at the sample's level. Due to intrinsic physical properties of electrons, they can only be produced, focused and used as irradiation source under high to ultra-high vacuum, which is the reason why the samples need to be able to withstand such conditions in an electron microscope chamber.

Also, the samples need to be conductive in order to be observable by electronic microscopy, since if the incident electrons are not evacuated, they end up building localised charges that manifest themselves on the images as bright contours artefacts. The samples that are not conductive by nature are made so by plasma or evaporation sputter coating using various conductive materials such as carbon, gold, tungsten, platinum, silver or palladium. The coating thickness is usually made just a few nanometres thick to ensure electrical conductivity of the samples surfaces without an overwhelming build-up of coating material that could compromise the observation.

When interacting with the sample, the incident beam produces several types of signals that can be detected and reconstructed into images using specific detectors located in the microscope chamber in order to obtain different information on the sample. The two detectors that were used for this work are:

- Secondary Electrons (SE): Produced by the interaction of the incident electron beam with a small volume under the surface of the sample, this signal is composed of electrons originally belonging to the sample that were ejected from it due to interactions with the incident beam's electrons. The SE signal does not give any information on the observed material nature but is very useful in obtaining topographical information of the observed area of the sample.

- **Backscattered Electrons (BSE):** Produced by a more important interaction volume compared to SE, this signal is composed of incident electrons that were reflected back due to interactions with the sample's matter on the atomic level. The BSE signal gives rather poor information of the sample's topography compared to SE, but provides very useful information on the atomic nature of the material it interacted with. Indeed, the brightness level of BSE obtained images indirectly reflects the average atomic number of atoms composing the observed material as well as its density. A higher brightness means a higher combination of the average atomic number and density. It is not possible to directly correlate a brightness level to a specific chemical composition using only BSE imaging but it gives the observer an exploitable relative contrast between the different materials and phases. When combined with other analytical methods or the knowledge of the sample's nature, it allows to identify and locate various materials and phases on the obtained images.

The images obtained by these detectors are produced by a sequential scanning of points located on the sample's surface by the electron beam. The signal obtained for each point is also detected sequentially and reconstructed into an image on a computer used to operate the microscope. It is important to note here that the scanning parameters also play an important role in the quality of the obtained images. A slower scanning will collect the signal for longer periods of time from each point, while a higher resolution will collect the signal from a denser matrix of points, both resulting in higher quality images at the expense of time needed to obtain them and electrons dose delivered to the sample.

The Focused Ion Beam (FIB) is used for specific applications in certain electronic microscopes additionally to the electron beam. The working principle of the FIB is similar to the electron beam with the difference that the FIB is composed of gallium ions. These ions are produced by a liquid gallium reservoir, accelerated in the FIB gun and focused into a beam using electromagnets. Due to their considerably bigger mass compared to electrons, the gallium ions are able to physically interact with the sample upon impact to the extent of being able to remove matter with a resolution similar to the electron beam. This makes the FIB an extremely powerful tool for electron microscopy as it allows to gain access to volumes of the sample located below its surface. The process of removing matter using the FIB is called milling and the removed matter is vaporised by the FIB into the vacuum surrounding the sample in the microscope chamber. It is however not uncommon that the removed matter re-deposits in an amorphous way onto the sample surfaces surrounding the volume it was milled away from. **It is of particular importance for this chapter to note that this re-deposition is more important under cryogenic conditions as the low temperature of the sample acts as a catalyst for preferential deposition.**

FIB can also be used to build up matter in combination with a Gas Injection System (GIS). This is done by introducing a needle above the surface of the sample that is able to locally release a flow of gaseous Platinum, Carbon or

Tungsten precursors. The interaction of the FIB with the gaseous precursor results in a layer built up of the relevant material on the surface of the sample.

Finally, FIB can also be used for imaging as the interaction of gallium ions with the sample also produces detectable signals. However, FIB is usually never used for imaging purposes apart from navigating the sample and focusing the beam as images obtained this way do not bring any additional benefit compared to the electron beam and result in a progressive and pronounced damage of the imaged surface. Nevertheless, extensive and repeated FIB imaging is necessary during the FIB-SEM nano-tomography process in order to compensate for the focus, beam and sample drift that occur over extended periods of time. The usage of GIS deposited sacrificial protection layer on the surface of the sample prior to the tomography allows to avoid damaging the sample itself.

## 3.3. Materials and Methods

### 3.3.1. Model cement paste

The model cement and the custom tailored polycarboxylate ether superplasticiser (PCE) used for this study were synthesised by Dr. Delphine Marchon accordingly to the protocol developed during her PhD thesis in our research group [28].

The model clinker is composed by 80%<sub>wt</sub> tri-calcium-silicate (C3S) and 20%<sub>wt</sub> of tri-calcium-aluminate (C3A). After grinding, the model clinker was stored under vacuum in a desiccator containing silica gel. Before the preparation of the fresh cement paste, calcium sulphate hemi-hydrate (6% by mass of model clinker) was added and manually mixed with the model clinker in a mortar for 5 minutes.

The PCE was synthesised by esterification of methyl polyethylene glycol side chains of 1'000 g·mol<sup>-1</sup> on previously polymerised backbones of about 5'300 g·mol<sup>-1</sup> with methacrylic acid monomers. The average number of side chains per molecule of the used PCE is estimated to 14.8.

Two types of samples were studied during this work. The first one that will be referred to from now on as “Reference” only contained model cement and ultrapure water. The second type of sample referred as “PCE containing” was composed of model cement, PCE superplasticiser and ultrapure water.

All model cement paste samples were produced at water cement ratio of 0.4. For the PCE containing samples, a dosage of 0.1%<sub>wt</sub> of PCE solid content by weight of model cement was added to the mixing water in direct addition. The

mixing was realised with a tachymeter-fitted IKA Eurostar overhead stirrer and a custom shaped stirring paddle allowing to mix small quantities of paste in a 10 ml PTFE beaker. 6.918 g of model cement was first mixed with 2.767 g of liquid for 30 seconds at 200 rpm followed by 2 additional minutes at 800 rpm. The hydration of the samples is halted 5 minutes after the moment of contact between the liquid and the model cement by the process of high-pressure freezing used in the preparation of samples for cryo-Microscopy.

### 3.3.2. High pressure freezing

High-pressure freezing (HPF) ensures the preservation of the samples microstructure by avoiding volumetric change and crystalline formation during the phase transition of water to ice that would take place if the freezing would occur at ambient pressure. This technique, the theory of which is described in details in Chapter 2 (section 2.1.2), takes advantage of the phase diagram of water (Figure 2.5 and Figure 2.6, pages 15 and 16). The formation involving volumetric change of crystalline Ih ice phase is avoided by forming the isovolumetric Ic amorphous phase of ice. The HPF process follows a rise in pressure to 2200 bars followed by an instant temperature drop to  $-196^{\circ}\text{C}$  using liquid nitrogen. As the dynamics of this process play a major role in the complete vitrification of water and thus the preservation of the samples' microstructure, the HPF cycle must be completed as fast as technically possible. In order to achieve that, the model cement paste is placed in hollow disk-shaped carriers, called planchettes, that are 5 mm in diameter and have a depth of 200  $\mu\text{m}$  representing a sample volume of  $3.9 \text{ mm}^3$ .

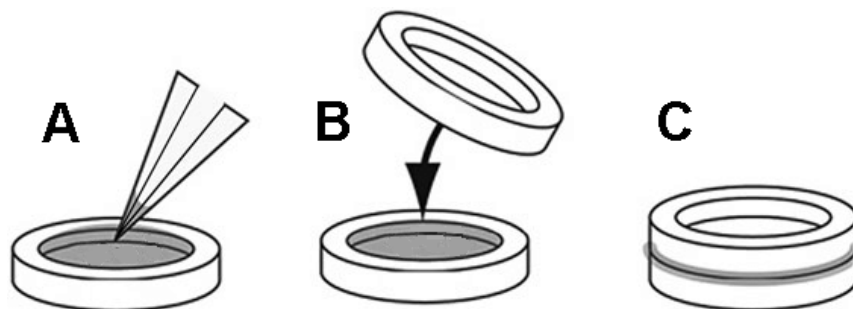


Figure 3.1: Sample preparation for high-pressure freezing. A: Cement paste is deposited in the hollow part of the planchette (5mm dia., 0.2mm deep). The amount of paste should be as close as possible to the planchette's volume to maximally avoid entrapped air or spillage in the next step. B: Another planchette's flat bottom is used to enclose the cement paste. C: Any excess of cement paste is wiped off making the sample carrier sandwich containing the cement paste is ready for HPF. Source: adapted from [60]



In order to ensure good thermal conductivity, the sample carrier planchettes are made of aluminium and are gold coated to avoid any chemical reaction between the fresh cement paste and the aluminium. The planchette containing the cement paste sample is closed by another one as can be observed in Figure 3.1. The dimensions of the resulting sample carrier sandwich are 6 mm in diameter and 1 mm in height, making it particularly challenging to manipulate once frozen.

The HPF process is carried out using an EM HPM100 high-pressure freezing machine from Leica Microsystems (Figure 3.2-A). The manual filling of the sample carrier sandwich with fresh cement paste is performed inside the middle plate of a plastic cartridge (Figure 3.2-B). The cartridge is then assembled and introduced in a semi-automated way in the HPF machine that is beforehand filled with approximatively 15 litres of liquid nitrogen. The HPF process takes place in an automated way almost instantaneously. The exact duration of the process can be monitored on the HPF machine's monitor and is considered to be successful if it does not exceed 25 milliseconds under the condition that a minimal pressure or 2'100 bars was reached.

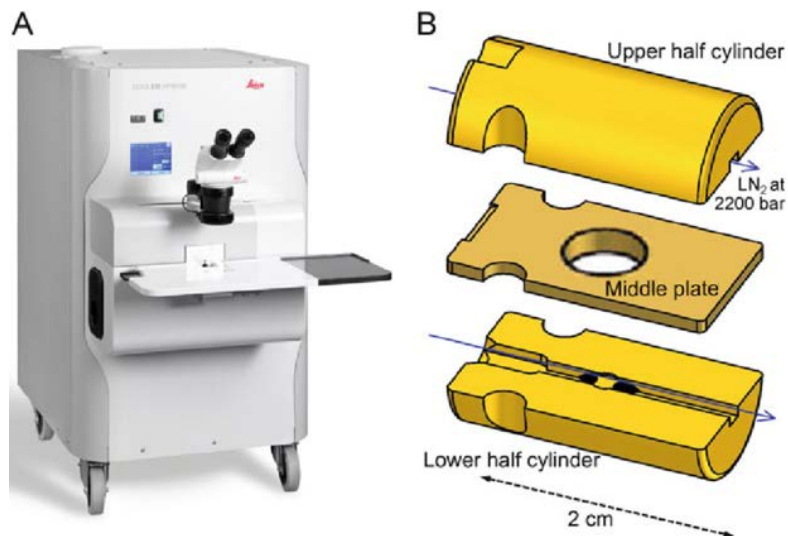


Figure 3.2: A: High-pressure freezing (HPF) machine EM HPM100. B: Exploded view of the cartridge system of the EM HPM100 for 6 mm sample carriers: Identical upper and lower half cylinders and a middle plate with bore for the sample carrier sandwich. Arrows indicate the flow of liquid nitrogen during the cooling process. Source: adapted from [61]

The cartridge containing the frozen sample carrier sandwich is immediately released by the machine into a liquid nitrogen filled container. It is important to note that from this point the samples have to remain at temperatures below - 120°C in order to prevent the vitreous ice from crystallisation as that would alter the cement paste microstructure. This is ensured by constantly keeping the high-pressure frozen samples in liquid nitrogen.

Also, if the sample carrier sandwich is opened at any point prior to its introduction in the vacuum cryo-coating machine (section 3.3.3), the sample must be discarded. Indeed, any brief contact between the vitrified cement paste and ambient air or partial vacuum would, on top of the risk of raising the sample's temperature above  $-120\text{ }^{\circ}\text{C}$ , result in an instantaneous formation of ice frost on the surface of the vitrified cement paste due to ambient humidity and the sample's temperature. Such a frost layer would make any further cryo-FIB-SEM tomography likely impossible as its thickness usually represents several times the depth accessible to observation with this technique. Usually, the sample carrier sandwiches remain closed due to the adherence of the vitrified sample contained inside. Nevertheless, it is not uncommon that the sandwich opens during the HPF process or its further manipulation, which makes it necessary to high-pressure freeze several samples in order to account for potential losses.

All manual manipulations of samples are performed in liquid nitrogen filled baths using metallic tweezers. These manipulations have to be carried out with special care and precision for both quality and safety reasons:

- The temperature range is considered to be “safe” for the sample (below  $-120\text{ }^{\circ}\text{C}$ ) as far as it stays in liquid nitrogen or in the space located within a couple of centimetres above a liquid nitrogen pool for short periods of time (below 5 seconds and under the condition that there is no air disturbance such as operator's breath or a draught).
- For the operator, a quick, precise and effective manipulation of the samples is essential. For this, the extremity of the metallic tweezers must reach liquid nitrogen temperature before touching the sample carrier sandwich. For this, before manipulating any sample, the tweezer's tips are first plunged a few seconds in an insulated liquid nitrogen until the tweezers' extremities stop boiling. This bath also contains the sample, so that from this point on, the operator has usually a dozen of seconds for sample manipulation prior to risking freeze burns on his/her fingers resulting from the progressive temperature drop of the tweezers. Wearing of thermally insulating gloves is impossible from a practical point of view, as they strongly affect the manipulation precision required because of the small size of the samples. The wearing of thin laboratory latex gloves is not recommended either as the sweat entrapped in the gloves acts as a thermal conductor potentially provoking faster and worse freeze burns.

Overall, efficient and safe manipulation of the samples comes with experience at the expense of the operator's learning curve involving several lost samples and minor freeze burns.

The sandwich carriers containing the vitrified cement paste are transferred and enclosed under liquid nitrogen inside special stainless-steel containers ensuring thermal inertia during their brief manipulation in ambient air. The samples inside these containers can be stored for an indefinite period of time in liquid nitrogen tanks that need to be regularly refilled.

### 3.3.3. Cryo-transfer and conductive coating

The samples' preparation prior to their insertion in the electronic microscope is a time-consuming process that involves multiple stages and resources. It requires about 25 to 40 litres of liquid nitrogen to manipulate the samples and to cool down the necessary equipment. The overall samples' preparation process can take from 1.5 to 3 hours depending on the operators' experience and unforeseen events. A graphic summary of this process is presented in Figure 3.3 (steps 4 and 5) including the previously performed mixing, high-pressure freezing and storage steps (1 to 3).

The sample carrier sandwiches are first taken out from storage and placed in an insulated bath filled with liquid nitrogen for manipulation. In this bath the samples are fixed onto a cryo-sample mount. This mount is composed of a semi-articulated metallic block ensuring thermal inertia that can be manipulated and transported by a cryo-transfer system between various pieces of equipment under cryogenic and vacuum conditions.

The cryo-transfer system VTC 100 from Leica Microsystems is composed of a lockable vacuum chamber and a manipulator allowing to grab the cryo-sample mount and move it within the chamber or to transfer it from the chamber in other equipment. The chamber of the VTC 100 is fitted with a base able to accommodate the cryo-sample mount that is connected to a small external reservoir of liquid nitrogen that needs to be regularly topped-up to ensure safe temperatures of the samples during transfers. It is important to note that transfers with the VTC 100 must be performed as fast and efficiently as possible as the integrated liquid nitrogen reservoir and the VTC 100 capacity to hold vacuum are estimated to about 5 to 10 minutes while the samples are under safe conditions.

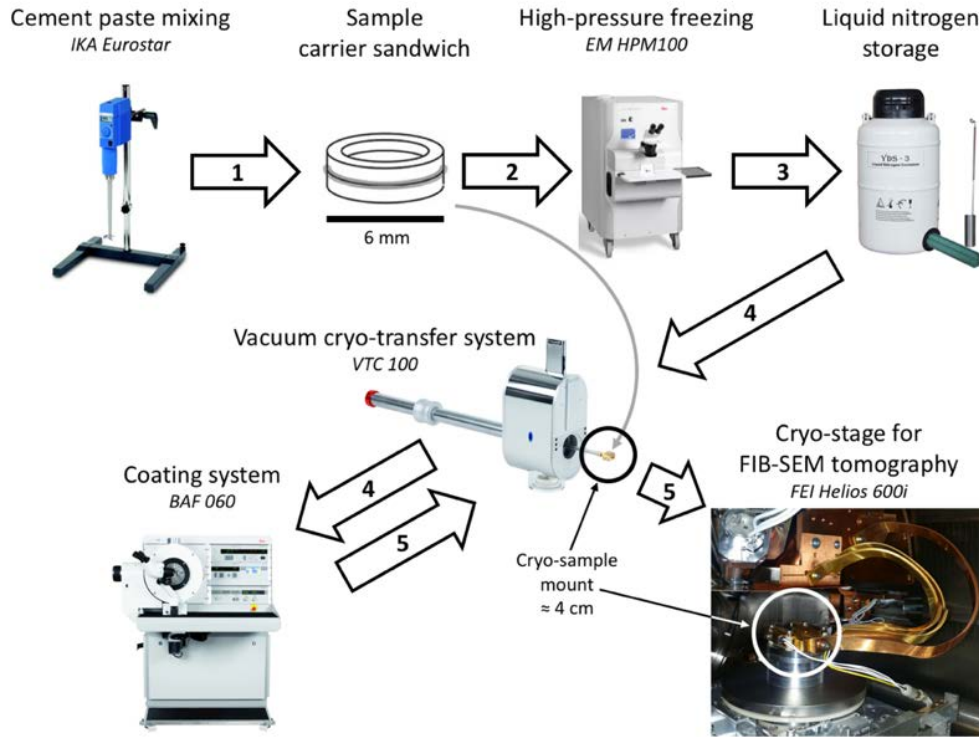


Figure 3.3: Cryo-samples preparation process: 1) The model cement paste is mixed with a tachymeter-fitted IKA Eurostar stirrer and deposited inside a sample carrier sandwich right after mixing. 2) The sample is high-pressure frozen using the EM HPM100 at the 5 minutes time mark after the beginning of mixing. 3) Frozen samples are kept in liquid nitrogen storage tanks until their analysis. 4) Up to two sample carrier sandwiches are fixed on a cryo-sample mount compatible with the electron microscope and transferred to the coating system BAF 060 using the vacuum cryo-transfer system VTC 100. 5) After removing the top planchette of the sample carrier sandwich inside the coating system and tungsten coating the exposed vitrified model cement paste to make it conductive, the sample is transferred by VTC 100 into the FEI Helios 600i electron microscope fitted with a cryo-transfer vacuum lock and a cryo-stage.

To make the samples conductive and therefore suitable for electron microscopy, a coating machine capable of handling cryo-samples, the BAF 060 is used. This machine is under high vacuum conditions and needs to be fed with a constant flow of liquid nitrogen during its use in order to keep the samples at safe cryogenic temperatures. The cooling process of the coating machine takes about 45 to 60 minutes that needs to be accounted in the workflow. The cryo-sample mount with the sample carrier sandwiches is transferred from the liquid nitrogen manipulation bath to the coating machine by using the cryo-transfer system and a vacuum lock mounted on the BAF 060. Once in the coating machine, the samples are under high vacuum and safe cryo-temperature conditions where they can be kept safely for extended periods of time.

The top planchettes of the sample carrier sandwiches are removed inside the coating machine with the help of a rotary blade thereby exposing the vitrified cement paste surface. From this point the samples need to be always kept in high vacuum in order to avoid frost formation on the samples' surfaces. The conductive coating is realised with a tungsten sputter coating integrated to the BAF 060. The ideal coating current, voltage and duration varies quite significantly depending on the condition of the sputtering anode and its preparation. The coating should be realised as slowly and gently as possible in order to reach a total coating thickness of about  $10 \pm 5$  nm.

Once the coating is finished, the cryo-sample mount together with the samples can be covered with the rotary blade acting as a cryo-shield and be kept in the coating machine until their transfer to the electronic microscope using the VTC 100 system.

### 3.3.4. Cryo-FIB-SEM tomography

#### 3.3.4.1. *Microscope setup*

The microscope used for this study is a FEI Helios 600i electron microscope<sup>1</sup> and was located at the Scientific Centre for Optical and Electron Microscopy (ScopeM) of ETH Zürich. Originally purposed for ambient temperatures FIB-SEM observations and in-situ TEM lamellae preparation, this machine can be adapted for observation under cryogenic conditions. These adaptations, that can be observed in Figure 3.4, include:

- A vacuum lock compatible with the VTC 100 cryo-transfer system allowing to introduce the cryo-sample mount in the microscope under low temperatures safe conditions and without breaking the vacuum.
- An exterior liquid nitrogen reservoir with automatic refilling allowing to keep the samples at safe temperatures throughout their observation.
- Inside the microscope chamber:
  - A heat sink cooled down by liquid nitrogen provided by the exterior reservoir.
  - A temperature controlled cryo-stage capable of fitting the cryo-samples mount introduced through the vacuum lock and connected to the heat sink with flexible thermal conductors.
  - A cryo-shield located above the samples connected to the heat sink.

---

<sup>1</sup> <https://scopem.ethz.ch/instruments-services/instruments-alphabetical/helios-600i.html>

If the microscope is used under both cryogenic and ambient temperatures conditions by different users, the heat sink, the cryo-shield and the cryo-stage need to be mounted prior to observations requiring cryogenic temperatures. The cryo-stage is fitted with a thermometer and a heating element connected to an exterior control panel allowing to monitor and adjust the samples' temperatures throughout the observation.

The role of the cryo-shield is to act as a sink for any gaseous contaminants present in the microscope chamber despite the low-vacuum. This is ensured by the cryo-shield always being at considerably lower temperatures compared to the samples, making it a preferential deposition surface and keeping the samples relatively free of contaminants.

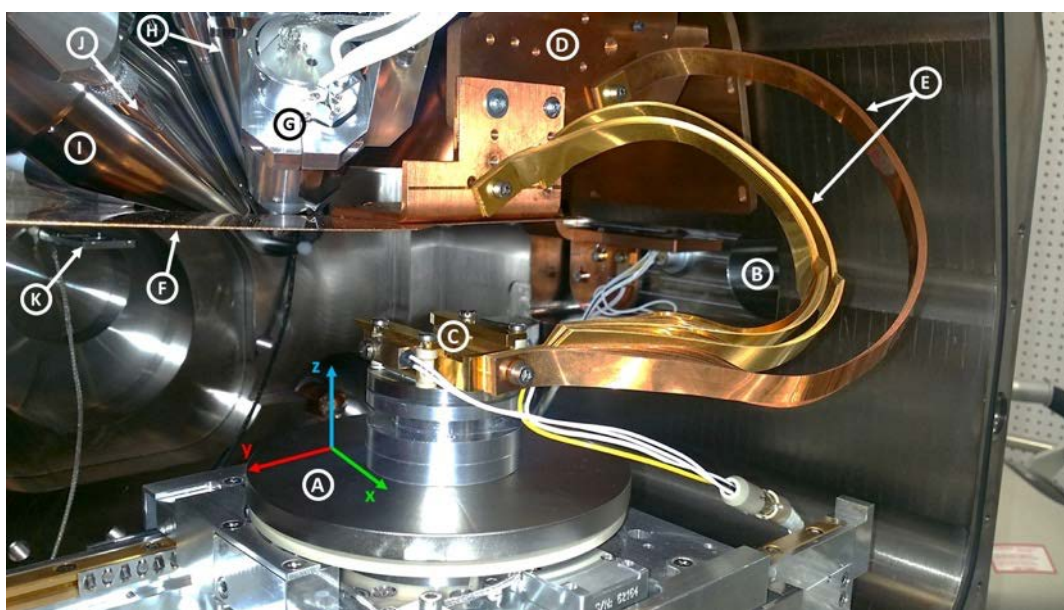


Figure 3.4: Inside of the FEI Helios 600i cryo-fitted dual-beam FIB-SEM microscope. A) 5-axis samples' stage. B) Vacuum lock for insertion of the cryo-sample mount. C) Cryo-stage capable of fitting the cryo-sample mount. D) Copper heat sink connected to outside liquid nitrogen reservoir. E) Copper and brass thermal conducting flexible bands connecting the cryo-stage to the heat sink. F) Copper cryo-shield connected to heat sink. G) Back scattered electron detector. H) Electron gun (behind G). I) Ion gun. J) Gas injection system (GIS). K) Secondary electrons detector.

It is important to note that at the time of this study, FEI was still developing their proprietary heat sink, cryo-stage and cryo-shield for this particular model of microscope. Therefore, some of these specific elements used in this work were prototypes from FEI or custom made by ScopeM.



For observations under cryogenic conditions, the microscope's cryo-stage requires to be cooled to cryogenic temperatures safe for the samples before introducing them in the observation chamber. This process takes 60 to 90 minutes until the cryo-stage reaches a temperature  $-150^{\circ}\text{C} \pm 5^{\circ}\text{C}$ . The quantity of liquid nitrogen required for cooling down the machine and for the observation depends on its planned duration. A conservative estimation would be 10 to 15 litres for cooling down and about 2 litres per hour of observation. It is crucial for the success of the observation that liquid nitrogen is always available in the cooling system's external reservoir as a lack of it would result in a progressive rise of the samples temperature potentially inducing spatial drift of the samples, sublimation of vitrified ice and formation of crystalline ice altering the samples microstructures.

#### *3.3.4.2. Tomography preparations*

After introducing the cryo-sample mount in the microscope chamber it is locked in place onto the cryo-stage allowing it to be moved, rotated and tilted by the 5-Axis sample's stage. This stage allows movements along the X, Y and Z axis as shown in Figure 3.4. Also, it is capable of rotations around the Z-axis and an additional one called the "tilting" axis, which is parallel to the X-axis and goes through the coincidence point between the electron and the focused ion beams. The angle between these two beams in the case of this microscope is equal to  $52^{\circ}$ , which locates the coincidence point at a working distance of 4.2 mm from the electron gun along the Z-axis. It is only when a sample's region of interest (ROI) is located at the coincidence point that it can be simultaneously observed by electron imaging and milled or observed by the focused ion beam as presented in Figure 3.5. The sample is referred to as "tilted" when its volume of interest (VOI) containing surface is located at the coincidence point and rotated at an angle of  $52^{\circ}$  around the tilting-axis facing the focused ion beam under a right angle.

Bringing the sample to the coincidence point position is the first step after introducing it in the microscope chamber. It is achieved by placing the sample's surface at a working distance of about 4.2 mm, finding a point of reference using SEM imaging and progressively increasing the tilt angle in steps of 5 to  $15^{\circ}$ . At each step the working distance is adjusted to keep the chosen point of reference in the centre of the image. Once this procedure is completed, it is checked that the point of reference is centred in both SEM and FIB images at tilt angles of 0 and  $52^{\circ}$ .



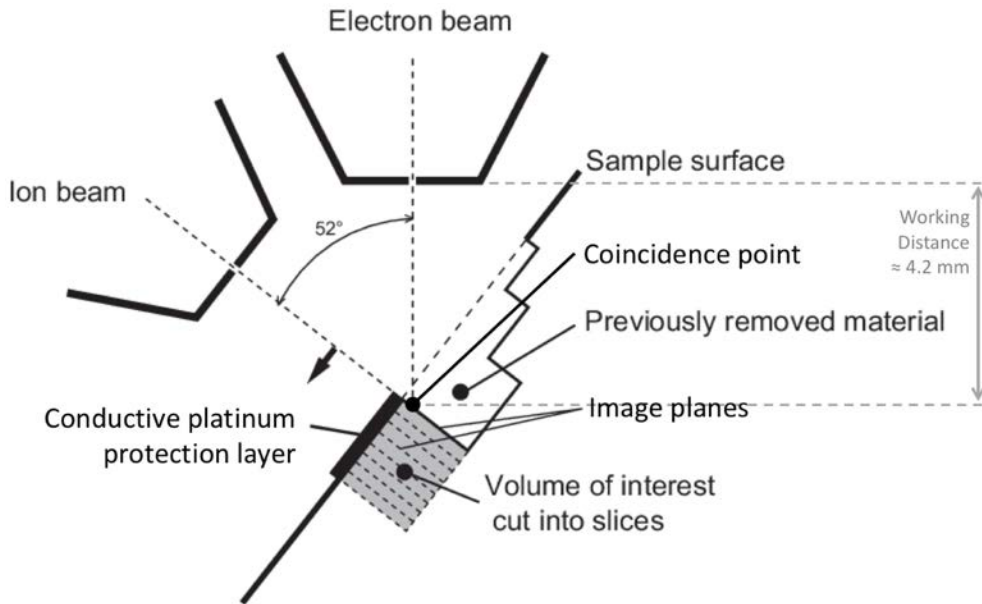


Figure 3.5: Schematic representation of the arrangement between the beams and the sample for FIB-SEM tomography. Source: Adapted from [62].

The tomographic process requires the sample's surface to be protected from ion beam imaging damage and be as smooth as possible in order to avoid what is commonly called "curtaining" artefacts originating from uneven milling of the image planes. Both are provided by the deposition of an additional conductive sacrificial protection layer. At ambient temperature conditions, this is usually done by an automatic process of the microscope software using the FIB in combination with the Gas Injection System (GIS). The GIS diffuses a gaseous Platinum precursor through a small needle very close to the sample's surface. The focused ion beam interacts with the precursor to create a platinum conductive layer of user defined thickness and geometry on the surface of the sample as can be observed in Figure 3.6.

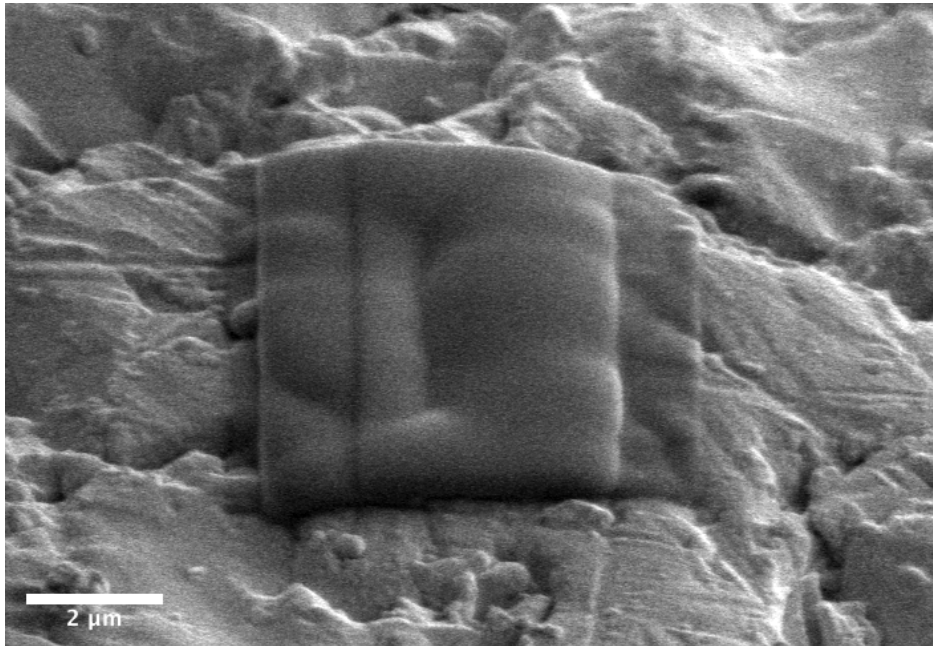


Figure 3.6: Surface of epoxy embedded model cement under ambient temperatures conditions. In the centre of the image a protection layer of rectangular shape deposited by GIS-FIB can be observed. For cryogenic conditions this layer will be made to cover a much broader part of the sample and the trench illustrated in Figure 3.7 will be cut into the sample through this layer. Image: Electron beam, SE detector, 52° tilt, adjusted brightness and contrast.

Under cryogenic conditions this automatic process cannot be used as it results in a deposition of a thick inhomogeneous and non-conductive layer of condensed precursor on the sample's surface due to its low temperature, making any further tomography process likely impossible. Therefore, a custom manually operated protection layer deposition protocol was implemented by trial and error during this project which requires maintenance administrator rights to gain access to advanced functions of the microscope:

1. Lower the temperature of the GIS system to 30°C. This process takes about 20 to 30 minutes that needs to be accounted for in the workflow.
2. Move the sample away from the tip of the GIS needle by lowering it by 1 mm from the coincidence point.
3. Insert the GIS needle and open the precursor flow for 5 seconds using maintenance override protocols of the microscope. This allows a semi-controlled deposition of an amorphous non-conductive layer of Platinum precursor on the surface of the sample. 5 seconds of precursor flow corresponds to a deposition of a layer of about 0.4 to 0.8  $\mu\text{m}$
4. After retracting the GIS needle and repositioning the stage at the coincidence point, the ROI is manually exposed to the focused ion beam with currents between 790 pA and 9.3 nA in order to make the previously deposited precursor layer conductive. A conductive strip is also created with the metallic

edge of the sample carrier planchette to ensure a correct evacuation of the electron charge.

5. This sequence is repeated three to four times to obtain a quasi-homogeneous conductive protection layer with a thickness of 1 to 2  $\mu\text{m}$ .

In order to gain access to imaging planes, a wedge-shaped trench is milled away by the FIB in front of the volume of interest (VOI) as shown in Figure 3.7. The dimensions of this trench for this work were usually about 60  $\mu\text{m}$  wide by 50  $\mu\text{m}$  long by 45  $\mu\text{m}$  deep giving an exploitable imaging surface of about 40 by 30  $\mu\text{m}$ . The FIB milling process is done automatically by the microscope accordingly to the designated location, geometry and parameters. The milling of a trench with such dimensions takes about 30 to 45 minutes depending on the selected ion beam operating current. In some cases, two additional cuboid shaped trenches were milled away on both sides of the VOI (Figure 3.7). The purpose of these trenches was to give additional space for the milled-away matter to be evacuated and therefore minimise the risk of contaminating the image surface during the tomographic process. The dimensions of these side trenches were usually about 15 to 20  $\mu\text{m}$  wide by 30 to 40  $\mu\text{m}$  long by 45 to 50  $\mu\text{m}$  deep for a total milling time of about 8 to 12 minutes per trench.

The final step after opening the trenches and before beginning setting up the tomography process is on the one hand to clean the imaging plane from potential contamination coming from milling the trenches and on the other hand to make the sample as flat and smooth as possible for the imaging process. This step also called “polishing” is done by milling a 400 to 500 nm thick slice off the imaging plane using the FIB at low current setting ensuring a gentle and homogeneous removal of matter.

At this point, images of the vitrified fresh model cement paste microstructure can be already acquired for qualitative analysis. Several of these images are presented and discussed in section 3.4.1 of this chapter.

### 3.3.4.3. FIB-SEM nano-tomography

The FIB-SEM nano-tomography process takes place in an automated way that nevertheless requires monitoring on a regular basis. The images that are used for three-dimensional reconstruction are acquired during this process by the BSE detector in order to be able to distinguish different levels of grey values produced by different observed phases: vitreous ice, unhydrated clinker and precipitated hydrates.

To setup the tomography process, also called “slice & view”, the first step is to make sure that the astigmatism and the lenses alignment of the electron and

focused ion beams are accounted for and corrected. Then both beams are focused on their respective surfaces of interest: the imaging plane for the electron beam and the sample surface for the focused ion beam. Brightness and contrast are adjusted for the BSE image in order to capture the widest range of grey levels without losing any information. The electron beam voltage, current, spot size, scanning speed and image resolution are also defined during this step. As the angle of incidence of the electron beam with the image plane is  $52^\circ$ , an automatic digital tilt correction has to be activated in order to take this angle into account and correct the image accordingly by stretching it vertically.

Using the “slice & view” module of the microscope’s operating software, a SE image using the focused ion beam is taken. This image is used to define the location of the volume of interest as well as the placement of a FIB alignment fiducial mark (Figure 3.7, Figure 3.8).

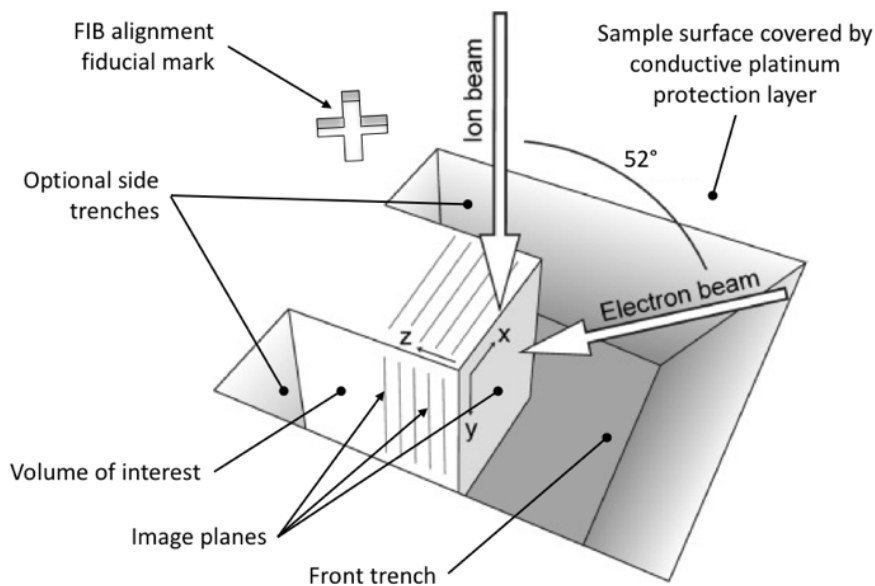


Figure 3.7: Schematic representation of FIB-SEM nano-tomography. The upper horizontal surface is covered with the protective sacrificial layer illustrated in Figure 3.6. Source: Adapted from [63]

This fiducial mark, usually of a distinct shape, is milled by the FIB prior to the tomography process. This mark is then used during the slice and view process to automatically account and correct for eventual spatial drift of the sample or the focused ion beam and to re-focus the ion beam. Once this step is complete some last and crucial parameters need to be defined before starting the slice and view process:

- Slicing thickness: This value corresponds to the thickness of each slice that will be milled by the FIB between each BSE image during the slice and view process. This value also defines the resolution of the third dimension of the tomography.
- Slices quantity: The number of slices desired for a given tomography. This number in combination with the slice thickness will define the total depth of the VOI that will undergo the tomography process.
- FIB milling current and voltage: While the voltage of the FIB is rarely changed from its optimal 30 kV setting, the current can be adapted to meet specific requirements. A lower current will usually result in gentler but slower milling providing better quality of image surface while a higher current will on the other hand result in a quicker but rougher milling making the overall tomography process faster at the expense of the risk of introducing milling artefacts on the image planes. Both lower and upper thresholds exist for the FIB current, which when exceeded result in poor quality milling.
- FIB imaging parameters: These parameters are used for making SE images before each slice to automatically account for the spatial drift of the sample or the focused ion beam with the help of the fiducial mark. These parameters are usually set to the lowest current values in order to minimise the damage done by the FIB.
- Beams re-focusing interval: While the electron beam is refocused by a constant distance corresponding to the slicing thickness at every slice independently of this parameter, it is possible to undergo an additional auto-focussing routine for both the focused ion and electron beam every defined amount of slices. As this routine adds a considerable amount of time to a slice and view iteration, it is usually performed every 10 to 20 slices.

Once these parameters are defined, the slice and view tomography process can finally begin. A standard iteration of this process corresponds to:

- (Optional) Run an automatic re-focusing routine of the focused ion beam.
- Take a SE image of the sample surface using the FIB and re-align the beam using the fiducial mark accounting for spatial drift (Figure 3.8).
- Mill a slice of defined thickness at the location of the previous imaging plane.
- Change the focus distance of the electron beam by the distance corresponding to a slice thickness.
- (Optional) Run an automatic re-focusing routine of the electron beam.
- Take a BSE image of the newly exposed imaging plane.
- Repeat from point 1. until the defined number of slices is reached.

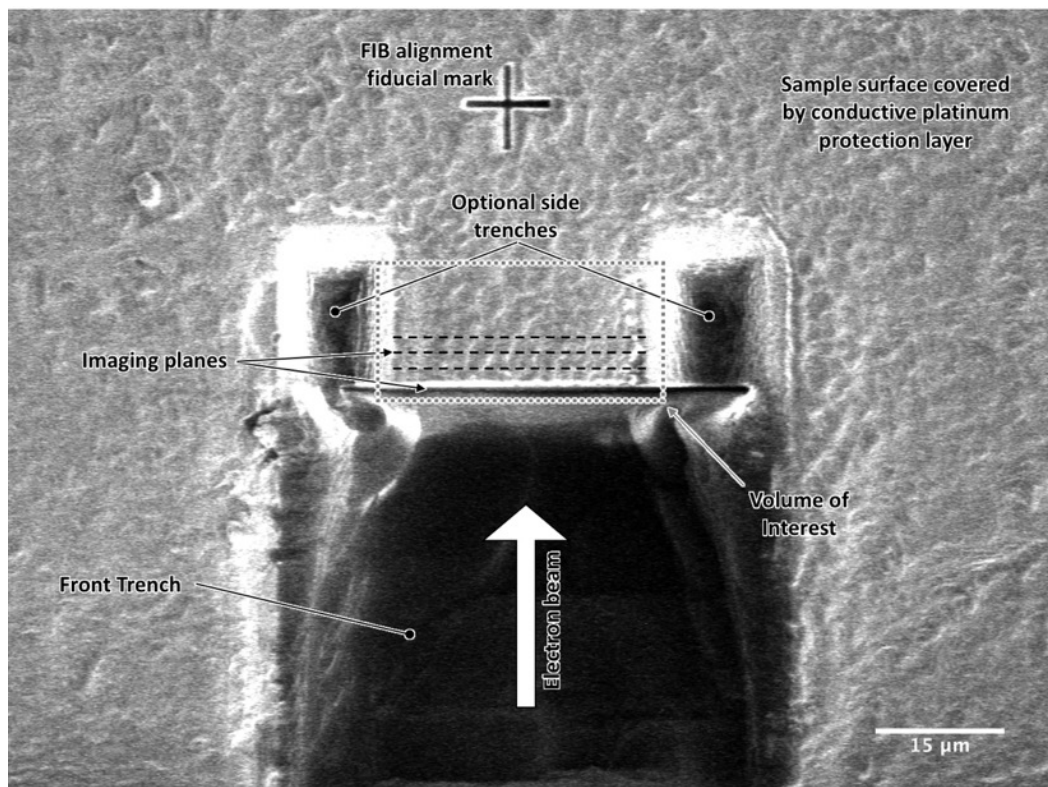


Figure 3.8: Example of FIB-SEM nano-tomography process. Image: Focused Ion Beam, SE detector, 52° tilt, adjusted brightness and contrast.

While the tomography process is automated from this point on it is nevertheless important to monitor it on a regular basis as various unforeseen issues might occur.

At this point it is also important to mention that this technique requires an important compromise between its precision and its execution time. While the time period required from the beginning of sample preparation to the beginning of the tomography process can be reduced to 4-5 hours with an efficient workflow and experience, the execution time of the tomography itself depends directly on its resolution. As an example, for this project, an isometric voxel size of 15 nm was originally chosen in order to be able to detect any hydrate particles with a size above 45 nm. This choice implies an imaging area of 21.6  $\mu\text{m}$  by 16.2  $\mu\text{m}$  at a resolution of 1440 by 1080 pixels and a slice thickness of 15 nm. With these parameters, one slice and view iteration was taking on average 1 minute and 27 seconds, resulting in an overall tomography speed along the third dimension of 620 nm per hour. Consequently, to obtain a tomography volume of 21.6  $\mu\text{m}$  by 16.2  $\mu\text{m}$  by 5.0  $\mu\text{m}$ , a total of 8 hours and 15 minutes of tomography time is needed. This brings the total workflow time to 13 to 14 hours when taking into account the sample preparation and an additional 1 to 2 hours needed at the end of the tomography to heat the cryo-stage back to ambient temperature and get the samples out of the microscope. A reduction of the tomography time is possible only at the expense of lower resolution or smaller tomography volumes.

## 3.4. Results & Discussion

### 3.4.1. Qualitative analysis of model cement pastes microstructures

BSE images of pastes' microstructures were obtained from the polished imaging plane prior to slice & view processes. Figure 3.9 shows typical examples of the observed microstructures. Three different grey levels can be distinguished on these images corresponding to the main three phases contained in these microstructures: the biggest and brightest particles are the unhydrated model cement particles. The almost black matrix corresponds to the amorphous ice and the smaller dark grey particles are the first precipitates formed within the first minutes of hydration, most likely ettringite and possibly C-S-H.

A comparison of the precipitated hydrates particles is presented in Table 3.1. These comparisons were obtained by image analysis on a limited number of particles and a limited number of images and thus must be considered to represent the qualitative rather than the quantitative differences. However, as explained below, nucleation and growth on ettringite is affected by many factors, so that the size changes reported in Table 3.1 can be in any case expected to change in relation to PCE dosage and fresh paste temperature or alkali content for example.



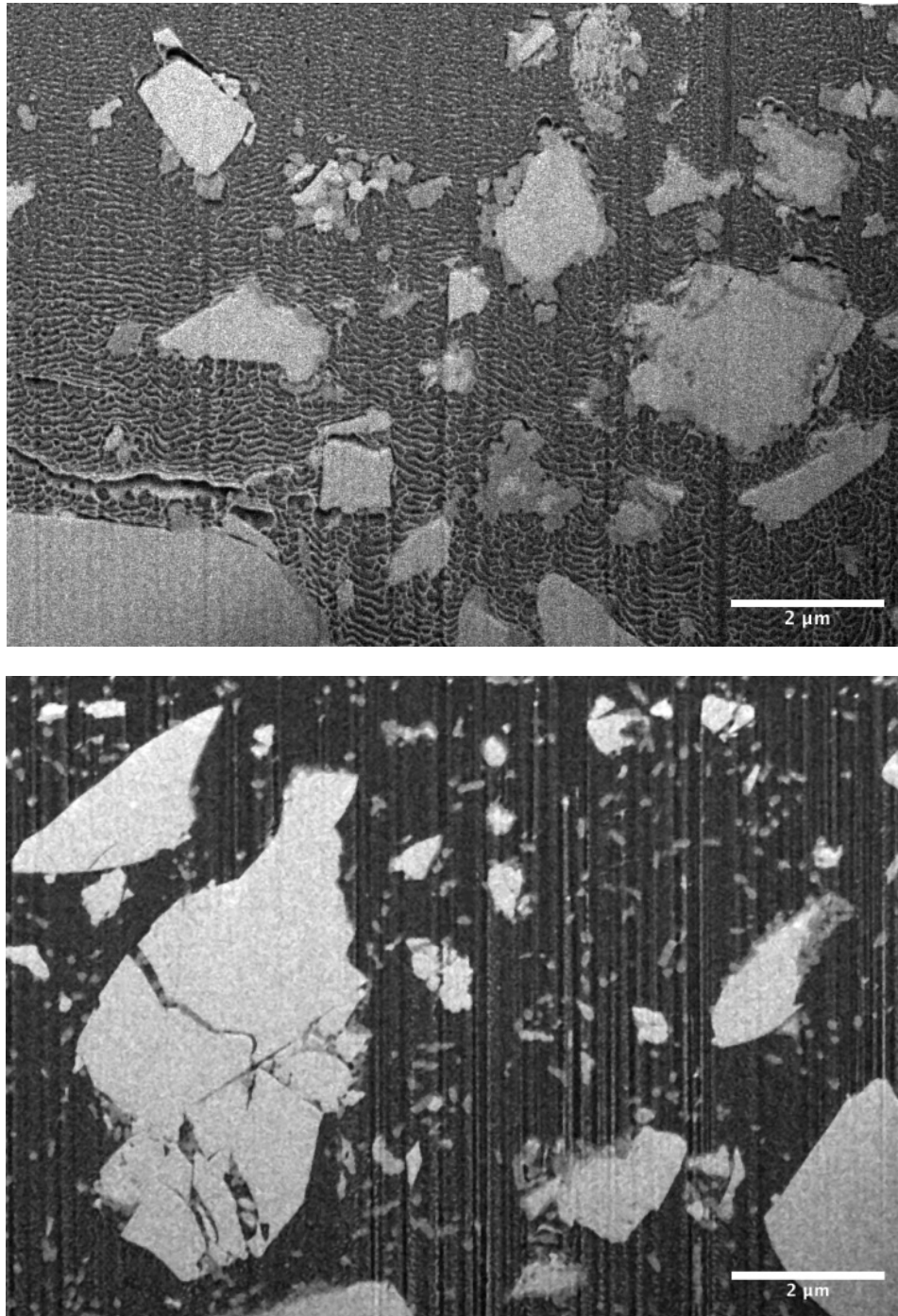


Figure 3.9: Model cement paste microstructure exposed after polishing. Top: Reference model cement paste without PCE. Bottom: Model cement paste containing PCE added in direct addition. Grey levels correspondence: light grey – unhydrated model cement particles, dark grey: first hydrate particles most likely ettringite and  $\text{C-S-H}$ , dark matrix: vitrified water. The pattern visible on the top image on the vitrified ice named “scaling artefact” is discussed in detail in section 3.4.2. Image: Electron beam, BSE detector,  $52^\circ$  tilt with correction, adjusted brightness and contrast, noise reduction by Gaussian Blur (0.7 and 0.4 px radius respectively for top and bottom pictures).

It is noticeable that the hydrates in the reference paste (Figure 3.9 top) seem to preferentially precipitate as larger particles mainly on the surface of the unhydrated model cement grains, while the particles observed in suspension in the matrix seem to exhibit a tendency to agglomeration. This observation contrasts with the microstructure of the PCE containing paste (Figure 3.9 bottom). Indeed, if some of the hydrates still seem to precipitate and stay on the surface of the unhydrated model cement grains, the hydration rim seems to cover less of their surface and be considerably thinner. A considerable number of smaller hydrates particles can also be observed to be well dispersed in the ice matrix indicating that the PCE might be stabilising hydrates nuclei in the model cement paste pore solution.

*Table 3.1: Qualitative comparison of hydrates particles properties. Values come from image analysis on a sufficient number of particles and images to give a qualitative comparison but not a quantitative one. (two images and about one hundred particles were used per type of paste)*

	Reference paste	PCE containing paste
Location	Preferential precipitation on the surface of unhydrated model cement particles.	Less precipitation on the surface of unhydrated cement particles. Considerably more particles seem dispersed in suspension.
Size	0.3 - 0.4 $\mu\text{m}$	0.1 - 0.15 $\mu\text{m}$
Amount	$\approx 1$ per $\mu\text{m}^2$	$\approx 4$ per $\mu\text{m}^2$
Aspect ratio	$\approx 1$	$\approx 2 - 3$

The increased number of smaller hydrate particles present in the PCE containing paste could also imply a higher specific surface area (SSA) of the solid content of this paste compared to the reference one under the condition that the volume of hydrates formed in both pastes is the same at the moment of their freezing. In fact, Marchon reports in her PhD that these PCEs increase the specific surface of this model cement after its contact with water [28]. While they do increase also the amount of ettringite, the most important contribution to the change in SSA appears to come through the change in the crystal size. It is worth noting that in another study on the impact of PCE on ettringite formation, Dalas et al. also reported an increase in SSA [8]. However, they found minor reduction in the total amount of precipitated ettringite. Nevertheless, as those experiments were conducted under very different conditions, our reference is the work of Marchon who used the same model cement and PCEs as in the present PhD.

The important interaction of PCE with ettringite during its formation is consistent with the practical experience that a higher amount of superplasticiser is needed in order to achieve an equal workability in case of direct addition in comparison to delayed addition. Indeed, there would be more surface for the polymer to adsorb and therefore a higher amount of polymer would be required to achieve similar particle dispersion and therefore workability. A much referenced discussion on the impact of PCE addition time refers to “organo-aluminate interactions” and mentions intercalation as a possibility [6]. This view was followed up by several publications that showed it is possible to intercalate PCEs in AFm [64,65]. However, related work by Giraudeau et al concluded that if samples are not dried, the PCEs would remain in the conformation that would favour steric hindrance [66]. It follows that the presence of PCEs intercalated in AFm is rather unlikely in cement pastes and that increase PCE consumption should rather be expected to come from a change in ettringite nucleation, itself leading to a change in SSA.

While the previously mentioned work by Marchon supports this, a viable measurement of the size and distribution of ettringite in pastes at early ages represents a missing piece of this puzzle. To obtain such spatially resolved measurement of ettringite in dispersed pastes was therefore one of our main targets for which we had intended to use FIB-SEM nano-tomography.

The previously stated observations seem correlated and corresponding to those obtained by Dr. Anatol Zingg during his PhD thesis [26]. However, in comparison to Dr. Zingg’s thesis, this work faced subsequent challenges and failed to obtain exploitable FIB-SEM nano-tomographies of fresh model cement pastes due to unexpected and up to this day unresolved imaging artefacts that could not be dealt with without the risk of introducing major biases in the experimental data and its interpretation. These issues are presented and discussed in details in section 3.4.2.

From the first images however, several observations can be made. A noticeable change in the aspect ratio of the hydrates is also observable. While the hydrate particles seem to have an aspect ratio close to 1 in absence of PCE, it seems to increase to values between 2 and 3 when PCE is present in the mixing water as reported in other studies [67,68]. This suggests that the amount of adsorbed PCE polymer depends on the crystallographic orientation of the hydrates faces, resulting in preferential growth happening in the direction of the planes with the least effective adsorption. Elongated shapes are common in hardened cement pastes for ettringite crystals. However, in many cases the most elongated crystals have grown in air voids and therefore result from a film fed growth whereby ions are provided by the matrix pore solution in contact with the crystal base. Beyond this, the general question of what factor affects crystal morphology is a complex one. For very slow processes it may be looked at through the Wulff equilibrium shapes derived from a minimisation of surface energy [69]. However, kinetics may also play a dominant role and modelling

such phenomena is substantially more complex. The topic of how molecular structure of PCEs affect ettringite nucleation and thereby ultimate crystal morphology is the topic of an ongoing PhD in our group.

### 3.4.2. Challenges faced during cryo-FIB-SEM nano-tomography

#### 3.4.2.1. *Artefact description*

While it was possible to obtain exploitable images of the polished imaging plane right before starting the slice and view process, an important imaging artefact issue was encountered early in the project during the tomography process itself. This artefact, which we have named “scaling artefact” because of its fish scales reminding pattern, can be observed over many samples to different extents as can be seen in Figure 3.9-top and Figure 3.10. Manifesting itself as what can be described as wave patterned and mainly horizontally oriented lines in the vitrified ice matrix, the scaling artefact was usually appearing and intensifying during the first two to five iterations of the slice and view process, after what its intensity and shape were remaining relatively constant throughout the whole tomography process. This artefact was observed on all samples regardless of whether they contained PCEs or not.

The main problem with this artefact is that its grey levels on BSE images are almost identical to the grey levels of the first hydrate particles. Additionally, the thickness of the scaling artefact lines is very close to the size of the first hydrate particles in PCE containing samples. As described above, in such cases the particles are much smaller and dispersed in the vitrified ice matrix where the artefact manifests itself. These two aspects of the scaling make any computer operated three-dimensional discretisation, reconstruction and analysis of the PCE containing samples microstructures impossible without almost certainly causing alterations of the microstructure through extensive image treatment. Indeed, the base of this process rests on grey levels thresholding in order to distinguish various phases present in the tomography. In a case where the artefact would have had similar grey levels but a considerably different size from a specific phase, it would have been possible to distinguish them by moderate image treatment algorithms that would remove the artefact without affecting the microstructure in a consequent way. However, due to the fact that the scaling artefact has both similar grey levels and size compared to the first hydrates present in PCE containing samples, the distinction between the two is almost impossible to make without getting into heavy image treatment that would compromise the very essence of the information we intended to gather in this project.

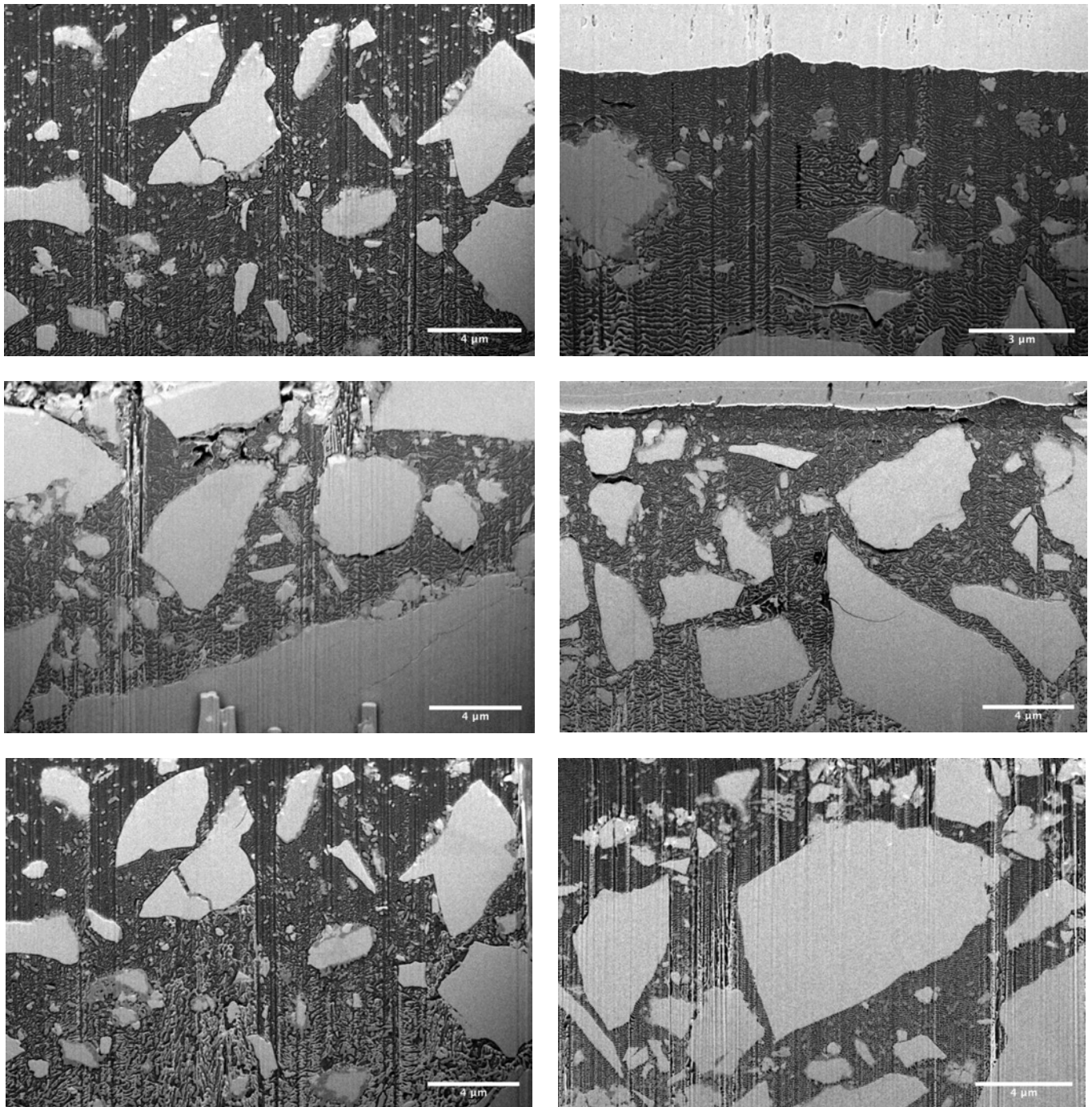


Figure 3.10: Manifestations of scaling artefact on various samples to various extents. Images: Electron beam, BSE detector, 52° tilt with correction, adjusted brightness and contrast, noise reduction by Gaussian Blur (0.7 px radius)

### 3.4.2.2. *Investigations on the origin of the artefact*

Due to the impossibility to deal with the scaling artefact with post-factum image treatment without avoiding the risk of biasing the project's results, a substantial amount of work was done attempting to eliminate the fish scales from appearing in the first place. Consulting with cryo-electron microscopy specialists from ScopeM but also from the Interdisciplinary Centre for Electron Microscopy (CIME) at EPFL and the Center for Microscopy and Image Analysis (ZMB) of the University of Zürich did not provide any viable clues on the origin of or viable solutions to the scaling. To the knowledge of all the consulted specialists, this artefact had never been encountered or reported before. In this regard, it is essential to underline that the vast majority of samples studied by cryo-FIB-SEM nano-tomography come from biology research. Consequently, the return of experience using this technique for material science is quasi inexistent in the cryo-electronic microscopy scientific community, which generally speaking exhibits a "rather limited interest in non-biology related usage of this technique".

As can be observed in Figure 3.10, the scaling artefact intensity usually exhibits a vertical gradient making it more pronounced toward the bottom of the pictures, corresponding to volumes located further from the sample's surface and deeper in the front trench. Therefore, our first suspicion was that the observed artefact might be originating from a high-pressure freezing issue resulting in partial crystallisation of the ice manifesting itself as the observed artefact.

To verify this hypothesis, a full revision of the EM HPM 100 high-pressure freezing machine was performed and new samples were frozen using 100  $\mu\text{m}$  deep planchettes instead of the originally used 200 $\mu\text{m}$  ones. The reduction of the sample's thickness allows to reduce the time needed to perform the high-pressure freezing and should have eliminated or at least substantially attenuated any potential freezing artefacts. To completely eliminate the hypothesis of an equipment related issue, additional samples were also frozen using a second high-pressure freezing machine kindly provided by the Center for Microscopy and Image Analysis (ZMB) of the University of Zürich. However, none of the newly frozen samples presented any reduction or noticeable change in the manifestation of the scaling artefact.

The next step of the investigation consisted in observing two control samples in order to verify to which extent the scaling artefact might be linked to the intrinsic nature of the samples.

The first control sample chosen for this investigation was a high-pressure frozen paste of water and quartz flour. The water to quartz flour mass ratio used in this control paste was calculated in order to correspond to the water to model cement volume ratio of the samples exhibiting scaling artefacts. The choice of using quartz flour was motivated by its similar particle size distribution and

nature to the model cement as well as by its inert behaviour in water in terms of ionic dissolution and reprecipitation.

The second control sample was chosen to be unhydrated model cement embedded in epoxy and observed under cryogenic conditions. As in the previous sample, the epoxy to model cement mass was calculated to correspond to the water to model cement volume ratio of the incriminated samples. After the model cement and epoxy paste was mixed, the sample was first left to harden inside a cryo-sample planchette and then high-pressure frozen prior to observation.

The idea behind these two control samples was to study the effect on the scaling artefact of separately changing the natures of the suspended particles and the suspension medium. The images obtained from the slice and view process of these two samples are presented in Figure 3.11.

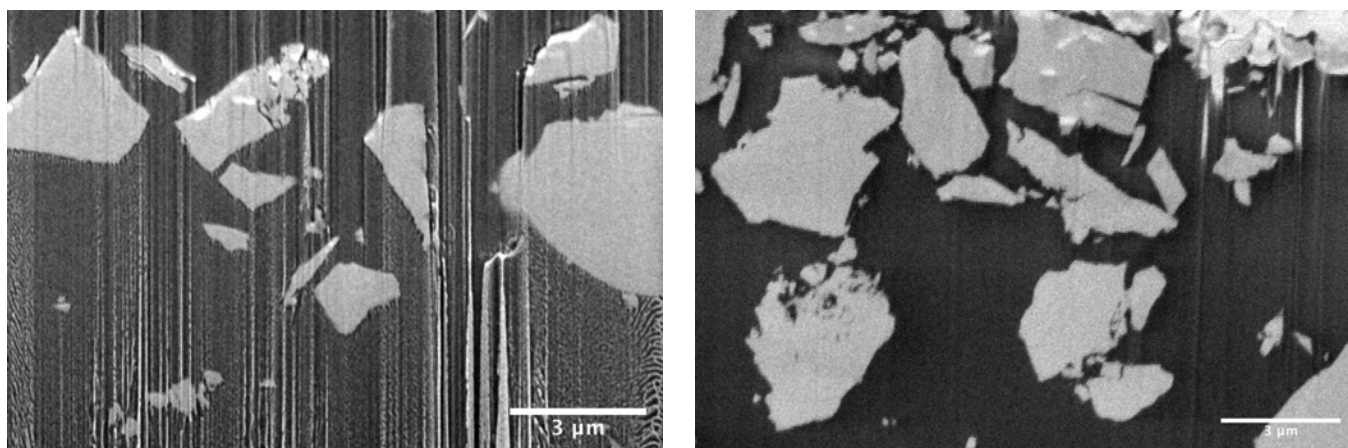


Figure 3.11: Control samples images obtained by cryo-FIB-SEM nano-tomography: Left: High-pressure frozen quartz flour in water. Right: Model cement paste embedded in hardened epoxy observed under cryogenic conditions. Images: Electron beam, BSE detector, 52° tilt with correction, adjusted brightness and contrast, noise reduction by Gaussian Blur (0.6 px radius)

While the frozen epoxy embedded model cement sample did not present any scaling artefacts during the slice and view procedure, the vitrified water and quartz flour paste did, although with a slightly lower intensity compared to the model cement and water pastes.

These results combined with the previously obtained ones eliminated the hypothesis of the scaling artefact originating from ice crystallisation possibly favoured by the ionic content of pore solution. Indeed, the quartz flour is inert in water and nevertheless also showed the scaling artefact. This allowed us to eliminate the hypothesis of the high ionic content of the pore solution may be shifting down the vitreous ice phase formation temperature and negatively impacting the safe temperature range of this ice phase.



Additionally, the absence of scaling on the frozen epoxy embedded model cement suggested that the artefact does not come alone from a high re-deposition tendency of the model cement. Rather, it points to a particular weakness of the vitrified ice in terms of resistance to either the focussed ion beam or the electron beam or both. This together with a particularly aggressive re-deposition of water due to the cryogenic conditions could be the source of our problems.

This hypothesis was consolidated inadvertently during a manual refocusing and astigmatism correction of the electron beam presented in Figure 3.12. Focusing the electron beam and correcting its astigmatism is usually done at a considerably higher magnification than the one intended for imaging, this for image quality reasons. On the sample in question, the first area highlighted in Figure 3.12-right on the top of the image was chosen to perform this operation. The magnification was increased on this particular area and after completing the focusing and astigmatism correction, the beam was inadvertently left scanning the area for several minutes by the operator. The resulting damage to the vitreous ice matrix became clearly visible when the magnification was returned to the one intended for imaging. For reproducibility purposes, this procedure was repeated a second time on the same sample resulting in the second damaged area highlighted in Figure 3.12-right. Additional samples not shown in this document suffered damage when this procedure was repeated.

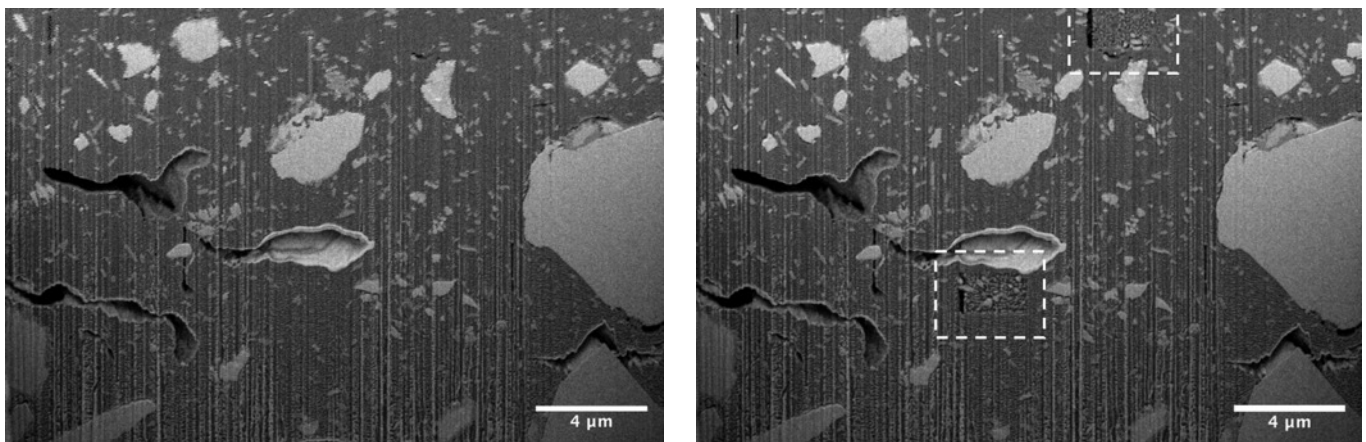


Figure 3.12: Localised damage of the vitrified ice matrix by the electron beam during its focusing. Left: Image plane before focusing. Right: Same image plane after focusing. The two areas highlighted in the right were used as magnification points in order to refocus the electron beam and correct its astigmatism. The beam was inadvertently kept scanning these areas for an extended period of time. Both areas present considerable and inhomogeneous damage of the vitrified matrix. It is also possible to observe on both pictures a considerable amount of re-deposition on the inside surfaces of the cavities truncated by the image plane. In particular the cavity located at the centre of both pictures presenting a relatively thick layer of bright amorphous re-deposition material. Images: Electron beam, BSE detector, 52° tilt with correction, adjusted brightness and contrast.

While refocusing and astigmatism correction is done at relatively high magnifications, the resolution and dwell time during this procedure are usually set in the medium-low range allowing a quick image response to the focus and astigmatism adjustments. These parameters together with the time taken for this operation define all together the energy dose that is delivered to the imaged area by the electron beam. During the slice and view process, BSE images are taken at lower magnification compared to focusing and astigmatism correction but at considerably higher resolution and dwell time in order to obtain good quality images. Therefore, the energy dose delivered to the image plane at each “view” step of the slice and view process might result in a localised temperature increase that is sufficient to damage the imaging surface by inhomogeneous sublimation of the vitreous ice matrix.

This damage and its link to the scaling artefact was confirmed by images taken after polishing and during tomography with both BSE and SE detectors as presented in Figure 3.13. Indeed, these reveal a pronounced inhomogeneous topographic aspect of the imaging planes in the SE images. It is important to note that the longer the electron beam was scanning the imaging area, the more pronounced the damage to the vitreous ice matrix was getting.

It became clear at this stage that the scaling artefact was at least partially originating from re-deposition of FIB milled matter onto the previously created damage by the electron beam on the vitrified ice surface. Based on this, our interpretation of the scaling artefact was elaborated and is schematically represented in Figure 3.14. Indeed, the imaging surface roughness induced by electron beam damage presented in Figure 3.13 - bottom row and illustrated in Figure 3.14 - top right, could be acting as a preferential location for amorphous redeposition of material milled away during the FIB slicing step (Figure 3.14 - bottom left). Even at low amounts, this redeposition would appear on the next BSE image with brighter levels of grey compared to vitrified ice due to the presence of the heavier atoms coming from the inorganic particles (Figure 3.14 - bottom right). Whether the redeposition does or does not also include water from the vitrified ice, this would create a highlight of the electron beam induced surface roughness created during the previous imaging step, which overall would explain the scaling artefact.

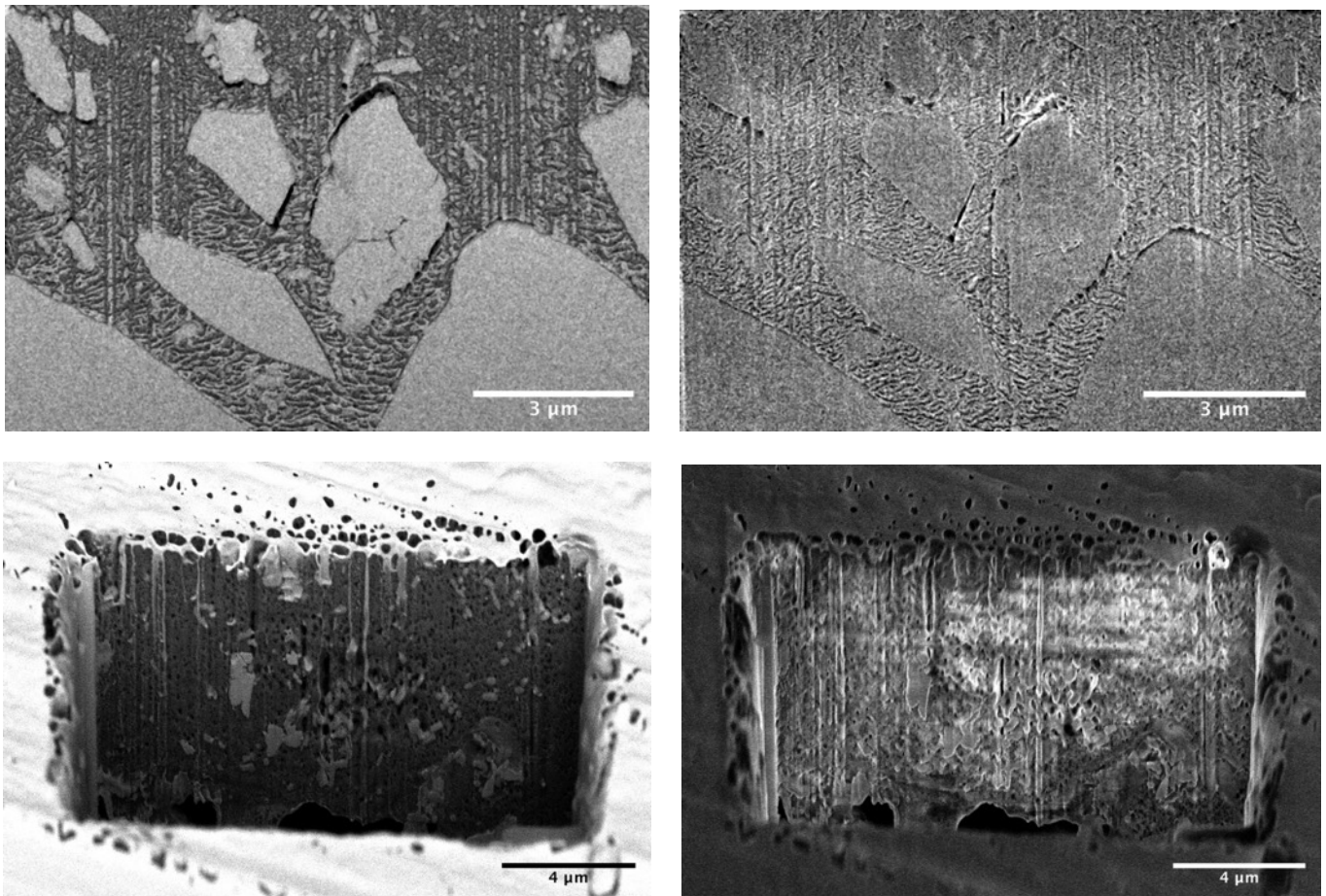


Figure 3.13: Topographic aspect of the scaling artefact. Top row: imaging plane during a slice and view process. Bottom row: images of a freshly polished surface plane taken after several images were taken at high resolution and dwell time. Left and Right columns show the same areas of samples imaged respectfully with BSE and SE detectors. Images: Electron beam, BSE and SE detectors, 52° tilt with correction, adjusted brightness and contrast.

The process described above and illustrated in Figure 3.14 explains the relative absence of the scaling artefact on freshly polished image planes, its progressive appearance during the first few iterations of the slice and view process and its perpetuation throughout the entirety of the tomography process. However, it only holds under the hypothesis that the depth of the SEM induced damage (surface roughness) is greater than the thickness of the slices defined for the slice and view process as the third-dimensional resolution of the tomography. For the originally chosen 15 nm slice thickness it is safe to assume that this is the case.

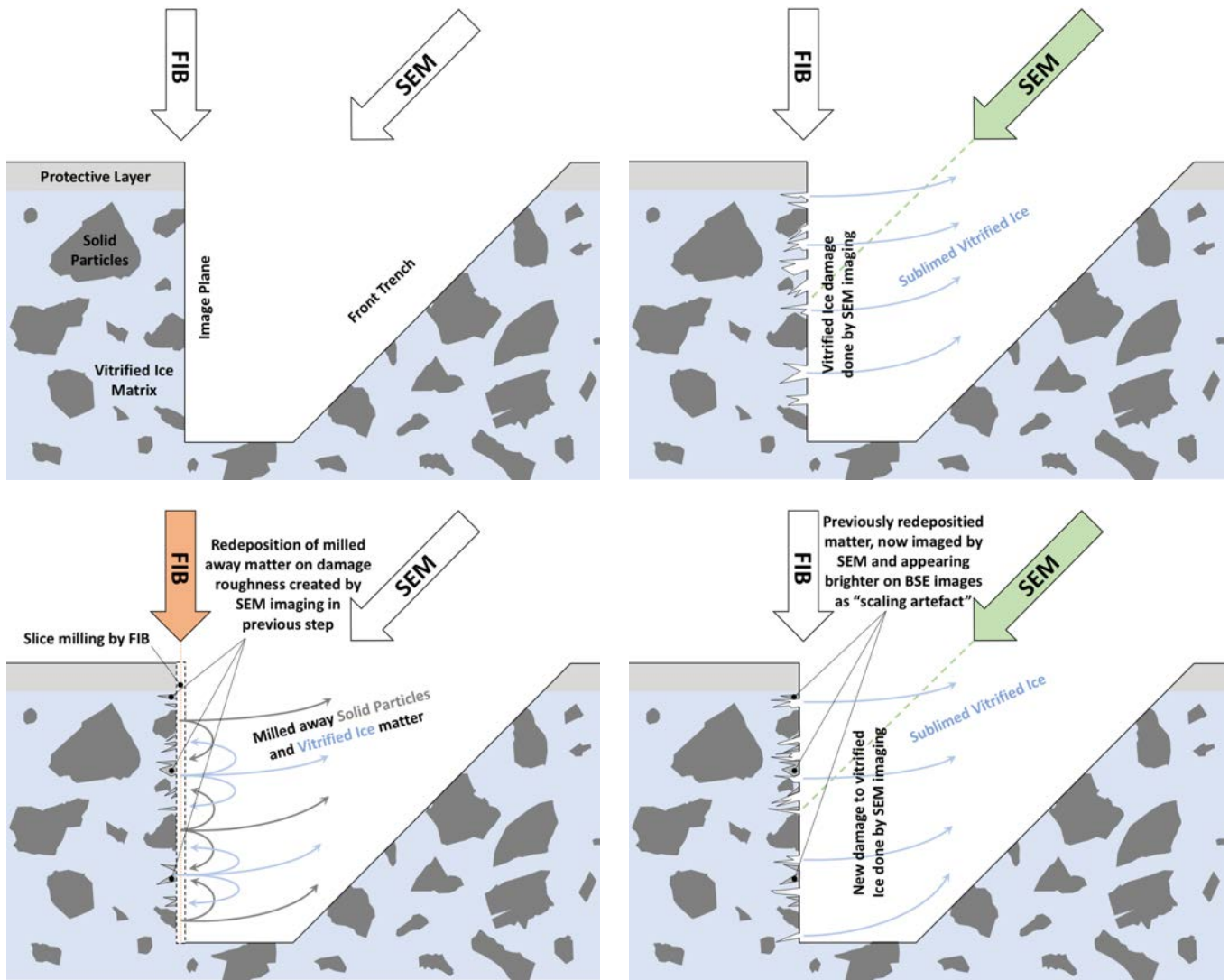


Figure 3.14: Schematic representation of the scaling artefact formation and perpetuation. Top-left: Step 0 - Sample right after Image Plane polishing. Top-Right: Step 1 - Imaging with SEM producing scaling artefact-free image while damaging the vitrified ice on the image plane. Bottom-Left: Step 2 - Milling away a tomography slice with the FIB while redepositing milled away matter onto the previously created damage (surface roughness). Bottom-Right: Step 3 - SEM imaging of the newly exposed image surface. Redeposition of matter from previous step appears brighter creating the scaling artefact while new damage is created to the vitrified ice by the SEM beam. Further, steps 2 (bottom-left) and 3 (bottom-right) are repeated, perpetuating the scaling artefact throughout all the tomography process.

Importantly with respect to our research objective, the above interpretation explains why the grey levels of the scaling artefact are very close to the hydrate particles ones. Hydrate particles exhibit BSE imaging grey levels brighter than vitrified ice but darker than unhydrated model cement, which is an expected behaviour as hydrates are by definition composed of atoms originating from both of these phases. Assuming that the redepot responsible for the scaling artefact is an amorphous mix of atoms coming from both milled away

unhydrated cement particles and vitrified ice, its similar grey levels to hydrate particles can be explained by a similar atomic composition. However, even if only little water is redeposited, the average signal between the underlying ice and the redeposited material from cement particles can be expected to give a grey level similar to hydrates. Overall, this seriously compromised our objective of identifying small hydrate particles dispersed in the aqueous phase.

### 3.4.2.3. Attempts to attenuate the artefact

The first steps taken in order to try to eliminate the scaling artefact were to increase the size of the front trench and add side trenches to the volume of interest in order to allow more space for a better evacuation of the re-depositing material. These trials did not provide any considerable decrease of the scaling artefact.

Another approach to the problem was to use different milling currents of the FIB during the slice and view process. While an increase of the milling current presented a worsening of the scaling artefact as well as the appearance of irregular milling artefacts of the imaging plane (Figure 3.15-right), the reduction of the milling current slightly reduced the intensity of the scaling artefact. However, a low current threshold was reached without being able to remove the scaling artefact in an exploitable way, while at the same time pillar artefacts due to under-milling appeared (Figure 3.15-left).

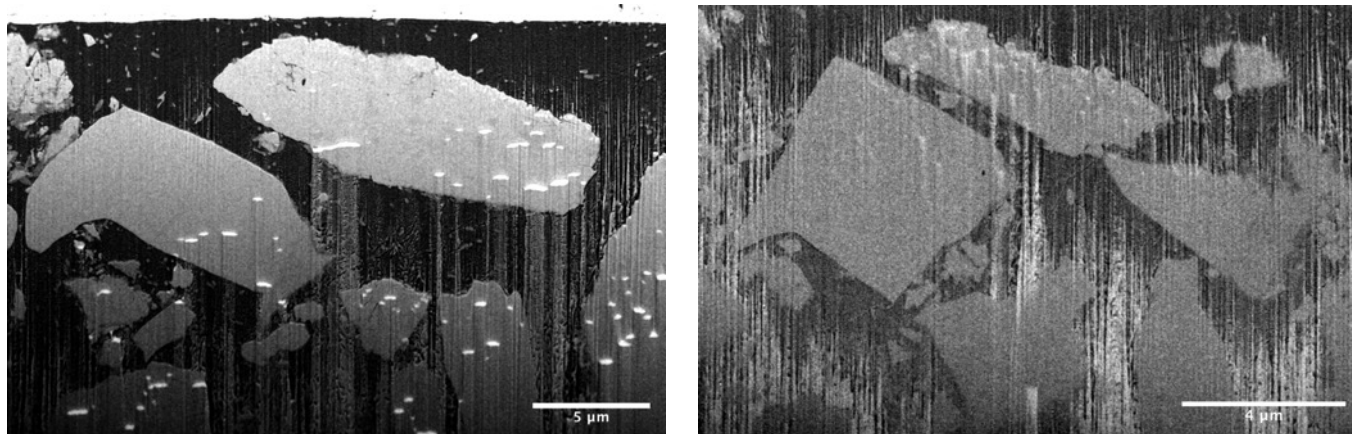
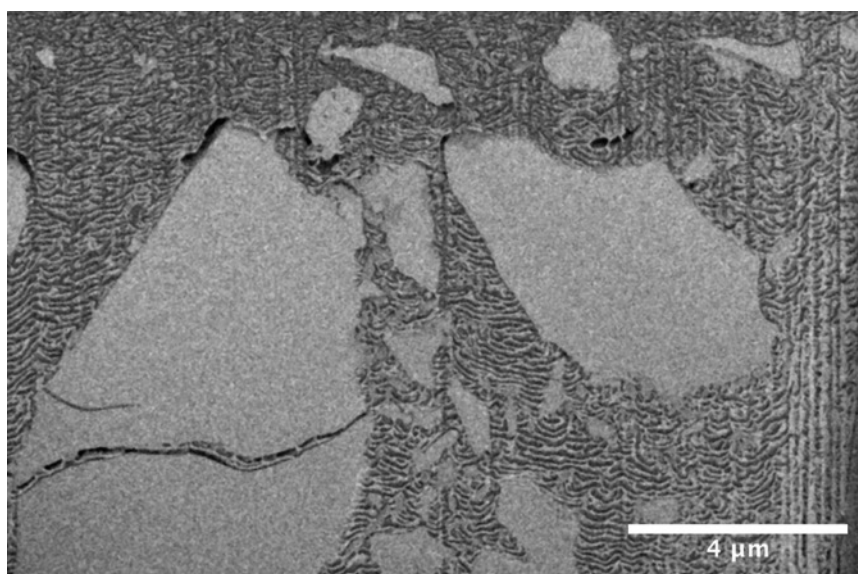


Figure 3.15: Impact of the FIB milling current. Left: Lower threshold of the current presenting pillars artefacts. Right: Higher threshold of the current presenting uneven milling and pronounced scaling artefact. Images: Electron beam, BSE detector, 52° tilt with correction, adjusted brightness and contrast, noise reduction by Gaussian Blur (0.7 px radius)

Yet another approach regarding the FIB milling during the slice and view process was tried, consisting of increasing the slice thickness. This modification was done knowingly at the expense of the tomography third-dimensional resolution originally defined to be 15 nm. The concept was to increase the slicing thickness in order to completely eliminate the surface damage roughness created by the electron beam at every slice and view iteration and make the next iteration's BSE image coming from a redepot-free face, similar to its state after polishing (Figure 3.14 – top left). With this objective, thicknesses of 30, 60, 100, 200, 500 and 1000 nm were tried, but without any success of attenuating the scaling artefact (Figure 3.16).



*Figure 3.16: Image taken during a slice and view process with a thickness of slices of 200 nm. Images: Electron beam, BSE detector, 52° tilt with correction, adjusted brightness and contrast, noise reduction by Gaussian Blur (0.6 px radius)*

This rather surprising result indicates that the origin of the scaling artefact cannot be alone explained by the SEM damage and FIB redeposition process described above in Figure 3.14 as the depth of the imaging surface damage created by the electron beam is unlikely to be greater than the slice thicknesses mentioned above. Accordingly to Potts the depth of the electron beam interaction volume for geological materials can be described by the model in Figure 3.17 [70].



$$x (\mu\text{m}) = \frac{0.1 E_o^{1.5}}{\rho}$$

where  $E_o$  = accelerating voltage (keV),  
and  $\rho$  = density ( $\text{g/cm}^3$ )

Figure 3.17: Model describing the electron beam interaction volume depth “x” for geological materials. Source: [70]

Considering that the default acceleration voltage of the FEI Helios 600i is 2 kV, which is relatively low compared to other microscopes usually operating in the 5 to 40 kV range, the electron beam interaction volume depths for model cement and vitrified ice would be 0.09 and 0.28  $\mu\text{m}$  respectively. Nevertheless, the model described in Figure 3.17 was developed specifically for geological materials to which the model cement belongs, but the true depth of the electron beam interaction volume for vitrified ice calculated with this model remains questionable. Therefore, we cannot exclude some form of modification of the vitrified ice, possibly resulting in roughness during the subsequent fibbing. Apart from this hypothesis, the results of these trials involving thicker slices remain to this point unexplained and suggest an even more complex origin to the scaling artefact involving hypothetical impacts of other parameters such as:

- A localised heating of the sample due to the energy dose brought by the focused ion or electron or both beams that would not have enough time to dissipate allowing to amplify and perpetuate the scaling artefact even with thicker slices.
- Unknown to the operator “black box” behaviour of the microscope’s hardware and/or operating software such as:
  - Different behaviour of the focused ion and electron beams during the automatic slice and view process in comparison to manual FIB imaging plane polishing and BSE imaging regardless of the same milling and imaging parameters.
  - An incomplete or only partial blanking of the electron beam during the FIB milling of the slices during the automatic tomography<sup>1</sup>.

A further large campaign of trials in order to attenuate the scaling artefact were conducted by adjusting the BSE imaging parameters. While reducing the

---

<sup>1</sup> NB: Due to the positive charge of Gallium ions and the negative charge of electrons, it is impossible to use both beams simultaneously as it results in uncontrollable collisions and unwanted effects between the two types of particles. A semi-simultaneous usage is possible in practice and implemented on certain Zeiss microscopes: it consists in interlacing focused ion and electron beams in a controlled way during the milling process in order to be able to observe it while it’s happening. However, the usage of both beams simultaneously or semi-simultaneously is not supposed to be possible on the FEI Helios 600i microscope.



electron dose seems to attenuate the scaling artefact, it comes at the expense of a loss in image quality. In fact, we reached the quality threshold needed for the project without being able to attenuate the scaling enough. This result indicates that a further reduction of the dosage delivered by the electron beam could lead to a manageable attenuation of the artefact. This can be achieved by lowering the electrons acceleration voltage and current even further. This reduction however translates in the need of using more sensible BSE detectors and therefore heavy hardware modifications of the electron microscope itself or even the usage of another microscope as the geometry of the chamber containing the sample and the construction of the electron column are known to play a consequent role in signal detection quality.

All parameters accessible to a standard user of the microscope used for this work were adjusted in order to minimise the artefact while keeping an exploitable image quantity: current, voltage, spot-size, resolution and dwell-time. Additionally, several advanced imaging parameters only accessible to a limited number of users in charge of the maintenance of the microscope were also “tweaked”, among which: scanning pattern, distance and overlap of each scanned spot, behaviour of the electron beam while moving from one scanning spot to the next and from one scanning line to the next and other advanced parameters. Similar adjustments were also tried for the FIB without consistently being able to attenuate the scaling artefact.

The last approach consisted of trying to perform the tomographies at different temperatures. The temperature of the cold-stage and therefore of the samples can be controlled through a dedicated console attached to the microscope. Without any temperature control target defined, the lowest attainable temperature with the particular cold stage used for this microscope is  $-150 \pm 5$  °C. Tomography attempts were performed at respectfully -140°C, -130°C and -125 °C to determine whether the rise of the samples’ temperature would result in less re-deposition and therefore a less pronounced scaling artefact.

The results of these later trials produced the opposite effect to the desired one with a considerably more important manifestation of the scaling artefact. Additionally, the damage done by the electron beam was observed to increase proportionally to the temperature. This damage behaviour is coherent with the fact that vitrified ice under ultra-high vacuum requires less energy to be sublimated under higher temperatures. The results of these trials confirm that the scaling artefact formation is heavily dependent on the SEM damage done to the vitrified ice described in Figure 3.14 – top right, onto which the milled away material during FIB slicing redeposits (Figure 3.14 – bottom left), thus creating light grey highlights in BSE images (Figure 3.14 – bottom right). It also indicates that the energy dose delivered by the SEM imaging translates into a localised rise of temperature leading to the previously mentioned damage.

These results show a possibility of attenuating of the scaling artefact by lowering the temperature of the samples under the condition that the preferential re-deposition due to the cryogenic temperatures do not get overwhelmingly worse under such conditions. Unfortunately, the prototypic cryo-stage available at the time of this work did not allow to lower the samples temperatures below the  $-150 \pm 5$  °C threshold.

While on the subject of temperature management, it is also important to underline that a certain suspicion arose during this project about the efficiency of the custom-made prototypic cryo-shield installed in the microscope and which is supposed to act as a preferential re-deposition surface by being at considerably lower temperatures compared to the samples. While temperature measurements of the cryo-shield were not possible during this work, it was believed that the usage of a less “custom-in-house-made” cryo-shield specifically designed for this microscope by its manufacturer may reduce the amount of re-deposition observed on the samples and therefore attenuate the scaling.

In the last attempt to achieve the main objective of this work, a second electronic microscope fitted for cryo-FIB-SEM nano-tomography was used. It was a Zeiss Auriga 40 CrossBeam using the newly developed and promising Zeiss ATLAS 5 system kindly provided by the Center for Microscopy and Image Analysis (ZMB) of the University of Zürich under the supervision of Dr. Andres Kaech. Unfortunately, despite promising first images obtained with this machine, other substantial issues appeared with this microscope, preventing its further use for our project. These arose as an inability to deposit a sacrificial protective layer and resulted in unmanageable damage of the sample during the slice and view process. Also, important charging problems due to the high voltage of the electron beam required by this machine were encountered and led to important charging artefacts and uncorrectable electron beam drifting. After several heavily unsuccessful attempts the idea of using this machine to conduct this project was abandoned.

### *3.4.2.4. Miscellaneous observations*

In the process of trying to attenuate the scaling artefact to manageable proportions, a certain number of inconsistent aspects that remain unexplained by this work were observed, two of which are worth mentioning before concluding this section:

The first can be observed in the majority of images presented above and in particular in Figure 3.18. The scaling artefact seems to be in certain cases more pronounced in areas located below unhydrated model cement grains (if the surface of the sample facing the FIB under a right angle is considered to be the top). This phenomenon is particularly confusing and unexplainable due to the

fact that gravity does not play any role in the re-deposition process as matter is milled away on an atomic level and sublimated directly into ultra-high vacuum of the microscope's chamber. Following a lead on this phenomenon, a few tomographies were attempted without deposition of the protective and sacrificial layer that could contribute to the re-deposition aspect of the scaling artefact. No particular impact on the scaling artefact was observed on samples without this protective layer while very heavy curtaining artefacts appeared due to the damage of the sample surface by FIB imaging.

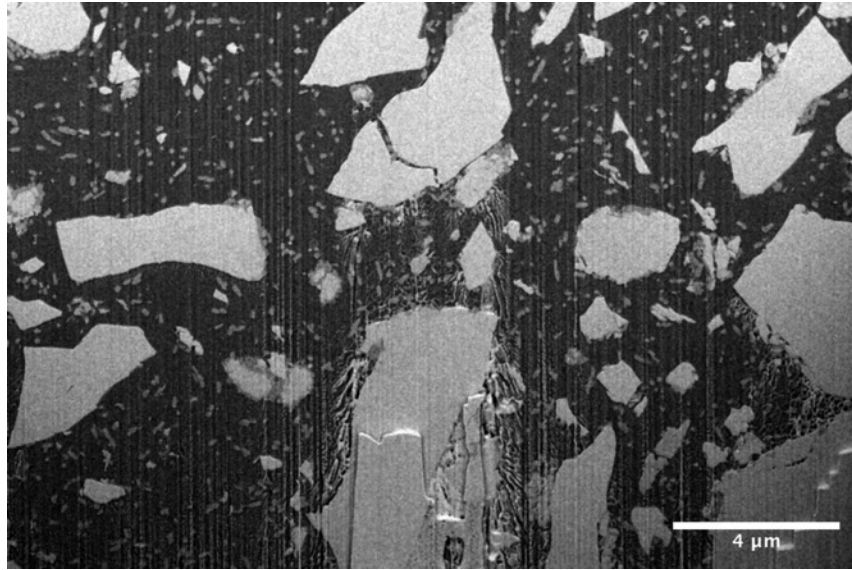


Figure 3.18: Example of more pronounced scaling artefact under unhydrated cement particles. Images: Electron beam, BSE detector, 52° tilt with correction, adjusted brightness and contrast, noise reduction by Gaussian Blur (0.4 px radius)

The observation of this aspect of the scaling artefact spawned the idea to perform tomographies on smaller volumes located right under the surface of the sample facing the FIB and containing little to no anhydrous cement particles in order to avoid the scaling artefact manifestation on the BSE images. However, due to the general inconsistency of this aspect and the fact that a reduced tomography volume chosen to contain a minimal amount of unhydrated model cement grain would be a biased observation of a non-representative volume of the sample, this idea was abandoned.

A very speculative explanation could be the orientation of FIB flux entraining the milled away matter preferentially towards the bottom of the trench, forcing its re-deposition on image surface areas located below anhydrous cement grains. However, the important inconsistency of this phenomenon's observation, together with the trials of increased slice thickness described above and the general lack of knowledge on this subject, do not allow to validate this interpretation or draw any solid conclusions regarding the scaling artefact.

The second aspect worth mentioning is the generally observed inconsistency of the scaling artefact manifestation. Indeed, it was often impossible to recreate a similar manifestation of the scaling artefact from one sample to another regardless of the facts that the samples were coming from the same mix, were frozen at the same time, prepared and observed in the microscope together while mounted on the same cryo-sample carrier under the same imaging and milling parameters. An example of the extreme intensity of the scaling is presented in Figure 3.19

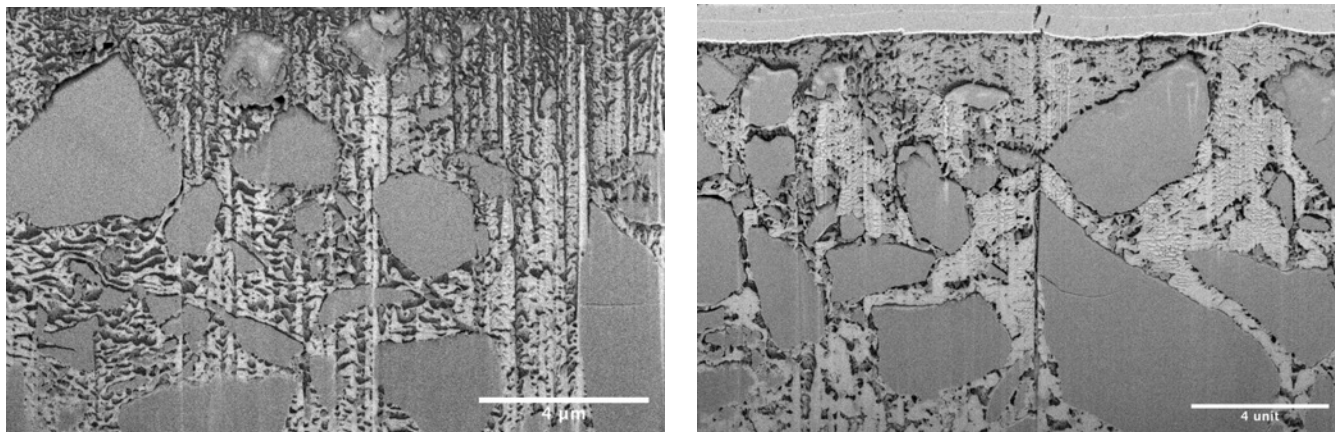


Figure 3.19: Heavy artefact. Images: Electron beam, BSE detector, 52° tilt with correction, adjusted brightness and contrast, noise reduction by Gaussian Blur (0.6 px radius)

#### 3.4.2.5. Previously unreported occurrence of scaling

The present work failed at eliminating or attenuating the scaling artefact to manageable proportions with image treatment that would not compromise biasing the obtained results and their interpretation. While doing this, it became apparent that previous work described in the introduction of this chapter as well as in the section 2.1.3 of Chapter 2 [ref zing thesis], faced similar issues.

Indeed Zingg's work is succinctly reporting a unique image treatment aimed at specifically eliminating what he calls the "waterfall effect" (referred in this work as "curtaining artefact") presented and described elsewhere [71]. However, Dr. Zingg's work neither reports the presence of any scaling artefact nor any treatment aimed at eliminating it despite that for one image for which the image treatment seems not to have been applied and in this case the scaling is clearly visible (Figure 3.20, top right). None of the other images presented in his thesis, including the ones originating from tomographies (Figure 3.21), present any traces of this scaling artefact.

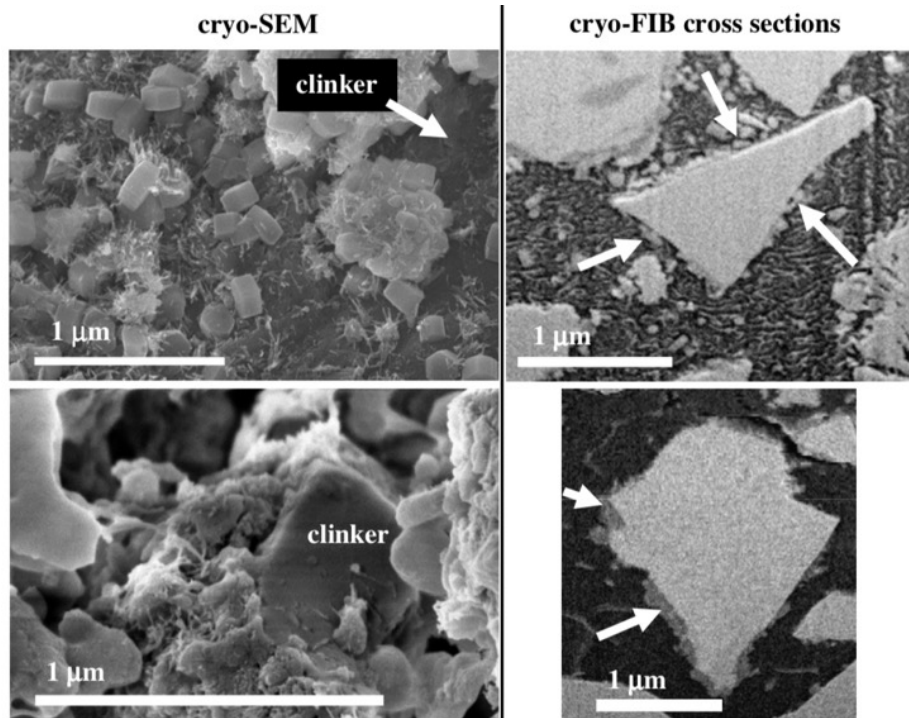


Figure 3.20: The only figure of Dr. Zingg's work exhibiting the scaling artefact (top right). Not a single other image used in his work, including those coming from tomographies as presented in Figure 3.21, were presenting or were reported presenting this artefact. Source: [26], original title of the figure: "The top left cryo-SEM image (cement suspension containing 0.7% of PCE 102-2, after 5 minutes of hydration) show a C3S surface (clinker, dark grey) with attached hexagonal short prismatic ettringite. Very fine C-S-H needles cover both, C3S and ettringite. Such individually deposited ettringite can also be observed in the cryo-FIB cross-section (top right), marked by arrows (cement suspension containing 0.7% of PCE 23-6, after 2 hours of hydration). As shown in cryo-SEM image (bottom left) mixtures of ettringite and C-S-H form dense hydration layer around a clinker particle (cement suspension after 2.5 hours of hydration) that can also be observed by cryo-FIB cross- sections (bottom right) where the arrows indicate the discontinuous hydration layer (cement suspension containing 0.2% of PCE 23-6, after 24 minutes of hydration)."

It is possible that Zingg's work was not faced with the same magnitude of the scaling artefact due to the usage of different microscopy equipment. However, the clear manifestation of this scaling in the upper right illustration of Figure 3.20 rather suggests that the image processing used to deal with the waterfall artefact may also have eliminated the scaling artefact, resulting in a constant smooth appearance of the water phase (Figure 3.21 as example). Given the different objectives of Zingg's research this can be understood, but it is very "unfortunate" that his PhD is not more transparent about this issue. The cumulative dissertation of that PhD probably was also not prone to including much details about challenging aspects of cryo-FIB-SEM nano-tomography. In particular, his conclusions drawn from quantitative analysis of frozen fresh cement pastes tomographies presented in Chapter 4 of his thesis [26] and

published as a Journal article [72] appear over enthusiastic in the light of our experience of the use of this method.

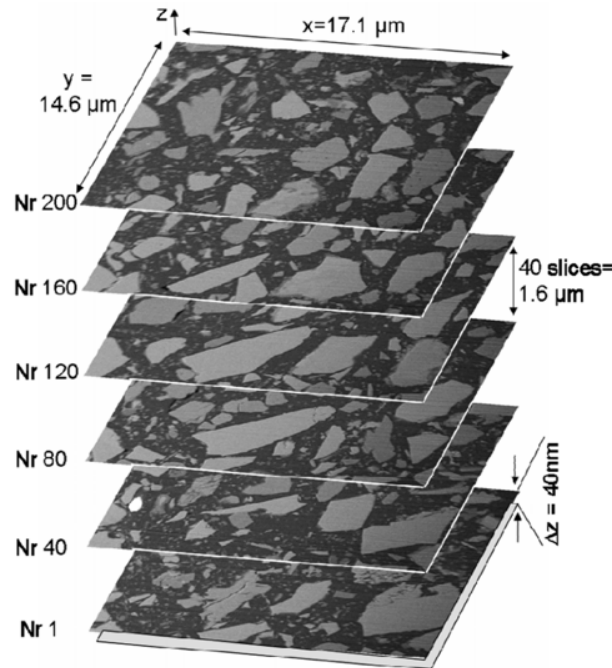


Figure 3.21: Example of tomography image data used in Dr. Zingg's work after they underwent a reported image treatment to remove the waterfall effect, and purposively an additional unreported heavy image treatment to remove the scaling artefact clearly visible on an image from the same work presented in Figure 3.20. Source: [26], original title of the figure: "Stack of images produced with cryo-FIB-nt from sample C6 (fresh cement paste, hydrated for 6 minutes, hydration was stopped with high- pressure freezing). Only every 40th image is shown from this stack and the distance in the z- direction is enlarged. The true distance in the z- direction between two succeeding images, e.g. between Nr. 1 and Nr. 2 (not shown) is 40nm. The total thickness of the stack with 230 slices is 9.2  $\mu$ m. The x-direction is parallel to the ion beam.

One issue appears relatively problematic for the broader cement research community. This is that the work of Zingg is often quoted to be a demonstration that cement hydration is not passivated at early stages by the formation of a thin hydrate layer. His results certainly show that the distribution of hydrate layers around cement grains is inhomogeneous and this result is reported not to be affected by the image processing applied to the waterfall artefact. However, regarding the possibility that a thinner layer may be present, the question may be raised about whether his results can indeed be used to claim that there is no such layer at all. Once again, this was not the objective of Zingg's work, but his published results and limited documentation on the occurrence of the scaling and image processing may be leading researchers to misinterpret an important question in cement hydration. On the more positive side, there is a lot of other

indications that cement hydration slows down for other reasons than the formation of a passivation layer. It is our opinion however, that the images reported by Zingg should not be embedded in that overall argumentation.

## 3.5. Conclusions and Outlook

While the main objective of this project to perform quantitative analysis of the impact of PCE superplasticisers on the nucleation and formation of first hydrate particles in a controlled system of a model cement paste was unsuccessful due to the scaling artefact, this project allowed a better understanding of this phenomena that can be used in future works.

In opposition to biological samples mainly composed of water and soft biological tissues for which cryo-FIB-SEM nano-tomography is usually used, fresh cement pastes exhibit a much more inhomogeneous structure as they are composed of hard and dense particles with a high average atomic number suspended in a pore solution. This inhomogeneity together with the observations and results obtained during this project regarding the scaling artefact (section 3.4.2), could partially explain why it seems to have never been observed before in biological samples.

Nevertheless, cryo-FIB-SEM nano-tomography still holds considerable promises for the study of unaltered fresh cement paste microstructure under the condition to find a methodological or technical solution to the scaling artefact without taking the risk of biasing the obtained data. The observations presented in the section 3.4.2 of this chapter, all together, seem to indicate that the scaling artefact and more generally speaking the challenges of cryo-FIB-SEM nano-tomography are most likely caused by several probably unrelated parameters originating from both the intrinsic nature of the samples as well as the specifics of the equipment used during this work. A study of which the goal would be a to resolve or at least attenuate the scaling artefact to manageable proportions would require a separate and fully-fledged project involving also possibilities to make hardware changes to part of the cryo-FIB-SEM nano-tomography instrumentation, as the stage temperature, cryo-shield and higher flexibility in defining the slice and view process. It is however important to underline that such a project might, like this one, strongly suffer from the “limited” interest of the cryo-electronic microscopy community for “non-biology” related topics”.

Nevertheless, this work showed that cryo-FIB-SEM microscopy can be used without resolving the scaling artefact issue for qualitative analysis of fresh cement pastes microstructures at the expense of a rather heavy, time and resource consuming process. The results obtained by qualitative analysis of a few polished image surfaces did not present any major discrepancies with the previously



realised work of Dr. Anatol Zingg [26]. However, in comparison to Dr. Zingg's thesis, the main objective of this work to perform quantitative analysis of model cement pastes microstructures using cryo-FIB-SEM nano-tomography, faced major holdbacks. Essentially, the scale of the particles we wanted to see and their grey-levels were on the same range as the scale effects. It later became apparent Dr. Zingg's might also have encountered the scaling problem, but most probably indirectly overcame it thanks to an image processing developed to deal with another artefact. This was not too critical for his research objective, but would have been devastating for ours.

In this work, the failure to obtain exploitable data due to scaling artefacts was knowingly assumed in order to avoid the risk of introducing major biases in the experimental data and its interpretation through heavy image treatment. We also hope that our experience will limit the risk of overinterpreting the images published by Zingg and co-authors for subjects as cement hydration, a question that had not been focussed on, but which often refers to their work to indicate the absence of a thin passivation layer in early stages of hydration.

**This underlines once again the crucial importance of transparently reporting any technique-related challenges, as well as the extent and implications of any treatments applied to raw data before publishing.** It is hoped that the transparent description of the trials done on this subject may help future researchers either to find solutions to the problem, or simply to avoid this challenge all together.

# Chapter 4 – HPFRC casted in 3D powder printed moulds

This chapter is based on the accepted and presented article [73] for the 2017 UHPFRC conference held by AFCG-ACI-*fib*-RILEM in Montpellier, France on 2 – 4 October 2017. The related work was conducted in a close collaboration with the *dbt* group from ETH Zürich as a bachelor students' project. My contribution to this project was mainly the development of the used mix design but also its' mechanical and rheological testing as well as the elaboration of the casting methodology implemented in this work. The majority of the experimental work was realised by bachelor students under my supervision.

## 4.1. Introduction

In what has been termed the “third industrial revolution”, digital fabrication has ushered in a new era of mass customisation in all forms of manufacturing, and now promises to be a disruptive technology in the construction sector. Freeform architecture, enhanced worker safety, and more sustainable structures are all possibilities with the rise of digital fabrication [9]. New forms of technology in construction are illustrating the type of freedom and new research challenges that digital fabrication brings, technologies such as layered extrusion and slip-forming, with the ability to “3D print” the material by placing it only where it is needed. A major issue that has been pointed out with these new technologies to construct reinforced concrete elements is the issue of reinforcement integration [9,29,36], as reinforcement is typically added post-hoc in layered extrusion structures, requiring another infill step. Therefore, there is a very high potential for these new digital fabrication technologies to offer new

perspectives on fibre reinforcement. In this work, we present the combination of binder jetting, a 3D printing technology, and high-performance fibre reinforced concrete (HPFRC), as a composite system to produce architectural elements.

#### 4.1.1. Binder jetting

Binder jetting is one of many different additive manufacturing technologies [74,75]. A liquid binder is selectively applied on successive thin layers of powder material. Its major advantages, compared to other 3D printing procedures, are the high resolution, the virtual absence of geometrical constraints and its availability at large scales of up to  $4 \times 2 \times 1 \text{ m}^3$ . These benefits make it particularly interesting for architectural applications [40,41,76,77] and in the following, some important predecessor projects are highlighted and illustrated in Figure 4.1.

A pioneer working in the field of 3D printing for architecture for already more than 10 years is Enrico Dini and his company D-Shape™ [39]. A Cartesian 3-axis frame made from aluminium trusses encloses a 4x4-meter print bed (Figure 4.1 top left). The produced Sorel cement objects exhibit an increased tensile strength compared to conventional cement [42], but demonstrate rather coarse resolution as demonstrated by the first entirely 3D printed pedestrian bridge in the world installed in the urban park of Castilla-La Mancha in Alcobendas, Madrid [78].

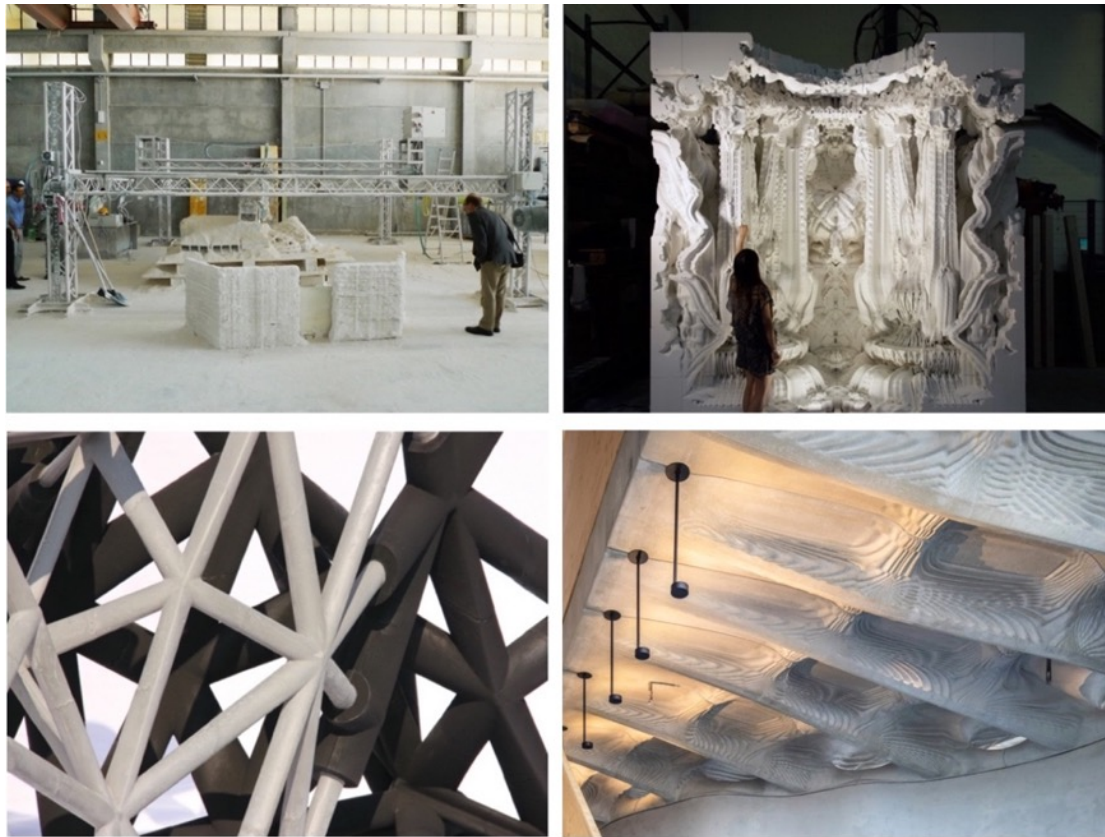
Digital Grotesque, the first fully immersive, enclosed, completely 3D printed structure was realised by Michael Hansmeyer and Benjamin Dillenburger [79]. The 3.2 m high, 16 m<sup>2</sup> large room is materialised with minute details at the threshold of human perception (Figure 4.1 top right). This is possible thanks to the layer height of a mere 0.13 mm. The total of 11 tons of pure 3D printed sandstone is discretised into blocks, stacked atop each other and carrying only its own weight. For exhibition safety purposes the structure was stabilised with vertical steel rods inserted in channels specially integrated in the structure for this purpose<sup>1</sup>.

The architect and researcher Philippe Morel of EZCT [80] has created a three-dimensional triangulated truss structure cast in ultra-high performance fibre reinforced concrete (UHPFRC) to demonstrate this material's load-bearing capacities (Figure 4.1 bottom left). The 3D-printed half shells are infiltrated with epoxy resin and assembled to form the hollow tubular mould prior to being cast. The structure has a very high surface quality; however it lacks any conventional reinforcement relying on the reinforcement capabilities of the concrete mix

---

<sup>1</sup> Personal communication from Prof. Dr. Benjamin Dillenburger.

integrated fibres. Additionally, formwork removal limits to some extent the geometric freedom.



*Figure 4.1: D-Shape printer (top left); Digital Grotesque (top right); UHPC truss structure from Philippe Morell (bottom left); Smart Slab in dfab house (bottom right)*

Design research firms such as Emerging Objects develop new powder / binder combinations able to be 3D printed using the binder jetting method. Printer system manufacturers and their binder suppliers also have their R&D departments extending the product portfolio to broaden the range of applications.

More recently even, binder jetting was used to produce formwork for the “Smart Slab” of the dfab house in Zürich [14] (Figure 4.1 bottom right). This project demanded the development of a new hybrid production method consisting in spraying shotcrete in a reusable binder-jetting 3D printed mold resulting in a consistent thickness thin freeform surface which then was used as a stay-in-place formwork for casting conventional concrete allowing fast production, good reinforcement bonding and concrete compactness in the structural beams. The resulting slabs allowed a total integration of additional structural elements such as post-tensioning ducts as well as secondary building infrastructure channels for water and electricity.

### 4.1.2. Binder Jetting as Stay-in-Place Formwork

In the above cases, the printed formwork is removed after the concrete hardened, and in most cases cannot be reused. In this section, we refer to applications of “stay-in-place formwork”, which refers to situations where the formwork is not removed.

A jump in scale and resolution was made with the realisation of the Swiss pavilion for the Architecture Biennale in Venice, 2016 [81]. “Incidental Space”, designed by Christian Kerez is a 9 m long and 6 m high room enclosed by a 2 cm thin shell of 2-3 cm glass fibres reinforced shotcrete<sup>1</sup> (Figure 4.2). Around a third of the formwork parts were 3D printed in sandstone and infiltrated with a release agent. No other known fabrication method would allow for the production of this level of detail.



Figure 4.2: *Incidental Space*, from Biennale 2016

Binder jetting presents the designer with excellent design freedom for geometric complexity which makes it a versatile production method for prefabricated architectural components. However, the relatively low flexural strength of the sand-based 3D printed material renders it unsuitable for structural applications.

---

<sup>1</sup> Personal communication from Prof. Dr. Benjamin Dillenburger.

This drawback can be overcome by combining the 3D printed sandstone with another material that has high structural capacity, such as concrete. To achieve this, a minimal digitally fabricated shell is used as formwork for casting HPFRC. 3D printing contributes with its excellent geometric flexibility and material efficiency, while concrete can take (almost) any shape given by the form and provides the load-bearing properties.

The porous nature of the 3D printed formwork makes the bond with the concrete very strong. This was apparent when removing a 9 mm layer of 3D printed formwork, as a water jet with 400 bar pressure was necessary. To avoid such a labour and energy intensive process, release agents can be used to coat the interface between the two materials.

Alternatively, the strong bond can be an opportunity and the 3D printed shell can act as a stay-in place formwork. This simplifies the fabrication process by eliminating the demoulding step, while the added dead load can be justified by additional functional roles that can be performed by the formwork. In this scenario, there is a differentiation in the way the two sides of the form are treated. The internal interface is smooth to optimise the flow of concrete, while the external surface integrates additional geometric articulation, textures and micro-structures for ornamental or functional purposes (e.g. acoustics, thermal dissipation, lighting integration).

## 4.2. Materials and Methods

### 4.2.1. Binder-Jetting 3D Printing Technology

Prototypes were manufactured with a large-scale binder jetting 3D printer (ExOne S-Max), designed for the sand moulded casting industry. The machine can produce parts within a print box of 1.8 x 1 x 0.7 m<sup>3</sup> with speeds of up to 85 l/h at 250 DPI resolution.

The first step in the 3D printing process is the preparation of the CAD model, which is sliced by a proprietary software into 500 horizontal sections at 0.3 mm intervals and sent to the 3D printer as bit maps. For each horizontal slice, a 0.3 mm thick coating of silica sand is evenly spread in the print box. The ink-jet print heads then selectively inject a furan-based organic binder reproducing the computed CAD slices. The selective injection of the binder is then followed by a brief heating of each slice by a moving halogen lamp in order to activate the furan-based binder and begin its curing. The binder cements the sand into a composite material similar to sandstone. In areas where no binder is deposited, sand retains its granular flow, while still providing at the same time support for subsequent layers above. After all the layers are 3D printed, the part is left to

finish its cure inside the 3D printer without additional heat in order for the binder to reach its maximum strength.

Following the curing stage, the solid 3D printed part is extracted from the surrounding unconsolidated sand inside the print-box. Loose sand particles that adhere to the part are vacuumed out or brushed off.

While the 3D printed part only acts as formwork and does not have any structural role in the final part, sufficient strength is necessary to prevent damages during transportation, site manipulation and concrete casting, in particular resistance to formwork pressure. Therefore, the last post-processing step is the application of an epoxy surface infiltration to the entire part. On the one hand this treatment hardens the exterior of the part making small details more resistant to dents, and on the other hand it doubles the overall flexural strength of the binder-jetting printed part to approximately 6.5 MPa.

Special tools may be required during the post-processing steps for reaching narrow, coiled or generally inaccessible geometric features for sand removal and epoxy painting.

#### 4.2.2. HPFRC Mix

The formulations of HPFRC used in this work were adapted from a mix design provided by Dr. Emmanuel Denarié from the Structural Engineering research group of EPFL. These adaptations involved the adjustment of the raw materials proportions and the mixing procedure due to the different sourcing of several dry materials, as well as the usage of a different superplasticiser and mixer. These adaptations were performed in an iterative way in order to meet the rheological requirements of this work as both the composition and the mixing procedure are known to have non-negligible impacts on the rheology of fresh high performance concretes [82,83].



#### 4.2.2.1. Formulation

The materials used for all mixes in this work and their proportions can be seen in Table 3.1.

Table 4.1: Materials used for the mixes.

Material	Name	Producer	Proportion [gr/gr <sub>cement</sub> ]
Cement	Durabat X-trem CEM I 52.5 N SR 5 PM-CP2	LafargeHolcim	1.000
Sand	0.1-0.45 mm	Baubedarf	0.755
Silica Flour	K6	Carlo Bernasconi AG	1.000
Silica Fume	Elkem Grade 971-U	Elkem	0.125
Superplasticiser	MasterGlenium ACE 30	BASF	0.093
Steel Fibbers Type I	6 x 0.15 mm	Dramix	0.325
Steel Fibbers Type II	10 x 0.16 mm	Dramix	
Steel Fibbers Type III	13 x 0.16 mm	Dramix	
Water	-	-	0.282

#### 4.2.2.2. Mixing Procedure

All mixes were produced using a Hobart A200N mixer except the up scaled mixes used for the slab element that were produced on a Collomatic 65/2 K-3 mixer. The mixing procedure consisted in first mixing all the dry components together for 5 minutes, followed by water addition and a low mixing speed for 1 minute before adding superplasticiser. Mixing was then continued at low speed for 6 minutes and then medium speed for 5 more minutes. Fibres were then added in two parts with 30 seconds slow mixing in between, and with 3 minutes mixing on low speed with all fibres.

#### 4.2.2.3. Measured properties

Mix workability was assessed with a mini-slump flow test [84]. Compression and bending strengths were measured on a Walter+Bai FTS Typ 502/4000/100 at 7 and 28 days on 4x4x16 cm prisms cured at 21 °C and 95% RH.

## 4.3. Results & Discussion

### 4.3.1. Digital design of the slab

To investigate the potential of 3D printed sandstone for acting as formwork for concrete, a slab component was designed using topology optimisation algorithms and fabricated in the proposed way.

Topology optimisation is an iterative computational process that works within a given discretised modelling space. For a specified set of loads and supports, the algorithm refines material distribution in order to meet one or more set performance targets (Figure 4.3). Topology optimisation can be used to reduce weight and improve functionality and structural performance of concrete building components [85]. While significant improvements can be achieved with this method, the resulting geometry is often too intricate to be fabricated in concrete with conventional methods [86]. Given the promise of complete geometric freedom with binder-jetting, the fabrication of such designs becomes possible.

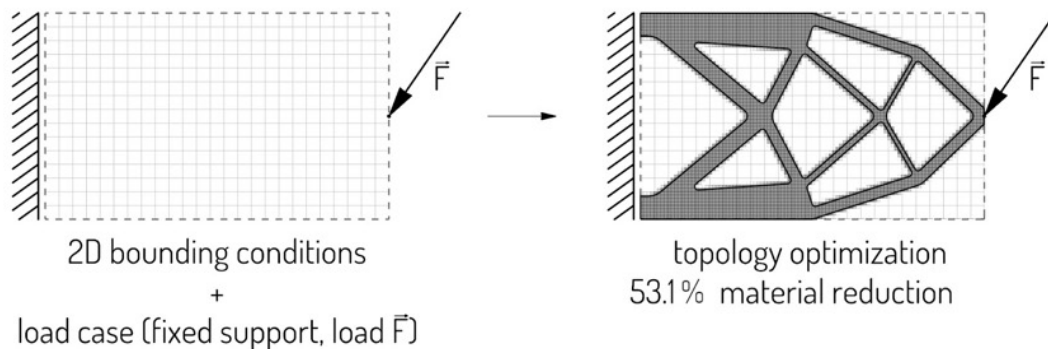


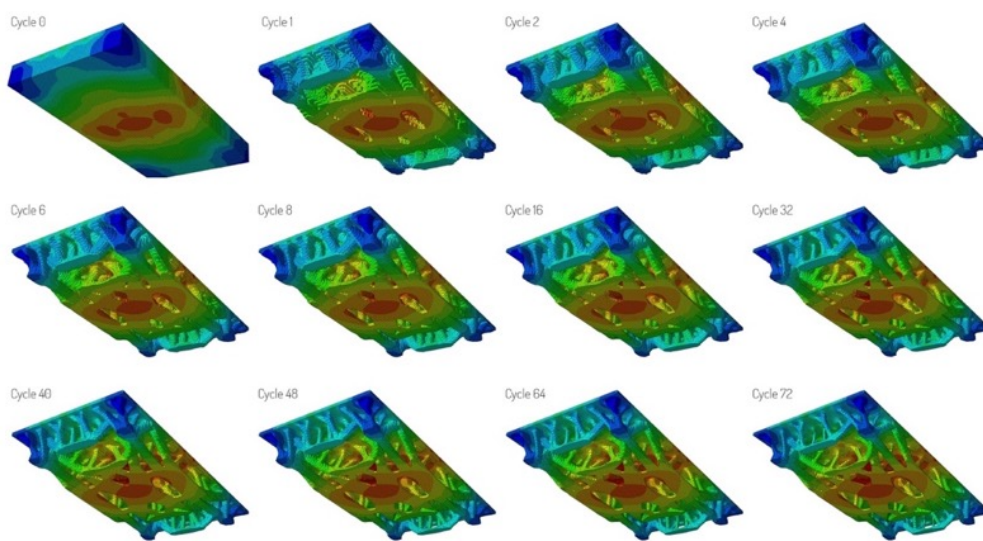
Figure 4.3: Topology optimisation for an example load case.

The prototype was developed through the TOSCA topology optimisation algorithm of Simulia ABAQUS, a commercial structural analysis software package (Figure 4.4). The  $1.8 \times 1 \times 0.15 \text{ m}^3$  design domain was discretised into 83,072 nodes with a volume of approximately  $3.4 \text{ cm}^3$  each. The target set for the optimisation process was to reduce material to a 0.18 set fraction of the initial volume while keeping to a minimum the von Mises stresses of the slab under uniform surface load. Boundary conditions were set to four simple supports located close to the corners.

The result has geometric features typical to topology optimisation algorithms: interconnected networks of narrow tubular structures with different

diameters. Further refinement of the design had to be included after the topology optimisation in order to address the fabrication constraints:

- Under-sampling artefacts resulting from the discretised nature of the topology optimisation process were corrected.
- Geometric features under 5 mm were considered too fragile for further manipulation and were discarded.
- Hollow geometric features under 20 mm were made solid as they are too narrow to permit 3D printing post-processing (unconsolidated sand removal and surface infiltration) and prevent the flow of concrete because of local fibre clogs.



*Figure 4.4: Topology optimisation iterations for the slab prototype*

Given the bigger geometric freedom possible with this construction technique (compared to more conventional CNC milled formwork), the architect's design intention regarding specific shape features, surface quality, ornamentation, edge details, etc. is easier to integrate for concrete building components.

In addition to the aesthetics, the reduction of used material and the geometry optimisation for in use static load, the obtained partially tubular design of the slab element can also prove quite beneficial in terms of potential fibre orientation that can be induced in the HPFRC mix during the casting process. Indeed, the flow of concrete during the pouring process may lead to a certain degree of preferential fibre orientation along the channels' axis [87] providing significant tensile strength increase compared to a random fibre orientation.

### 4.3.2. Mix requirements and optimisation

Several requirements were stated for the fibre reinforced mix used in this project. As the main challenge was the infilling of the slab element, a good workability of the mix was necessary in order to be able to flow properly through the channels.

The first step of optimisation was realised by measuring the mini-slump spreads of mixes containing various amounts of superplasticiser. These mixes were kept at constant W/C ratio of 0.347 by considering the water contained in the superplasticiser and adjusting the amount of added water. The mix used for this optimisation was containing Type II fibres. As can be observed in Figure 4.5, a narrow maximum plateau of the mini-slump test was observed for a superplasticiser dry extract between 2.75 and 3.00%. Further in the study the amount of 2.75% was used.

Three different types of fibres (presented in Table 3.1) were tested for both mechanical properties and workability. In all following tests the amounts of water, fibres and superplasticiser were kept constant.

All additional relevant data gathered during the mix design process can be found in Appendix A.

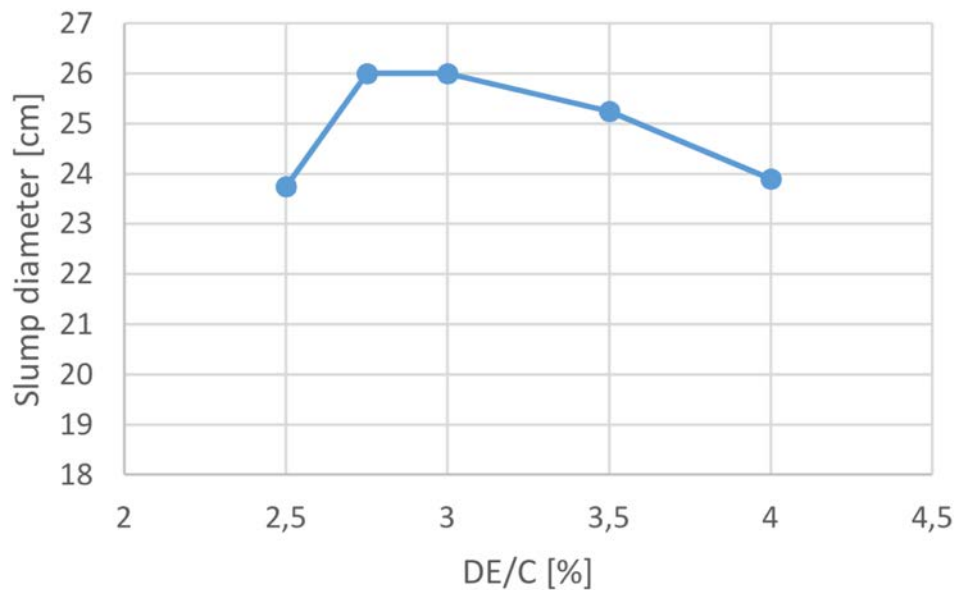


Figure 4.5: Superplasticiser dry extract content vs. slump diameter.

#### 4.3.2.2. Filling tests

The suitability of the three types of fibres containing mixes to flow through the printed channels was tested by infilling both straight and L-shaped 3D sand printed tubes as presented respectively in Figure 4.6 and Figure 4.7. These tests were realised as a complement to the mini-slump flow test in order to be closer to the infilling conditions of the slab element.



Figure 4.6: Straight tubes with varying diameters (from left to right: diameters of 50, 40, 30, 25, 20, 15, 10, 7.5 and 5mm), 6x0.15mm fibres (top); 10x0.16mm fibres (middle); 13x0.16mm fibres (bottom).

As can be observed in Figure 4.6, the flow distance decreases with the increase of the fibre length and the decrease of the channel diameter which is to be expected. Also, for fibres of type II and III it is clear that the flow distance decreases with the decrease of the bending radius of the L-shaped tubes as one can observe in Figure 4.7.

This provides important information for any further development and optimisation of bigger elements containing channels. Indeed, from the results obtained during this work the following rule of thumb was applied for casting bigger elements in order to avoid possible clogging resulting in unfilled portions of the element: In the given proportion of the studied mix, the fibre length should be less or equal to the radius of the narrowest channel. Expressed with respect to the diameter, a more natural representation of the “jamming dimension”, this rule would be: “the diameter of the tubes to be infilled must be at least twice bigger than the length of the used fibres, but to be on the safe side a factor of three ought to be taken”.

This rule can be applied in two different ways either by fixing the narrowest channel diameter and choosing the adequate fibre length, or by fixing the required mechanical properties through mix design and adjusting the element channels sizes. While the first option was used in this work, the second one was further used during the designing phase of a HPFRC and FMD printing combined concrete canoe which is presented and discussed in Chapter 5 of this manuscript.

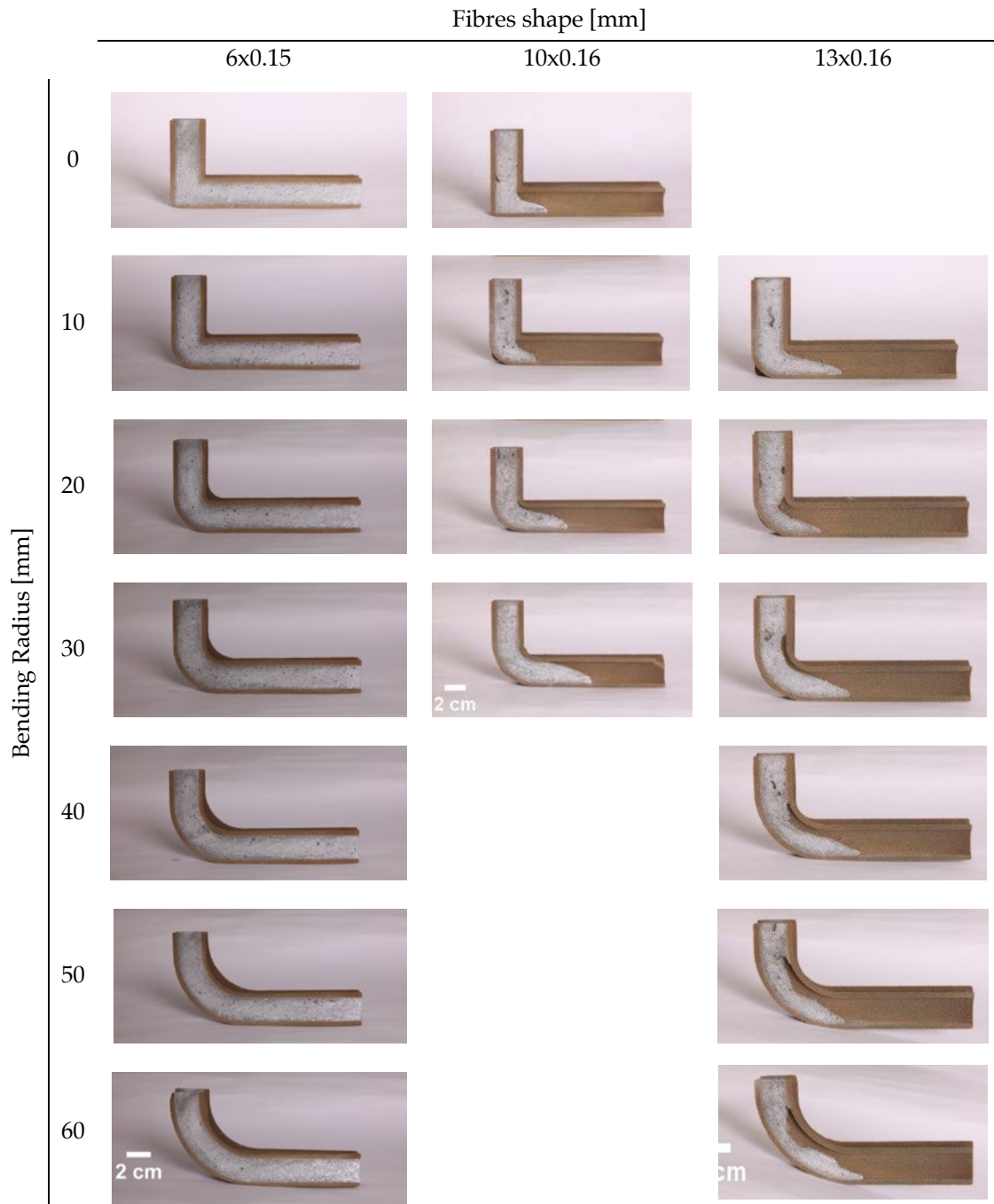


Figure 4.7: L-shaped tubes with varying bending radii. Arms on both sides of each L-shaped tube were originally 15cm long with an internal diameter of 20 mm.



Additional tests showed that 3D sand prints have a certain limit regarding the formwork pressure. Indeed, several of the infilled forms burst during infill because of pressure applied by the concrete. Epoxy coating provides an additional tensile resistance of the 3D printed sand formwork and has been applied to the final slab element in order to reduce formwork burst risk as well as water sorption from the infilled concrete mix.

Additional infill testing prototypes were made accordingly to the findings described above prior to the casting of the final slab element. None of them presented major filling defects as can be observed in Figure 4.8.



*Figure 4.8: Infill testing prototypes, final slab corner (top); abstract cavity (bottom).*

### 4.3.2.3. Resulting mechanical properties

Mechanical properties of the tested mixes are presented in Figure 4.9. As expected, a noticeable increase in flexural strength is observable when increasing the fibre length. This increase is less visible but still present for the compressive strength.

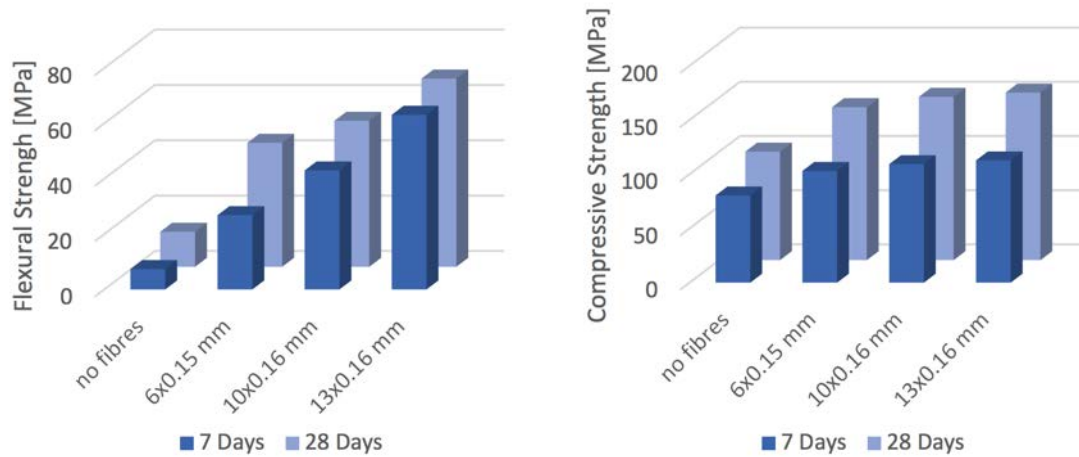


Figure 4.9: Flexural (left) and compressive (right) strengths of different fibre types.

Considering these results together with the filling tests described previously it was decided to use the mix containing type II fibre (10x0.16mm) for the final slab element. This choice was made as a compromise between the mix workability (fluidity) and the desired strength of the slab. All diameters of the slab were also checked and adjusted in order to be at least twice larger in diameter than the length of the chosen fibres in order to limit the clogging risk during casting. A limitation of the mix, however, comes from a lack of strain-hardening behaviour in flexion as can be observed in Figure 4.10. This clearly limits the potential structural application of this particular mix and prototype, and remains a required avenue for research for the implementation of this type of technology in a meaningful way.

Additional data on other mixes tested during this work can be found in Appendix A.

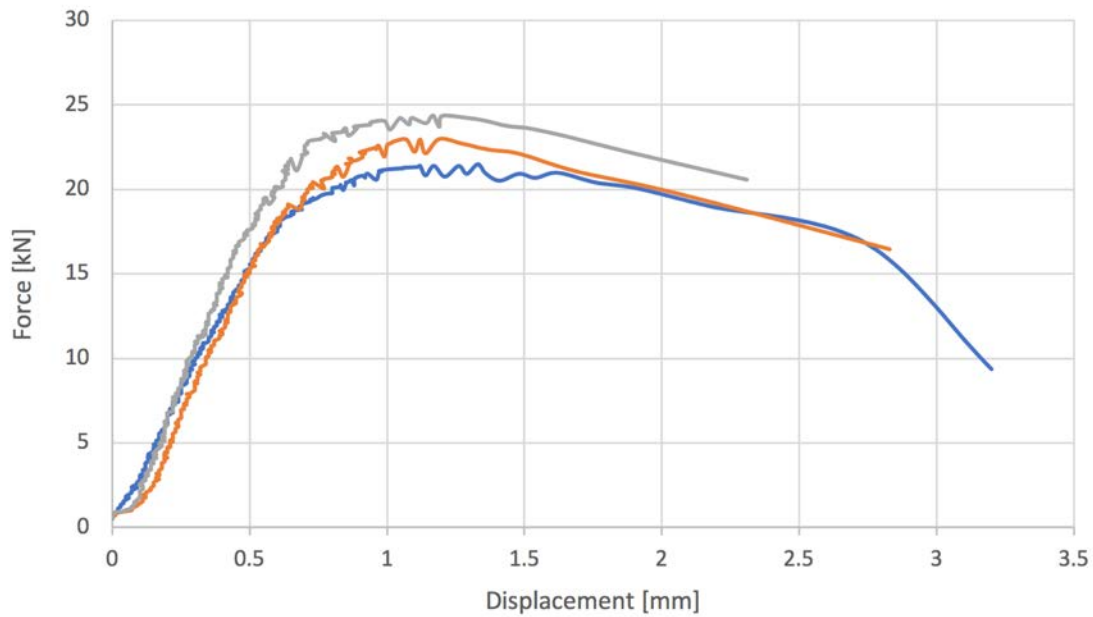


Figure 4.10: 7-days load displacement diagram for the 13x0.16 mm fibres containing HPFRC.

### 4.3.3. Slab element preparation and infill

The final slab element 3D model was adjusted accordingly to the findings described in section 4.3.2.2. The diameters of the slab element channels were all ensured to be greater than 20mm as the chosen HPFRC mix selected for the infill was containing 10x0.16mm fibres. The curvature radii of non-branching parts of the channels were chosen to be above 100mm in order to ensure optimal flow of the concrete mix.

The sand formwork was printed off-site by our specialised industrial partner Christen Guss AG and shipped to our laboratory a few days before casting. All channels of the formwork underwent a thorough vacuum cleaning using a thin tube in order to ensure the total absence of loose sand that could have been left there by the printing process. Some channels presented minor holes that were repaired with quick-setting plaster prior to casting. The ready for casting formworks can be observed in Figure 4.11 (top left)



Figure 4.11: Top view of element, pre-infill (top left); Bottom view of element, post-infill (top right); Infill process (bottom left); Final element after casting (bottom right).

The finished slab element and its casting process is shown in Figure 4.11 (respectively right and bottom left). In order to ensure a maximum quality of the infill, the fibre reinforced mix was cast through one side of the main channels until it was overflowing from other smaller channels minimising the chance of air pockets trapped inside. It is important to note here that no additional pressure aid was used during the casting to help the flow of the mix. No additional hydrostatic pressure was built-up with a column of liquid above the top part of the mould and the whole casting process went only by pouring freshly mixed concrete directly in the formwork as can be observed in Figure 4.11 (bottom left).

The amount of fibre reinforced concrete necessary for the infill of the slab element was produced in three batches, with fibre addition occurring just before infill of any batch. Four lifting anchors were positioned on the top of the slab element for further manipulation of the finished product. It was then hermetically covered with plastic film and let to cure for 7 days prior to moving.

As the final slab element was purposed for exhibition, no mechanised tests were performed on it in order to test its structural strength. It however underwent what could be called typical load test as can be seen in Figure 4.11 (bottom right) of six people standing and simultaneously jumping on it while positioned on the four designed loading points without any noticeable cracks or

structural failure. For aesthetics the exterior sand 3D printed lost formwork was spray painted in a light grey colour as one can see in Figure 4.11 (top right).

## 4.4. Conclusions and Outlook

The successful casting of the slab element shows very interesting perspectives for this kind of technology in the future for both aesthetics and mechanical optimisation of structural elements.

The possibility to develop a strain hardening behaviour of the infill mixes would provide an unconditional improvement to the structural properties of such composite elements. However, strain-hardening behaviour usually implies higher fibre amounts and lengths which would reduce the mix workability and require usage of larger channels. Considering the possible channel geometry of elements such as those presented in this work, important improvements should be realised both on the fibre reinforced concrete mix formula as well as on the elements design. Here there is a clear potential of multifactorial optimisation between the optimisation of the strength, the mechanical properties and the design. Typically, the material optimisation will reach certain limits and its properties, including rheology, will then have to be incorporated at the design stage to allow reliable form filling and best use of its mechanical performance.

This optimisation process, that at the design stage will clearly have to rely on advanced computational methods, can additionally be enriched, by considering the flow induced fibre orientation. This would be also very interesting and beneficial. It would involve a proper design of the channels network coupled with adequate fibre orientation metrology. In terms of modelling, it will however not be possible at this stage to model explicitly the orientation of the fibres. However, a promising approach is to map the velocity vectors and assume that these indicate the direction of fibre orientation [87]. This makes it a problem that can be tackled numerically and would deserve experimental verification, for example using such X-ray micro CT to image the fibre orientation directly. Clearly this experimental is labour intensive, but as a validation tool coupled with numerical simulations, it would be invaluable.

Upscaling the production of such elements presents several challenges, but opens very interesting possibilities such as the direct integration of precise post-tensioning ducts inside the elements. This was applied for the Smart Slab at the DFAB House [14], whereby, the concrete in that case was applied by shotcreting (as for the Incidental Space project).

While the production of fibre reinforced concrete on large scale is manageable nowadays, 3D printing is still an emerging technology. Current research considers making 3D printing a more accessible technology, with lower

costs, improved speed and lower environmental impact. Nevertheless, the proposed method only relies on 3D printing to produce a minor proportion of the final product, which has however a major impact on overall performance, behaviour and aesthetics. The results of this study provided direct feedback into the implementation of previously mentioned instance of this technology, the Smart Slab, on the NEST building at the Swiss Federal Institute for Materials (Empa) in Dübendorf, Switzerland, completed and inaugurated in beginning 2019.

# Chapter 5 – HPFRC casted in FDM printed moulds

This chapter is based on the published and peer reviewed paper [88] in *Gestão & Tecnologia de Projetos, Design Management and Technology, Periódico Científico do Instituto de Arquitetura e Urbanismo da USP*, 2018. The related work was conducted in collaboration with the *dbt* group from ETH Zürich as a bachelor students' project. My contribution to this project was the follow up of the design stage of the presented concrete canoe and the supervision of physical testing performed during this work as well the production process of the canoe. The majority of the presented work was realised by bachelor students under my supervision. The work described in sections 5.2.3, 5.2.4 and 5.2.5 was conducted by Andrei Jipa from *dbt* research group. Additionally, to the canoe project itself, the author realised additional counter-pressure casting trials presented in sections 5.2.9 and 5.3.2 in collaboration with the *dbt* research group that provided the 3D printed formworks necessary for these trials as well as manual help in order to perform them.

## 5.1. Introduction

In the previous chapter we presented the use of binder jetting as a way to produce a formwork for a topologically optimised structure, allowing ultimately to reduce the amount of concrete needed for a given load bearing capacity. It represented an example of how formal flexibility has applications beyond architectural aesthetics. Indeed, the recent rise in computational form-finding tools such as topology optimisation has demonstrated how considerable material savings can be achieved by manipulating the geometry of structures and distributing material precisely where it is most needed, without affecting, or sometimes even improving the overall performance and functionality. Designing with material efficiency as a goal can be achieved through ribbings, porosity



gradients, hierarchical articulations, venations and other similar geometric features [89].

Given the dominant proportion of concrete used around the world, the ability to optimise concrete structures for reducing material use can have a global impact in releasing pressure from natural resources and reducing the carbon footprint of buildings and infrastructure. However, this excellent potential of concrete is only enabled by complex optimised shapes, and achieving such shapes is in turn limited by the capacity to fabricate the necessary formwork (Chapter 2, section 2.2.3).

Designing topologically complex concrete elements with material economy in mind is therefore facing the limitations of the available formwork fabrication methods. A compromise has to be made between material efficiency and formwork fabrication costs.

To aid in this dilemma, digital fabrication of formwork is already being investigated. Production of formwork for non-standard concrete elements can be done by CNC milling of foam blocks [86], actuated moulds [90], robotic extrusion [91], robotic hot wire cutting [92], or robotic welding [93]. Certain types of lightweight formwork can also be produced with patterning fabric [94] or with knitting [95]. However, these approaches can be resource-intensive as regards the necessary time and labour (robotic cutting and milling tools are slow and wasteful processes, while fabrics require extensive patterning) and/or have limitations regarding the geometries that can be produced (e.g. no undercuts for milling, provision for collision-free robotic tool-head access paths, only ruled surfaces for wire-cutting and only smooth anticlastic surfaces for fabrics).

To overcome these limitations, different 3D printing technologies have already been proposed for formwork, such as binder jetting of sand presented in discussed in Chapter 4 [73,96]. Binder jetting is particularly interesting because of its precision, great level of geometric flexibility and availability in large scale. Still, certain geometric features, such as long tubular voids are difficult to achieve because of the necessary post-processing steps, such as unbonded sand removal and surface infiltration for stability. Moreover, due to the frail nature of the 3D prints, very thin free-standing features, such as millimetre-thick shells are also a challenge.

This chapter presents another 3D printing technology, fused deposition modelling (FDM) that has also been proposed for fabricating formwork [97]. However, taken “off the shelf”, this approach has some inherent limitations that we address to enable its use for large scale fabrication. With this objective, we built upon the state-of-the-art of 3D printed formwork and optimised the 3D printing process. From the materials point of view, we mainly addressed the question of controlling the concrete rheological and mechanical properties by adapting the formulations of high-performance fibre reinforced concrete

developed for the topologically optimised ceiling element using sand binder jetting 3D printed lost formwork presented in the previous chapter of this thesis. In particular, an important amount of work was dedicated to deal with the hydrostatic pressure of concrete in a mechanically rather weak sub-millimetric FDM 3D printed formwork during casting. This work resulted in a new process named “counter-pressure casting” that was developed and used to produce a topologically optimised concrete canoe. Additionally, to that, a series of exploratory trials were performed after the completion of the canoe in order to better understand the mechanics and limitations of counter-pressure casting targeted at future improvements of this process for it to be integrable in a more industry-oriented production.

## 5.2. Methodology

To pursue the goals above, the methodology follows the design and fabrication process of a four-meter-long functional concrete canoe, dubbed *skelETHon* due to the resemblance of its structural system with a biological skeleton (Figure 5.1). The canoe demonstrates how even for complex load-cases, computational optimisation can facilitate material reduction and effectively enable a concrete boat for two people to be light enough to float.



Figure 5.1: *skelETHon*, the four-metre-long canoe made entirely out of concrete. (dbt, PCBM, ETH Zürich, 2017)

### 5.2.2. Why a Concrete Canoe?

At a first glance, a concrete canoe is a counter-intuitive challenge and may seem a parody project of sorts, akin a steel plane. Nonetheless, the first usage of reinforced concrete in an attempt to build functional ships goes back to the

middle of the ninetieth century and up to the end of the second world war with concrete barges serving in the pacific<sup>1</sup>.

Concrete canoe competitions have a long-standing tradition, having been organised in the US since the 1960s. They are currently a well-respected international phenomenon, attracting crowds of hundreds of participants at annual or biennial regatta events organised in more than 20 countries around the world.

*skelETHon* took part in the 16th Concrete Canoe Regatta in June 2017 in Cologne, Germany. Approximately 1`000 participants registered 90 concrete boats and raced them for 200 metres at a flat-water racing facility on the Rhine river (Figure 5.19). This particular race route included two 100-metre-long straight lines where the hydrodynamic designs could demonstrate their top-speeds, as well as a 180° turn to prove the stability of the boats and cornering skills of the competitors. The German Regatta is an important event, with major industrial sponsors. While also a sporting event, it mainly draws scientific interest for demonstrating innovations in concrete construction methods. The canoe regattas in Germany have been over the years stepping stones for research projects which have since become valuable contributions to the scientific community, like Mesh Mould [93] and Smart Dynamic Casting [98].

Apart from a similar scale to building components, a canoe has complex load-cases, which make it a representative case-study for architecture. The canoe has to be designed for the floating load-case in water (self-weight, live point loads from two people, and a distributed support force provided by the hydrostatic pressure) as well as for a transport load-case on land (two support points and self-weight) (Figure 5.2).

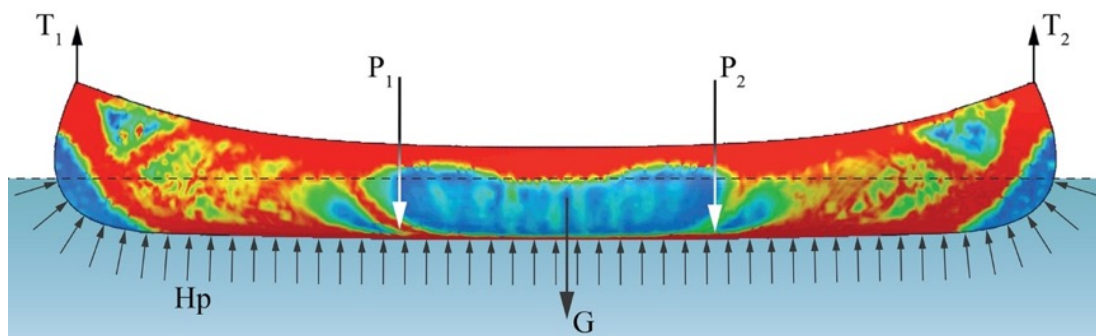


Figure 5.2: The two different load-cases used for the topology optimisation of the canoe: a) the floating load-case in water: self-weight ( $G$ ), live point loads from two canoeists ( $P_1$ ,  $P_2$ ), and a distributed support force provided by the hydrostatic pressure ( $H_p$ ); and b) a transport load-case on land: two support points ( $T_1$ ,  $T_2$ ) and self-weight. (dbt, PCBM, ETH Zürich, 2017)

<sup>1</sup> [https://en.wikipedia.org/wiki/Concrete\\_ship](https://en.wikipedia.org/wiki/Concrete_ship)

When designing a canoe, two aspects have to be considered: the structural integrity and waterproofing. Inspired by traditional wood and canvas canoes, these two functions are separated in two different construction layers:

- a) The waterproofing of the canoe is ensured by a two-millimetre-thick outer “skin” made of highly fluid cement mortar painted on cotton semi-flexible cotton textile stretched over the skeletal structure of the canoe similar to a flysheet of a tent. This process is described in-depth in a filed patent application and is not covered by this chapter [99].
- b) The structural integrity is provided by an inner “skeleton” (Figure 5.3) that is fabricated using a 3D printed formwork casted with high-performance steel fibre-reinforced concrete, documented in this chapter (section 5.2.8).



Figure 5.3: The complex concrete “skeleton” that provides the structural integrity for the canoe. (dbt, PCBM, ETH Zürich, 2017)

### 5.2.3. Design through Topology Optimisation

Already presented and discussed in Chapter 4, topology optimisation is an iterative computational process that determines the most efficient spatial configuration of material distribution in order to maximise certain performance criteria (Figure 5.4). The algorithm works within a confined, discretised space, with a set of given boundary conditions, i.e. loads and supports.

The starting point of the design was the outer shape of a traditional wood and canvas canoe for two persons. The 3D model was created based on its plan and elevation projections from a stock image (Figure 5.5). This solid volume containing two cavities for the canoeists served as the input solution space for the topology optimisation algorithm (Figure 5.6).

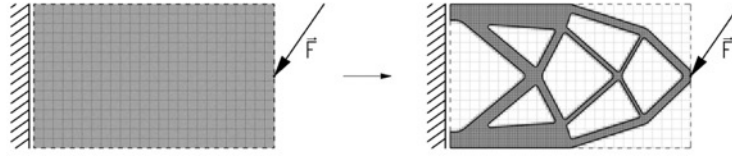


Figure 5.4: Sample topology optimisation of a simple rectangular design space with a single point load (left). After the topology optimisation, only 30% of the material is kept and distributed in order to minimise the deflection of the part (right). (dbt, ETH Zürich, 2017)

For *skeleTHon*, the TOSCA engine of SIMULIA Abaqus was used to perform a simple topology optimisation. The design space was discretised into predominantly cubic nodes of approximately  $15 \times 15 \times 15$  mm edge length. The supports and loads were defined for the two separate load cases as described above. The optimisation goals were to reduce material to a 0.15 set fraction of the initial volume while keeping to a minimum the strain energy of each node. The parameters used in the algorithm to describe the behaviour of concrete were a density of  $2'400 \text{ Kg/m}^3$ , a Young's modulus of 50 GPa and a Poisson ratio of 0.2. The compressive and tensile strengths of concrete can be used in the algorithm to constrain the optimisation to safe results.

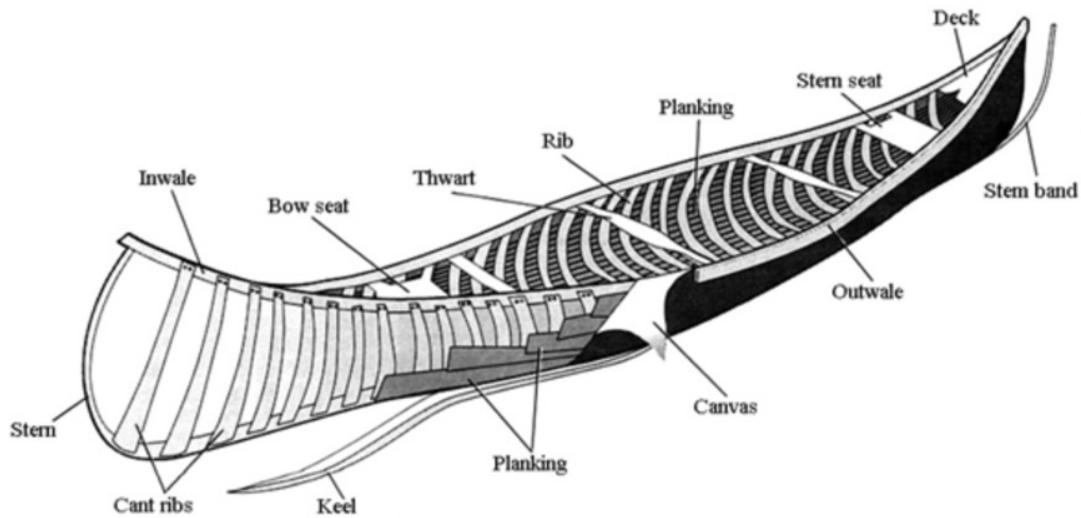


Figure 5.5: Traditional canoe shape used as starting point for the creation of the bounding volume. The structural skeleton of the concrete canoe is inspired by the ribs, keel and thwarts of the traditional canoe. (John Earle, *The Virginia Beach Beacon*)

The result of a topology optimisation is the amount of strain energy and stresses calculated for every single node. When the predefined threshold of desired volume reduction is applied, a branching structure of ribs and tubes remains that optimally guides the forces through the structure. Some are explicitly present, others only indicated by a gradient of porosity. This raw result



serves as the input for the next step, where principal axes are retraced with a cage of NURBS curves, along crystallised, dense conglomerates of nodes.

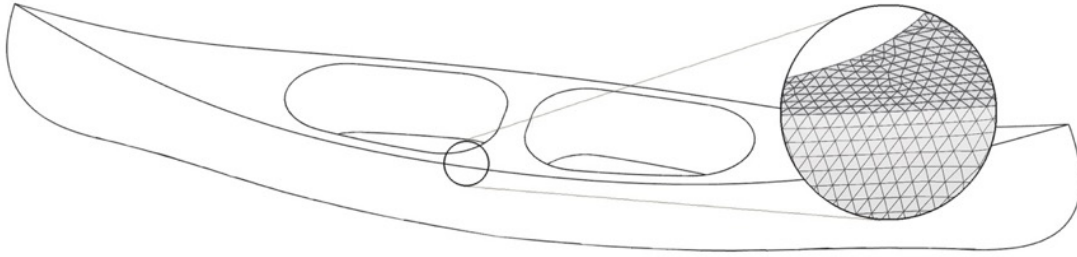


Figure 5.6: Bounding volume discretised into cubic nodes of ~15 mm edge length. (dbt, ETH Zürich, 2017)

At this stage, the axes can be adjusted slightly to tailor for any constraints of the fabrication process. In areas with lower density, additional auxiliary axes are introduced to limit the size of the open fields in the skeleton. This is because the waterproofing skin can only span over a limited surface, and whenever an opening is above this threshold, intermediary support is required (Figure 5.7).

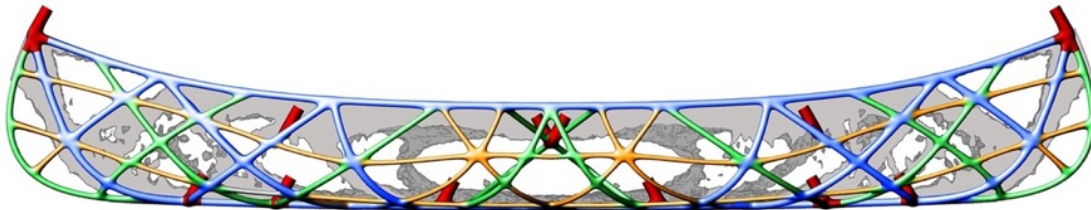


Figure 5.7: Elevation view of the structural skeleton. The initial solution space volume is reduced to the 15 % containing the nodes with the highest stress values (grey). Depending on these stress values, the resulting smooth pipes have three different diameters: 35 mm (blue), 25 (green) and 15 mm (orange). Additional inlet and outlet tubes (red) are strategically added. (dbt, ETH Zürich, 2017)

This network of axes lines is then converted into the final formwork geometry of connected tubes by a custom volumetric modelling tool. Representing the pipes as signed distance functions (FRep) is a very robust method less prone to failure with complex topologies or various pipe diameters meeting at acute angles than other methods based on explicit boundary representation (BRep) geometry. Depending on the amount of stress the tubes take, they are classified in three different groups of 15, 25 and 35 mm diameter (Figure 5.7). After creating the entire skeleton of pipes, a 3D Gaussian convolution kernel is applied to smoothen the sharp creases at the pipe intersection and thereby improve both the concrete casting and the force flow (Figure 5.8).

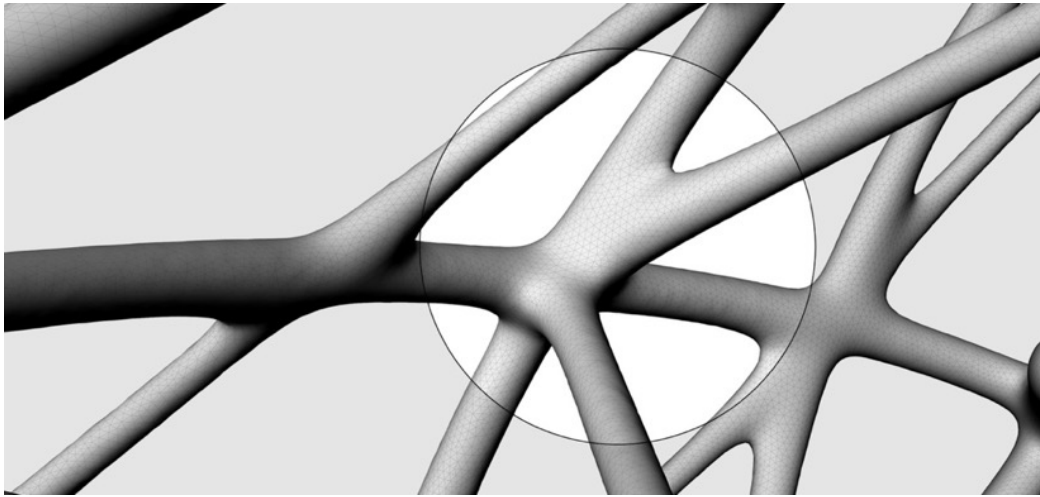


Figure 5.8: The intricate network of tubes of the structural skeleton featuring complex spatial 3D nodes, with three to six “bones” coming together smoothly. (dbt, ETH Zürich, 2017)

#### 5.2.4. FDM 3D Printing

For the fabrication of the skeleton, FDM 3D printing was used first to produce the formwork. FDM is a widely available 3D printing technology in which molten material is extruded and hardens immediately after the deposition. The deposition progresses in consecutive horizontal layers that are generated as slices through a digital model of the part to be fabricated.

In particular for *skelETHon*, FDM was chosen because among the different 3D printing technologies, it is unique for its capability of producing large-scale and stable shells with thicknesses below 0.5 mm. Other 3D printing technologies are either capable of producing precise thin shells (such as selective laser sintering, stereolithography and certain metal 3D printing technologies) or have large printing volumes (like binder jetting), but no other 3D printing method combines both large scale build volumes and the capacity to produce sub-millimetre shells. Moreover, the advantage of FDM is its accessibility, low cost and compatibility with a wide range of cheap plastics.

Out of this wide variety of plastics (biodegradable, water soluble, fibre-reinforced, flexible, conductive, magnetic, glow in the dark, low-shrinkage, bioplastics, etc), translucent polylactic acid (PLA) was selected for the canoe. The choice was due to its versatility, low shrinkage factor, relatively good mechanical properties and environmentally-friendly pedigree (PLA is compostable, recyclable and based on renewable raw materials). Furthermore, PLA is relatively stable when exposed to environmental factors (humidity and temperature variations) and it can be 3D printed in a wide domain of parameters, at temperatures between 180° and 240°C, with printing feed-rates of up to 300 mm/s.



FDM can resolve details with a precision of a tenth of a millimetre. This enabled the integration of a very fine functional surface texture on the formwork, in the range of 0.5 to 2 mm. This texture was introduced to increase the contact area and improve adherence between the skeleton and the waterproofing concrete layer (Figure 5.21).

Despite all its advantages however, FDM 3D printing also has a number of inherent limitations, which are addressed by this research separately:

- a) FDM is regarded as a slow fabrication process, usually able to produce volumetric flow-rates of  $15 \text{ cm}^3/\text{hour}$  and resolve 0.1mm features. With well-tuned machines, flow-rates as high as  $100 \text{ cm}^3/\text{hour}$  can be reached, but resolving power increases to 0.2 mm (i.e. less precision). The relatively slow speed of the 3D printing process is discussed in section 5.2.5. *Submillimetre Formwork for Concrete*.
- b) The limited amount of cantilever layers that can be reached in relation to each other (Figure 5.9). This is further discussed in section 5.2.6. *Formwork Fabrication*.
- c) The limited build volume of the 3D printers required a discretisation of the whole canoe in smaller parts which have to be assembled prior to casting. This limitation is further discussed in section 5.2.7. *Discretisation*.

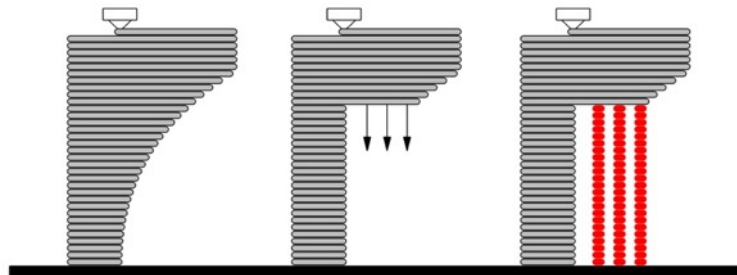


Figure 5.9: Fabrication limitations of FDM 3D printing. Below a certain threshold, horizontal layers can cantilever freely (left); Beyond this threshold, gravity would cause deformations and artefacts (middle); this can be resolved by introducing auxiliary support structures (in red, right). These support structures are mechanically removed or chemically dissolved at the end of the process. (dbt, ETH Zürich, 2017)

### 5.2.5. Submillimetre Formwork for Concrete

In order to address the slow fabrication speeds, the unique capabilities of the FDM process were exploited to radically reduce the thickness of the formwork shell to submillimetre dimensions. For FDM technology, fabrication time is roughly directly proportional with the volume of the part. Therefore, by producing a very thin shell, which is only 0.8 mm in thickness, the overall 3D printing volume was reduced to a minimum and this had a considerable impact

on the overall printing time. By comparison, even the thinnest binder-jetted formworks are roughly ten times thicker [96].

Such an extreme reduction in the thickness of the formwork has further implications:

- a) It minimises tolerances and maximises dimensional accuracy due to reduced thermal shrinkage. For a given temperature variation, the linear and volumetric thermal shrinkage are a fixed percentage of the initial length and volume respectively. For PLA cooling down to room temperature after 3D printing, the linear shrinkage is ~0.25 to 0.3 %. Thus, a 0.8 mm shell will only shrink ~2  $\mu\text{m}$ .
- b) Considerable formwork material reduction and lower embodied energy for concrete construction overall, given the significant proportion of resources that the formwork represents in conventional concrete constructions. For reference, a commercial lightweight formwork system needs around 30 kg of formwork/m<sup>2</sup> of concrete, while for the canoe, only 1 kg/m<sup>2</sup> was necessary. The robustness of the proposed system is naturally very low by comparison, but this is addressed in the next section *5.2.6 Formwork Fabrication*.
- c) Without any release agents and postprocessing steps, the plastic formwork is relatively easy to remove.
- d) Reduced labour and stream-lined construction process: faster off-site fabrication time for the formwork, reduced cost of transportation to site and easier on-site manipulation and assembly.

### 5.2.6. Formwork Fabrication

Early fabrication tests have shown that in order to prevent 3D printing artefacts such as disconnected layers, over- or under-extrusion and local material deposits, the spatial orientation of the hollow formwork tubes had to be at least 35° as measured from a horizontal plane. This prevented the need to 3D print auxiliary support structures as described in Figure 5.10, which would have increased printing time unnecessarily. In order to suit this constraint, a shape optimisation step was performed following the topology optimisation, in which the angles of the tubes were adjusted to avoid very low inclinations (Figure 5.10).

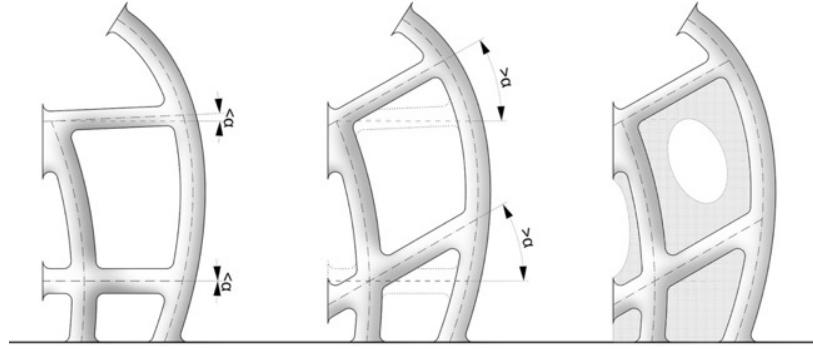


Figure 5.10: Diagrammatic section through a 3D printed part. In order to avoid auxiliary supports, the tubes are adjusted to achieve a minimal angle above an empirically determined threshold ( $\alpha > 35^\circ$ ). Lastly, membrane-like support structures are introduced to stabilise free-standing tubular structures (right). (dbt, ETH Zürich, 2017)

Another early empirical observation was that for taller parts, the movement of the gantry of the 3D printer caused vibrations that had a negative effect on the quality of tall and thin free-standing tubular parts. In order to prevent this, an auxiliary membrane-like support structure was parametrically introduced. This temporary support interconnects all the tubes in order to increase the stiffness of the part and reduce vibrations while printing (Figure 5.10 and Figure 5.11). Unlike a more conventional solid support system (Figure 5.9), these membranes did not bear the loads of the cantilevering layers, but only stiffened the free-standing geometric features in order to limit mechanically-induced vibrations. For reference, the membrane-like structures used for the *skelETHon* formwork represent only about 6% of a conventional solid support system.



Figure 5.11: A 700-mm tall sample 3D printed part of the skeleTHon formwork. In order to prevent quality issues for taller parts, a membrane-like auxiliary support structure is introduced. (dbt, ETH Zürich, 2017)

### 5.2.7. Discretisation

Very large industrial FDM 3D printers exist, such as BigRep One, with a build volume above 1 m<sup>3</sup> and Big Area Additive Manufacturing with a volume of 5.8 m<sup>3</sup> [100]. However, for the canoe only five basic entry-level consumer 3D printers were used. Four of them were Ultimaker Original+ 3D printers with build volumes of 210 × 210 × 205 mm. Two of these were modified with an extended vertical gantry, Z-Unlimited, commercialised by RooieJoris, to reach heights of up to 1'200 mm, for a total volume of 52.9 litres each. The fifth 3D printer used was marginally larger, the Raise3D N2+, which has a build volume of 56.3 L (305 × 305 × 605 mm). While more robust 3D printing facilities would certainly benefit from this method especially for larger scale architectural applications, the basic machines used for this project demonstrated the undemanding nature of the process and offered a good setup for investigating discretisation.

In order to address the limited volume of the 3D printers, the whole geometry was discretised in order to fit the print volume of the largest available printer. Thus, the formwork was split into 84 parts fitting 305 × 305 × 605 mm (Figure 5.12). Due to the two planes of symmetry of the boat, there were only 21 unique parts, plus their mirrored transformations.

Due to the intricate geometry, the size of the parts varied considerably, with bounding box volumes between 3.1 and 25.9 litres. This opened the opportunity to use the smaller 3D printers for the smaller parts in order to distribute the fabrication time. Each part took between 4.5 hours for the smallest and 56 hours for the largest pieces to print, with an overall printing time of just under 1`000 hours.

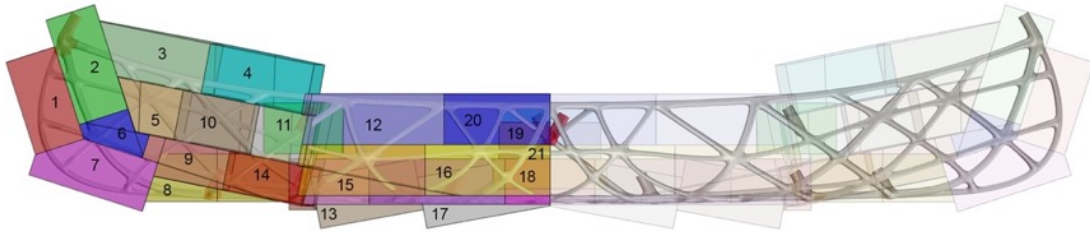


Figure 5.12: The 21 unique parts of the formwork that had to fit the maximum volume of the 3D printers. (dbt, ETH Zürich, 2017)

Before casting the skeleton, the independent pieces had to be joined together (Figure 5.13). This was done through chemical welding with dichloromethane, which is an organic solvent for PLA and punctual application of epoxy resin for most fragile joints.

The usage of this particular solvent presents similar hazard levels to the usage of acetone that also can be used for this particular application with a slightly lower efficiency. Using dichloromethane requires the usage of appropriate personal protective equipment, ventilation and fire hazard controls. An implementation of such a cold-welding technique should not present major problems for industrial applications safety-wise as its usage would be similar to products such as paint thinners, lacquers, varnishes and other organic solvents already massively used in certain industrial branches. Productivity-wise, this way of welding 3D printed parts would preferably need to be automated to a certain extend for industrial applications in order to avoid extensive man-hours expenses due to the alternative manual aspect of this process as it was performed for this project.

A 2 mm flange was integrated at each of the connections providing a wider welding area. This detail is visible at the top of the component in Figure 5.11. The solvent is applied locally with a brush and dissolves the PLA on both sides of the connection. The dichloromethane is highly volatile and it evaporates in a few seconds, leaving a solid connection purely made out of PLA.

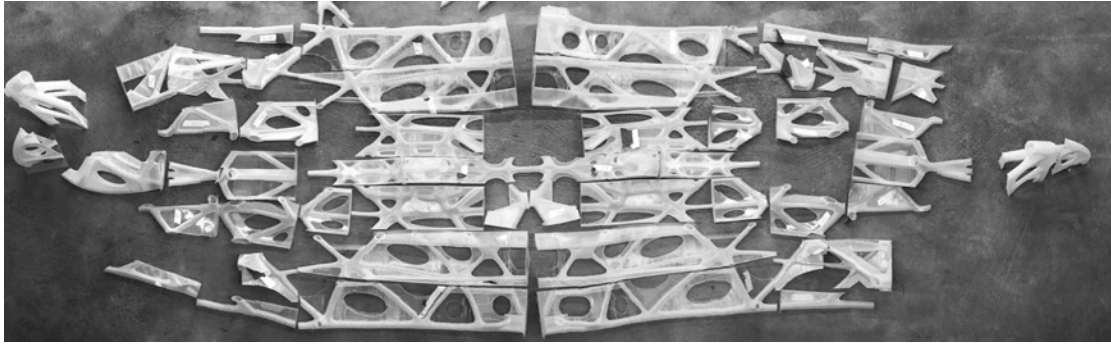


Figure 5.13: The 84 3D printed pieces before assembly. (Moritz Studer, ETH Zürich, 2017)

Finally, once the skeleton was assembled, a layer of transparent Polyester resin was applied on the surface in order to increase its mechanical properties during casting (Figure 5.14).



Figure 5.14: The 84 3D printed pieces assembled and ready for casting. (dbt, PCBM, ETH Zürich, 2017)

### 5.2.8. Concrete Casting

For the casting process, high-performance fibre-reinforced concrete (HPFRC) reinforced with 10x0.16mm steel fibres was used. The materials and methods used for the formulation of HPFRC as well as its development and properties are described in Chapter 4 of this thesis. The usage of HPFRC for this application presents a certain amount of substantial advantages. The low yield stress and high viscosity rheological behaviour of the HPFRC satisfies the necessary requirements to flow through the thin tubular geometric features of the canoe. In particular, the trials realised during the development of this HPFRC formulation described in Chapter 4, allowed to determine a minimal fibre length to channel diameter ratio ensuring a clogging-free flow of the HPFRC in bended tubular shaped conduits that was considered for the designing of the canoe

formwork. Another advantage of the HPFRC, and certainly the most important for this particular application, is its integrated reinforcement provided by the steel fibres it contains. Indeed, these bring considerable additional mechanical resistance in traction compared to a fibre-free concrete without any additional reinforcement. This feature of HPFRC presents a particular advantage in combination with topologically optimised structures such as this concrete canoe as it allows a homogeneous integration of reinforcement in a formwork that by its nature would make the installation of more traditional reinforcement solutions particularly challenging or close to impossible.

It is also important to underline here that, as described earlier, the essence of topologically optimised structures is to considerably reduce the amount of material used for their fabrication. While this aspect might at first glance imply a reduction of the overall environmental footprint of a topological optimised element in comparison to a traditional one it can also result in the need of using materials with higher mechanical properties to compensate for their volumetric reduction. For example, other type of solicitations may lead to higher requirements in bending and tension that a non-topologically optimised element might otherwise have. Moreover, a higher performance material may allow even further reductions in the mass of the topologically optimised structure.

HPFRC is a good example of such a material as it brings these additional mechanical advantages, but at the cost of a substantial increase of environmental footprint per volume of concrete compared to a traditional one. Lower water-cement ratios used in HPFRC imply a more important amount of dry materials per volume of final concrete. Another very important factor is the elimination of coarse aggregates, which also increases the amount of cement per volume. The combined increase in cement and reduction in water leads to a substantial increase in the amount of used admixtures such as PCE superplasticisers originating from petrochemical manufacturing that becomes important in terms of cost and probably also in terms of environmental footprint. Also, the additional manufacturing required to produce steel fibres in comparison to standard reinforcement steel might add up to the overall environmental footprint increase linked to the usage of high-performance steel-fibre-reinforced concrete.

An evaluation of the environmental footprint of the FDM printing process of the formwork is also to be considered, including the production, usage and recycling of the 3D printing PLA filament as well as the relatively important energy consumption of FDM 3D printers destined to melt the plastic. Overall, although a complete life cycle analysis being beyond the scope of this project, it is strongly recommended to perform one for any eventual future production of topologically optimised elements fabricated by using FDM printed formworks casted with HPFRC against a more traditional approach [101,102].



One of the critical issues related to concrete casting in submillimetre formwork is the build-up of hydrostatic pressure. The hydrostatic pressure ( $\sigma_h$ ) is the stress that is uniformly exerted by the fluid concrete on the formwork bellow a given height  $h$  of concrete. Given the gravitational acceleration  $g$ , the hydrostatic pressure is also depending on the density  $\rho$  of the HPFRC and is independent of the diameter of the formwork tubes:

$$\sigma_h = \rho_{HPFRC} \cdot g \cdot h_{HPFRC} \quad \text{Equ. 1}$$

Preliminary tests showed that the 0.8 mm thick PLA formwork chosen for this project was unable to withstand the hydrostatic pressure of HPFRC ( $\rho \approx 2400 \pm 50 \text{ kg/m}^3$ ) for casting heights greater than about 100 mm. The breaks in the formwork generally happen along the contact surface between consecutive 3D printed layers where the tensile strength is lower due to the weak layer-to-layer interface or at geometrical features of the formwork resulting in extensive localised stress accumulations.

In order to prevent the potential damages to the formwork caused by hydrostatic pressure, an auxiliary material was used to exert a counter-pressure on the formwork from the outside. To this effect, the canoe formwork was placed in a wooden box (Figure 5.15) that was simultaneously being filled with sand while concrete was being cast inside the formwork (Figure 5.16). The level of the sand surrounding the formwork was synchronised with the level concrete inside the formwork. Nevertheless, it is important to note that in this configuration the sand is not able to counteract the entirety of the hydrostatic pressure of the HPFRC. The loose sand placed in the box around the FDM printed formwork does not behave like a fluid to which the HPFRC can be assimilated, but rather responds to principles of soil mechanics<sup>1</sup> that for a soil at rest links the pressure exerted by sand vertically  $\sigma_v$  to the pressure it exerts horizontally (laterally)  $\sigma_h$  as follows:

$$\sigma_h = K_0 \cdot \sigma_v \quad \text{Equ. 2}$$

with  $K_0$  being the coefficient of earth pressure at rest that can be expressed in different ways, but which is empirically considered to be equal to 0.45 – 0.50

<sup>1</sup> The author would like to thank Prof. Dr. Alexander Puzrin for his precious input on the soil mechanics aspects used in this section.

for non to slightly compacted dry sand [103]. The vertical pressure exerted by the sand  $\sigma_v$  it can be expressed as:

$$\sigma_v = \gamma_{sand} \cdot h_{sand} \quad \text{Equ. 3}$$

where  $\gamma_{sand}$  is the sand bulk density expressed in  $\text{kN/m}^3$  and is equal to  $14 - 16 \text{ kN/m}^3$  depending on the properties and compaction of the sand, and  $h_{sand}$  the height of the sand column.

By injecting the given numerical values in Equ. 2 and Equ. 3 it comes out that the lateral pressure of sand is proportional to a value between 6.3 and 8 times the height of the sand column  $h_{sand}$ . By doing a similar calculation for the hydrostatic pressure of the HPFRC using Equ. 1, we find that the lateral pressure exerted by the HPFRC is proportional to 24 times the height its column. Therefore, it can be assumed that at equal heights the sand counteracts between 26 and 33 % of the HPFRC hydrostatic pressure depending on the sand properties and compaction.



Figure 5.15: The canoe formwork was placed in a simple box that was simultaneously being filled with sand while concrete was being cast inside the formwork (dbt, PCBM, ETH Zürich, 2017)

These relatively low values combined with the rather complex structure of the canoe's formwork as well as the presence of numerous weak point due to the cold welding of the 84 pieces presented in Figure 5.13 and Figure 5.14 could partially explain the non-negligible leakage issues that were encountered during the casting of the canoe. To address this problem, additional trials regarding counter-pressure casting were performed in order to understand the limits and the mechanics of this technique and propose possible solutions to improve it. These trials are described in section 5.2.9 and their results are presented and discussed in section 5.3.2.

Apart from offering some resistance to the hydrostatic pressure, the sand bed surrounding the formwork can also neutralise any potential breaks of the thin shell, by consolidating the formwork locally and preventing extensive concrete leaks.

In fact, the sand bed ends-up playing a similar role as the unprinted sand left in place when as in Chapter 4, ink jetting is used to produce a formwork. However, the placing of this sand is much easier, faster and it's granulometry does not play a such major role compared to binder-jetting. There is however potential to increase the "flow stopping" performance of the sand by optimising its particle size distribution.

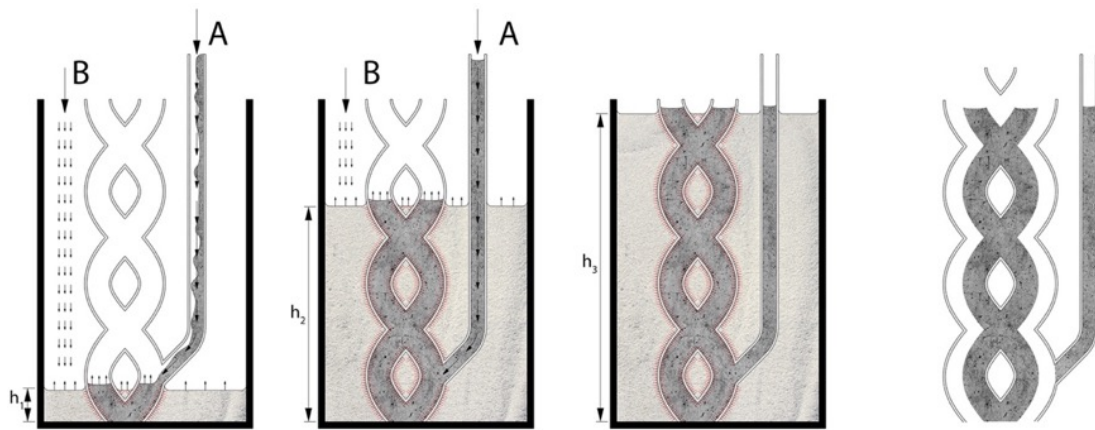


Figure 5.16: Step-by-step diagram showing the simultaneous infill of concrete through the bottom of the formwork (A) and of counter-pressure material (B). The final step consists of the removal of the formwork and casting inlet. (dbt, PCBM, ETH Zürich, 2017)

Getting back specifically to the production of the concrete canoe, the casting was initiated through inlets at the bottom of the formwork. This implies that the level of the concrete inside the shell rises uniformly. The transparent PLA formwork permits a visual inspection of the filling process to prevent air bubbles being trapped in complex nodes. As the concrete level reaches higher points, the sand bed on the outside is gradually filled to provide the necessary counter-pressure (Figure 5.16). The height difference between the cast concrete and the sand bed, was on the order of 2 cm which, as mentioned above, allows to exploit the PLA transparency for quality control of the casting process.

It turned out that one inlet point was not enough for the entire canoe. This probably results from a combination of viscous drag increasing in relation to the tube length. This slows down the flow rate, providing more time for thixotropic build up at the extremity of the casting. Together with the low, but not zero initial yield stress of the HPFRC, this can ultimately cause the flow to stop and incomplete formwork filling.

In order to overcome this, ten inlet tubes were used instead, evenly distributed throughout the lower part of the canoe. At the highest points of the canoe, two further outlet points were provided in order to permit the air to evacuate the formwork. Air getting trapped inside the formwork is a significant risk, especially in horizontal tubes, where concrete flows in from both ends. Therefore, the canoe was tilted at an angle of  $5^\circ$  to the horizontal plane. This ensured that none of the tubes were perfectly horizontal and that the concrete infill could be done progressively. Thus, all ten inlets were not used simultaneously from the beginning, but rather in a sequence, whenever the concrete level would reach their corresponding infill point (Figure 5.17).

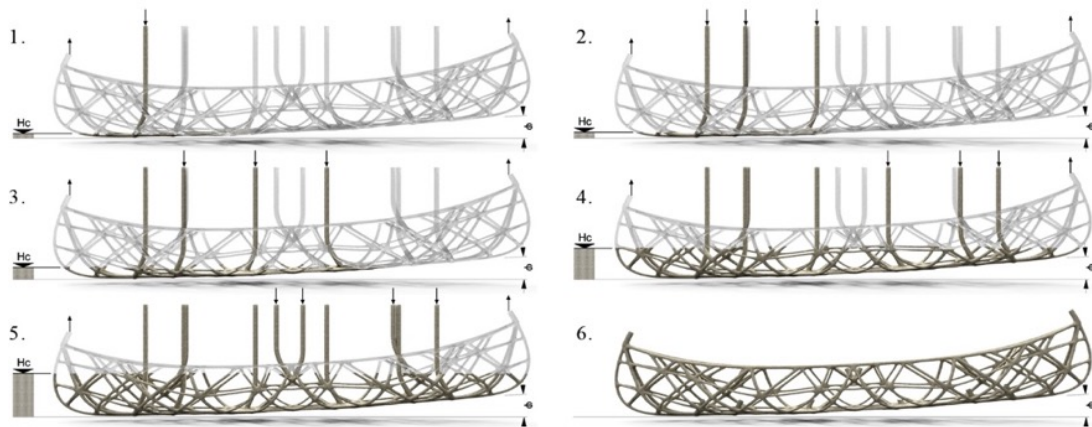


Figure 5.17: The casting sequence of the concrete canoe. The ten inlet points are situated at different heights in the lower part of the formwork. Casting starts through the lowest inlet point (1). The level of concrete inside the formwork ( $H_c$ ) raises gradually. Higher inlet points are used progressively as  $H_c$  increases (2-5). Once the entire canoe is filled, the inlet tubes are removed mechanically (6). (dbt, PCBM, ETH Zürich, 2017)

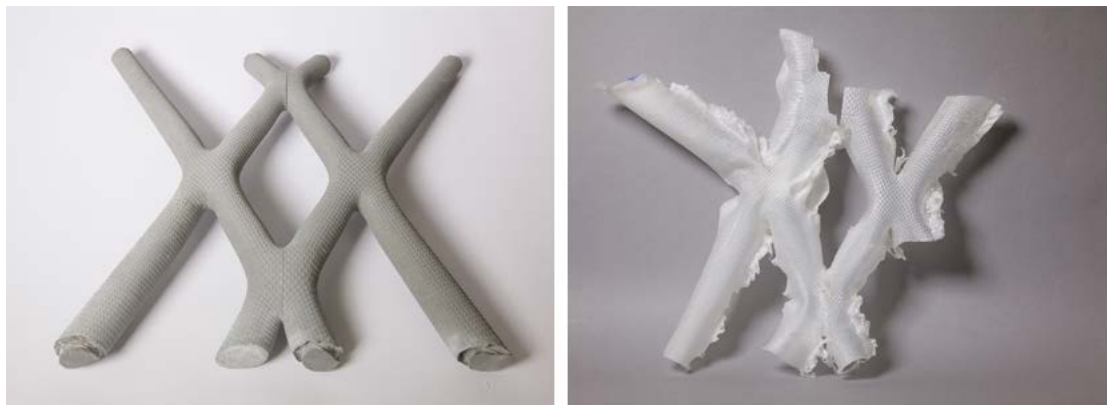


Figure 5.18: HPFRC prototype (left) after the removal of the submillimetre formwork (right). (dbt, PCBM, ETH Zürich, 2017)

Following the concrete casting, the PLA formwork provides the perfect enclosure for concrete curing, preventing water evaporation. After curing for seven days, a heat-gun was used to supply moderate heat ( $\sim 200^{\circ}\text{C}$ ) and make it easier for the formwork to be peeled off (Figure 5.18).

### 5.2.9. Additional counter-pressure casting trials

The concrete canoe project had a strictly defined time line due to its nature and goal to participate in the 2017 Beton Kanu Regatta. This is why it was decided after the completion of this main objective to perform a series of additional tests regarding the counter-pressure casting process based on the return of experience obtained during the fabrication of the *skelETHon*. The goal of these trials was to study the mechanics and limits of sand counter pressure casting of HPFRC into sub-millimetric FDM printed plastic formworks and bring potential improvements to this process.

In order to do so, it was decided to use a simple setup composed of a straight tube-shaped formwork of 60 mm inner diameter and 120 cm long, 3D printed in two pieces of 60 cm each which were cold welded together with the same method as the concrete canoe. The other parameters of the FDM 3D printing were kept as close as possible to those used for the canoe with the formwork thickness fixed to 0.8mm and the usage of the same semi-transparent PLA 3D printing filament. The tube-shaped formwork was filled with the same HPFRC formulation that was used for the canoe from the bottom of the tube fixed vertically inside a wooden box with inner dimensions of 30 by 30 by 150 cm. One of the lateral sides of the box was made out of a plexiglass in order to be able to monitor the sand infill speed in order to match it to the HPFRC level rising speed inside the tube. The HPFRC was casted into the tube formwork through a flexible feeding tube with an internal diameter of 35 mm connected to the bottom of the counter pressure casting box while its other extremity through which the HPFRC was introduced with the help of a funnel was placed at the same height as the top of the counter pressure casting box, corresponding to 30 cm above the top of the tube formwork. In a similar way to the canoe this placement allowed to use gravity as the only driving force of the casting process. A general view of the setup after casting and hardening of the HPFRC and removing the counter-pressure casting sand is presented in Figure 5.22.

Three trials were realised and will be presented and discussed in details in section 5.3.2. Two of these trials were performed inside a wooden box with sand as counter-pressure material. The only difference between these two trials was the usage of manual help to increase the sand compaction by taping the wooden box throughout its filling process with a plastic mallet, thus making one of these trials relying purely on the loose packing of the sand filled in the box.



The third trial was performed without any counter-pressure casting medium in order to observe a reference behaviour of the formwork.

More trials destined to prove the repeatability of those described above and additional ones to reach a potential quality and productivity improvement of the overall counter-pressure casting process were scheduled to be performed late March, April and early May 2020. However, due to the unfortunate timing they were not carried out because of the emerging Covid-19 pandemic situation leading to the lock-down of ETH Zürich research facilities on March 16<sup>th</sup> 2020 and the timeline of this PhD. Therefore, these non-performed trials will be presented, described and discussed as an outlook to this work in section 5.3.3 of this chapter.

## 5.3. Results and Discussion

### 5.3.1. Concrete canoe

At the 16th Concrete Canoe Regatta (Figure 5.19), *skelETHon* received the first prize for design innovation, being commended for the ingenious use of digital fabrication to indirectly produce the intricate concrete skeleton structure. The design and fabrication process of this canoe highlighted the harmonious compatibility between the additive digital fabrication process and the topology optimisation used for form-finding purposes.

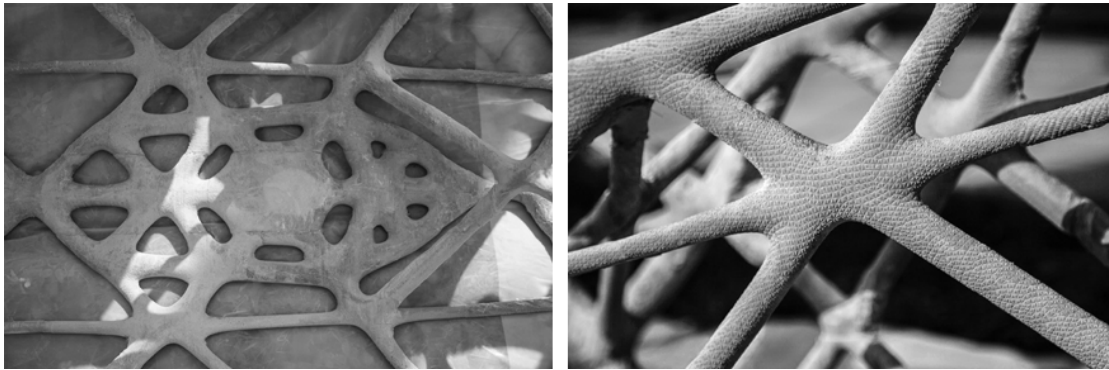


Figure 5.19: *skelETHon* at the 16th Concrete Canoe Regatta in Cologne, Germany (dbt, PCBM, ETH Zürich, 2017)

A key achievement was to keep the thickness of the formwork in the 0.6 to 1 mm range in order to minimise material use and keep fabrication time to a minimum. This was made possible by the unique properties of FDM 3D printing. The relatively expensive and time-consuming 3D printing process is only used for the very thin shell that defines the shape. This is possible because all the

structural stability of the formwork during casting is provided by the counter-pressure casting sand bed surrounding the formwork.

Freeing the 3D printed shell from the need to provide stability, also allowed an unprecedented geometric freedom to be possible with concrete. Due to the topology optimisation algorithm used in the design, concrete was used in a very efficient way, with bones of various thicknesses being optimally distributed to provide maximum stiffness for the frame (Figure 5.20). The skeleton weighed just under 80 Kg, while the final weight, including the waterproofing layer was 114 Kg. Such an intricate topology, with unique spatial nodes where between three and six linear elements meet at custom angles (Figure 5.8), with various degrees of smoothness, would be otherwise impossible to fabricate with any other production process.



*Figure 5.20: A wide range of geometric features resulted from the topology optimisation algorithm, with denser areas occurring on the keel, where the point loads from the canoeists are concentrated (left); and more open nodes on the hull, where only distributed loads are present (right) (dbt, PCBM, ETH Zürich, 2017)*

Another key achievement was to transfer faithfully a sub-millimetre surface texture from the 3D printed formwork to the concrete (Figure 5.21). This texture maximises the contact area with the waterproofing skin. Extrapolating this capability to architecture, these fine and precise surface treatments could fulfil other roles, such as acoustic diffusion, haptics or ornamentation for structural building elements.





Figure 5.21: High resolution texture on the surface of the *skelETHon*. This texture maximises the contact area with the waterproofing concrete skin. (dbt, PCBM, ETH Zürich, 2017)

Such a high-resolution texture would otherwise be challenging and time-consuming to achieve with subtractive processes like milling or hot wire cutting. While not unlimited, the geometric freedom offered by FDM certainly complements the other digital fabrication processes available for making formwork. A single fabrication process able to produce any geometry in large scale is not available at the moment, but FDM can be a very efficient tool in producing highly specialised geometries, such as networks of tubes and thin shells, impossible to fabricate otherwise.

The use of a sand powder bed to counter the hydrostatic pressure is reminiscent of the casting of metal objects in weak formworks, whereby the sand bed in that case also acts to attenuate thermal gradients during cooling. The use of this bed ends up serving an analogous role to the non-printed sand that may be left in place when ink-jetting is used to produce formworks. However, the procedure presented in this chapter is more robust and much faster.

It is also important to note that sand is a granular material and not a Newtonian fluid. It therefore has a capacity to carry high compressive loads as well as some shear. The latter increases with load and confinement. For our case it means that the higher is the sand bed, the greater is its ability to resist the hydrostatic pressure of the concrete. As the levels of both the concrete and the sand are raised simultaneously, it means that the system can possibly resist very high loads and allow tall objects to be produced. However, as explained in section 5.2.8, soil mechanics suggests that the sand height should be three times that of concrete to fully resist the hydrostatic pressure. Some suggestions about how to improve this situation, making counter-pressure casting more efficient are presented in section 5.3.3.2. Apart from this, it can be expected that local

failures of the mould would become a limiting factor, with possible material loss becoming problematic.

To limit material loss in case of local failure of the mould, it may be possible to revisit the HPFRC in the light of research done for casting concrete in mesh mould [104,105]. Indeed, in that work the concept of “Spaghetti and meat balls” was introduced. The idea is to prevent concrete flowing out of the gaps of the mesh by causing a combined jamming of the fibres and the aggregates. For this, the size and amount of both the fibres and aggregates should be adjusted with respect to the gap size. Transposed to our concern of mould breakage, we could do this by defining a critical crack size, taking this to be smaller or equal to the typical gap between sand particles in the bed.

## 5.3.2. Characterisation of counter-pressure effectiveness

### 5.3.2.1. *Brief description of counter pressure-casting experiments*

Both tube elements casted with the usage of sand counter pressure casting took approximatively 50 to 55 minutes to be filled, representing an average casting speed for this particular setup of 6 ltr/hr for a total volume estimated to 5.3 ltr (3.4 ltr for the tube element and 1.9 ltr for the feeding tube). While the exact HPFRC rise speed was not continuously measured, it was noted to gradually slow down the higher the concrete level was rising. This is an expected behaviour considering the high viscosity of the HPFRC and that the filling was driven by gravity.

For one sample the sand was vibrated as placed to increased its packing density. As explained previously, this should increase the effectiveness of the sand bed to oppose the concrete hydrostatic pressure.

The sand was removed from the box after a few days and both tubes casted with sand counter-pressure were presenting the same kind and pattern of damage (Figure 5.22). The lower halves of the tubes were covered in sand glued to them by what could be assumed minor concrete leaks homogeneously spread across the surface of the plastic formwork while the top halves did not present any kind of damage. After brushing off the sand with a metallic brush a clearer pattern of the damage was observable (Figure 5.23).



Figure 5.22: Tube element after casting and hardening of the HPFRC and removing of the counter pressure casting sand (both tubes casted with counter-pressure casting were presenting the same kind and pattern of damage). Left: Overview. Right: Lower half.

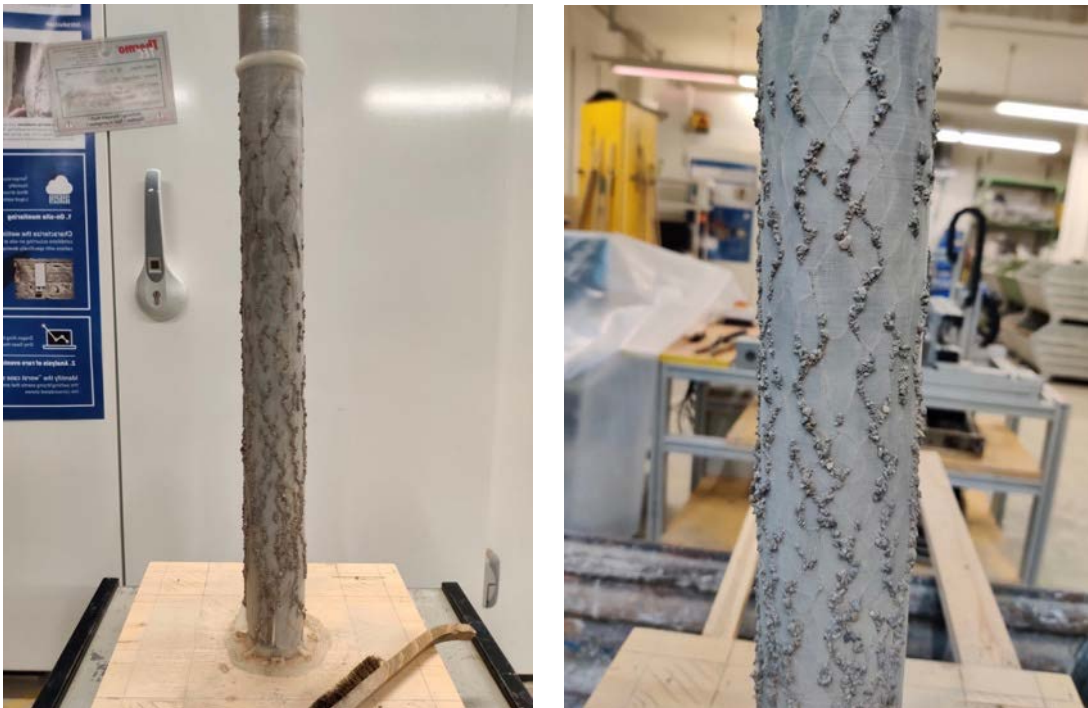


Figure 5.23: Bottom half of the tube element after brushing-of the sand. Left: Overview. Right: Detail of lower half.

### 5.3.2.2. *Nature of observed damage with counter-pressure casting*

After brushing off the sand, it became clear that the damage can be described as an interconnected network of cracks with “zig-zag” shape reminding the pattern created by lightning. While the damage to the formwork seemed substantial, no apparent leakages of HPFRC could be observed.

#### *Geometry changes induced by the damage*

A clear slight barrelling deformation of the lower halves of the tubes could be observed. This deformation could be put in parallel with recesses of concrete observed at the top of the tubes (Figure 5.24). Indeed, as the feeding tube was sealed-off at the end of the casting when the HPFRC level was reaching the top of the tubes, any barrelling deformation of the lower halves of the tubes after this point and before the setting of concrete would result in a recess of the concrete level in the tubes. The recesses measured on both tubes were 62mm and 43mm respectively for the loose sand and the manually compacted one. This represents 5.2 and 3.6% of the total volume of the tubes respectfully.

While the reproducibility of these results was not verified due to the poor timing of the Covid-19 epidemic, the decrease of the barrelling deformation due to an increase of the counter-pressure sand compaction seem a justified behaviour accordingly to Equ. 2 and Equ. 3 in section 5.2.9, as an increase of the compaction would lead to a higher bulk density of the sand and therefore a higher lateral pressure exerted on the formwork. Also, when the barrelling deformation is occurring, the displacement of the sand around the formwork might increase its compaction even further to a point of equilibrium when the deformation is stopped.

Sand with a higher initial compaction would allow less absolute deformation before reaching this equilibrium compared to a less compacted one. While this hypothesis needs to be confirmed by more experimental work, it suggests a potential solution to minimise the deformations of a failed FDM printed formwork by increasing the counter-pressure sand compaction by using a formwork vibrator attached to the counter-pressure box. The usage of these kind of vibrators must nevertheless be done with care as excessive vibrations could also lead to a segregation of the steel fibres contained in the HPFRC.

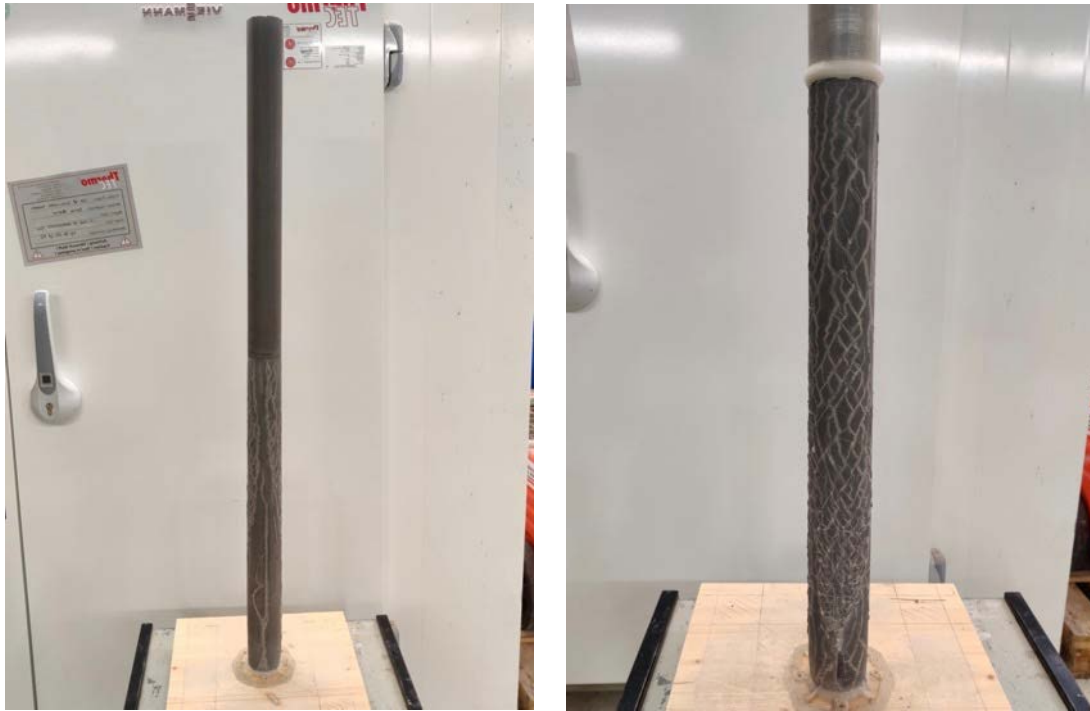


*Figure 5.24: Recess of HPFRC on the top of the tube element.*

#### *Damage nature and origin*

After removing the plastic formwork (Figure 5.25), a better view of damage pattern for the lower halves of the tubes and the surface finish of the upper halves were observable (Figure 5.26). While the upper halves were presenting a very nice and convincing surface finish similar to the one observed on the concrete canoe, the lightning pattern of the formwork failure could clearly be observed on the lower halves of the tubes. This pattern was consisting of less than a millimetre-high protrusions of concrete running along the formwork cracks and presenting a slight decolouration areola that is usually characteristic of localised water bleeding. It is important to note that no steel fibres were present in this pattern or sticking out in an apparent way making the tube manipulation by hand totally safe.





*Figure 5.25: Tube element after removing the plastic formwork. Left: Overview. Right: Lower half.*



*Figure 5.26: Surface details of the tube element after removing the plastic formwork. Left: Detail of the lower half. Right: Detail of the upper half.*

After a closer inspection of the formwork failure pattern it was noted that all the cracks in the lower halves of the tubes seem to originate from a few bigger ones located at the very bottom of the tubes (Figure 5.27 left), while they seem to stop right before the cold welding joint between the two formwork halves (Figure 5.27 right).

This observation was pointing toward a crack initiation at the bottom of the formwork followed by a branching propagation upwards that was finally stopped at the cold welding joint due to the presence of thicker formwork in this area. This behaviour seemed to indicate that the formwork failure was initiated where the hydrostatic pressure was at its maximum at the bottom, which is highly plausible. It also indicates that while the pressure on the formwork resulting from the concrete hydrostatic pressure and the counter-pressure of the sand was enough to initiate the failure at the bottom of the formwork (1.2 m columns on concrete and sand), the pressure at the bottom the top half of the formwork (0.6 m columns) was not enough to initiate a failure as no damage was observed in the upper half of the tube.



Figure 5.27: Surface details of the lower half of the tube after removing the plastic formwork. Left: Detail of the bottom of the element. Right: Detail of the middle of the element at the level of the cold welding of the two formwork halves.

This observation led to the idea of performing a test allowing to determine the threshold height and therefore pressure above which failure occurs. This can be achieved by printing a similar tube-shaped formwork that would integrate thicker formwork rings every few centimetres. Once casted, the sections of



formwork in between rings above the threshold would present failure while the ones below this threshold wouldn't. This could allow to determine with more precision the critical height of an element above which formwork failure is susceptible to occur.

While this test was not performed in this work, again due to the Covid-19, it is nevertheless important to underline the fact that its results would be quantitatively applicable for this specific setup only as many factors seem to impact the threshold height of a casted element such as: sand granulometry, sand compaction, counter-pressure box geometry, formwork thickness, element shape and others. However, this kind of test could still provide theoretical data in order to better understand the failing mechanisms of this process in order to improve it.

#### *5.3.2.3. Nature of failure for direct casting*

In order to have a better understanding of the formwork failure mechanisms, a third tube was casted without any counter pressure casting and monitored throughout the whole casting process.

##### *Failure description*

As expected, the failure occurred at the bottom of the tube as can be observed in Figure 5.28 at a concrete height of 84 cm in the formwork around the 30 minutes mark of the casting. This corresponds to a hydrostatic pressure of about 20 kPa, giving a tensile hoop stress in the PLA mould of similar magnitude. As this is very substantially lower than the tensile strength of PLA 3D printed parts usually ranging around 30-60 MPa depending on the print properties and conditions as well as the PLA filament quality [106–108], it can be expected that any of the following reasons may be causing this premature failure: flaws and/or inhomogeneities in the 3D print, stress corrosion, differential stress. Delamination of the layers can be excluded, since as explained below the failure is perpendicular to the layers.



*Figure 5.28: Formwork without counter-pressure casting after failure while HPFRC is leaking out. The maximum height the concrete reached in the formwork was 84 cm.*

While the height achieved is much lower than what could be expected from a pure tensile strength failure of the mould, it is nevertheless substantially higher than the 10 cm height at which failure was occurring during the concrete canoe preliminary tests described in section 5.2.8. Similarly, it is much larger than the general return of experience from the *dbt* research group regarding FDM printed formwork that were usually not holding concrete heights above 15-20 cm before failing when not using any kind of counter-pressure method. Considering that the FDM printing parameters of the tubes were the same as the concrete canoe formwork, the only possible explanation of this important difference is the impact of the formwork geometry itself on its failure mechanisms. Indeed, the usage of a straight vertical tube can be considered as one of the most advantageous and robust geometry as it doesn't present any curves or sharp angles, and maybe apart from a sphere present the best geometrical configuration to resist hydrostatic pressure loads. This makes it of course a rather biased geometry to directly compare to more realistic ones that may be used in digital fabrication but provides a well-defined and controlled system for studying the FDM 3D printed formwork failure mechanisms.

*Time-resolved observation of the failure*

This geometrical impact of the formwork was also confirmed by the close-up observation of the failure initiation at the bottom of the tube presented in Figure 5.29. While the exact moment of the visual failure appearance is estimated to have occurred 2 to 3 minutes before the first snapshot presented in Figure 5.29, the time stamps are given relatively to the first image.

From the first snapshot presented in Figure 5.29 it becomes clear that the first crack appeared vertically right in between two stiffeners present at the bottom of the formwork that were originally placed there in order to minimise the chance of breaking the formwork during its manipulation after it was fixed to the wooden base. Their placement induced a localised load case of the formwork under hydrostatic pressure by restraining the areas in contact with the stiffeners and provoking a vertical crack in between them. This behaviour demonstrates that the failure of thin FDM 3D printed formwork follows the principle of the weakest link here illustrated by the geometrical placement of stiffeners.

On the first four snapshots in Figure 5.29, the beginning of the lightning pattern propagation of the cracks can also be observed confirming the fact that all the damage observed on the tubes discussed above seems to originate from a limited number of cracks provoked by the presence of stiffeners. Their propagation then continues upwards creating the lightning-shaped damage pattern before being stopped by the thicker area of the formwork at the cold-welding joint location. This observation contrasts with the leakage defects noticed on the concrete canoe that were in their majority located at cold welding joints. This difference can be partially explained by the much more complex overall geometry of the canoe's formwork and therefore a poorer quality of welding at specifically complex nodes of the canoe's formwork.

The fact that the thicker area of the tube formwork stopped the propagation of cracks indicates that a smart variation of the formwork thickness or an overall thicker formwork would logically lead to less or no failure. This approach would however imply a non-negligible increase of printing time as well as plastic and energy consumption, all directly proportional to the total volume of the formwork material.

Another interesting observation that can be made on the 1'00" snapshot in Figure 5.29 is that the material leaking out of the formwork at this precise moment doesn't seem to contain any fibres. This observation corroborates the hypothesis made in section 5.2.8 about the steel fibres being able to clog leakages happening through cracks considerably smaller compared to the fibers size and also explains the absence of fibres in the damage protrusions of tubes described above.

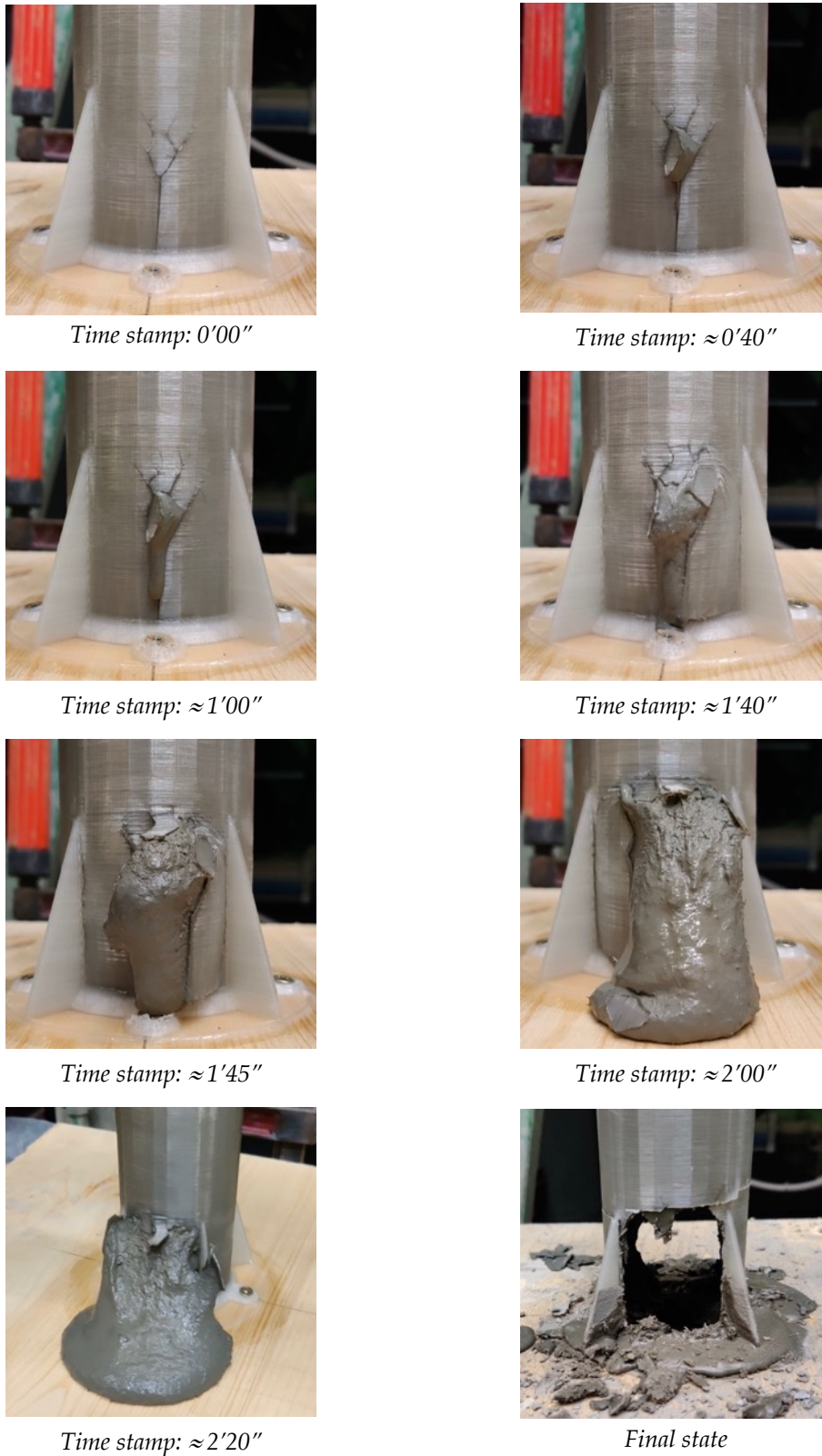


Figure 5.29: Timeline snapshots mosaic of formwork failure. Time stamps are indicated relatively to the first image.

### 5.3.3. Suggested follow-up experiments

As explained in section 5.2.8, several additional trials were scheduled to be performed to better understand the failure mechanics of thin FDM 3D printed formworks filled with HPFRC and potentially improve the overall process. These trials were unfortunately not performed due to the Covid-19 pandemic and the lockdown of ETH Zürich research facilities. These are briefly summarised below, along with a couple of other ones that were not discussed up to this point.

#### 5.3.3.1. *Stress induced corrosion*

Exploratory tests were performed by Andrei Jipa (*dbt* research group) and Dr. Lex Reiter (PCBM research group) regarding the impact of high alkaline mediums such as concrete pore solution on PLA mechanical properties. While the detailed results of this work are still to be eventually published, it was clearly observed that PLA plastic presents a considerable mechanical weakening in presence of highly alkaline solutions pointing towards a poor chemical resistance of this particular plastic to concrete.

While it is out of the scope of this work to present the details of these results or try to explain the chemistry involved in this behaviour, the usage of different kind of 3D printing plastic filaments to perform counter-pressure casting tests as the ones presented in this section seems like a viable exploratory work.

As a wide variety of filaments is currently easily commercially accessible, trials with formworks printed out of ABS, PETG and Nylon would be the first ones to be tried out because of their availability and supposedly good mechanical and chemical resistances. Other more exotic emerging filaments such as the Cyclic Olefin Copolymer (COC) from the manufacturer Creamelt could also present promising perspectives accordingly to its datasheet<sup>1</sup>.

However, the very popular usage of PLA in the 3D printing community compared to other types of filaments is mainly linked to its ease of printing and its eco-friendliness. The inherent additional challenges and issues of using other filaments such as higher printing temperatures, slower printing speeds, important warping, higher price, higher environmental footprint and others must be considered if used for printing thin formworks for concrete casting.

---

<sup>1</sup> <https://creamelt.com/wp/materials/coc/?v=18a5f226e926>

### 5.3.3.2. *Density of counter-pressure material*

As discussed in section 5.2.8 and above, the compaction and density of the sand used as counter-pressure medium plays a major role in the failure mechanism of thin FDM printed formworks. As demonstrated in section 5.2.8, sand can only compensate to 26 to 33% of the hydrostatic pressure of the HPFRC if keeping concrete and sand levels equal.

From a practical point of view, burying the formwork in sand to a depth three to four times higher than its height does not appear as a very viable solution, particularly not for industrial applications. Another approach would be to artificially increase the density of the sand that could be realised through different techniques of which the most effective seems to use a mix of sand and lead granules<sup>1</sup>. Indeed, if mixed together in the right proportions with sand, 2-5 mm in diameter spherical lead granules could theoretically increase the density of the counter-pressure medium in order to counteract the hydrostatic pressure enough or entirely to avoid any failures of the plastic formwork. Lead granules of such dimensions can be rather easily purchased in large amounts from lead manufacturers originally destined to basalt purposes or lead shot ammunition. However, while such sourcing might raise ethical questions, the usage of lead shot also brings important challenges of health, environmental and recycling issues due to its material nature that needs to be considered and assessed.

### 5.3.3.3. *Lightweight concrete*

Another approach involving the production of less mechanically demanding elements would be the replacement of HPFRC by lightweight concrete resulting in hydrostatic pressures equal or at least much closer to the counter-pressure provided by the sand. While the usage of lightweight concrete would not allow to produce important load bearing structures such as the concrete canoe or the ceiling element presented in Chapter 4, such an approach could be very interesting in order to produce ornamental or thermally insulating elements with the geometrical freedom and resolution provided by FDM 3D printing.

As reported by Suraneni et al [109], fiber reinforced self-compacting concrete can be produced with densities down to 1'400 kg/m<sup>3</sup> for tensile and compressive strengths respectively of 7 and 36 MPa. While not high strength concrete, this can nevertheless be sufficient for many applications and is certainly worth further consideration.

---

<sup>1</sup> The author would like to thank Prof. Dr. Alexander Puzrin for his precious input on the matter.

## 5.4. Outlook

The production of the *skelETHon* canoe and the additional counter-pressure casting trials highlighted a number of areas that can be addressed in future research in order to make this method suitable for streamlined large scale production. These are divided in three parts respectively describing needs in: - Casting Technology, - Mould production and - up-take by industry

### 5.4.1. Casting Technology needs

We begin with the concrete technology aspects as they relate most to the authors core contribution to this work:

- a) The sand box solution to counter the hydrostatic pressure in a thin formwork appears to be a “smart and easy” solution to an otherwise complex problem even if some challenges due to several intrinsic aspects of the overall process need to be overcome such as the only partial compensation of the hydrostatic pressure by sand.
- b) An optimisation of the counter pressure material would be worth exploring. This could include optimising its particle size distribution, improving its packing upon placing, but importantly also using other materials of higher density as lead granules [110].
- c) Possibilities of playing on the mix design, not only to make the material castable, but also to allow it to block in case of mould rupture appears as an exciting perspective.
- d) Using light-weight self-compacting fibre reinforced concrete could potentially double the limiting casting height, while nevertheless offering mechanical performance sufficient for many applications.
- e) The transparency of the plastic formwork and the slight height difference between the levels of the concrete and the sand bed offers a simple and effective means of casting quality control.
- f) Partially due to its current inconsistencies, the process is presently fundamentally suitable for off-site prefabrication of construction elements. The nature of the casting process where the concrete infilling has to be correlated with the sand-bed counter-pressure is only suitable in a controlled environment. This is because the concrete infill does not happen uniformly as initially predicted. Due to the variable friction with the formwork, wider tubes get filled up faster than narrow ones, which causes different concrete levels at different areas of the formwork. In order to overcome this issue, computational fluid dynamics simulations could be used to design a strategy for positioning inlets as well as adjust the diameters of the formwork tubes in order to ensure a predictable level of concrete throughout the casting process.



- g) Another type of simulation that could potentially give valuable insight into this process would be the analysis of the behaviour of the steel fibre reinforcement in such a tubular structure, especially around complex nodes. The consistent orientation of the fibres is critical in ensuring the bending strength of concrete, but the behaviour of the fibres throughout the casting process is difficult to anticipate intuitively. Combined with an empirical method such as X-ray computed tomography (CT) scanning of physical prototypes this could inform the geometry of such skeletons in a meaningful way (Figure 5.30).

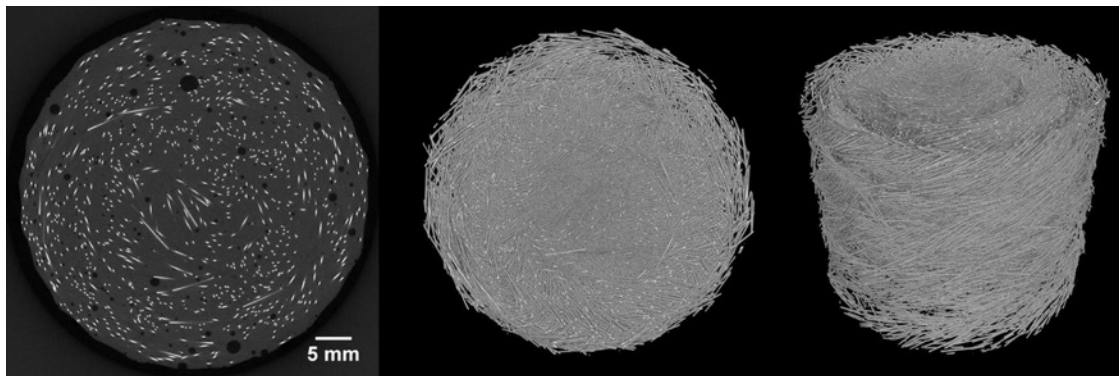


Figure 5.30: Preliminary CT scan of a concrete tube, showing the distribution and orientation of the steel fibre reinforcement, as well as air bubble inclusions. (Image courtesy of Michele Griffo, Empa, Dübendorf, Switzerland)

## 5.4.2. Mould printing needs

Apart from the concrete technology aspects, this work has highlighted many issues regarding the printing of formworks:

- a) The speed and reliability of the 3D printing process often caused issues, mostly related to the specific type of hardware used. An FDM machine with multiple hot ends, optimised for sustained printing in large volumes would be of great benefit to this research.
- b) The stability of a complex formwork such as the canoe can still be problematic at welding points. This is partially due to the large number of parts in which the formwork had to be discretised as a consequence of the small 3D printers used. 3D printing tolerances accumulate in the welding process and cause weaknesses. These weaknesses can lead to leaks of concrete during the casting process. While the sand bed quickly neutralises the leaks, the consistency of the formwork fabrication has to be addressed.
- c) As PLA plastic seems to present a particular weakness to alkaline solutions, the possibility of using other types of plastic 3D printing

filaments should be addressed while keeping in mind the additional printing constrains that their usage could bring.

- d) A proactive approach during the design stage is necessary in order to optimise the FDM printed formwork for a better sturdiness to concrete counter-pressure casting and minimise the number of potentially weak points that would lead to failure during the casting process caused by a “weakest link” behaviour. As a few examples of such a proactive approach:
- Avoiding sharp angles and load cases that could lead to important localised constrains.
  - Integrating support elements in the formwork to reduce unavoidable localised constrains.
  - Accounting for a homogeneous placement of the counter-pressure medium.

### 5.4.3. Industrial process needs

In regard to possible uptake of this process by industry it should be noted that:

- a) The process has the potential of becoming quite robust, particularly for the concrete, basic rheology tests before casting will be reliable predictors of the casting success.
- b) Large boxes with automatic delivery and easy recycling of the sand can be imagined. A moving dispenser and recycling system could be developed to allow many boxes to be used.
- c) Multiple parallel printers will have to be used, probably printing 7 days a week and 24 hours for the process to be effective
- d) Health and safety issues for the solvent used for the chemical welding may require special considerations.
- e) Optimisation of the casting inlets, sequence as well as fibre orientation introduce many case-specific considerations that will call for a build-up of expertise, probably involving different simulation tools.
- f) In all cases it is expected that producing topologically optimised structure to reduce material use and weight of an object, would represent an important potential, so that expertise in the type of software used in this chapter would be needed.
- g) A complete life cycle analysis of a representative element produced by the presented overall technique should be performed in comparison to a more classical approach using reinforced concrete and traditional formwork in order to assess its potentially positive or negative environmental impact.

## 5.5. Conclusion

The fabrication process tested with the canoe shows how a cutting-edge digital fabrication technology can be used minimally to fabricate a thin shell formwork that accurately defines the shape, while the stability of the formwork is transferred to a common secondary material, such as sand. The gradual sand filling process, combined with the transparency of the formwork allows live feedback on the casting process, which is critical for intricate geometries.

This novel process can be extrapolated and directly adapted for the design and prefabrication of large, load-bearing, concrete architectural components. The size of the canoe, approximately  $4 \times 0.7 \times 0.7$  m is representative for a building component such as a column, a beam or a façade element and the infrastructure necessary for the casting (i.e. containers for sand) is easily available. The key achievements demonstrated with the canoe can make a big difference in the way concrete is used in architecture: almost unconstrained geometric freedom, significant weight reduction, lightweight formwork and high precision for on-site assembly.

The complexity of the formworks possible, combined with the excellent rheological properties of HPFRC open up an entirely new family of shapes for concrete building elements: microstructures, free form surfaces, highly detailed textures, precise articulations and convoluted topologies.

With 3D printing, each fabricated part can be unique, since the manufacturing process does not involve the use of expensive moulds that need to be re-used to make them cost-effective. 3D printing one-of-a-kind pieces of formwork, for customised concrete elements specifically tailored for their individual purpose is therefore possible, with no cost or time penalties. These are the first steps towards the mass-customisation of buildings through non-standard, prefabricated concrete components that integrate structural, functional and aesthetic solutions, as well as additional features such as weight reduction and a smart assembly logic.

# Chapter 6 – Conclusions and Outlook

Due to the overall structure of this PhD thesis, both of this chapter's sections are sub-divided in two parts allowing to separately present the conclusions and outlook of the cryo-FIB-SEM nano-tomography and digital casting related works.

## 6.1. Cryo-FIB-SEM nano-tomography of fresh model cement pastes

### 6.1.1. Main Outcomes

One of the main outcomes of this work was to provide important insights into the challenges faced when using cryo-FIB-SEM nano-tomography in order to provide unbiased quantitative data of fresh cement pastes microstructures. This heavily equipment and experience relying technique originally developed for studying water-containing biological samples, holds a great potential for three-dimensional microstructure observation and analysis with a resolution of modern scanning electron microscopy with, if all goes well, only minor to no alterations. The usage of this technique to study the effect of PCE on the nucleation and formation of the first hydrate particles in a controlled system made of model cement paste and custom-tailored superplasticiser presented a scientifically appealing solution. In particular, compared to other methods where the removal or substitution of water still present in the transient fresh state of concrete leads to an alteration of its true microstructure.

While being able to provide a few exploitable images of the fresh model cement microstructure for qualitative analysis from polished image planes prior to the tomography “slice and view” process, this work faced an imaging issue

during this process dubbed the “scaling artefact”. Appearing during the first slices in areas corresponding to vitrified ice and persisting throughout the entirety of the tomography process, the nature, the size and the grey levels of this artefact made the three-dimensional discretisation and analysis of the tomography impossible due to their very close similarity to those of the first hydrate particles (see section 3.4.2.1, Chapter 3). This behaviour was particularly problematic for fresh model cement pastes samples containing PCE in direct addition which were exhibiting considerably smaller and dispersed hydrate particles. The artefact could have been attempted to be removed by image treatment, but due to its nature the imaging details regarding the first hydrates would have been lost. This is the reason why the image treatment solution was discarded at an early stage of this work in order to avoid presenting scientifically biased results and interpretation of the most important information of our objective.

Numerous investigations were performed to determine the origin of the artefact in order to try to attenuate or eliminate it. While this work presents only a hypothetical explanation as to the artefact origin, it is believed to be caused by an important number of relatively unrelated parameters. However, as explained in detail in section 3.4.2.2 (Chapter 3), the main origin of the artefact is believed to be linked to a combination between the damage done to the vitrified ice by the electron beam during imaging and the redeposition of dense atomic matter coming from the ion beam milling of unhydrated cement grains on this damage during the tomography process.

An important amount of trials in order to identify the origin and find ways to attenuate or remove the scaling during the tomography process was realised, unfortunately without success. These trials included attempts to resolve the issue through the following approaches:

- Possibility of the scaling originating from a freezing artefact
- Usage of reference samples: Vitrified quartz flour and water paste and frozen model cement and epoxy paste
- Opening of a wider front trench and using of side trenches around the volume of interest.
- Usage of different FIB milling currents
- Increasing the FIB milling slice thickness at the expense of the third-dimension resolution
- Adjusting the electron imaging parameters
- Attempting tomographies at different temperatures
- “Tweaking” of advanced parameters of the electron and ion beams

Finally, in a last attempt to carry out the main goal of this work a different microscope was used without success due to different and mainly equipment related issues.

While the main goal of this work was not achieved, it allowed an important insight of the challenges that can be faced when attempting to use cryo-FIB-SEM nano-tomography for studying fresh cement pastes microstructures. In comparison to biological samples which, to the knowledge of the author, were never reported to present any scaling artefact. The issue with cement pastes is believed to originate from their high inhomogeneity in terms of very dense particles suspended in vitrified ice with their respective resistances to FIB milling and electron beam damage being radically different compared to biological samples usually composed of a vast majority of water with a rather homogeneous distribution of a small amount of heavier atoms.

A metaphorical way to present the problem would be to attempt cutting thin and straight slices from a clod of butter with a relatively sharp knife without leaving any cutting induced pattern on the remaining piece of the clod. In the case of biological samples, the butter would contain fresh grapes representing cells as an example, while the hydrated cement particles would be represented by hazelnuts. While a clean slice through butter containing grapes would be easily achievable, a slice through hazelnuts containing butter would be much more difficult to realise without leaving some kind of cutting damage on the remaining piece of the clod.

Presented in section 3.3 of Chapter 3, this work also highlighted the overall complexity of the cryo-FIB-SEM nano-tomography process which is often underrepresented in publications.

The qualitative results provided by this work confirm the impact of PCE direct addition on the nucleation, formation and dispersion of first hydrates in a fresh cement paste. Indeed, a higher amount of smaller and more dispersed hydrate particles was observed in samples containing PCE. These results are adequate with observations reported by other works.

Finally, this work shed light upon the unfortunate and often recurring lack of proper reporting of technique-related challenges and detailed data treatment (including the potential biases introduced by them) in published research. In particular, the total absence of reporting of the scaling presence became clear in the work of Dr. Anatol Zing's PhD who used cryo-FIB-SEM nano-tomography to study fresh cement pastes containing commercially sourced superplasticisers. The clear appearance of the scaling artefact on one single image of this work in opposition to all other image data where it is absent without any mention of the issue itself or ways to deal with it calls to nuance some of that work's conclusions often referred to in other researches. Zingg's work may have faced a weaker manifestation of the scaling due to the usage of different microscopy equipment. However, even if he extensively faced the scaling artefacts, the image treatments do not affect the main observations of his work. Nevertheless, further interpretations of his published images as well as an assessment of the potential of the method do suffer from this, which underlines the need for transparency in

reporting. Since the time of their publication, journals have taken important steps in offering authors more space to present experimental details in supplementary materials and make original images openly accessible. In view of our results, this is a very valuable evolution that can limit unfounded reinterpretation of previously published works.

### 6.1.2. Outlooks

While this work failed to achieve its main goal to obtain exploitable quantitative microstructural data from fresh model cement pastes, it nevertheless highlighted the highly praised potential of cryo-FIB-SEM nano-tomography technique to study unaltered water containing microstructures at high resolutions.

This work provided several possible directions to deal with the encountered scaling artefact. It is hoped that with improvement in instrumentation and a better understanding of the scaling artefact, the day may come where cryo-nano-tomography will bring interesting and needed data to advance understanding of fresh concrete microstructural mechanics allowing further efficiency and properties improvement both in applications and fundamental admixtures research. These directions are:

- Usage of lowest acceptable settings regarding FIB milling and SEM imaging (current, voltage, spot size, dwelling and resolution) in order to minimise the energy dose delivered to the sample and therefore reducing the potential damage and redeposition believed to be responsible for the artefact. These parameters have still to remain in a range that provides acceptable image quality and resolution in order to be able to perform the required quantitative analysis.
- Usage of a different microscope or a different set of microscope hardware that might be more adapted for studding frozen cement pastes such as a more sensible BSE detector and/or a different chamber geometry.
- Related to the previous point: performing the tomographies at lower temperatures. This can be achieved with the usage of more efficient cryo-stage and overall a better cooling system of the microscope including an efficient cryo-shield.
- Make the usage of cryo-electron microscopy for material science purposes more appealing to the cryo-electron microscopy community and microscope manufacturers through closer collaboration and promises of relevant milestone publications.
- Establishing a close collaboration with the microscope's manufacturer in order to get insights on the potential "black box behaviour" of their equipment involved in the automatic "slice and view" process.



Overall, the main outlook of this work is that further investigations in order to try to deal with the scaling artefact have to be undertaken in order to obtain unbiased qualitative data on fresh concrete microstructure that could lead to very promising results in the field of concrete material science. These investigations could be performed within a specially dedicated project or as part of a collaborative work on cryo-electron microscopy.

This work also highlighted the unconditional importance of proper and detailed reporting of any kind of data treatment performed within a published research work for transparency reasons and in order to avoid unwillingly misleading other researchers.

## 6.2. Digital Casting

### 6.2.1. Main Outcomes

The main outcome of this part of the thesis was to explore and develop two innovative processes in the field of concrete digital fabrication and in particular digital casting. In collaboration with the *dbt* research group (D-ARCH, ETH Zürich) and over two bachelor student projects supervised by the author, two new processes involving the production of structurally sound topologically optimised concrete elements were developed using different approaches on the topic of thin digitally fabricated formworks.

In comparison to other techniques of digital casting (see section 2.2.3, Chapter 2), the processes developed during this work were intentionally devoid of any advanced concrete setting and hardening controls while relying on the digitally produced formworks to shape the final elements: a ceiling/flooring element and a functional concrete canoe. The usage of topological optimisation in combination with digital casting processes represents well the very essence of concrete digital fabrication as it allows an important reduction of the used concrete while making possible the production of intricate free-form geometries originating from topology optimisation.

This reduction of concrete usage coupled with the resulting complex tubular shaped formworks led to the usage and development of a high-viscosity and low yield stress high-performance steel-fibre reinforced (HPFRC) concrete that could at the same time fulfil both the rheological and enhanced mechanical aspects required for such specific applications.

The major rheological challenge regarding the casting of the produced elements was to ensure the homogeneous filling of the tubular shaped structure coming from the topological optimisation. Therefore, an important work of formulation of the HPFRC was realised in order to assure both rheological and

mechanical properties of the mix. A formulation kindly provided by Dr. Emmanuel Denarié from the Structural Engineering group of EPFL was adapted to the needs of the project. These adaptations involved adjusting the formulation and the mixing procedure, due to the replacement of certain dry materials and the superplasticiser. Also, three different lengths of steel fibres were tested in order to extrapolate the minimal channel diameter to fibre length ratio in order to avoid clogging. The results of these tests provided several suitable HPFRC formulations with low shear stress and high viscosity that were able to flow without clogging in tubular samples presenting same channel diameters and bends as the final elements ones.

#### *Topologically optimised ceiling element*

The first element produced in this work was a  $1.8 \times 1 \times 0.15 \text{ m}^3$  topologically optimised ceiling element the sub-centimetric formwork of which was fabricated using sand binder-jetting 3D printing (Chapter 4). This stay in place formwork was able to sustain the hydrostatic pressure of HPFRC during the casting process due to the decent mechanical properties of sand binder-jetting 3D prints and the relatively low height of the casted element. The element was successfully filled with the developed HPFRC formulation following a special casting sequence ensuring a homogeneous filling of the entirety of the element without any additional help such as pumping of concrete vibration. While the final element was never cut open to verify its adequate filling as it was destined for an exhibition, it was able to successfully sustain the weight of six adults standing on it while itself sitting on its four designed support points. While the production of this element demonstrated the very appealing potential of using sand binder-jetting to produce stay in place formworks for digital casting applications, its importance even if constantly decreasing cost makes its usage for digitally fabricating formworks among the least competitive at present day. Nevertheless, the ability of sand binder-jetting 3D printing to achieve extremely complex free form with resolutions hardly achievable by other means makes this technique considerable for specific industrial applications especially if its cost continues to drop in the near future.

#### *skelETHon concrete canoe*

The second element produced during this work was a topologically optimised four-meter-long concrete canoe designed to accommodate two rowers (Chapter 5). Manufactured to participate in the 2017 Concrete Canoe Regatta in Germany, the *skelETHon* canoe was fabricated by plastic Fused Deposition Modeling (FDM) 3D printing of its formwork filled with HPFRC.

The name of the canoe is originating from the skeletal shape of its load bearing structure that was obtained by topological optimisation of a traditional canoe. This topological optimisation process, realised by the *dbt* research group, produced a tubular shaped skeletal formwork that was then 3D printed by FDM using semi-transparent Polylactic Acid (PLA) polymer filament. Due to the consequent dimensions of the canoe, the sub-millimetric formwork (0.8 mm thick in average) was printed in 84 distinct pieces that were then cold welded together using dichloromethane solvent. An important work of FDM 3D printing optimisation was realised by the *dbt* research group including the segmentation of the whole formwork and the integration of custom developed 3D printing supports in order to achieve both high efficiency and quality required by the relatively short timeframe of the project.

Due to the relatively weak mechanical properties of such a thin plastic formwork, an important amount of work was dedicated to develop and optimise a specific casting technique that could counteract this weakness. Indeed, preliminary tests indicated that the FDM 3D printed formwork was not able to sustain the hydrostatic pressure of the HPFRC for casting heights greater than about 10 cm before failing resulting in concrete spillage that would result in the impossibility to cast the over 40 cm high canoe. Therefore, a specific casting technique named counter-pressure casting was developed. It consists in placing the FDM 3D printed formwork in a box that is progressively filled with sand during the casting by keeping up and matching the levels of sand and HPFRC thanks to the semi-transparent aspect of the PLA used to produce the formwork. While accordingly to soil mechanics, loose dry sand placed this way is able to counteract only 26 to 33% of the hydrostatic pressure of the HPFRC, this technique allowed to successfully produce the load bearing skeletal structure of the concrete canoe with only a few minor to medium leakages of concrete that occurred in their majority at complex cold welding joints and that were grinded away in post processing.

Considering the important amount of HPFRC that had to be casted in the canoe formwork and the inevitable loss of its rheological properties over time, a special attention was dedicated to the placement of casting inlets (ten in total) and outlets (two in total) in order to ensure the best filling of the formwork while ensuring the evacuation of any entrapped air pockets. The formwork was placed under an overall angle of 5° and filled by sequentially using inlets connected at different heights of the formwork.

The relatively easy removal of the FDM formwork was realised with the usage of heat-guns after curing period of seven days. The waterproofing of the canoe was assured by a liquid mortar painted cotton fabric stretched over and sewed onto the skeletal load bearing structure.

The *SeIETHon* concrete canoe successfully participated in the 2017 Beton Kanu Regatta in Germagny, an event occurring every two years gathering

together concrete canoe enthusiasts as well as major concrete material science research groups as well as important industrial partners. Winning the first award for design innovation, this demonstrator showed the great potential of using thin FDM 3D printed formworks in combination with reinforcement integrating HPFRC in order to produce structurally viable topologically optimised elements with complex geometries. In opposition to sand binder-jetting 3D printed formworks, the usage of FDM 3D printing shows a much greater potential to keep the “complexity for free” promise of concrete digital fabrication due to the important availability and lately increasing competitiveness this widely spreading technique among both industries and DIY / makers communities.

For industry, the counter-pressure casting offers a couple of very important advantages: - Ease of implementation, - Reduced sensitivity to controlling both concrete rheology AND hydration simultaneously, - Excellent surface finish.

Considering this potential, additional work was realised to characterise counter-pressure casting effectiveness and this brought to light the following results:

- The geometry of the formwork plays a crucial role in its failure mechanics. In comparison to the complex geometry of the concrete canoe, a straight vertical 6 cm in diameter tube with the same formwork thickness and without counter-pressure material failed at a height of about 84 cm.
- The failure of the PLA formwork follows the principle of “the weakest link”. A time-resolved observation of the failure of the vertical tube formwork showed that the failure initiation occurred in a localised zone where the placement of stiffeners provoked and increased localised stress. The observation of the failure pattern on tubes casted with usage of counter-pressure suggests that the failure is then able to propagate following fracture mechanics throw-out large surfaces of the formwork.
- The compaction and density of sand used as counter-pressure material plays an important role in the amount of hydrostatic pressure that the sand can counteract.
- The mechanical resistance of PLA seems considerably reduced in presence of alkaline mediums such as concrete pore solution pointing towards a probable stress induced corrosion weakness of PLA in such mediums.

Overall, this work allowed the development of two new promising digital casting processes, one of which may be considered as having possibly inspired another digital casting technique called Eggshell and described in section 2.2.3.3 (Chapter 2, Figure 2.18, page 30). Nevertheless, both developed techniques require further improvements and development before reaching a level where they could be integrated in industrial mass production.

## 6.2.2. Outlook

While this work demonstrated the potential of using digitally fabricated thin formworks in combination with HPFRC without any advanced setting and hardening controls, the two presented techniques offer room for efficiency and quality improvement.

While the main issue with sand binder-jetting 3D printed formworks remains up to this day its cost efficiency regarding its use as a free form concrete formwork, a certain amount of questions also arises about its capacity to withstand important concrete induced hydrostatic pressures for tall elements. A proper investigation of the mechanical limits of such prints regarding this point would be interesting to perform. In the case this issue comes out to limit the maximum height of such produced elements, an approach similar to the one developed for the concrete canoe with counter-pressure casting could be an interesting and elegant solution.

Regarding the use of FDM 3D printed formworks, its appealing cost efficiency and complexity resolution makes it a very good candidate for future production upscaling and industrial integration. Nevertheless, the recurring localised formwork failures in the currently used setup require further investigations, guidelines and trials in order to minimise their impact on the quality of the produced element. Based on the results of this work the main recommendations would be:

- The usage of different type of polymer 3D printing filament to produce the formwork that could present better chemical resistance to alkaline environments.
- The usage of denser and/or better compacted counter-pressure materials in order to increase the amount of counteracted hydrostatic pressure originating from concrete.
- The usage of fibre-reinforced light weight concrete instead of HPFRC in order to reduce the hydrostatic pressure at the expense of mechanical properties.
- A proactive approach during the design phase of the elements in order to account for the specificities of FDM 3D printing, counter-pressure material placement and localised stress/strain concentrations possibly leading to failure.
- The usage of faster and more efficient FDM 3D printers to minimise printing time.

From a more general point of view and regarding both developed techniques an in-depth investigation work on induced fibre orientation within the elements by flow orientation or other techniques such as electromagnetic fields could bring a considerable improvement to the overall mechanical

properties of such elements allowing an even more aggressive topological optimisation.

Finally, a detailed investigation of the impact on environmental footprint of these techniques have to be performed prior to any industrial integration. As described in section 5.2.8 of Chapter 5, topology optimisation, even if reducing the overall amount of used materials, also calls for usage of a larger amount of raw materials such as cement per unit of volume in order to increase the mechanical properties of concrete to compensate for its decreased amount. Materials such as HPFRC also usually require the usage of CEM I type of cement that has a bigger environmental footprint compared to blended cements and uses important amounts of chemical admixtures to counteract low  $w/c$  ratios. On the formwork side, the energy and petrochemical products consumptions such as 3D printing filaments or furan binders used for sand binder-jetting have also to be considered in an overall full Life Cycle Analysis that have to be performed for these techniques and compared to more traditional approaches in order to have a clear image of their true environmental footprint impact.

# References

- [1] J.M. Crow, The concrete conundrum, *Chemistry World*. 5 (2008) 62–66.
- [2] G. Gelardi, S. Mantellato, D. Marchon, M. Palacios, A.B. Eberhardt, R.J. Flatt, Chemistry of chemical admixtures, in: *Science and Technology of Concrete Admixtures*, Elsevier, 2016: pp. 149–218. <https://doi.org/10.1016/B978-0-08-100693-1.00009-6>.
- [3] R.J. Flatt, N. Roussel, C.R. Cheeseman, Concrete: An eco material that needs to be improved, *Journal of the European Ceramic Society*. 32 (2012) 2787–2798. <https://doi.org/10.1016/j.jeurceramsoc.2011.11.012>.
- [4] J. Cheung, L. Roberts, J. Liu, Admixtures and sustainability, *Cement and Concrete Research*. 114 (2018) 79–89. <https://doi.org/10.1016/j.cemconres.2017.04.011>.
- [5] D. Marchon, S. Kawashima, H. Bessaies-Bey, S. Mantellato, S. Ng, Hydration and rheology control of concrete for digital fabrication: Potential admixtures and cement chemistry, *Cement and Concrete Research*. 112 (2018) 96–110. <https://doi.org/10.1016/j.cemconres.2018.05.014>.
- [6] R.J. Flatt, Y.F. Houst, A simplified view on chemical effects perturbing the action of superplasticizers, *Cement and Concrete Research*. 31 (2001) 1169–1176.
- [7] D. Marchon, P. Juilland, E. Gallucci, L. Frunz, R.J. Flatt, Molecular and submolecular scale effects of comb-copolymers on tri-calcium silicate reactivity: Toward molecular design, *J. Am. Ceram. Soc.* 100 (2017) 817–841. <https://doi.org/10.1111/jace.14695>.
- [8] F. Dalas, S. Pourchet, D. Rinaldi, A. Nonat, S. Sabio, M. Mosquet, Modification of the rate of formation and surface area of ettringite by polycarboxylate ether superplasticizers during early C3A–CaSO4 hydration, *Cement and Concrete Research*. 69 (2015) 105–113. <https://doi.org/10.1016/j.cemconres.2014.12.007>.
- [9] T. Wangler, E. Lloret, L. Reiter, N. Hack, F. Gramazio, M. Kohler, M. Bernhard, B. Dillenburger, J. Buchli, N. Roussel, R. Flatt, Digital Concrete: Opportunities and Challenges, *RILEM Technical Letters*. 1 (2016) 67–75. <https://doi.org/10.21809/rilemtechlett.2016.16>.
- [10] B. Khoshnevis, Automated construction by contour crafting—related robotics and information technologies, *Automation in Construction*. 13 (2004) 5–19. <https://doi.org/10.1016/j.autcon.2003.08.012>.
- [11] B. Khoshnevis, D. Hwang, K.-T. Yao, Z. Yeh, Mega-scale fabrication by Contour Crafting, *International Journal of Industrial and Systems Engineering*. 1 (2006) 301–320. <https://doi.org/10.1504/IJISE.2006.009791>.



- [12] E. Lloret-Fritschi, F. Scotto, F. Gramazio, M. Kohler, K. Graser, T. Wangler, L. Reiter, R.J. Flatt, J. Mata-Falcón, Challenges of Real-Scale Production with Smart Dynamic Casting, in: T. Wangler, R.J. Flatt (Eds.), *First RILEM International Conference on Concrete and Digital Fabrication – Digital Concrete 2018*, Springer International Publishing, Cham, 2019: pp. 299–310. [https://doi.org/10.1007/978-3-319-99519-9\\_28](https://doi.org/10.1007/978-3-319-99519-9_28).
- [13] K. Dörfler, N. Hack, T. Sandy, M. Giffthaler, M. Lussi, A.N. Walzer, J. Buchli, F. Gramazio, M. Kohler, Mobile robotic fabrication beyond factory conditions: case study Mesh Mould wall of the DFAB HOUSE, *Constr Robot.* 3 (2019) 53–67. <https://doi.org/10.1007/s41693-019-00020-w>.
- [14] M.A. Meibodi, A. Jipa, R. Giesecke, M. Bernhard, M. Leschok, K. Gaser, B. Dillenburger, Smart Slab: Computational Design and Digital Fabrication of a Lightweight Concrete Slab, in: *Acadia 2018 Recalibration: On Imprecision and Infidelity: Proceedings of the 38th Annual Conference of the Association for Computer Aided Design in Architecture*, Association for Computer Aided Design in Architecture (ACADIA), Mexico City, Mexico, 2018: pp. 434–443. [http://papers.cumincad.org/data/works/att/acadia18\\_434.pdf](http://papers.cumincad.org/data/works/att/acadia18_434.pdf).
- [15] P.-C. Aïtcin, R.J. Flatt, *Science and Technology of Concrete Admixtures*, Elsevier, 2016. <https://www.elsevier.com/books/science-and-technology-of-concrete-admixtures/aitcin/978-0-08-100693-1>.
- [16] R. Flatt, I. Schober, Superplasticizers and the rheology of concrete, in: *Understanding the Rheology of Concrete*, Elsevier, 2012: pp. 144–208. <https://doi.org/10.1533/9780857095282.2.144>.
- [17] J. Plank, E. Sakai, C.W. Miao, C. Yu, J.X. Hong, Chemical admixtures — Chemistry, applications and their impact on concrete microstructure and durability, *Cement and Concrete Research.* 78 (2015) 81–99. <https://doi.org/10.1016/j.cemconres.2015.05.016>.
- [18] G. Gelardi, R.J. Flatt, Working mechanisms of water reducers and superplasticizers, in: *Science and Technology of Concrete Admixtures*, Elsevier, 2016: pp. 257–278. <https://doi.org/10.1016/B978-0-08-100693-1.00011-4>.
- [19] D. Marchon, R.J. Flatt, Impact of chemical admixtures on cement hydration, in: *Science and Technology of Concrete Admixtures*, Elsevier, 2016: pp. 279–304. <https://doi.org/10.1016/B978-0-08-100693-1.00012-6>.
- [20] B. Lothenbach, W. Frank, Influence of superplasticizers on the hydration of Portland cement, in: *12th International Congress on the Chemistry of Cement*, Montreal, Canada, July 8-13, 2007, At Montreal, Canada, 2007.
- [21] D. Marchon, F. Boscaro, R.J. Flatt, First steps to the molecular structure optimization of polycarboxylate ether superplasticizers: Mastering fluidity and retardation, *Cement and Concrete Research.* 115 (2019) 116–123. <https://doi.org/10.1016/j.cemconres.2018.10.009>.
- [22] F. Ridi, E. Fratini, P. Luciani, F. Winnefeld, P. Baglioni, Tricalcium Silicate Hydration Reaction in the Presence of Comb-Shaped Superplasticizers: Boundary Nucleation and Growth Model Applied to Polymer-Modified Pastes, *J. Phys. Chem. C.* 116 (2012) 10887–10895. <https://doi.org/10.1021/jp209156n>.

- [23] J. Dubochet, M. Adrian, J.-J. Chang, J.-C. Homo, J. Lepault, A.W. McDowell, P. Schultz, Cryo-electron microscopy of vitrified specimens, *Quart. Rev. Biophys.* 21 (1988) 129–228. <https://doi.org/10.1017/S0033583500004297>.
- [24] M. Adrian, J. Dubochet, J. Lepault, A.W. McDowell, Cryo-electron microscopy of viruses, *Nature*. 308 (1984) 32–36.
- [25] H. Moor, Theory and Practice of High Pressure Freezing, in: Steinbrecht R.A., Zierold K. (Eds) *Cryotechniques in Biological Electron Microscopy*, Springer Berlin Heidelberg, 1987.
- [26] A. Zingg, Cement-Superplasticizer Interaction: Link between Macroscopic Phenomena and Microstructural Data of the Early Cement Hydration, ETH Zürich, 2008. <https://doi.org/10.3929/ethz-a-005556687>.
- [27] C. Villinger, G. Neusser, C. Kranz, P. Walther, T. Mertens, 3D Analysis of HCMV Induced-Nuclear Membrane Structures by FIB/SEM Tomography: Insight into an Unprecedented Membrane Morphology, *Viruses*. 7 (2015) 5686–5704. <https://doi.org/10.3390/v7112900>.
- [28] D. Marchon, Controlling cement hydration through the molecular structure of comb copolymer superplasticizers, ETH Zurich, 2016. <https://doi.org/10.3929/ethz-a-010798278>.
- [29] R.A. Buswell, W.R. Leal de Silva, S.Z. Jones, J. Dirrenberger, 3D printing using concrete extrusion: A roadmap for research, *Cement and Concrete Research*. 112 (2018) 37–49. <https://doi.org/10.1016/j.cemconres.2018.05.006>.
- [30] R.J.M. Wolfs, F.P. Bos, T.A.M. Salet, Early age mechanical behaviour of 3D printed concrete: Numerical modelling and experimental testing, *Cement and Concrete Research*. 106 (2018) 103–116. <https://doi.org/10.1016/j.cemconres.2018.02.001>.
- [31] A. Perrot, D. Rangeard, A. Pierre, Structural built-up of cement-based materials used for 3D-printing extrusion techniques, *Mater Struct.* 49 (2016) 1213–1220. <https://doi.org/10.1617/s11527-015-0571-0>.
- [32] R.J.M. Wolfs, A.S.J. Suiker, Structural failure during extrusion-based 3D printing processes, *Int J Adv Manuf Technol.* 104 (2019) 565–584. <https://doi.org/10.1007/s00170-019-03844-6>.
- [33] T.A.M. Salet, Z.Y. Ahmed, F.P. Bos, H.L.M. Laagland, Design of a 3D printed concrete bridge by testing, *Virtual and Physical Prototyping*. 13 (2018) 222–236. <https://doi.org/10.1080/17452759.2018.1476064>.
- [34] DBT, ETH Zürich, Concrete Choreography, Origen Festival, Riom, Switzerland, (2019). <http://dbt.arch.ethz.ch/project/concrete-choreography/>.
- [35] T. Wangler, N. Roussel, F.P. Bos, T.A.M. Salet, R.J. Flatt, Digital Concrete: A Review, *Cement and Concrete Research*. 123 (2019) 105780. <https://doi.org/10.1016/j.cemconres.2019.105780>.
- [36] D. Asprone, C. Menna, F.P. Bos, T.A.M. Salet, J. Mata-Falcón, W. Kaufmann, Rethinking reinforcement for digital fabrication with concrete, *Cement and Concrete Research*. 112 (2018) 111–121. <https://doi.org/10.1016/j.cemconres.2018.05.020>.

- [37] H. Kloft, H.-W. Krauss, N. Hack, E. Herrmann, S. Neudecker, P.A. Varady, D. Lowke, Influence of process parameters on the interlayer bond strength of concrete elements additive manufactured by Shotcrete 3D Printing (SC3DP), *Cement and Concrete Research*. 134 (2020) 106078. <https://doi.org/10.1016/j.cemconres.2020.106078>.
- [38] I. Dressler, N. Freund, D. Lowke, The Effect of Accelerator Dosage on Fresh Concrete Properties and on Interlayer Strength in Shotcrete 3D Printing, *Materials*. 13 (2020) 374. <https://doi.org/10.3390/ma13020374>.
- [39] E. Dini, D-Shape, (n.d.). <https://d-shape.com/>.
- [40] D. Lowke, E. Dini, A. Perrot, D. Weger, C. Gehlen, B. Dillenburger, Particle-bed 3D printing in concrete construction – Possibilities and challenges, *Cement and Concrete Research*. 112 (2018) 50–65. <https://doi.org/10.1016/j.cemconres.2018.05.018>.
- [41] G. Cesaretti, E. Dini, X. De Kestelier, V. Colla, L. Pambaguian, Building components for an outpost on the Lunar soil by means of a novel 3D printing technology, *Acta Astronautica*. 93 (2014) 430–450. <https://doi.org/10.1016/j.actaastro.2013.07.034>.
- [42] E. Dini, Method for automatically producing a conglomerate structure and apparatus therefor, (n.d.). <https://patents.google.com/patent/US8337736B2/en> (accessed October 9, 2019).
- [43] E. Dini, M. Chiarugi, R. Nannini, Method and Device for Building Automatically Conglomerate Structures, US20080148683A1, 2008. <https://patents.google.com/patent/US20080148683A1/en> (accessed April 7, 2020).
- [44] E. Lloret-Fritschi, T. Wangler, L. Gebhard, J. Mata-Falcón, S. Mantellato, F. Scotto, J. Burger, A. Szabo, N. Ruffray, L. Reiter, F. Boscaro, W. Kaufmann, M. Kohler, F. Gramazio, R.J. Flatt, From Smart Dynamic Casting to a growing family of Digital Casting Systems, in: *Digital Concrete 2020, 2nd RILEM International Conference on Concrete and Digital Fabrication*, Cement and Concrete Research, Eindhoven, Netherlands, 2020.
- [45] G.A. Catenacci, Method of slip forming concrete, US4152382A, 1979. <https://patents.google.com/patent/US4152382A/en> (accessed April 8, 2020).
- [46] E. Lloret Fritschi, Smart Dynamic Casting - A digital fabrication method for non-standard concrete structures, ETH Zurich, Switzerland, 2016. <http://hdl.handle.net/20.500.11850/123830> (accessed October 30, 2019).
- [47] L. Reiter, R. Käßmann, A.R. Shahab, T. Wangler, R.J. Flatt, Strategies to wake up sleeping concrete, in: *ICCC 2015 Beijing: The 14th International Congress on the Chemistry of Cement*, Abstract Book, ICC 2015 Beijing, 2015: p. 340. <https://www.research-collection.ethz.ch/handle/20.500.11850/108066> (accessed April 8, 2020).
- [48] A. Szabo, L. Reiter, E. Lloret-Fritschi, F. Gramazio, M. Kohler, R.J. Flatt, Mastering Yield Stress Evolution and Formwork Friction for Smart Dynamic Casting, in: *Digital Concrete 2020, 2nd RILEM International Conference on*

- Concrete and Digital Fabrication, Cement and Concrete Research, Eindhoven, Netherlands, 2020.
- [49] A. Szabo, L. Reiter, E. Lloret-Fritschi, F. Gramazio, M. Kohler, R.J. Flatt, Adapting Smart Dynamic Casting to Thin Folded Geometries, in: First RILEM International Conference on Concrete and Digital Fabrication – Digital Concrete 2018, Cement and Concrete Research, Zürich, Switzerland, 2018.
- [50] L. Reiter, T. Wangler, A. Anton, R.J. Flatt, Setting on demand for digital concrete – Principles, measurements, chemistry, validation, in: Digital Concrete 2020, 2nd RILEM International Conference on Concrete and Digital Fabrication, Cement and Concrete Research, Eindhoven, Netherlands, 2020.
- [51] A. Szabo, Digital Casting of Thin Folded Concrete Structures, in: Digital Concrete 2020 (Abstract Submitted), Eindhoven, Netherlands, 2020.
- [52] A. Colmant, M. Graf, N. Neff, Digital Casting: A large folded structure demonstrator, (2019).
- [53] R.H. Lab, Think formwork–reduce cost, Structure Magazine. 14 (2007). <https://www.structuremag.org/?p=6141>.
- [54] J. Burger, E. Lloret-Fritschi, F. Scotto, T. Demoulin, L. Gebhard, J. Mata-Falcón, F. Gramazio, M. Kohler, R.J. Flatt, Eggshell: Ultra-thin 3D Printed Formwork for Concrete Structures, In Press for: 3D Printing and Additive Manufacturing. (2020).
- [55] M.C.G. Juenger, R. Siddique, Recent advances in understanding the role of supplementary cementitious materials in concrete, Cement and Concrete Research. 78 (2015) 71–80. <https://doi.org/10.1016/j.cemconres.2015.03.018>.
- [56] E. Gallucci, P. Mathur, K. Scrivener, Microstructural development of early age hydration shells around cement grains, Cement and Concrete Research. 40 (2010) 4–13. <https://doi.org/10.1016/j.cemconres.2009.09.015>.
- [57] P.J.M. Monteiro, A.P. Kirchheim, S. Chae, P. Fischer, A.A. MacDowell, E. Schaible, H.R. Wenk, Characterizing the nano and micro structure of concrete to improve its durability, Cement and Concrete Composites. 31 (2009) 577–584. <https://doi.org/10.1016/j.cemconcomp.2008.12.007>.
- [58] K.L. Scrivener, Backscattered electron imaging of cementitious microstructures: understanding and quantification, Cement and Concrete Composites. 26 (2004) 935–945. <https://doi.org/10.1016/j.cemconcomp.2004.02.029>.
- [59] J.E. Rossen, K.L. Scrivener, Optimization of SEM-EDS to determine the C–A–S–H composition in matured cement paste samples, Materials Characterization. 123 (2017) 294–306. <https://doi.org/10.1016/j.matchar.2016.11.041>.
- [60] P.-F. Jia, H.-J. Li, W. Yang, Transmission Electron Microscopy (TEM) to Study Histology of Pollen and Pollen Tubes, in: Methods in Molecular Biology, 2017: pp. 181–189. [https://doi.org/10.1007/978-1-4939-7286-9\\_15](https://doi.org/10.1007/978-1-4939-7286-9_15).

- [61] A. Kaech, U. Ziegler, High-Pressure Freezing: Current State and Future Prospects, *Methods in Molecular Biology* (Clifton, N.J.). 1117 (2014) 151–71. [https://doi.org/10.1007/978-1-62703-776-1\\_8](https://doi.org/10.1007/978-1-62703-776-1_8).
- [62] L. Keller, L. Holzer, R. Wepf, P. Gasser, B. Münch, P. Marschall, On the application of focused ion beam nanotomography in characterizing the 3D pore space geometry of Opalinus clay, *Physics and Chemistry of the Earth*. 36 (2011) 1539–1544.
- [63] J.A. Taillon, C. Pellegrinelli, Y.-L. Huang, E.D. Wachsman, L.G. Salamanca-Riba, Improving microstructural quantification in FIB/SEM nanotomography, *Ultramicroscopy*. 184 (2018) 24–38. <https://doi.org/10.1016/j.ultramic.2017.07.017>.
- [64] L. Ferrari, J. Kaufmann, F. Winnefeld, J. Plank, Interaction of cement model systems with superplasticizers investigated by atomic force microscopy, zeta potential, and adsorption measurements, *Journal of Colloid and Interface Science*. 347 (2010) 15–24. <https://doi.org/10.1016/j.jcis.2010.03.005>.
- [65] L. Ferrari, J. Kaufmann, F. Winnefeld, J. Plank, Multi-method approach to study influence of superplasticizers on cement suspensions, *Cement and Concrete Research*. 41 (2011) 1058–1066. <https://doi.org/10.1016/j.cemconres.2011.06.010>.
- [66] C. Giraudeau, J.-B. d’Espinose de Lacaillerie, Z. Souguir, A. Nonat, R.J. Flatt, Surface and Intercalation Chemistry of Polycarboxylate Copolymers in Cementitious Systems, *Journal of the American Ceramic Society*. 92 (2009) 2471–2488. <https://doi.org/10.1111/j.1551-2916.2009.03413.x>.
- [67] L. Ferrari, J. Kaufmann, F. Winnefeld, J. Plank, Impact of particle size on interaction forces between ettringite and dispersing comb-polymers in various electrolyte solutions, *Journal of Colloid and Interface Science*. 419 (2014) 17–24. <https://doi.org/10.1016/j.jcis.2013.12.041>.
- [68] A. Lange, J. Plank, Formation of Nano-Sized Ettringite Crystals Identified as Root Cause for Cement Incompatibility of PCE Superplasticizers, in: K. Sobolev, S.P. Shah (Eds.), *Nanotechnology in Construction*, Springer International Publishing, Cham, 2015: pp. 55–63. [http://link.springer.com/10.1007/978-3-319-17088-6\\_6](http://link.springer.com/10.1007/978-3-319-17088-6_6) (accessed June 12, 2015).
- [69] S. Galmarini, A. Aimable, N. Ruffray, P. Bowen, Changes in portlandite morphology with solvent composition: Atomistic simulations and experiment, *Cement and Concrete Research*. 41 (2011) 1330–1338. <https://doi.org/10.1016/j.cemconres.2011.04.009>.
- [70] P.J. Potts, Electron probe microanalysis, in: P.J. Potts (Ed.), *A Handbook of Silicate Rock Analysis*, Springer Netherlands, Dordrecht, 1987: pp. 326–382. [https://doi.org/10.1007/978-94-015-3988-3\\_10](https://doi.org/10.1007/978-94-015-3988-3_10).
- [71] B. Münch, P. Trtik, F. Marone, M. Stampanoni, Stripe and ring artifact removal with combined wavelet — Fourier filtering, *Opt. Express*, OE. 17 (2009) 8567–8591. <https://doi.org/10.1364/OE.17.008567>.
- [72] L. Holzer, P. Gasser, A. Kaech, M. Wegmann, A. Zingg, R. Wepf, B. Muench, Cryo-FIB-nanotomography for quantitative analysis of particle structures in

- cement suspensions, *Journal of Microscopy*. 227 (2007) 216–228. <https://doi.org/10.1111/j.1365-2818.2007.01804.x>.
- [73] N. Ruffray, M. Bernhard, A. Jipa, N. Montague De Taisne, F. Stutz, T. Wangler, R.J. Flatt, B. Dillenburger, Complex architectural elements from HPFRC and 3D printed sandstone, in: Montpellier, France, 2017: pp. 135–144. [https://www.rilem.net/publication/publication/490?id\\_papier=11239](https://www.rilem.net/publication/publication/490?id_papier=11239).
- [74] M. Upadhyay, T. Sivarupan, M. El Mansori, 3D printing for rapid sand casting—A review, *Journal of Manufacturing Processes*. 29 (2017) 211–220. <https://doi.org/10.1016/j.jmapro.2017.07.017>.
- [75] Y.W.D. Tay, B. Panda, S.C. Paul, N.A. Noor Mohamed, M.J. Tan, K.F. Leong, 3D printing trends in building and construction industry: a review, *Virtual and Physical Prototyping*. 12 (2017) 261–276. <https://doi.org/10.1080/17452759.2017.1326724>.
- [76] A. Pierre, D. Weger, A. Perrot, D. Lowke, Penetration of cement pastes into sand packings during 3D printing: analytical and experimental study, *Mater Struct*. 51 (2018) 22. <https://doi.org/10.1617/s11527-018-1148-5>.
- [77] D. Weger, D. Lowke, C. Gehlen, 3D printing of concrete structures using the selective binding method – Effect of concrete technology on contour precision and compressive strength, in: 2016.
- [78] IAAC, 3D printed bridge, (n.d.). <https://iaac.net/project/3d-printed-bridge/>.
- [79] M. Hansmeyer, B. Dillenburger, Printing Architecture - Castles Made of Sand, in: *Fabricate: Negotiating Design & Making*, Fabio Gramazio, Matthias Kohler and Silke Langenberg, Zürich, n.d.: pp. 92–97.
- [80] Voxeljet, Sand Molds for Ultra-High Performance Concrete, (2014). <http://www.voxeljet.de/en/industries/foundries/casting-of-concrete/>.
- [81] Incidental Space, A Project by Christian Kerez at the Swiss Pavilion (2016), n.d. <https://biennials.ch/home/ProjectDetail.aspx?ProjectId=23>.
- [82] O. Mazanec, D. Lowke, P. Schießl, Mixing of high performance concrete: effect of concrete composition and mixing intensity on mixing time, *Mater Struct*. 43 (2010) 357–365. <https://doi.org/10.1617/s11527-009-9494-y>.
- [83] P. Schießl, O. Mazanec, D. Lowke, SCC and UHPC — Effect of Mixing Technology on Fresh Concrete Properties, in: C.U. Grosse (Ed.), *Advances in Construction Materials 2007*, Springer, Berlin, Heidelberg, 2007: pp. 513–522. [https://doi.org/10.1007/978-3-540-72448-3\\_52](https://doi.org/10.1007/978-3-540-72448-3_52).
- [84] P. Stähli, Ultra-fluid, oriented hybrid-fibre-concrete, (2008). <http://e-collection.library.ethz.ch/eserv/eth:31102/eth-31102-02.pdf>.
- [85] L.L. Beghini, A. Beghini, N. Katz, W.F. Baker, G.H. Paulino, Connecting architecture and engineering through structural topology optimization, *Engineering Structures*. 59 (2014) 716–726. <https://doi.org/10.1016/j.engstruct.2013.10.032>.
- [86] A. Søndergaard, P. Dombernowsky, Unikabeton Prototype, in: London, 2011.

- [87] L. Martinie, J.-F. Lataste, N. Roussel, Fiber orientation during casting of UHPFRC: electrical resistivity measurements, image analysis and numerical simulations, *Mater Struct.* 48 (2015) 947–957. <https://doi.org/10.1617/s11527-013-0205-3>.
- [88] A. Jipa, M. Bernhard, N. Ruffray, T. Wangler, R. Flatt, B. Dillenburger, Formwork fabrication freedom for a concrete canoe, *Gestão & Tecnologia de Projetos*. 14 (2019) 25–44. <https://doi.org/10.11606/gtp.v14i1.148264>.
- [89] A. Jipa, M. Bernhard, M. Meibodi, B. Dillenburger, 3D-Printed Stay-in-Place Formwork for Topologically Optimized Concrete Slabs, in: *TxA Emerging Design + Technology*, San Antonio, Texas, USA, 2016.
- [90] S. Oesterle, A. Vansteenkiste, A. Mirjan, Zero waste free-form formwork, in: *Second International Conference on Flexible Formwork, ICFF. CICM and University of Bath, Dept. of Architecture and Civil Engineering*, 2012.
- [91] N. Hack, W. Lauer, S. Langenberg, F. Gramazio, M. Kohler, Overcoming Repetition: Robotic Fabrication Processes at a Large Scale, *International Journal of Architectural Computing*. 11 (2013) 285–299. <https://doi.org/10.1260/1478-0771.11.3.285>.
- [92] R. Rust, F. Gramazio, M. Kohler, Spatial Wire Cutting: Cooperative robotic cutting of non-ruled surface geometries for bespoke building components, in: *Living Systems and Micro-Utopias: Towards Continuous Designing, Proceedings of the 21st International Conference on Computer-Aided Architectural Design Research in Asia (CAADRIA 2016)*, Melbourne, Australia, 2016.
- [93] N. Hack, W. Lauer, F. Gramazio, M. Kohler, Mesh Mould: Robotically Fabricated Metal Meshes as Concrete Formwork and Reinforcement, *Architectural Design*. 84 (2014) 44–53.
- [94] D. Veenendaal, M. West, P. Block, History and overview of fabric formwork: using fabrics for concrete casting, *Structural Concrete*. 12 (2011) 164–177. <https://doi.org/10.1002/suco.201100014>.
- [95] M. Popescu, L. Reiter, A. Liew, T. Van Mele, R.J. Flatt, P. Block, Building in Concrete with an Ultra-lightweight Knitted Stay-in-place Formwork: Prototype of a Concrete Shell Bridge, *Structures*. 14 (2018) 322–332. <https://doi.org/10.1016/j.istruc.2018.03.001>.
- [96] M. Aghaei-Meibodi, M. Bernhard, A. Jipa, B. Dillenburger, The Smart Takes from the Strong, in: *Fabricate 2017: Rethinking Design and Construction*, University of Stuttgart, Germany, 2017.
- [97] B. Peters, Additive Formwork: 3D Printed Flexible Formwork, in: *ACADIA 14: Design Agency*, Los Angeles, 2014.
- [98] E. Lloret, A.R. Shahab, M. Linus, R.J. Flatt, F. Gramazio, M. Kohler, S. Langenberg, Complex concrete structures: Merging existing casting techniques with digital fabrication, *Computer-Aided Design*. 60 (2015) 40–49. <https://doi.org/10.1016/j.cad.2014.02.011>.
- [99] M. Fontana, R.J. Flatt, D. Marchon, L. Reiter, Switzerland Patent No. EP 2 902 183 A1, E. P. Office, n.d.



- [100] B.K. Post, R.F. Lind, P.D. Lloyd, V. Kunc, J.M. Linhal, L.J. Love, The Economics of Big Area Additive Manufacturing, in: Oak Ridge National Laboratory (ORNL), Oak Ridge, TN (United States). Manufacturing Demonstration Facility (MDF), Solid Freeform Fabrication 2016: Proceedings of the 26th Annual International, 2016.
- [101] I. Agustí-Juan, G. Habert, Environmental design guidelines for digital fabrication, *Journal of Cleaner Production*. 142 (2017) 2780–2791. <https://doi.org/10.1016/j.jclepro.2016.10.190>.
- [102] I. Agustí-Juan, G. Habert, An Environmental Perspective on Digital Fabrication in Architecture and Construction, 21st International Conference on Computer-Aided Architectural Design Research in Asia (CAADRIA 2016), Melbourne, Australia, 2016. (n.d.).
- [103] G.W. Clough, J.M. Duncan, Earth Pressures, in: H.-Y. Fang (Ed.), *Foundation Engineering Handbook*, Springer US, Boston, MA, 1991: pp. 223–235. [https://doi.org/10.1007/978-1-4757-5271-7\\_6](https://doi.org/10.1007/978-1-4757-5271-7_6).
- [104] L. Gebhard, R.J. Flatt, N. Roussel, Spaghetti and meatball concrete or the art of engineered jamming, in: 2018. <https://www.research-collection.ethz.ch/handle/20.500.11850/314462> (accessed May 18, 2020).
- [105] H. Heller, T. Wangler, N. Hack, A.N. Walzer, R.J. Flatt, Challenges in full scale filling of a digitally fabricated leaky formwork, in: 2018. <https://www.research-collection.ethz.ch/handle/20.500.11850/312952> (accessed May 18, 2020).
- [106] B.M. Tymrak, M. Kreiger, J.M. Pearce, Mechanical properties of components fabricated with open-source 3-D printers under realistic environmental conditions, *Materials & Design*. 58 (2014) 242–246. <https://doi.org/10.1016/j.matdes.2014.02.038>.
- [107] T. Letcher, M. Waytashek, Material Property Testing of 3D-Printed Specimen in PLA on an Entry-Level 3D Printer, in: *American Society of Mechanical Engineers Digital Collection*, 2015. <https://doi.org/10.1115/IMECE2014-39379>.
- [108] S.R. Rajpurohit, H.K. Dave, Tensile Strength of 3D Printed PLA Part, in: M.S. Shunmugam, M. Kanthababu (Eds.), *Advances in Additive Manufacturing and Joining*, Springer, Singapore, 2020: pp. 103–114. [https://doi.org/10.1007/978-981-32-9433-2\\_8](https://doi.org/10.1007/978-981-32-9433-2_8).
- [109] P. Suraneni, P.C. Bran Anleu, R.J. Flatt, Factors affecting the strength of structural lightweight aggregate concrete with and without fibers in the 1,200–1,600 kg/m<sup>3</sup> density range, *Mater Struct*. 49 (2016) 677–688. <https://doi.org/10.1617/s11527-015-0529-2>.
- [110] Friedli Balz, Pizzetti Luca, Hauswirth Dominik, Puzrin Alexander M., Ground-Buried Fiber-Optic Sensors for Object Identification, *Journal of Geotechnical and Geoenvironmental Engineering*. 145 (2019) 04018109. [https://doi.org/10.1061/\(ASCE\)GT.1943-5606.0002001](https://doi.org/10.1061/(ASCE)GT.1943-5606.0002001).
- [111] N.P. Hack, Mesh Mould: A robotically fabricated structural stay-in-place formwork system, PhD Thesis, ETH Zurich, 2018. [https://www.researchgate.net/publication/325362607\\_Mesh\\_Mould\\_A\\_robotically\\_fabricated\\_structural\\_stay-in-place\\_formwork\\_system](https://www.researchgate.net/publication/325362607_Mesh_Mould_A_robotically_fabricated_structural_stay-in-place_formwork_system).

- [112] H. Lindemann, R. Gerbers, S. Ibrahim, F. Dietrich, E. Herrmann, K. Dröder, A. Raatz, H. Kloft, Development of a Shotcrete 3D-Printing (SC3DP) Technology for Additive Manufacturing of Reinforced Freeform Concrete Structures, in: T. Wangler, R.J. Flatt (Eds.), First RILEM International Conference on Concrete and Digital Fabrication – Digital Concrete 2018, Springer International Publishing, Cham, 2019: pp. 287–298. [https://doi.org/10.1007/978-3-319-99519-9\\_27](https://doi.org/10.1007/978-3-319-99519-9_27).
- [113] I. Dressler, N. Freund, D. Lowke, Control of Strand Properties Produced with Shotcrete 3D Printing by Accelerator Dosage and Process Parameters, in: F.P. Bos, S.S. Lucas, R.J.M. Wolfs, T.A.M. Salet (Eds.), Second RILEM International Conference on Concrete and Digital Fabrication, Springer International Publishing, Cham, 2020: pp. 42–52. [https://doi.org/10.1007/978-3-030-49916-7\\_5](https://doi.org/10.1007/978-3-030-49916-7_5).
- [114] N. Hack, H. Kloft, Shotcrete 3D Printing Technology for the Fabrication of Slender Fully Reinforced Freeform Concrete Elements with High Surface Quality: A Real-Scale Demonstrator, in: F.P. Bos, S.S. Lucas, R.J.M. Wolfs, T.A.M. Salet (Eds.), Second RILEM International Conference on Concrete and Digital Fabrication, Springer International Publishing, Cham, 2020: pp. 1128–1137. [https://doi.org/10.1007/978-3-030-49916-7\\_107](https://doi.org/10.1007/978-3-030-49916-7_107).
- [115] V. Mechtcherine, V.N. Nerella, H. Ogura, J. Grafe, E. Spaniol, M. Hertel, U. Füssel, Alternative Reinforcements for Digital Concrete Construction, in: T. Wangler, R.J. Flatt (Eds.), First RILEM International Conference on Concrete and Digital Fabrication – Digital Concrete 2018, Springer International Publishing, Cham, 2019: pp. 167–175. [https://doi.org/10.1007/978-3-319-99519-9\\_15](https://doi.org/10.1007/978-3-319-99519-9_15).
- [116] T. Marchment, J. Sanjayan, Penetration Reinforcing Method for 3D Concrete Printing, in: F.P. Bos, S.S. Lucas, R.J.M. Wolfs, T.A.M. Salet (Eds.), Second RILEM International Conference on Concrete and Digital Fabrication, Springer International Publishing, Cham, 2020: pp. 680–690. [https://doi.org/10.1007/978-3-030-49916-7\\_68](https://doi.org/10.1007/978-3-030-49916-7_68).
- [117] L. Hass, F. Bos, Bending and Pull-Out Tests on a Novel Screw Type Reinforcement for Extrusion-Based 3D Printed Concrete, in: F.P. Bos, S.S. Lucas, R.J.M. Wolfs, T.A.M. Salet (Eds.), Second RILEM International Conference on Concrete and Digital Fabrication, Springer International Publishing, Cham, 2020: pp. 632–645. [https://doi.org/10.1007/978-3-030-49916-7\\_64](https://doi.org/10.1007/978-3-030-49916-7_64).
- [118] O. Geneidy, S. Kumarji, A. Dubor, A. Sollazzo, Simultaneous Reinforcement of Concrete While 3D Printing, in: F.P. Bos, S.S. Lucas, R.J.M. Wolfs, T.A.M. Salet (Eds.), Second RILEM International Conference on Concrete and Digital Fabrication, Springer International Publishing, Cham, 2020: pp. 895–905. [https://doi.org/10.1007/978-3-030-49916-7\\_87](https://doi.org/10.1007/978-3-030-49916-7_87).
- [119] J. Burger, E. Lloret-Fritsch, F. Scotto, T. Demoulin, L. Gebhard, J. Mata-Falcón, F. Gramazio, M. Kohler, R.J. Flatt, Eggshell: Ultra-Thin Three-Dimensional Printed Formwork for Concrete Structures, 3D Printing and Additive Manufacturing. 7 (2020) 48–59. <https://doi.org/10.1089/3dp.2019.0197>.
- [120] A. Jipa, M. Bernhard, B. Dillenburger, Submillimetre Formwork: 3D-Printed Plastic Formwork for Concrete Elements, in: Texas Society of

- Architects, Austin, Texas, USA, 2017.  
[https://www.researchgate.net/publication/327792655\\_Submillimeter\\_Formwork\\_3D-Printed\\_Plastic\\_Formwork\\_for\\_Concrete\\_Elements](https://www.researchgate.net/publication/327792655_Submillimeter_Formwork_3D-Printed_Plastic_Formwork_for_Concrete_Elements).
- [121] N. Ruffray, From Fresh Concrete Microstructure to Digitally Fabricated HPFRC: A Challenging Journey up from the Nanoscale in Search of Precious Macro-Applications, PhD Thesis, ETH Zürich, 2020.
- [122] A. Szabo, E. Lloret-Fritschi, L. Reiter, F. Gramazio, M. Kohler, R.J. Flatt, Revisiting Folded Forms with Digital Fabrication, in: Blucher Design Proceedings, Editora Blucher, Porto, Portugal, 2019: pp. 191–200.  
[https://doi.org/10.5151/proceedings-ecaadesigradi2019\\_126](https://doi.org/10.5151/proceedings-ecaadesigradi2019_126).
- [123] A. Szabo, L. Reiter, E. Lloret-Fritschi, T. Wangler, F. Gramazio, M. Kohler, R.J. Flatt, ACDC: The Admixture Controlled Digital Casting and Its Application to Thin Folded Concrete Structures, in: F.P. Bos, S.S. Lucas, R.J.M. Wolfs, T.A.M. Salet (Eds.), Second RILEM International Conference on Concrete and Digital Fabrication, Springer International Publishing, Cham, 2020: pp. 956–966. [https://doi.org/10.1007/978-3-030-49916-7\\_93](https://doi.org/10.1007/978-3-030-49916-7_93).
- [124] M. Elsayy, K.-H. Kim, J.-W. Park, A. Deep, Hydrolytic degradation of polylactic acid (PLA) and its composites, Renewable and Sustainable Energy Reviews. 79 (2017) 1346–1352. <https://doi.org/10.1016/j.rser.2017.05.143>.
- [125] C.Y. Tham, Z. Abdul Hamid, Z.A. Ahmad, H. Ismail, Surface Engineered Poly(lactic acid) (PLA) Microspheres by Chemical Treatment for Drug Delivery System, Key Engineering Materials. 594–595 (2013) 214–218.  
<https://doi.org/10.4028/www.scientific.net/KEM.594-595.214>.
- [126] T. Casalini, F. Rossi, A. Castrovinci, G. Perale, A Perspective on Polylactic Acid-Based Polymers Use for Nanoparticles Synthesis and Applications, Front. Bioeng. Biotechnol. 7 (2019).  
<https://doi.org/10.3389/fbioe.2019.00259>.
- [127] E. Costa, P. Shepherd, J. Orr, T. Ibell, R. Oval, Automating Concrete Construction: Digital Design of Non-prismatic Reinforced Concrete Beams, in: F.P. Bos, S.S. Lucas, R.J.M. Wolfs, T.A.M. Salet (Eds.), Second RILEM International Conference on Concrete and Digital Fabrication, Springer International Publishing, Cham, 2020: pp. 863–872.  
[https://doi.org/10.1007/978-3-030-49916-7\\_84](https://doi.org/10.1007/978-3-030-49916-7_84).
- [128] T. Wangler, Digital Concrete: Research and Applications, in: Proceedings of the 10 Th International Concrete Congress, Istanbul, 2019.  
[http://manisa.imo.org.tr/resimler/ekutuphane/pdf/18392\\_19\\_31.pdf](http://manisa.imo.org.tr/resimler/ekutuphane/pdf/18392_19_31.pdf).

# Appendix A : HPFRC formulation design data

All additional relevant data gathered during the formulation design process of the high-performance fibre-reinforced concrete used for digital casting demonstrators presented and discussed in Chapter 4 and Chapter 5, can be found on the next page.



# Appendix B : Resolving stress induced corrosion of FMD 3D printed formwork to enable digital counter- pressure casting

This appendix presents a submission ready draft of a paper on resolving counter-pressure casting stress induced corrosion issues presented in Chapter 5 of this manuscript. Several results regarding this topic were acquired in final form between the submission of the manuscript and its defence. Following the recommendation of the jury to include these results in the final version of the manuscript and publish them, we are doing both in the form of this submission ready draft.

## Abstract

The rapid growth of interest towards concrete digital fabrication reflects the current aspiration for better, smarter, faster and greener construction means. Among a broad variety of techniques developed by our community, digital casting presents clear advantages regarding dimensional precision, geometrical freedom and surface finish of the produced elements. In contrast to robotic slip forming, the usage of digitally fabricated formworks requires simpler equipment. It however calls for easily shaped formworks, typically best 3D printed for example by fused deposition modelling (FDM). While such moulds can be easily fabricated with a wide range of commercially off-the-shelf available 3D printers, a shortcoming is the susceptibility of many polymers to stress induced corrosion, particularly when in contact with high pH solutions typical for cementitious materials.

This paper confirms the problem posed by this type of stress-induced corrosion and presents two very effective means of circumventing it: A silicon coating and cyclic olefin copolymer (COC).

Apart from this, in the specific case of counter-pressure casting (CPC), hydrostatic pressure must be resisted by a powder bed surrounding the formwork. The efficiency of such beds is examined and a particular mix of sand and lead is shown to be particularly effective, provided its density is regulated to balance stress principles derived from soil mechanics.

Presented applications include the successful counter-pressure casting of thin prismatic formworks with a concrete height up to 3 meters as representative of typical inter-floor load-bearing elements. The combination of counter-pressure and stress corrosion control is shown to be essential for such achievement, that highlight the potential of this approach as a viable member of the concrete digital casting family.

## B.1. Introduction

Digital fabrication with concrete is rapidly gaining interest and a variety of approaches have been proposed, as for example extrusion printing[10,29,31], Smart Dynamic Casting [12,46,49], Mesh Mould [13,93,111], Shotcreting [112–114] and powder bed printing [40,41]. All these processes have their respective advantages and shortcomings. Overall, however, the question of reinforcement appears to represent a main challenge, particularly for extrusion printing which is the widest spread of all these processes [36,115–118]. Thus, approaches in which reinforcement may be preplaced and the concrete casted, without causing



failure of the mould can be seen as offering substantial advantages in terms of easy regulatory adoption for structural elements [44,46,119].

The work presented in this article is a follow-up of a project realised in 2017, which consisted in producing a topology optimised high performance fibre reinforced concrete (HPFRC) canoe [88]. The canoe's 0.8mm thick formwork was 3D printed by fused deposition modelling (FDM) using transparent polylactic acid (PLA) filament [120]. In order to minimise the risks of failure of the formwork, a special casting procedure of the canoe's structure was developed: counter-pressure casting (CPC). This can be considered as a member of the broader family of digital casting processes [44,46,48]. CPC consists of placing the formwork inside a wooden box which is gradually filled with sand, the level of which is kept equal to the rising concrete during the casting by taking advantage of the translucent aspect of the formwork. Sand acts as a counter-pressure to the hydrostatic pressure of concrete, therefore stabilising the formwork during the casting process and reducing the formwork's load. Special attention was paid first to formulating the HPFRC in order to assure a continuous flow in the formwork without clogging and second to the casting procedure itself in order to avoid entrapped air pockets [73,121].

While adding a certain complexity to the casting process through the handling of the counter-pressure material, this approach is beneficial in comparison to both traditional [9] and other digital casting approaches. The geometrical freedom of FDM printed formworks combined with topology optimisation allows an important reduction of materials usage and cost in comparison to traditional wooden formworks [53]. When compared to other digital formwork casting approaches such as Eggshell [119] or the usage of thin tensioned foils for folded structures [122,123], CPC brings the non-negligible advantage of avoiding the need to finely control the setting and hardening of concrete through setting on demand [50,123], allowing a much wider choice of casting materials.

However, during the realisation of the concrete canoe project, important formwork failures and concrete leakages were observed on both casting prototypes and the canoe itself. Expected stresses were considerably lower than what would have been needed for failure of the 3D printed PLA. While these failures could not be addressed upstream at that time due to the project time constraints, the follow-up work presented in this article investigates the origin of these failures and brings practical solutions to avoid them, thus fully enabling the potential of CPC of thin FDM printed formworks.

## B.2. Materials and Methods

### B.2.1. FDM 3D printed formworks

Two types of plastic filaments were used during this study to produce the tested elements: transparent PLA NX-1 from *extruder* (Lauterach, Austria) and transparent cyclic olefin copolymer (COC) from *Creamelt* (Rapperswil-Jona, Switzerland). Two geometries were tested during this study: tubular and prismatic.

Tubular samples were printed with an inner diameter of 60 mm and a wall thickness of either 0.8 or 0.4 mm. Such samples were first printed in two 60 cm long parts and cold welded together using dichloromethane as can be observed in Figure B.2, left. As it became clear during the study that failure of the tubes was always occurring at their bottom, the 3D printed part of the tubes was then reduced to a height of 150 mm (e.g. Table B.1) and connected to a rigid PVC tube of similar diameter in order to reach an equivalent hydrostatic pressure of concrete. This strategy of adding a PVC tube on top of a 3D printed sample was also used for the prismatic samples (see Figure B.1).

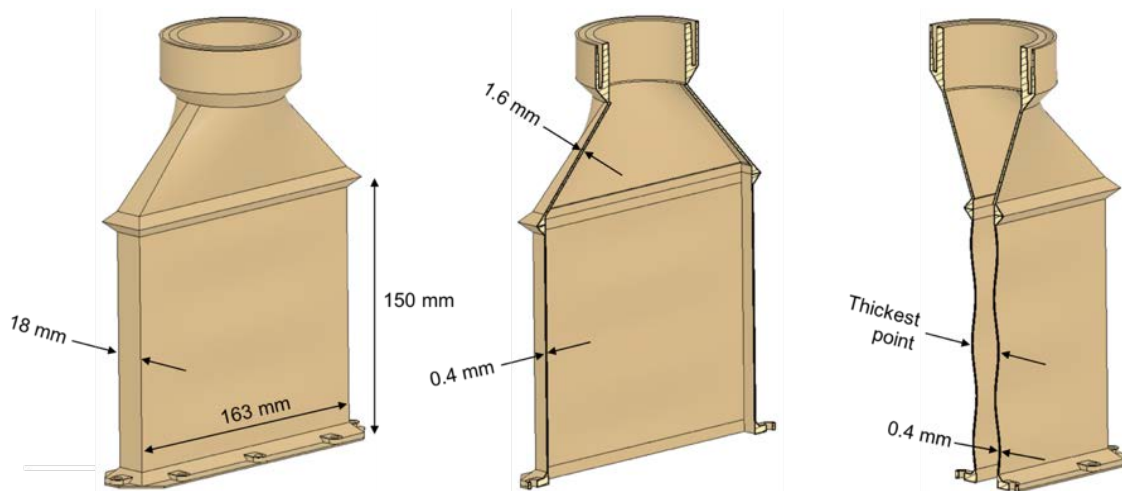


Figure B.1: Prismatic samples geometry. The effective dimension of the thickest point was  $25 \pm 2.0$  mm and  $28 \pm 0.3$  mm respectively for PLA and COC printed formworks.

The prismatic shape was selected to obtain formworks which deformations resulting from hydrostatic pressure of cast concrete would be amplified and easier to measure in comparison to a tubular shape which only presents Hoop stresses in the given configuration. However, FDM printing of straight thin walls is challenging as the warping of the plastic during the printing process tends to provoke an uncontrollable buckling resulting in a random barrelling of the printed walls. To minimise this effect and obtain more

reproducible dimensions, a defined wave pattern was introduced in the two large walls (163x150 mm) of the formwork (Figure B.1, right) in order to control the barrelling effect. This proved to be effective and resulted in effective dimensions of  $25\pm 2.0$  mm and  $28\pm 0.3$  mm respectively for PLA and COC printed formworks at their thickest point of the formwork as shown in Figure B.1, right.

### B.2.2. Inverted three points bending tests

In order to evaluate the role of stress induced corrosion on the strength of our 3D printed moulds, we used a three-point bending test. Modifications of this test were made for a study specifically examining stress induced corrosion of various 3D printed polymeric materials. Details of the method were kindly provided to us by Dr. Reiter (ETHZ) and can be looked up in an upcoming publication. The most important aspect of the test is the measurement of the flexural stress and strain curve on standardised samples, loading span and speed as described in EN ISO 178. The major modification of the standardised setup is the vertical inversion of the loading points in order to have the sample's face under tension facing upwards allowing to keep it in contact with a liquid during the test by depositing it on its surface.

The printing parameters of the 4x10x80 mm samples were chosen to better represent the load underwent by the formwork under hydrostatic pressure. Indeed, the orientation of the print and of the filling of the three-points bending tests were matched to correspond as closely as possible to those of the formworks in which the fused plastic is deposited in a mono-directional orientation parallel to the printing bed and ultimately perpendicular to the horizontal hydrostatic pressure of concrete.

For each case considered, three samples were measured from which the average and the standard deviation were determined. Samples were tested either: - in their dry state, - in contact with water, - or in contact with a 0.1 molar NaOH solution used to represent an alkaline environment similar to fresh concrete.

As shown in the later, the strength of PLA samples was severely affected by the NaOH solution, which is why we also tried applying different coatings to protect the PLA: two types of transparent acrylic varnishes, latex and molding silicone (all off the shelf commercial products). The coating of the samples was realised by dipping one of their 4x10 mm faces in the respective coatings and letting them cure accordingly to their respective supplier defined curing times in a vertical position prior to testing. Coatings minimal curing times were as follows: - Molding silicone: 1hr, - Latex = 4 hrs, - Acrylic varnishes = 12 hrs.

When used in combination with printed formwork elements, the coating material was poured inside the formwork that was then manually rotated in order to assure a complete coating of its inside. The formwork was then suspended in a vertical position to allow the excess of coating material to drip off the formwork until its' complete curing.

### B.2.3. Concrete Casting

#### *B.2.3.1. Concrete formulation and mixing procedure*

The work presented in this article was realised with the same HPRFC formulation used in 2017 to produce the topologically optimised concrete canoe *skelETHon*[88]. This formulation was originally developed and tested in 2016 to produce a topology optimised ceiling element[73].

#### *B.2.3.2. Counter-pressure casting*

Two different counter-pressure materials were tested during this work: an all-purpose sand; and a mix of quartz sand and lead granules. The second counter-pressure material was obtained by mixing together a mono-sized 0.1–0.45 mm quartz sand together with lead spherical granules with a diameter of 2.5 mm. The mass proportions of this mix were 79.2% of lead granules for 20.8 % of quartz sand (33.5% and 66.5% respectively by volume). The purpose of this mix was to increase the bulk density of loose sand acknowledged to have a value between 1.4 and 1.6 depending on its compaction[103]. The obtained sand and lead granules mix have a bulk density value of 4.8 allowing to increase the counter-pressure on the formwork in comparison to loose sand alone as explained in section B.3.1 of this article.

When casted in a counter-pressure configuration, the formwork was installed in a fitting wood box, one side of which was made out of transparent plexiglass allowing to observe and match the concrete and counter-pressure material levels during the casting. During the casting, the box was gradually filled with counter-pressure material in order to always keep a height difference between concrete and counter-pressure material levels under 5 cm. For formworks that were coated with non-transparent materials such as molding silicone, a metallic weight attached to a string was used to sound the levels of concrete and counter-pressure material. Once the formwork was completely filled, it was covered with an additional of 5 to 10 cm of counter-pressure material and let to cure for at least 24 hours prior to removing it from the box.

After removal of the cured element, the structural soundness of the formwork was assessed and final dimensions were measured. Variations with respect to the initial dimensions are presented in section B.3 of this article. They are given respectively to the tubular samples' diameter (60 mm) or to the prismatic formwork maximal deflection of its 163x150 mm walls in comparison to the dimensions presented in section B.2.1.

## B.3. Results and Discussion

### B.3.1. Preliminary PLA testing

To investigate the failure mechanics of PLA formwork, several tubular samples were casted (Figure B.2).

The first tube (Figure B.2, left) was casted without any counter-pressure material. This tube showed a failure at its bottom for a concrete height of 82 cm representing a hydrostatic pressure of 19.3 kPa with a concrete density of 2'400 kg/m<sup>3</sup>. At this particular hydrostatic pressure, the resulting Hoop stress at the bottom of the tube can be estimated to be equal to 146.7 kPa, representing 2.8% of the 53 MPa nominal tensile strength by the filament manufacturer. This result points toward a considerable chemical vulnerability of PLA to concrete resulting in stress induced corrosion and failure of the formwork for relatively low hydrostatic pressures if no counter-pressure or coating measures are put in place.

All tubes casted with sand as counter-pressure material showed a similar failure pattern presented in Figure B.2, centre. The failure only occurred on the lower halves of the tubes originating from a set of cracks at their bottom as observed in the sample without counter-pressure material described above. The rest of the failure presents an aspect of crack propagation mechanism resulting in an integrity failure of the lower halves of the tubes and a diametral deformation of up to +5.3 mm. The crack propagation appears to be stopped at the welding joint between the two halves of the tubes while the upper halves remain undamaged. These results indicate that the usage of sand as counter-pressure material is not sufficient to prevent a 0.8mm thick PLA formwork failure due to stress induced corrosion for concrete heights equal or greater than the one tested (1.2 meters).

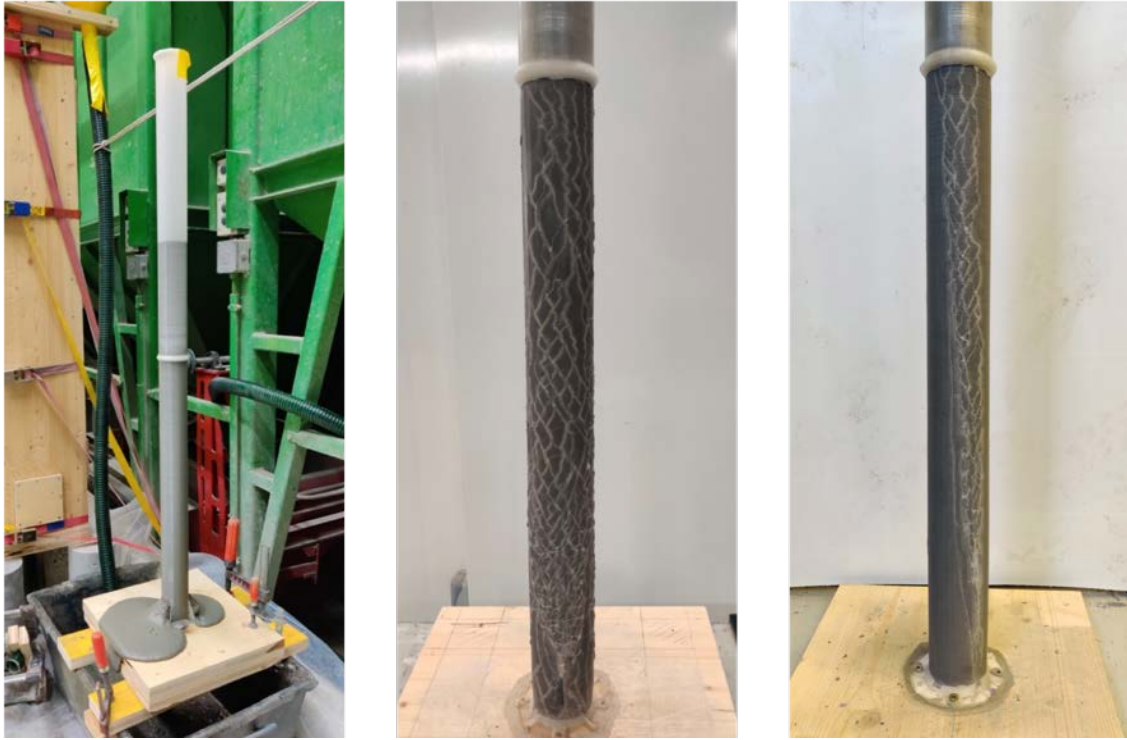


Figure B.2: Preliminary tests on PLA tubular formwork. Left: formwork failure without CPC at a concrete height of 82 cm. Centre: formwork failure with sand CPC. Right: formwork failure with sand and lead granules CPC.

In a trial to counteract the previously described failures, a first approach was implemented consisting in artificially increasing the sand density in order to increase the counter-pressure on the formwork. According to soil mechanics, the vertical and horizontal pressures exerted by a column of loose sand are not equal in contrast to a column of liquid and their relation is described as follows[103]:

$$\sigma_h = K_0 \cdot \sigma_v \quad (\text{B.1})$$

where  $\sigma_h$  is the horizontal pressure,  $\sigma_v$  the vertical one and  $K_0$  is the coefficient of earth pressure at rest considered to be equal to 0.45 - 0.5 for dry loose sand[103].

Considering that loose sand has a bulk density of 1'400 - 1'600 kg/m<sup>3</sup> depending on its compaction, we can deduce that sand can only counteract 26 to 33% of the concrete hydrostatic pressure. Therefore, in order to match the counter-pressure on the formwork to the hydrostatic pressure of concrete, a mix of sand and lead granules with a bulk density of 4'800 kg/m<sup>3</sup> was used as counter-pressure material (please refer to section B.2.3.2). Unfortunately, the tubes casted in this configuration presented the same type of failure (Figure B.2,

right) as the ones casted with only sand (Figure B.2, centre) with a diametral deformation measured of up to +1.7 mm.

Stress-induced corrosion is not only linked to the applied stress but also to the time-resolved chemical degradation of PLA in alkaline environments[124,125]. Therefore, even a slight difference between the counter and hydrostatic pressures could lead to the weakening of the formwork and its failure during the concrete's setting time frame, measured by isothermal calorimetry to be about 5.5 hours for the used HPFRC. While the diametral deformation seems to be reduced by the increase of counter-pressure, its non-zero value shows that regardless of the theoretical matching of counter and hydrostatic pressures, a deformation was still able to occur after the formwork's failure. The origin of this phenomena could be linked to the additional compaction required to attain a full mechanical lock of the counter-pressure material and would be worth looking into from a soil mechanics perspective.

These last results showed that PLA cannot be successfully used as concrete 3D printed formwork material without addressing its weakness to the alkalinity of concrete and finding an appropriate protective coating to mitigate the effects of stress induced corrosion. This led us to perform mechanical investigations regarding these aspects by using three-points bending testing.

### B.3.2. Stress induced corrosion attenuation investigations

In order to investigate the vulnerability to stress induced corrosion in alkaline environments of PLA and COC 3D printed parts, as well as to find a suitable coating for protecting PLA, inverted three-point bending tests were performed. The results of these tests are reported in Figure B.3.

While uncoated dry PLA presents an average flexural tensile strength of 109.7 MPa, a drop of 16 and 81 % of this value is observed when the sample is respectively in contact with water and 0.1 M NaOH solution (pH = 13). Even if PLA is not considered to be soluble in water, it undergoes a degradation driven by the hydrolysis of the polymer's backbone by water molecules[126]. In a highly alkaline environment, this hydrolysis is accelerated by the high concentration of OH<sup>-</sup> ions[124,125]. Combined to the tensile stress underwent by the samples during the test, this explains the losses in tensile strength due to stress induced corrosion. The pH of fresh concrete's pore solution varying between 12 and 13, it is safe to assume that the failures of PLA printed formwork described above resulted from the same phenomena explaining the abnormally poor mechanical resistance. The observation of distinctive cracks throughout the three-points bending samples in contact with alkaline solution also supports this interpretation.



Among the tested PLA coatings, none brought a significant increase in flexural tensile strength in the dry state compared to the uncoated sample (Figure B.3) allowing us to assume that the results obtained while in contact with alkaline solution are only dependant on the protection efficiency of the coatings in this configuration.

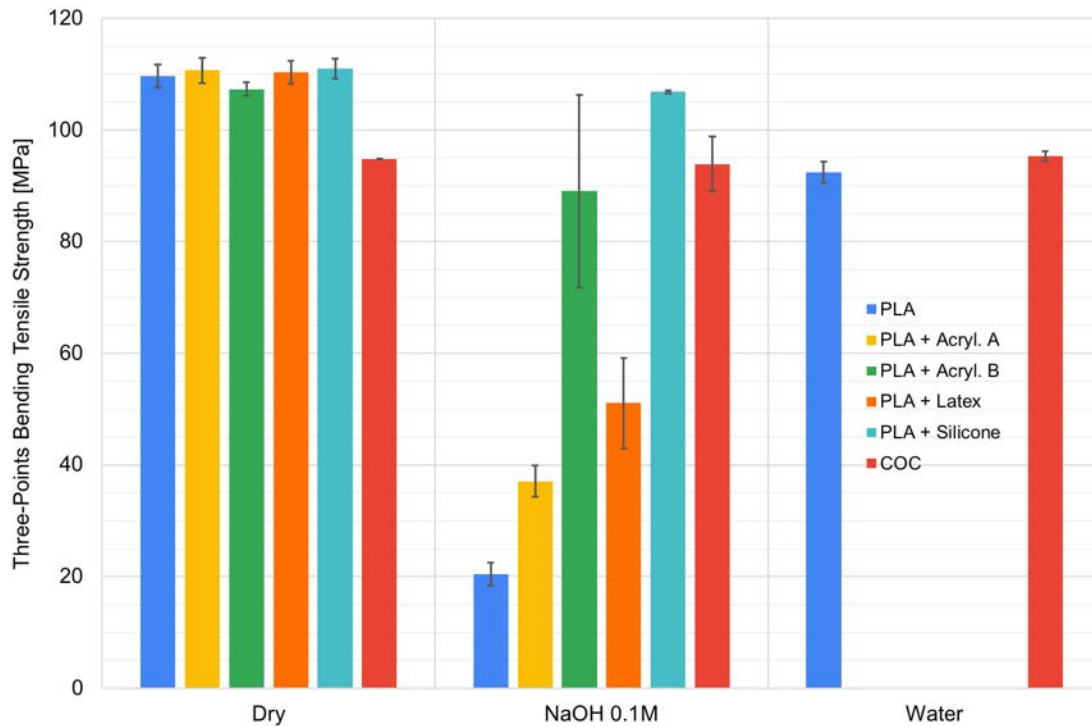


Figure B.3: Three-points bending tests results. Samples were tested in the following three states: - dry, -while in contact with water, - while in contact with a 0.1 M solution of NaOH (pH=13). For each data set, the given result is equal to the average of three samples while the error bars represent the standard deviation.

The results obtained for the coated PLA samples in contact with the 0.1 M NaOH solution show a considerable vulnerability of acrylic varnishes and latex coatings to alkaline environment, even if the acrylic varnish B seems to improve the resistance compared to both to the acrylic varnish A and the latex. Nevertheless, the important standard deviation obtained for this particular varnish does not offer much confidence in terms of achieving a robust protection.

Results obtained for the silicone coated PLA samples in contact with 0.1 M NaOH solution do not show any significant decrease in tensile strength in comparison to the dry uncoated ones. Therefore, this particular coating is fully adequate to protect PLA from highly alkaline solutions. It was therefore chosen

for application on the inside of printed formworks filled with concrete as presented in section B.3.3 of this article.





Apart from the question of PLA coatings, Figure B.3 also shows that COC samples did not present any significant variations in tensile strength when in contact with water or 0.1 M NaOH solution. Combined to the relative ease for FDM printing with this material, these results identify COC as a very promising candidate for concrete formwork 3D printing as presented in in section B.3.3 of this article.

### B.3.3. Enabling failure-free counter-pressure casting

#### B.3.3.1. Tubular formworks

Following the results obtained from three-points bending tests, a first series of tubular formworks were casted without counter-pressure as presented in Table B.1.

*Table B.1: Short tubes formwork tests Results. The concrete height for each sample was 120 cm and assured by the filling of an above connected rigid PVC pipe. Times at failure are given respectively to the end of the filling.*

Formwork Material & Thickness	PLA 0.8 mm		PLA 0.8 & 0.4 mm	COC 0.8 & 0.4 mm
Coating	None	Acrylic Varnish A	Molding Silicone	None
Result				
Time at Failure	≈ 15 mins	≈ 60 mins	N/A	N/A

The first formwork made of uncoated PLA was tested in order to verify that the new setup using shorter 3D printed parts and PVC tubes was reproducing the same type of failure as the fully 3D printed tubes presented in section B.3.1. The observed failure presented in Table B.1 confirmed this hypothesis. Additionally, due to a faster concrete filling rate in comparison to the samples presented in section B.3.1, the time dependency of the failure process was observed as it occurred 15 minutes after the entire filling of the 120 cm high sample highlighting the time-dependency nature of PLA stress induced corrosion.






In order to verify the reproducibility of the three-points bending tests, a tubular sample coated with acrylic varnish A was tested. The result confirmed the vulnerability of this coating to concrete alkalinity as the failure occurred about 60 minutes after the filling of the formwork. The 45 minutes difference with the uncoated formwork could correspond to the additional time required to the degradation of the coating.

Both silicone coated PLA and COC tubes did not present any failures or measurable deformations during these tests. These results confirm that molding silicone is an adequate coating that can be used to protect PLA formworks from stress induced corrosion and failure, therefore enabling the full potential of this versatile 3D printing material for usage in concrete digital fabrication. The absence of failure on COC 3D printed formworks demonstrates the chemical resistance of this material in alkaline environments observed during the three-points bending tests.

### B.3.3.2. Prismatic formworks


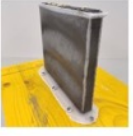

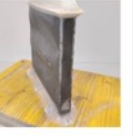
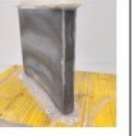
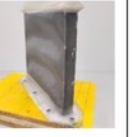



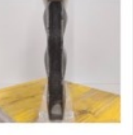
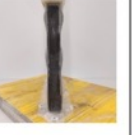

The results obtained on prismatic formworks are presented in Table B.2 and Table B.3 respectively for silicone coated PLA and COC. These results demonstrate that CPC can be successfully used to avoid failure of thin 3D printed formworks when stress induced corrosion is prevented.

Table B.2: PLA molding silicone coated prismatic formwork test results. The concrete height for each sample above 15 cm was assured by the filling of an above connected rigid PVC pipe. Maximum deflection is given for the largest faces of the prism.

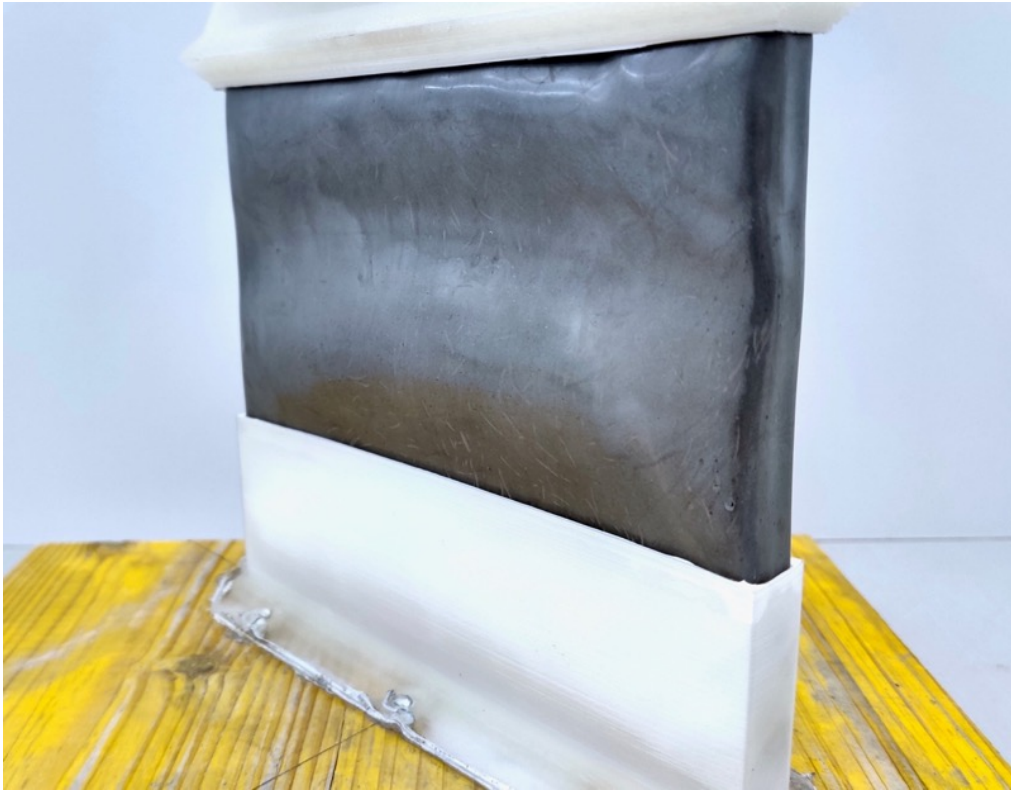
Counter-pressure Material	None			Sand	Sand & Lead Granules
Concrete Height	None	15 cm	$\approx 30$ cm	120 cm	
Result					
Maximum Deflection	$\pm 2.0$ mm	+11.9 mm	N/A	+3.7 mm	+1.6 mm

While silicone coated PLA formwork shows a barrelling deformation in comparison to the COC one for the 15 cm high samples casted without CPC, the other samples show a similar behaviour for both materials. 120 cm high samples casted without counter-pressure exhibit failure at concrete heights of about 30 cm. This similar behaviour between the two materials can be explained by their relatively similar tensile strength as presented in Figure B.3, in addition to the geometry of the formwork having been kept identical.

Table B.3: COC prismatic formwork test results. The concrete height for each sample above 15 cm was assured by the filling of an above connected rigid PVC pipe. Maximum deflection is given for the largest faces of the prism.

Counter-pressure Material	None			Sand	Sand & Lead Granules	
Concrete Height	None	15 cm	≈ 30 cm	120cm		300 cm
Result						
						
Maximum Deflection	±0.3 mm	+2.5 mm	N/A	+3.9 mm	+0.8 mm	+0.3 mm

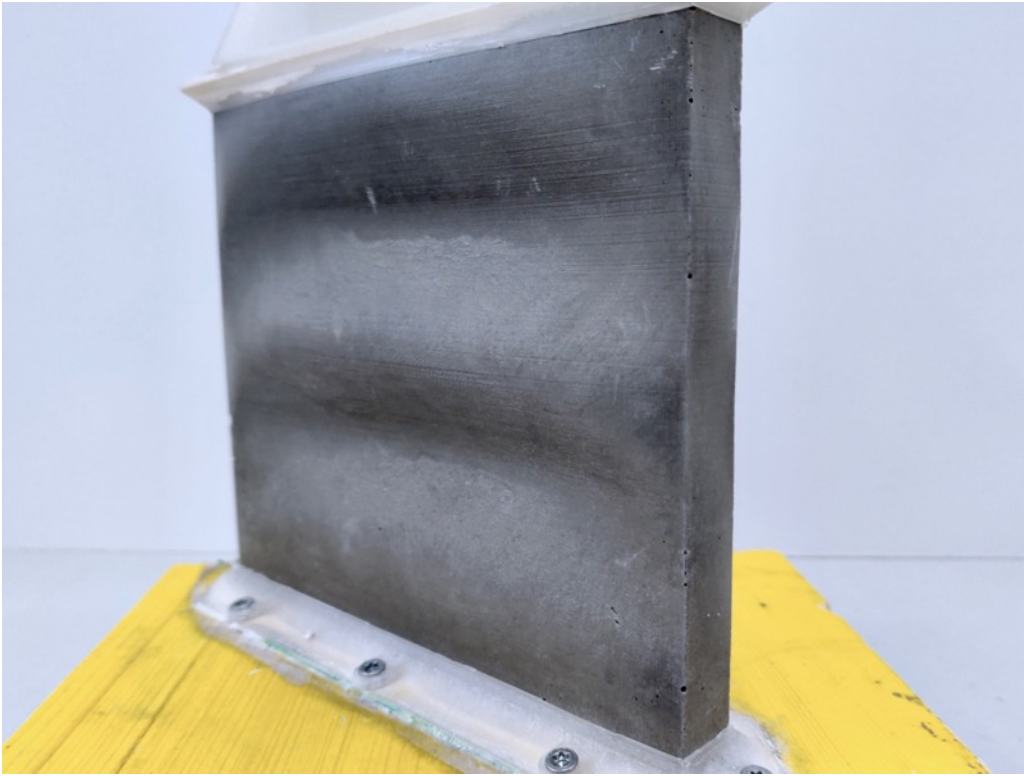
Samples casted with CPC did not present any failure while a variable deflection of the prisms' largest faces was observed as presented in Table B.2 and Table B.3. For both formwork materials, this deflection is considerably reduced by using sand and lead granules rather than sand only as counter-pressure material. When compared to the failure of prismatic samples discussed above, these results show that sufficient counter-pressure enables the casting of thin FDM printed formworks with a geometry otherwise prone to deformation and failure. These results also demonstrate that the approach of increasing the counter-pressure material bulk density presented in section B.3.1 reduces the dimensional changes of these kind of formworks.



*Figure B.4: Molding silicone coated PLA prismatic sample surface finish.*

From an aesthetic point of view, the surface finish obtained with silicone coated PLA and COC formworks are respectively presented in Figure B.5 and Figure B.6. It is important to note that while the COC formwork shows a mildly rough surface finish typical to FDM printed formworks where the printing layers are observable, the silicone coated PLA formwork shows a surprisingly pleasing, slightly glossy and totally smooth finish. This result is of particular interest as no additional surface treatments are required on either of the two formwork materials, allowing a choice of which surface finish is best suited for the desired application.





*Figure B.5: COC prismatic sample surface finish.*

The successful casting of a COC prismatic sample withstanding 3m of concrete hydrostatic pressure without failure or major deformation proves that this technique can be vertically upscaled and used to produce elements such as inter-floors columns. It enables the production of such elements with the geometrical freedom of FDM printing and with the liberty of using any kind of concrete that would be able to flow without clogging in the chosen formwork and without having the constraint of controlling its setting and hardening behaviour as casting takes place. While the integration of reinforcement in such elements would bring an additional complexity, it would broaden the range of structural performances that could be achieved. Interesting combination may also involve the combination of fibers and established continuous reinforcement systems, included but not limited to steel rebars. This technique brings additional promising opportunities into the growing concrete digital casting community and offers reasonable solutions to insuring structural integrity for highly loaded elements[35,36,115,127].



### *B.3.3.2. Outlooks*

Several outlooks are worth mentioning regarding CPC:

- While the usage of sand and lead granules as counter-pressure brought a significant improvement in dimensional changes, its use remains delicate from both health and recycling points of view. Indeed, working with this material produces a considerable amount of dust potentially contaminated with lead. Strict usage of dust removal systems and personal protective equipment such as dust masks, gloves and goggles is therefore imperative. The disposal and recycling of this material also requires special attention as it need to be treated in a dedicated way. The usage of a lead-free counter-pressure material would therefore be something worth looking into. This could be for example achievable by using a sand and steel granules mix in proportions that would match the desired bulk density (e.g. ratios of 85/15 by mass or 52/48 by volume respectively for carbon steel spherical granules dia. 2.5mm and 0.1–0.45 mm quartz sand would give a mix with a bulk density of 4'800 kg/m<sup>3</sup>).
- All performed tests were realised on relatively vertical formworks. Therefore, the question of the reliability of this technique on formworks containing horizontal overhangs would need to be assessed as the counter-pressure material has limited flow properties.
- If this technique were to be upscaled for industrial applications, it remains mainly suitable for off-site prefabrication of geometrically complex elements.

Finally, as a more general outlook beyond the strict case of CPC, the very good performance of both silicon coated PLA and COC are promising for other digital casting applications. In particular, for egg-shell[119] it would allow to work with a less tight control on the setting time, making it easier to place the material in a reliable and robust way.

## B.4. Conclusions

Counter-pressure casting has the potential of becoming a well appreciated and extensively used digital fabrication process in its own right. Important advantages that it has to offer include the easy inclusion of reinforcement, reduced reliance on a tight control of concrete setting and hardening kinetics, excellent surface finish, great ease of use, as well as a large range of formwork geometries accessible by FDM printing.

This paper demonstrate that two conditions are needed to achieve this potential. First the density of the powder bed must be selected to offer enough resistance to the hydrostatic pressure exerted by the concrete in the printed formwork. Second, the formwork must be resistant to stress induced corrosion that results from a combination of the high pH of cementitious materials and from the hydrostatic pressure.

The two solutions presented to the problem of stress induced corrosion can find a much broader application in digital casting processes relying of 3D printed formworks. All in all, those solutions as well as the general solutions presented for CPC should open the door to a wide variety of applications in the concrete digital fabrication community, highlighting once again the concept of “complexity for free”[128].

## Acknowledgements

The authors are thankful to Dr. Lex Reiter for instructions on the stress corrosion testing protocol, as well as to Heinz Richner and Andi Reusser for their help in caring out CPC experiments.